Winter 12-15-2018

DETECTION, CONTAINMENT AND SCALING RELATIONS OF NEAR SOURCE EXPLOSIONS IN GRANITE THROUGH MOMENT TENSOR REPRESENTATIONS

Mason MacPhail
mmacphail@smu.edu

DETECTION, CONTAINMENT AND SCALING RELATIONS OF

NEAR SOURCE EXPLOSIONS IN GRANITE THROUGH

MOMENT TENSOR REPRESENTATIONS

Approved by:

_____

Brian Stump
Albritton Chair of Geological Sciences

_____

Heather DeShon
Associate Professor of Earth Sciences

_____

Robert Gregory
Professor of Earth Sciences

_____

Chris Hayward
Director, Geophysics Research Program

_____

Robert Reinke
Defense Threat Reduction Agency

DETECTION, CONTAINMENT AND SCALING RELATIONS OF NEAR SOURCE EXPLOSIONS IN GRANITE THROUGH MOMENT TENSOR REPRESENTATIONS

A dissertation Presented to the Graduate Faculty of

Dedman College at

Southern Methodist University

in

Partial Fulfillment of the Requirements

for the degree of

Doctor of Philosophy

with a

Major in Geophysics

by

Mason MacPhail

B.S., Physics, University of Texas, Arlington

December 15, 2018

MacPhail, Mason B.S., Physics, University of Texas, Arlington

Detection, Containment and Scaling Relations of
Near Source Explosions in Granite Through
Moment Tensor Representations

Advisor: Professor Brian Stump

Doctor of Philosophy conferred December 15, 2018

Dissertation completed December 7, 2018

The Source Phenomenology Experiment (SPE) was a series of nine, single-fired chemical explosions within the Morenci Copper mine in Arizona. Its purpose was to design, detonate, record and analyze seismic waveforms from these single-fired, partially and fully contained explosions. Ground motion data from the SPE are analyzed in this study to assess the uniqueness of the source representation of these explosions and its ability to resolve yield and depth when containment and geology or physical parameters of the source region may have a range of possible values. The P-wave velocities (V_p) at the test site are well constrained by seismic refraction surveys, but the accompanying shear wave velocities (V_s) are less constrained. In order to assess the effects of source depth and V_s model on the seismic moment tensors, Green's functions were computed for different source depths as well as different V_s models, holding the V_p model constant. The Green's functions for the 16, near-source stations were calculated using a one-dimensional velocity model developed from the SPE employing

reflectivity modeling in order to include spherical wave effects, body waves and surface waves, focusing on observations in the 37-680 m range. The compensated linear vector dipole and explosion components of the Green's functions are compared to quantify the possible effects of source depth and V_S on the source representation on expected explosion contributions. For the forward model, Green's functions with variable depths of burial (DOB) and V_S are convolved with a time function based on the Mueller-Murphy (1971) isotropic source function produce synthetic seismograms for assessing possible tradeoffs between depth and yield in the source models. Our study suggests that the original SPE model parameter values used are most representative of the geology. Subsequently, observational data inversions are conducted within the frequency domain and moment tensors are decomposed into deviatoric and isotropic components to evaluate the effects of containment and yield on the resulting source representation. Isotropic moments are compared to those for other contained explosions as reported by Denny and Johnson (1991) and are in good agreement with their scaling results. Isotropic and M_{ZZ} moment tensor spectra are compared to Mueller-Murphy (1971), Denny-Johnson (1991) and revised Heard-Ackerman (Patton, 2012 b) models and suggest that the larger yield explosions with the most confinement fit the models best. Secondary source effects resulting from free surface interactions, including the effects of spallation, contribute to the resulting moment tensors, which include a CLVD component. Hudson diagrams, using frequency domain moment tensors, are computed as a tool to assess how these containment scenarios affect the source representation. Our analysis suggests that, within our band of interest (2-20 Hz), as the frequency increases, the source representation becomes more explosion like,

peaking at around 20 Hz. These results guide additional analysis of the observational data and the practical resolution of physical phenomenology accompanying underground explosions.

TABLE OF CONTENTS

LIST OF TABLES

Chapter 1 Tables

Chapter 2 Tables

Chapter 3 Tables

LIST OF FIGURES

Chapter 1 Figures

Chapter 2 Figures

Chapter 3 Figures

Appendix Figures

ACKNOWLEDGMENTS

This work could not have been accomplished without the help and guidance of my advisor, Brian Stump, and everyone else in the Earth Sciences department. I would also like to thank David Yang for his source model help. I am forever grateful to my wife, Cassidy, for being so patient and understanding along the way and to my parents for their love and support.

INTRODUCTION

The Non-Proliferation Experiment (NPE) (Denny et al, 1996), conducted by the Department of Energy (DOE), oversaw the detonation 1.29 million kilograms of ammonium nitrate fuel oil (ANFO) at Rainier Mesa in an attempt to discriminate nuclear explosions from other chemical explosions used worldwide for engineering purposes. Results from the NPE showed that a chemical explosion couples more energy into the surrounding medium than that of an equivalent yield nuclear explosion, giving the chemical explosion roughly twice the amplitude than that of a nuclear explosion of the same yield (Goldstein and Jarpe, 1994). Comparison of Hunters Trophy (HT) nuclear explosion and NPE at near-source distances indicates that within the bandwidth of 0.36 to 100 Hz, there is no apparent spectral difference between the nuclear and single-fired chemical source (Stump et. al., 1999). This experiment showed that seismic waveforms from nuclear explosions are identical to chemical explosions (accounting for the coupling difference) and that the contained chemical explosions from the Source Phenomenology Experiments (SPE), the subject of this dissertation, are analogous to underground contained nuclear explosions. Because of the identical nature, source physics experiments utilizing chemical explosions can be used to assess seismic source characterizations appropriate for nuclear explosions. We are motivated to assess the uniqueness of the source representation by constraining the effects of yield, depth and geology on the representation. Yield estimation of a nuclear explosion gives insight into the development of nuclear weapons programs and can serve as a predictive mechanism of their nuclear progress. The type of fissile

material used in the detonation device, architecture of detonation, supply of neutrons and whether fission is used to promote fusion of smaller atoms are all known steps in increasing yield.

By constraining the source effects of depth and yield, interactions at the free surface become more apparent. For a contained explosion, a compressional wave leaves the source and travels upward to the free surface, where because of the stress-free boundary condition, it reflects as a tensile wave traveling away from the free surface (Sharpe, 1942). Near-surface materials can fail in tension as a result of this wave moving away from the surface sending these layers into ballistic free fall until, as a result of gravity, they eventually re-impact and subsequently deposit momentum into the surficial layers. This effect has been investigated by a number of people (Chilton et al., 1966; Eisler et al., 1966; Rinehart, 1985) and not only complicates the source time function but also, given an adequate yield or source depth, generates a non-spherical secondary spallation force that affects the source geometrical representation (Stump, 1985).

Results of scaling analysis indicate that the yield, depth of burial and emplacement medium contribute first order effects to the seismic spectrum for detonations (Mueller and Murphy, 1971). Considering two observations at a common distant station, for two proximate detonations, and assuming the transfer function to be linear, spectral ratios cancel propagation effects, providing a relative measure of the source differences used to constrain the source model (Mueller & Murphy, 1971).

A point isotropic explosion source theoretically generates no direct shear waves and therefore observed shear waves from a point source must be generated by secondary sources such as spallation, other free surface interactions, scattering and wave conversions at velocity discontinuities (Stevens et al., 2009) from the energy initially leaving the source. The conversion

and scattering processes remove energy from the isotropic source and under some circumstances can re-radiate it as shear waves, impacting estimates of source strength. The fact that, in all source comparisons of the Hunters Trophy and NPE, the spectral ratios of the transverse components of motion are indistinguishable from those produced by either the vertical or radial components argues that the transverse component of motion from an explosion is generated at very close distances (Stump et al., 1999), while retaining information of relative source strength.

There is currently no accepted comprehensive physical model for shear wave generation by explosions that has been shown to be quantitatively consistent with the wide range of observations from explosion sources (Stevens et al., 2003). A physical understanding of the generation of shear energy is also important in the development and application of seismic techniques for discriminating earthquakes and mining explosions from contained single-fired explosions (McLaughlin et al., 2004) as well as from earthquakes.

The seismic moment tensor is a general representation for both natural and man-made seismic sources. Under conditions that the source can be assumed small compared to the wavelengths of the waves, a second order tensor composed of six unique force couples is an appropriate representation. A linear relationship is established between observed ground motions, a set of Green's functions in the frequency domain and this second order moment tensor (Stump and Johnson, 1977). Utilizing the linearity of the system, synthetic seismograms can be built by the convolution of the Green's functions and an appropriate source model. These synthetic seismograms may be compared against real data to verify the source model and the geology or propagation model in order to accurately model the observed seismograms. Given a set of observed ground motions and known geologic structure for which numerical Green's

functions can be computed, the source moment tensor or source representation can be recovered using linear inverse theory.

Data utilized in the three chapters of this dissertation come from the Source Phenomenology Experiment (*SPE - Arizona*). The SPE was a series of nine, contained and partially contained chemical explosions within the porphyry granite body at the Morenci Copper mine in Arizona. The purpose of these experiments was to detonate, record and analyze seismic waveforms from these single-fired explosions in order to characterize the explosion seismic source representation for granite as well as assess absolute coupling in a number of containment conditions.

The first chapter focuses on characterizing the uniqueness of explosion source representations by evaluating seismic data from a single-fired contained chemical explosion (shot B4) within the Morenci Arizona copper mine using frequency domain moment tensor source inversion. The source geometry, depth, yield and geology all play crucial roles in both the initial and possible secondary seismic sources that might deviate from a simple spherical model of the explosion. The focus is on the assessment of the uniqueness of the seismic source representation in terms of the effects and possible trade-offs between yield, depth and geology. The geologic model from the SPE is analyzed and assessed in order to understand how source depth and model parameters, such as shear wave velocity, affect the resulting source model and can be constrained.

The second chapter compares shot B4, from chapter one, to shots B6 and B10 in an attempt to better understand yield and containment effects. These shots are all detonated at the same depth, but because of their varying yields, have different containment and coupling. The resulting isotropic moments are compared to other chemical and nuclear explosions as well as

existing models in order to assess the appropriateness of these models to extrapolate to other conditions. Hudson diagrams, plotted as a function of frequency for the moment tensor, provide a separation of isotropic, deviatoric and compensated linear vector dipole source components documenting changes in the source representation as a function of frequency that may be important for both event discrimination and yield determination.

Chapter three also explores yield but focuses on containment effects as the sources analyzed are detonated closer to a free face or free surface, typical of mining explosions. This study uses the full suite of nine explosions from the SPE. Three detonations at the free face, three detonations twice that distance from the free face (twice burden) but at the same source depth, and three detonations twice the depth of the previous six explosions. These sets of explosions each have varying yields as well. This investigation probes how the source representation is affected by containment as well as yield and bridges to typical source configurations characteristic of mining explosions.

These three chapters guide new analysis of observational data that improves understanding of the practical resolution of physical phenomenology accompanying underground explosion sources.

REFERENCES

Chilton, Frank, J. D. Eisler, and H. G. Heubach. "Dynamics of spalling of the earth's surface caused by underground explosions." *Journal of Geophysical Research* 71.24 (1966): 5911-5919.

Denny, Marvin, et al. "Seismic results from DOE's Non-Proliferation Experiment: A comparison of chemical and nuclear explosions." *Monitoring a Comprehensive Test Ban Treaty*. Springer Netherlands, 1996. 355-364.

Eisler, J. D., F. Chilton, and FM T. Sauer. "Multiple subsurface spalling by underground nuclear explosions." *Journal of Geophysical Research* 71.16 (1966): 3923-3927.

Goldstein, P., and S. Jarpe, (1994). Comparison of chemical and nuclear explosion source spectra from close-in, local and regional seismic data, *Proceedings of the Symposium on the Non-Proliferation Experiment (NPE): Results and Implications for the Test Ban Treaties,* Rockville, Maryland, CONF 9404100, Lawrence Livermore National Laboratory, 19-21 April 1994.

Mueller, Richard A., and John R. Murphy. "Seismic characteristics of underground nuclear detonations Part I. Seismic spectrum scaling." *Bulletin of the Seismological Society of America* 61.6 (1971): 1675-1692.

McLaughlin, Keith L., Jessie L. Bonner, and Terrance Barker. "Seismic source mechanisms for quarry blasts: modelling observed Rayleigh and Love wave radiation patterns from a Texas quarry." *Geophysical Journal International* 156.1 (2004): 79-93.

Patton, H. J. (2012b). A revised cavity radius scaling relationship for explosions detonated in a 530 granite medium, Los Alamos National Laboratory, LA-UR-12-27099, pp. 12.

Rinehart, Eric. "Shear wave generation of near-surface spall." *Journal of Geophysical Research: Solid Earth (1978–2012)* 90.B6 (1985): 4567-4576.

Sharpe, Joseph A. "The production of elastic waves by explosion pressures. II. Results of observations near an exploding charge." *Geophysics* 7.3 (1942): 311-321.

Stevens, Jeffry L., Heming Xu, and G. Eli Baker. "An upper bound on Rg to Lg scattering using modal energy conservation." *Bulletin of the Seismological Society of America* 99.2A (2009): 906-913.

Stevens, J. L., et al. "The physical basis of Lg generation by explosion sources, paper presented at 25th Seismic Research Review: Nuclear Explosion Monitoring: Building the Knowledge Base." *Natl. Nucl. Security Admin., Washington, DC* (2003).

Stump, Brian W., D. Craig Pearson, and Robert E. Reinke. "Source comparisons between nuclear and chemical explosions detonated at Rainier Mesa, Nevada Test Site." *Bulletin of the Seismological Society of America* 89.2 (1999): 409-422.

Stump, Brian W. "Constraints on explosive sources with spall from near-source waveforms." *Bulletin of the Seismological Society of America* 75.2 (1985): 361-377.

Stump, Brian W., and Lane R. Johnson. "The determination of source properties by the linear inversion of seismograms." *Bulletin of the Seismological Society of America* 67.6 (1977): 1489-1502.

CHAPTER 1

THE EFFECTS OF ASSUMED SOURCE DEPTH AND SHEAR WAVE STRUCTURE ON ESTIMATED MOMENT TENSORS FOR SMALL, CONTAINED CHEMICAL EXPLOSIONS IN GRANITE

Motivation

This study focuses on characterizing the uniqueness of explosion source representations by evaluating seismic data from a single-fired contained chemical explosion within a copper mine in Morenci, Arizona, using frequency domain moment tensor source inversion. The source geometry, depth, yield and geology all play crucial roles in constraining both the initial and possible secondary seismic sources that might deviate from a simple spherical model for the explosion.

The focus of this chapter is on the assessment of the uniqueness of the seismic source representation by quantifying the effects and possible trade-offs between yield, depth and geology. Mueller and Murphy, 1971, found that scaling relations derived for the isotropic seismic source functions are dependent on yield, depth of burial (DOB) and emplacement medium for the nuclear explosions. Furthermore, the constraint of source depth and yield is critical to the assessment of seismic interactions with the free surface and resulting secondary source contributions. For example, in a contained explosion, a compressional wave leaves the

source and travels upward to the free surface and reflects as a tensile wave providing a mechanism to deposit upward momentum into the layers above the detonation. This reflected wave not only complicates the source representation but also, given an adequate yield or source depth, can generate a non-spherical secondary spallation force that impacts the source representation (Day et al., 1983; Stump, 1985; Patton, 1990).

The Non-Proliferation Experiment (NPE) (Denny et al., 1996) conducted by the Department of Energy (DOE) detonated 1.29 million kilograms of ammonium nitrate fuel oil (ANFO) at Rainier Mesa in an attempt to identify similarities and possible differences between nuclear and chemical explosions. Empirical comparison between the Hunters Trophy (HT) nuclear explosion and the NPE at near-source distances illustrate that within the bandwidth of 0.36 to 100 Hz, there is no apparent spectral difference between the nuclear and single-fired chemical source (Stump et al., 1999). These results suggest that chemical explosions can be utilized to empirically explore explosion source models that are applicable to nuclear explosions. Although historically researchers have called for a doubling of the chemical explosion yield (Goldstein and Jarpe, 1994), Patton, 2015, suggests that the chemical explosion is identical to that of the nuclear explosion and a doubling of chemical yield is inappropriate. Bonner et al (2013) also found that a doubling of chemical yield was inappropriate for their data. They tested the original DJ91 formulation by doubling the chemical yield in their explosions and used DJ91 to estimate the larger moments. They found that the resulting synthetics were significantly larger than the observed data and would have needed to include the effects of source damage or adjust the Q values and gas porosity to unrealistic values.

Discrimination of underground nuclear explosions from earthquakes using seismic observation motivates a physical understanding of the similarity and differences of source

functions for both explosions and earthquakes. In 2006, 2009, 2013, 2016 and 2017 the Democratic People's Republic of Korea (DPRK), North Korea (NK), conducted six underground nuclear tests at the Punggye test site around Mount Manthap in northeastern NK. Some of these explosions, particularly in 2006, had small magnitudes, resulting in limited detections and location uncertainties (Murphy et al., 2010, 2011; Selby, 2010; Wen and Long, 2010). These events and their associated waveforms have consequences for yield estimations as well as the robustness of the M_S versus m_b discriminant (Kim and Richards, 2007; Bonner et al., 2008, 2011; Koper et al., 2008; Patton and Taylor, 2008; Zhao et al., 2008, 2012; Chun et al., 2011). These explosions excited surface waves much more efficiently than nuclear explosions in other regions of the world, creating anomalously high M_S estimates. Based on the M_S to m_b ratios, the 2006 explosion was in the earthquake category and the 2009 sat directly on the discrimination line (Murphy et al., 2013). Constraint of source depth as well as local material is important to both estimation of yield and the physical interpretation of the seismic observations used in discrimination.

Explosions, theoretically, generate no shear waves, but S-waves are commonly observed. Non-isotropic components of nuclear explosions are thought to be one cause of shear energy (Dreger and Woods, 2002). Released tectonic strain is another (Press and Archambeau, 1962). Pollutz et al. (2015) suggest that SV energy arises mostly from P-to-S conversions at subhorizontal discontinuities. More recently, Stroujkova, Leidig and Bonner, 2015, found that S/P amplitude ratios suggest that significant S-wave energy can be caused by opening of tensile fractures and spall. Patton and Taylor, 2008, and Antoun et al, 2011, found that shear energy is caused by material damage to the material directly surrounding the source.

The seismic moment tensor is a general representation for both natural and man-made seismic sources that completely describes the equivalent forces of general seismic point sources (Jost and Herrmann, 1989; Aki and Richards, 2002; Minson and Dreger, 2008). Sources of seismic energy separate into specific populations according to their deviation from a pure double-couple and ratio of isotropic to deviatoric energy. Hudson, 1989, introduced two-dimensional graphical source type plots dependent on the three principal moments that provide a method of interpreting the source in terms of its isotropic, deviatoric and linear vector dipole components. Ford, 2008, applied this analysis to 11 earthquakes and 3 collapses (1 cavity and 2 mine) producing source-type plots along with their associated 95% confidence regions. Ford, Dreger and Walter, 2009, calculated the deviatoric and isotropic source components for 17 explosions at the Nevada test site as well as 12 earthquakes and 3 collapses in the surrounding region, using a regional time domain full waveform inversion for the complete moment tensor. More recently, Vavryčuk, 2011, 2015, and Tape and Tape (2012a, b; 2013) have investigated the decomposition, geometric representation and source type interpretation of the general moment tensor. Chiang et al., 2014, applied this methodology to data from the 1988 U.S.-Soviet Joint Verification Experiment and 2 more nuclear explosions 10 years later at the Chinese Lop Nor test site.

The isotropic and CLVD components of the moment tensor representation have ramifications for yield scaling and explosion source models. Mueller and Murphy, 1971, developed a seismic spectrum scaling model based on an analytical approximation to the nuclear seismic source function and found that cube root scaling is inappropriate. Denny and Johnson (1991) (DJ91) discuss analytical explosion models considering instantaneous rise times, finite rise times and ones with and without steady-state values. DJ91 conducts a regression analysis of

the relationships of moment and corner frequency parameters to the cavity size. They find that cube root scaling is appropriate. Patton (2012) in correspondence with Jack Murphy, revises MM71 with a more appropriate cavity radius scaling relationship for granite due to different static pressure values predicted by equivalent formulation of the MM71 model and Stevens and Day (1985).

Source Phenomenology Experiment (SPE - *Arizona*)

In order to experimentally address some of the issues related to the contained explosion seismic source representation, the Source Phenomenology Experiment (SPE) was conducted by a consortium formed between Weston Geophysical, Southern Methodist University, the University of Texas at El Paso, Los Alamos National Laboratory and Lawrence Livermore National Laboratory. The goals of the experiments were to quantify differences between contained single-fired chemical explosions (a proxy for nuclear explosions) and delay-fired mining explosions as well as to provide a data set to constrain the explosion source function (Bonner at al., 2005). The SPE was conducted at both Black Mesa coal-mine and Morenci copper mine in eastern Arizona in order to better understand the effect of different propagation paths and geologic settings on the source representation.

The Black Mesa coal-mine is in northeastern Arizona along the Arizona-Utah border, about 450 km north of Morenci. Experiments at this site were designed to quantify sources and wave propagation in a softer, sedimentary rock setting. Nine explosions with varying confinements were detonated. A portion of the nine were point source detonations in a test pit in order to examine the effects of depth, explosive weight and confinement on the generated seismic energy. The second set of experiments included detonations of linear sources more closely related to mining production shots (10 m borehole separation) designed to examine

source spatial effects as well as coupling along the free face of the mine. Source inversions for the single-fired explosions at Black Mesa have been reported previously (Yang and Bonner, 2009).

The Morenci Copper Mine, located in southeastern Arizona along the Arizona-New Mexico border, has porphyry copper deposits estimated at 56 Ma. Local geology reflects the tectonic origins of the deposit as represented by the diabase dikes, granite porphyry, hornfels, and quartz monzonite formed during the Laramide intrusive episode (Titley, 1981). The intrusions were accompanied by hydrothermal fluids that result in copper minerals being deposited in the pores of the igneous rocks. This site was chosen for the second half of the SPE in order empirically constrain the seismic source representation in harder rock material, the granites in particular. A series of nine, single and simultaneously fired, contained chemical explosions were detonated at this location as well. The single-fired explosions consist of small patterns of simultaneously detonated boreholes. Borehole configurations, explosive load, stemming, burden and spacing were identical to the Morenci Mine production practices at the time of the tests. The only unusual variable, with respect to normal mining processes, was the borehole depth, which were increased while maintaining the total explosive load in order to explore the effect of source depth on the seismic waveforms and associated source representation. Additional sources were detonated to quantify the effect of source distance from the free face and total explosive weight.

Typical drilling at the mine produced 31 cm diameter boreholes with depths of 18.3 m loaded with 12.2 m of ammonium nitrate fuel oil (ANFO) and 6.1 m of stemming, accommodating 773 kg of explosives. Simultaneous detonation of one, four, and eight boreholes provided nominal explosive weights of 773, 3091, and 6182 kg (Stump and Zhou, 2007). Shots

B1, B2 and B7 were detonated with a burden (the distance between free face and borehole) of 9 m and 12 m centroid depth (**Figure 1.1**). Shots B3, B5 and B8 were detonated at a standard centroid depth of ~12 m but with twice burden (18 m). Shots B4, B6 and B10 were detonated at twice depth with a centroid of 30 m. **Table 1.1** contains shot descriptions for all 9 shots detonated within Morenci mine. **Figure 1.1** shows a map of the test bench with the nine shots with the test site geometry detailed in **Figures 1.2** and **1.3**. Instrumentation deployed across the test bench is included in **Figure 1.1** and spans from instruments very close to the explosions, which capture non-linear processes such as near surface spallation, to more distant stations that document linear-elastic wave propagation (circles surrounding the explosion locations).

A variety of instrument types were deployed (**Figure 1.1**) on the test bench at distance ranges of 35 – 680 m in order to capture the wavefield from within the region of tensile failure out to linear elastic propagation. The closest stations (8, 9, and 10) were equipped with high-*g* (~10's g) Endevco accelerometers. Low-*g* accelerometers (~ 1 g) (Terra Technology) were deployed at greater ranges (stations 2, 3, 4 and 5). At the farthest near-source ranges low-*g* accelerometers and velocity transducers (Mark Products L4C3D) were collocated (stations 1, 6 and 7) (Bonner et al., 2005).

Test Bed Model

This chapter focuses on the effect of assumed source depth and assumed Green's functions on the resulting source characterization in an effort to identify the sensitivity of model parameters on the estimate of the final source characterization. A single explosion, shot B4, and associated waveforms provides the basis to assess the effects of assumed shear velocity and source depth. B4 was detonated at 30 m depth and had an estimated yield of 3.08×10^{-3} kt with a scaled depth of burial of 206 m/kt$^{1/3}$. For our study, 30 m depth is assigned the standard burial

depth. Subsequent work (Chapter 2) addresses the broader issues of coupling and yield scaling utilizing the full suite of explosions.

A refraction study was completed within the mine to constrain the emplacement and propagation path geology. **Figure 4** summarizes the results of the refraction study with the compiled structure models for V_p, V_s, ρ (density), attenuation $Q\alpha$ and $Q\beta$ (Bonner et al., 2005). V_p structure is estimated using the first arrivals of P-waves while the accompanying V_s structure is less resolved. R_g dispersion curves estimated from data recorded on the N-S broadband station profile were used to provide V_s constraints (Hayward et al., 2004). The empirical dispersion curves vary systematically with distance, which implies a lateral variation in the velocity structure across the mine (Bonner et al, 2005). The spacing of the stations used in the dispersion analysis was approximately 0.5 km, a much larger spatial scale than the explosion test bed. The estimated shallow layering and source emplacement characteristics at the test site are displayed in **Figure 1.5**. The first three layers are the most important role in terms of source coupling and near-source propagation compared to the six deeper layers below the source.

Green's functions were computed using the reflectivity approach (Müller, 1985) for different source depths as well as the different V_s structures, holding the V_s constant based on the resolution of the site characterization data. This technique is utilized in order to capture spherical wave effects that capture contributions from body and surface waves that are appropriate to the near-source observations. In order to assess the effects of source depth and V_s on the seismic moment tensors, Green's functions for a range of assumed source depths and shear wave velocities were computed. Based on the well-constrained V_p and increased

uncertainty in V_S, Poisson's ratio, ν, is used to quantify the range of possible elastic materials. The impact of these changes on the Green's functions and inversions are illustrated in the subsequent section. A baseline Poisson value of 0.25 is used with variations from 0.15 (fastest) to 0.40 (slowest). **Table 1.2** includes constrained V_S the top four layers and the possible V_S values based on the range of Poisson values. The range of source DOB and V_S structures are evaluated in order to explore the importance of these assumptions to the resulting explosion source characterization, especially when secondary sources may contribute to the resulting source function.

Forward Model

Forward synthetics are initially investigated by convolving a Mueller-Murphy (1971) source time function developed from a source scaling study (Zhou and Stump, 2005) with the reflectivity Green's functions calculated using the compiled velocity and Q model. The model parameters used in the Mueller-Murphy model are defined in **Table 1.3**. Green's functions covering the distances of the 16 stations in **Figure 1.1** were calculated based on the one-dimensional velocity model. The CLVD and explosion components of the Green's functions are analyzed in order to quantify the effects of assumptions related to source DOB and V_S structure on the expected explosion-like components of the source representation. Subsequently, noise is added to these same synthetics prior to inversion to assess the impact on the full recovery of the seismic moment tensor based on the station distribution in this study. Green's functions are computed using the one-dimensional reflectivity approach (G. Müller, 1985) where reflectivities and transmissivities are calculated by recursive methods as the waves propagate through the layers over a half space.

CLVD and explosion Green's functions for three source depths are displayed in **Figures 1.6** and **1.7**. The 30 m source is the standard centroid depth for shot B4. Both the CLVD and explosion Green's functions are dominated by energy in the 2 – 12 Hz band due to the surface wave contributions (**Figures 1.6 and 1.7**) with P-waves at higher frequencies. Radial synthetics at 683 m for the explosion source at the three source depths (15, 30 and 60 m) have similar body wave amplitudes and shapes (**Figure 1.6**). Surface wave amplitudes for the same three source depths decrease by as much as 10 times from the shallowest to the deepest source, documenting the strong depth dependence. There is no clear depth dependence for frequencies above 20 Hz. The vertical explosion Green's function components exhibit similar effects. Source depth effects for the CLVD component at 683 m are much less (**Figure 1.7**) with the lower frequencies, 0.1-10 Hz, showing a slight depth dependence. Frequencies above 10 Hz show no depth dependence. These results suggest the possibility of a strong trade-off between source depth and the lower frequency moment tensor source estimate. Higher frequencies indicative of body waves may be less sensitive to depth.

Green's functions at the 683 m range and 30 m DOB were also computed for Poisson values of 0.15, 0.25 and 0.40. (**Figures 1.8 and 1.9**). In the case of the explosion Green's functions (**Figure 1.8**), slower velocity models produce radial surface wave amplitudes smaller by as much as a factor of 4 and that are also delayed in time. Body wave amplitudes for the slower models are also smaller. There is little effect of shear wave velocity on the vertical P-waves, with amplitudes as much as 3 times higher than the surface waves. In the case of the vertical component surface waves in the 0.1-10 Hz band, faster shear wave velocities have higher amplitudes, highest around 10 Hz (~3x for 0.15/0.4 Poison values). The CLVD radial and vertical synthetics for the range of Poisson values document strong surface wave effects from

0.1-20 Hz with increased amplitudes by as much as a factor of 4-5 for the slower shear wave velocity structures (**Figure 1.9**). Above 20 Hz there is no visible dependence on shear wave structure, similar to the depth effects.

Spectral ratios of the Green's functions were computed to illustrate the frequency dependent differences between the DOB and V_S model effects. **Figure 1.10** compares the explosion vertical components for the DOB comparisons at a range of 683 m. In general, these ratios illustrate that the lower frequencies, dominated by surface waves, increase in amplitude with decreasing depth while the spectral differences are less sensitive to depth for the higher frequencies representative of the body waves. Constructive and destructive interference at high frequencies show depth effects as exemplified by subtle shifts in locations of peaks and troughs for individual spectra.

Spectral ratios of the vertical and radial components of motion for the shear wave model comparison show similar trends, so only the vertical ratios are documented in **Figures 1.10** and **1.11**. Distance has a secondary effect on these ratios. For the CLVD case, amplitude ratios at frequencies less than 20 Hz increase with decreasing shear wave velocity. Above 20 Hz, where the body waves dominate, the depth effect is greatly reduced. The shear wave velocity effect for the explosion component is much reduced relative to the CLVD source with the slowest velocity producing lower or comparable amplitudes below 20 Hz. Similar to the explosion case, above 20 Hz the spectral amplitudes for the different velocity models are similar.

These forward synthetics suggest trade-offs between source depth, Poisson's ratio and source representation. The strong depth effects for the explosion Green's functions (**Figures 1.6 and 1.11**) with amplitudes decreasing with increasing source depth contrast with the strong

effect of Poisson's ratio on the CLVD component where higher amplitudes are predicted for models with slower shear velocities. These results motivate the exploration of the dependence of the moment tensor source on assumptions related to source depth and shear wave model in order to assess a range of possible acceptable source models.

Data Inversions

Synthetic and real data inversions were completed as part of this investigation in order to assess the range of possible source models. Synthetic data inversions were first completed to better evaluate how noise, azimuth and distance affect the full moment tensor recovery. Real data inversions were subsequently completed and analyzed using the observed seismic data from the SPE.

In the time domain the general source characterization including all force couples becomes,

$$U_k(t) = G_{ki,j}(t) \otimes M_{ij}(t), \tag{1}$$

where U_k are the observations, $G_{ki,j}$ are the Green's functions, M_{ij} is the seismic moment tensor and $\otimes$ represents convolution. In the frequency domain the representation can be written,

$$U_k(f) = G_{ki,j}(f) \bullet M_{ij}(f), \tag{2}$$

where again, U_k are the observations, $G_{ki,j}$ are the Green functions, M_{ij} is the seismic moment tensor and $\bullet$ represents multiplication. $M_{ij}(f)$ can then be estimated by inverting the matrix, $G_{ki,j}(f)$ and multiplying by $U_k(f)$:

$$U_k(f) \bullet G^{-1}_{ki,j}(f) = M_{ij}(f) \tag{3}$$

An inverse Fourier transform is then used to transform the observations and moment tensor back into the time domain.

Synthetic inversions

Using synthetic data and the Green's functions for the SPE structure, a frequency domain moment tensor inversion at every frequency was completed to estimate the moment tensor. These synthetic inversions were done to quantify the effects of variable distance and azimuthal coverage on the expected recovery of the moment tensor under varying noise conditions. When noise amplitude approached 10% of the signal amplitude, the moment tensor recovery was degraded. Two synthetic inversion studies were conducted using three and four stations with, respectively, 180 and 360 degrees of azimuthal coverage. Both inversion studies provided fully recovered moment tensors. With the 8 stations and 180 degrees of azimuthal coverage, the SPE has a more robust geometry than both synthetic tests where the moment tensor is fully recovered. A secondary purpose of these inversions was to investigate possible biases introduced into the source estimation by assumptions related to the shear wave velocity model and depth of the source as illustrated in the previous Green's function discussion. The condition numbers as a function of frequency were calculated at every frequency. Typically, condition numbers below 100 were found. The spread in eigenvalues for these synthetic inversions are small and all components of the moment tensor are well resolved across the entire frequency band. Although the synthetic inversions indicate some sensitivity to noise, the fact that the observational data has a signal to noise ratio of around three orders of magnitude when averaging the signals and noise, motivates the next steps of applying these inversions to the real data.

Actual data inversions

Data analysis is confined to shot B4 as this explosion is fully contained at 30 m DOB and provides the basis to focus on possible trade-offs between geological model estimates and the resulting moment tensors. Inversions were performed using ground motion data from all eight receivers within the linear elastic zone from 150-700 m range in **Figure 1.1**. The data does not have full azimuthal coverage but with 3 components per station and a total of 24 channels, the solutions are over determined.

The first inversion used the 30 m DOB and Green's functions with $\nu = 0.25$. The estimated moments of the six seismic moment tensor components are displayed in **Figure 1.12**. The M_{ZZ} component is the largest and roughly twice the size of Myy and M_{ZZ}, documenting the LVD nature of this source estimate. The off-diagonal components, M_{yz}, M_{XZ} and M_{XY} have peak ratios relative to M_{ZZ} of 0.42, 0.42 and 0.23. Signal and noise, both in the time and frequency domain, were evaluated from the moment tensor components (**Figure 1.13**) and the observations (**Figure 1.14**). In both the moment tensor components and the observations, the signal rises above the noise around 1-2 Hz and have signal to noise ratios of over 100. The small amount of noise did not dramatically affect the fully recovered moment tensor.

The estimated moment tensors are used to predict the data which are compared to the observed seismograms at distances greater than 150 m. **Figure 1.15** displays fitted and observed seismograms for this data set without filters. Removing the radial or the transverse component data from the inversion does not yield better fits. The data suggests that removing the transverse is more detrimental to the fits than removing the radial based on the fitted and observed seismograms. Inversions were also performed using data scaled as $r^{1.5}$ and r^2, these fits are

compared but not displayed. The original scaling, proportional to distance, yielded the best fits without filtering. **Figures 1.16a** and **1.16b** compare the fits to the observations, bandpass filtered from 2-20 and 2-10 Hz respectively. 2-20 Hz is the band of interest and where it is believed that our Green's functions are most applicable, but filtering from 2-10 Hz yielded the best fits.

As a measure of effectiveness of all the inversion for the range of V_S models and source depths, a mean cross-correlation value for all stations is calculated for each inversion. With 2-20 Hz as our bandwidth of interest, the average cross-correlation for the inversion with a depth of 30 m and a Poisson's ratio of 0.25 has a mean value of 0.72 using all the stations within the linear elastic zone (150-680 m). Radial and transverse component cross-correlation values have less than 5% variation from the vertical component. **Figure 1.17** summarizes mean cross-correlation values for all of the inversions, bandpass filtered form 2-20 Hz. The suite of inversions includes six shear wave velocity models (Poisson's ratio 0.15 to 0.40) with the three source depths (15, 30, 60m) using all the data. Cross-correlation values for our standard velocity model using a Poisson value of 0.25 have the highest mean value while average fits decrease for the higher and lower Poisson values. Mean cross-correlation values for the deepest source (60 m) have the lowest values. Both the 15 and 30 m source depths provide improved fits to the data for all velocity models with some preference for the 30 m depth using the preferred velocity model. The radial and transverse show similar trends with degrading cross-correlation values with slower shear wave velocities, but on average the Z component fits are slightly better. Based on the degree of fits, the preferred model is $\nu = 0.25$ and source depth of 30 m.

Moment-rate tensor spectrums of both the isotropic trace (M_{tr}) and M_{zz} components were calculated for shot B4 to investigate how well the components fit the Mueller and Murphy, 1971, Denny and Johnson, 1991, and Revised Heard and Ackerman (Patton, 2012 b), source models for granite. **Figure 1.18** displays the M_{zz} and M_{tr} amplitude spectra for shot B4 plotted with the three source models described above. The source spectra follow the predicted Mueller Murphy, 1971, especially at higher frequencies as the Denny and Johnson model predicts a lower corner frequency than observed. The model is closer to the M_{tr} estimated than the enhanced M_{zz} at the longer periods.

Three source medium dependent properties are investigated to better understand how they affect the Mueller and Murphy, 1971, granite source model and its ability to match the moment tensor estimates. The source medium proportionality factor, *k*, the medium dependent A/A_{cal}, *r*, and the compaction factor, *d*, are varied, keeping all other Mueller and Murphy, 1971, granite source properties constant. Holding these other properties constant, *k*, *r* and *d* are given values of tuff, rhyolite, granite (for control), shale and salt. *k* does not affect the model greatly. It controls overshoot but the small changes do not noticeably affect long period amplitude or corner frequency, f_c. *r* has a significant effect on overshoot (as much as 6 times greater) and f_c (4.7-10.9 Hz) due to the broad range of values (0.23– 12). In our investigation, an increase in d increases the long period amplitudes. An increase from 0.6 to 1.0 doubled the long period amplitude and thus could be used to model the difference between the M_{tr} and M_{zz} long-period levels.

Granite source models were then calculated investigating constant scaled depths of burial, holding yield constant and constant yield holding scaled depth of burial constant. With a constant

scaled depth of burial and an increasing yield, as expected, long period amplitude increases and f_c decreases. With a constant yield and an increasing scaled depth of burial, long period amplitude decreases and f_c increases.

Using the known yield for shot B4, a Mueller and Murphy, 1971, source model for granite was calculated. Instead of yield, the source models were calculated using a range of cavity and elastic radii to find the best fit for the Mueller and Murphy, 1971, model. A cavity radius of 3.44 m and an elastic radius of 89 m best matched the Mueller and Murphy, 1971, source model using a yield of 0.0031 kt with granitic source medium properties.

Interpretation

Hudson (1989) diagrams are used to visualize moment tensor source estimates and are used to interpret the explosion source functions. Ford, Dreger and Walter, 2009, perform a series of source inversions for the May 2009 North Korean nuclear explosion using intermediate period (10-50 sec) complete waveform modeling. They found that a pure explosion yields a scalar seismic moment that fits the data almost as well as the full solution. They also compare the resulting moment tensor to source estimates for nuclear explosions at the Nevada Test Site as well as earthquakes using Hudson diagrams. The North Korean Nuclear Explosion plots within the same region as the other nuclear explosions and separate from the earthquakes.

Using the eighteen moment tensors inverted in this study, including moment tensors estimated with the range of assumed depths of burial and S-wave structure, source type plots were constructed in order to assess how the geological model and source depth assumptions affected the source representation. In our case the Hudson diagrams are plotted using frequency domain results. **Figure 1.19** displays a Hudson diagram plotting the computed moment tensor

inversion at every delta *f* frequency using the standard SPE model (depth = 30 m and ν = 0.25) from 0.06-20 Hz. The highlighted rectangle used in **Figure 1.19** provides a more focused view of the results shown in later figures. The diagrams document a source representation that changes as a function of frequency in a similar manner for all velocity models and source depths. At the lowest frequencies the source plots are close to the linear vector dipole representation consistent with the large M_{zz} component with movement towards the pure explosion source representation with increasing frequency. This result suggests that the degree of symmetry of explosion source model may be frequency dependent and that the higher frequencies or shorter wavelengths provide the most isotropic characterization.

Similar Hudson diagrams accompany the moment tensor inversions for different assumed source depths and Poisson's ratios. For the DOB changes, as depth increases, energy shifts from the 1-10 Hz band to the 10-20 Hz band (**Figure 1.20**). For the shear wave model changes, as V_S increases, energy in the 10-20 Hz band increases for all 3 trace components. At higher V_S, the M_{ZZ} value approaches that of the M_{XX} and M_{YY}, producing the most isotropic source representation (**Figure 1.21**). **Figure 1.22** displays the source type plots for the range of shear models with an assumed source depth of 30 m. As V_S increases, the source representation again becomes more explosion-like, shifting closer to a pure explosion on the Hudson diagram at the highest frequencies. Changing source depth of burial, in our source representation investigation, shows no systematic trends in source type space.

With the shifts, as a function of frequency, from a CLVD to explosion source representation demonstrated in previous inversions, the "CLVDness" is quantified. The ratio of

M_{ZZ} to the averaged M_{XX} and M_{yy} is calculated. **Figure 1.23** displays these estimates for all models at all source depths. As the assumed source depth becomes greater, the resulting source representation becomes more explosion like. As shear wave velocity is increased, the source representation also becomes more explosion-like.

These results document trade-offs between assumptions about source depth and shear wave velocity around the explosion. All assumed geological models and source depths produce source estimates that start at the low frequencies as CLVD and then move toward a pure explosion with increasing frequency. The degree to which the resulting source is purely isotropic at high frequencies is a function of the assumed source depth and shear wave velocity structure around the explosion. The preferred model maintains a Poisson's ratio of 0.25 and the actual source depth of 30 m. The fitted versus observed seismogram analysis yielded the highest correlations and this is what future models will be based upon.

Isotropic and deviatoric components of the moment tensor were calculated in both time and frequency domain. **Figure 24** displays yield vs moment modified from Denny and Johnson (1996) comparing chemical explosions (W < 0.001 kt) and nuclear explosions (W > 1 kt) to this study's explosion. For each population of models, as shear wave increases and depth decreases, the moments increase with depth of burial having the largest effect of moment increase.

Conclusions

This study characterized the seismic source function for a small, contained explosion detonated in granite. The representation utilized in this study is the frequency domain moment tensor. An important part of this study has been the assessment of how the source representation

depends on assumptions of source depth and shear wave velocity when compressional velocity structure around the explosion is well constrained.

Three-component, near-source seismic data were recorded from the explosion and the P-wave structure at the test site was estimated from a refraction survey. A starting shear wave model was constrained by R_g dispersion analysis but lacked resolution in the shallow layers where the explosion was emplaced. Possible ambiguities in source depth as a result of the combination of direct energy coupled by the explosions and secondary effects resulting from free-surface interactions suggest a need to investigate the effect of assumed source depths on the resulting source interpretation as well.

Synthetic seismograms based on the velocity structure in the Morenci copper mine were calculated. Poisson's ratio was varied holding the V_P constant as well as varying source depth in order to investigate the impact of these assumptions on the resulting synthetics and moment tensor estimates. Spectral ratios of the raw Green's functions from these model were evaluated both in the time and frequency domain in order to help with the interpretation of their impact on the resulting moment tensors. Moment tensor inversions were later performed with the suite of source depths and Poisson's ratios to document their effects on the source representation and identify a best source estimate. Source type plots were used to interpret the source representation.

The depth of burial study utilized the Green's functions developed for the SPE and placed the source at different depths assessing near field wave propagation including interactions at the free surface. The variable DOB Green's function components, both CLVD and explosion, have a large partition of energy in the 2–12 Hz band due to the surface wave contributions. There is no clear depth dependence for frequencies above 20 Hz. For the 2-20 Hz band explosion

component, the shallower the source, the greater the amplitude. The variable DOB CLVD Green function components have less depth dependence than the explosion components. Shallower DOB waves have greater amplitude below 20 Hz.

Holding the P-wave constant, the Poisson's value was raised and lowered to decrease and increase, respectively, the S-wave velocity of the geologic layering in the model. For the explosion variable shear wave velocity structure Green's function components (**figure 1.8**), there is a strong depth dependence for the higher frequency bands above 10 Hz. The slower velocities have lower amplitudes for all waves. Surface waves are delayed in time whereas the P-waves all arrive at the same point in time. The surface waves for the CLVD component exhibit a more pronounced effect of Poisson's ratio on surface wave amplitude, with as much as seven times higher amplitude for the slowest V_s models below 20 Hz.

Using actual data from the SPE and Green's functions representing the geologic structure in Morenci copper mine, the moment tensor was fully recovered. The inversion using the standard depth and Poisson value, produced horizontal dipoles (M_{xx} and M_{yy}) which are roughly half the size of M_{zz} consistent with an LVD source, thus suggesting that the free surface interactions are important for these chemical explosions. The deviatoric components ranged from 0.23 to 0.42 the moment of the M_{zz} component, illustrating that a purely isotropic model cannot completely explain the observations and suggests the presence of a secondary non-spherical source. The M_{xz} deviatoric component, although smaller than the force dipoles, is still significant and motivates further investigation of secondary sources, possibly due to the local geometry around the mine.

Observations from the SPE are compared to predictions based on the recovered moment tensors. Cross-correlation values are used to quantify the fits for each station with the mean of all the stations for a single inversion used to assess the inversions. For the standard Morenci model (30 m DOB and 0.25 Poisson's ratio), we investigated the fits over a wide range of frequency bands. First, cross-correlation values were computed using the full bandwidth of the data with a mean value of 0.55. Using the more limited frequency band of 2-20 Hz gave a value of 0.72. The band giving the highest cross-correlation value was the 2-10 Hz band, 0.88. This 33% increase from the unfiltered correlation value that reflects the improved adequacy of the Green's functions at lower frequencies. Comparing all the propagation models with the range of Poisson's ratios (**Figure 1.23**), the V_s model with $\nu = 0.25$ performs the best, with degradation of fits for both the faster and slower velocities. Similar assessment of the effects of source depth on fits illustrates that the best fits accompany the standard depth of burial of 30 m although the 15 m depth of burial also produces good fits.

Isotropic and deviatoric components of the moment tensor were calculated in both time and frequency domain. For each population of models, as shear wave increases and depth decreases, the moments increase with depth of burial having the largest effect of moment increase.

Moment rate spectrum from shot B4 was compared to MM71, DJ91 and MMP12 (**Figure 1.19**). The DJ91 corner frequency is too low to accurately model our data whereas the MM71 and MMP12 have corner frequencies that do. The difference in long period amplitude between MM71 and MMP12 is small compared to the spread in our data but are still too high to accurately model our moment rate spectra. In the future, parameterization of our data to create a more accurate model will be done.

Hudson diagrams were used to visualize frequency dependent changes in source mechanism based on the inversions. At the lowest frequencies, the source plots close to the linear vector dipole consistent with the large M_{zz} component and then move towards the pure explosion source representation as frequency increases. This result suggests that the degree of symmetry in explosion source model may be frequency dependent and that the higher frequencies or shorter wavelengths provide the most isotropic characterization. Evaluating different V_S models illustrates that as V_S slows, the source representations become more explosion-like and as the S-wave velocity increases, the source representations become more CLVD-like (**Figure 1.23**).

As noted in the motivation, the ratio of the vertical force dipole, M_{zz}, relative to the two horizontal dipoles, M_{xx} and $M_{yy,}$ may provide a quantification of the importance of free surface interactions on the source function and the local generation of surface waves. Calculating the ratio for all models for the 0.6-20 Hz frequency band, as seen in **figure 1.23**, as the shear wave velocity slows, the ratio becomes more explosion like. For the 0.6-20 Hz frequency band, as depth becomes greater, the ratio also becomes more explosion like.

TABLES

Table 1.1 – SPE Shot descriptions

Shot Description	Date	Time* (UTC)	Yield Estimate (kt)	Centroid Depth (m)	Scaled Depth $\left(\frac{m}{kt^{\frac{1}{3}}}\right)$
B1 - Single Hole Free Face	18-Aug-03	20:18:15.1	$0.77\text{x}10^{-3}$	12.2	129
B2 - Four Hole Free Face	18-Aug-03	20:28:40.3	$3.08\text{x}10^{-3}$	12.2	81
B3 - Single Hole 2x burden	18-Aug-03	21:35:10.0	$0.77\text{x}10^{-3}$	12.2	64
B4 - Four Hole 2xdepth	18-Aug-03	18:46:51.8	$3.08\text{x}10^{-3}$	30.5	203
B5 - Four Hole 2x burden	18-Aug-03	19:04:35.4	$3.08\text{x}10^{-3}$	12.2	81
B6 - Single Hole 2x depth	18-Aug-03	19:26:02.7	$0.77\text{x}10^{-3}$	30.5	322
B7 - Eight Hole Free Face	18-Aug-03	19:51:00.3	$6.17\text{x}10^{-3}$	12.2	64
B8 - Two Hole 2x burden	18-Aug-03	20:10:39.1	$1.54\text{x}10^{-3}$	12.2	102
B10 - Eight Hole 2x depth	18-Aug-03	21:06:22.0	$6.17\text{x}10^{-3}$	30.5	161

* Shot time based on the first arrival at closest site

Table 1.2 – Constrained V_p for the top four layers of the model and their respective V_s based on the altered Poisson values.

V_p	Layer top depth	Faster V_s model V_s for ν =.15	Baseline V_s model V_s for ν = .25	Slower V_s model V_s for ν = .4
.6096 km/s	0.000 km	0.3912 km/s	0.3522 km/s	.2489 km/s
3.048 km/s	0.005 km	1.956 km/s	1.760 km/s	1.244 km/s
3.721 km/s	0.023 km	2.388 km/s	2.148 km/s	1.519 km/s
4.487 km/s	0.150 km	2.879 km/s	2.590 km/s	1.832 km/s

Table 1.3 – Source model parameters used for this experiment.

V_p	V_s	ρ	Source depth	Yield
3.72 km/s	1.52 km/s	2.2 g/ccm	30 m	$6.2x10^{-3}$

FIGURES

Figure 1.1 – Map of the 16 near-field accelerometers, velocity transducers and shot locations. The larger circle is the elastic radius developed from analyzing accelerometer data to determine where spall occurred. The inside elasic radius is determined from cavity scaling relations using a MM71 granite source model.

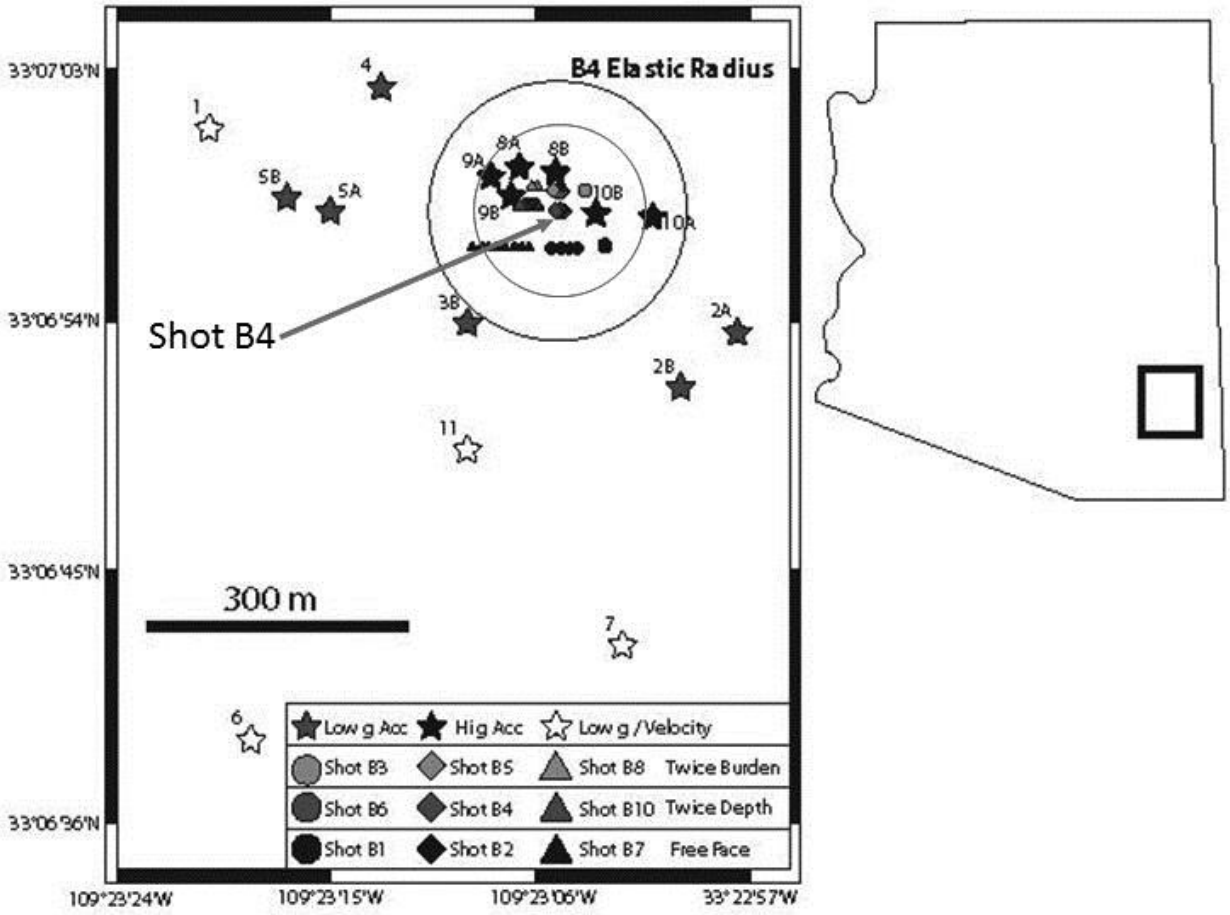

Figure 1.2 – The layout of the refraction survey on the test bed.

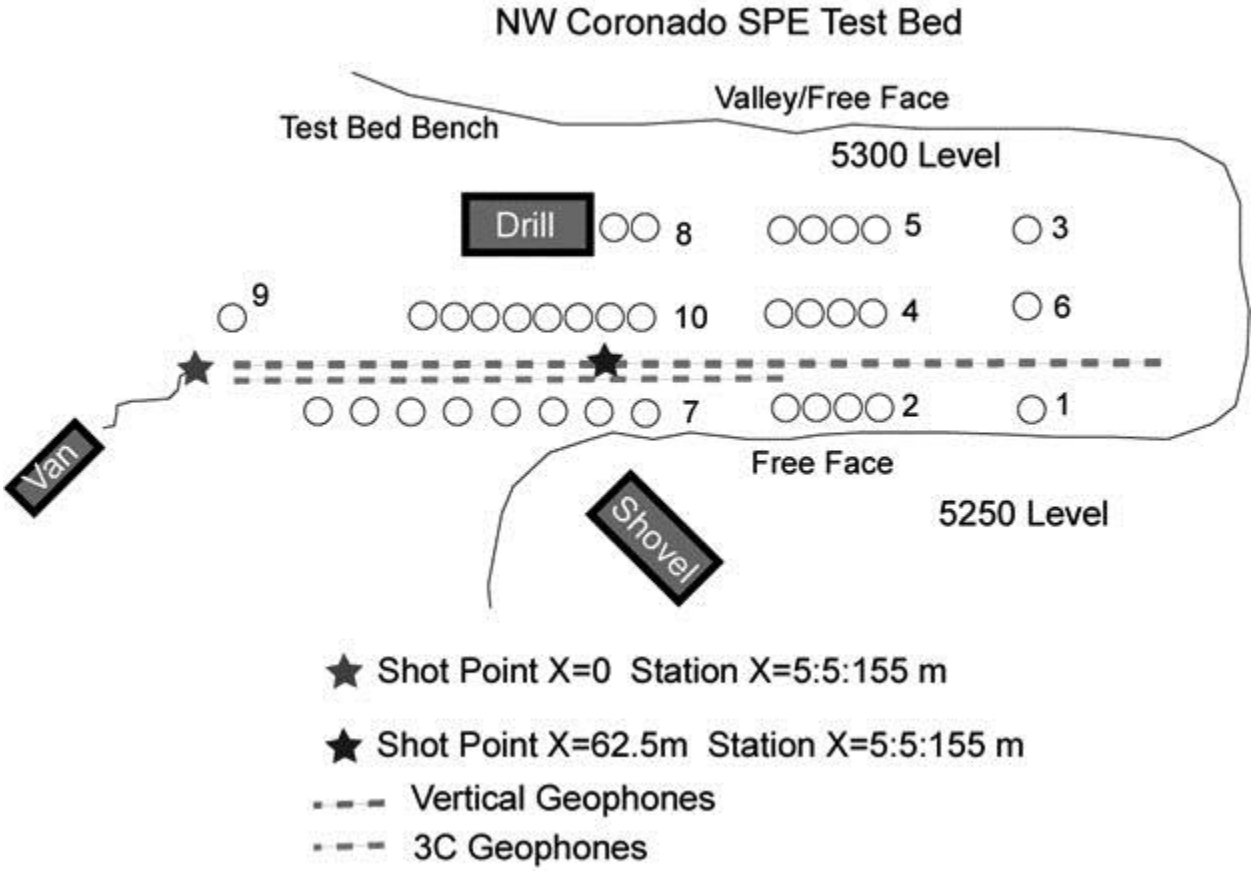

Figure 1.3 – The shot site was located on a bench to utilize three explosion scenarios

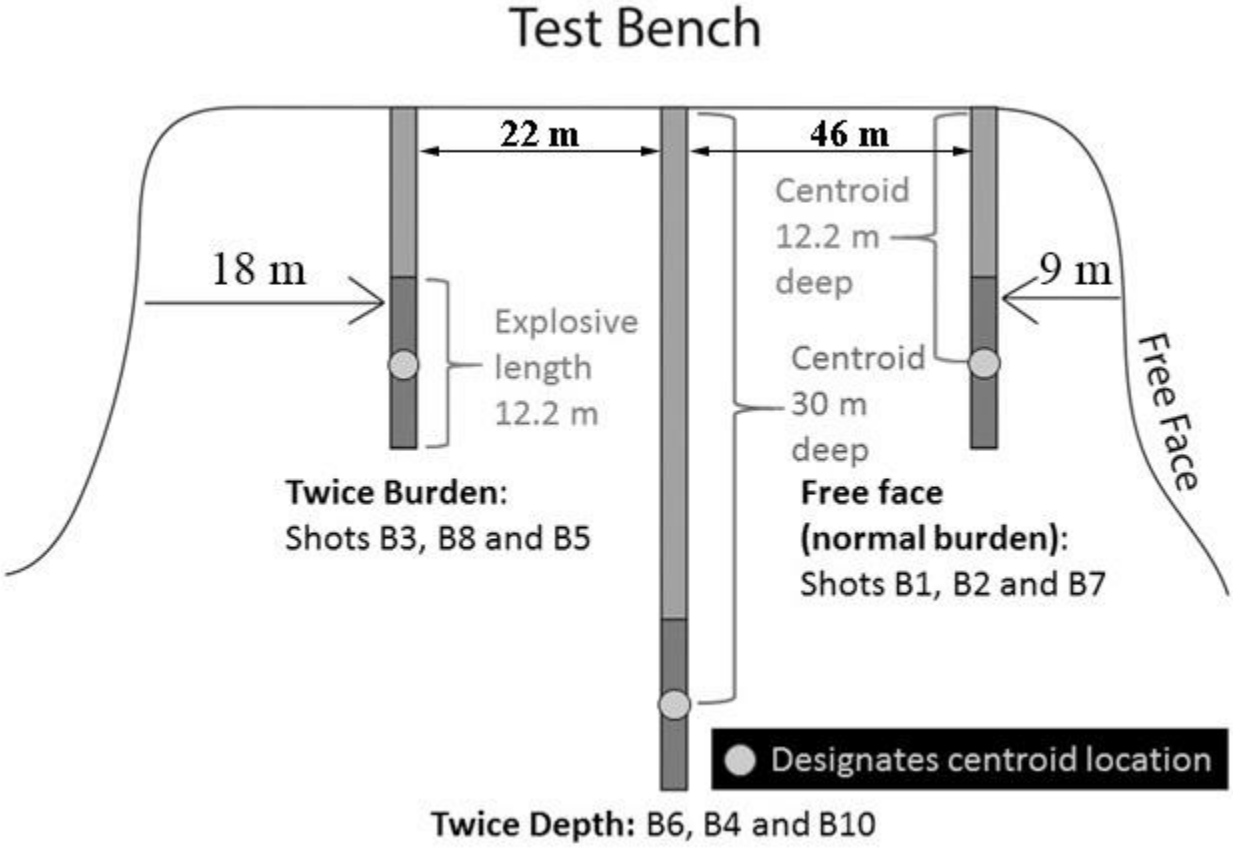

Figure 1.4 – One dimensional structure model for the copper mine displaying V_p, V_S, density, P and S-wave attenuation coefficients and Poisson's ratio for the nine layers.

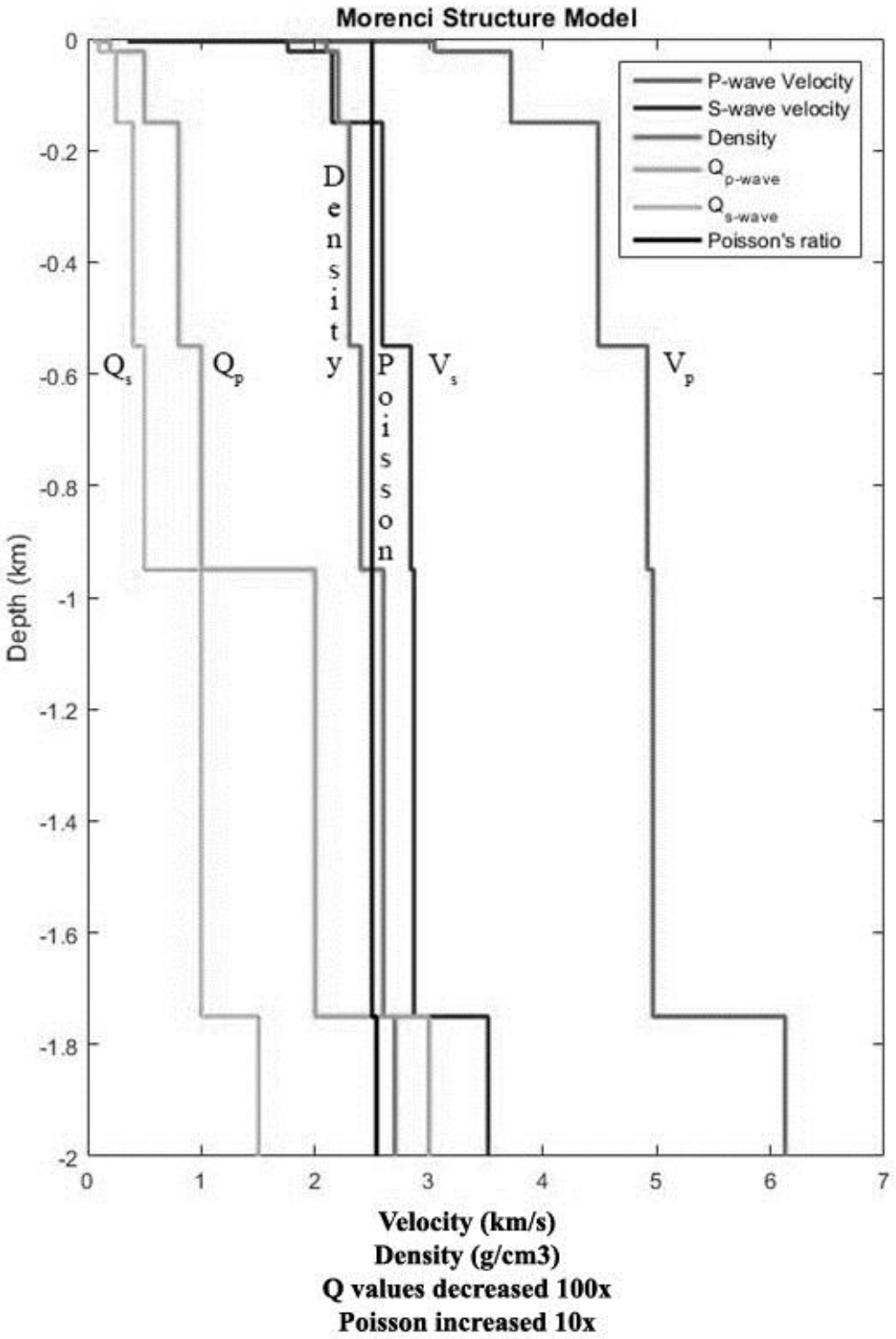

Figure 1.5 – Shallow geologic layers below Morenci copper mine.

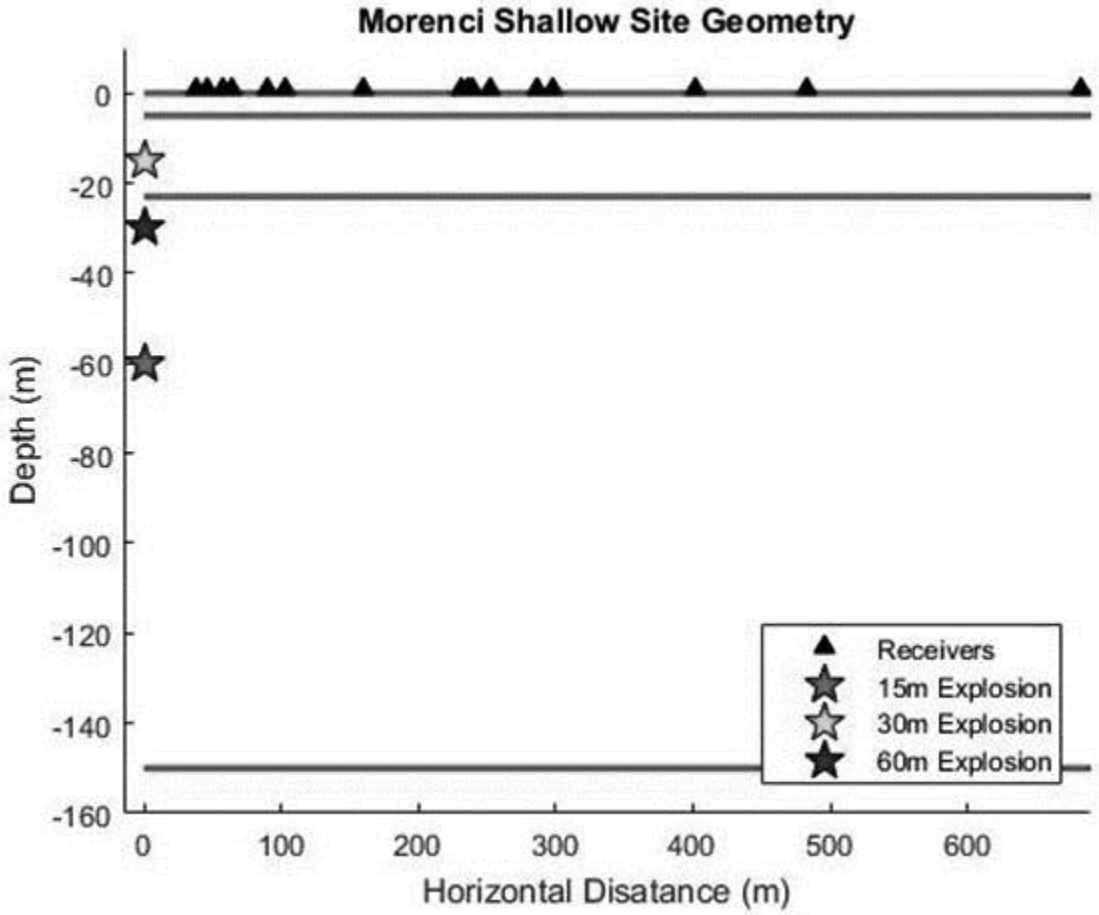

Figure 1.6 – Variable DOB explosion radial Green's function component at 683 m distance. Dark, medium and light traces are sources at half (15 m), standard (30 m) and twice (60 m) DOB respectively.

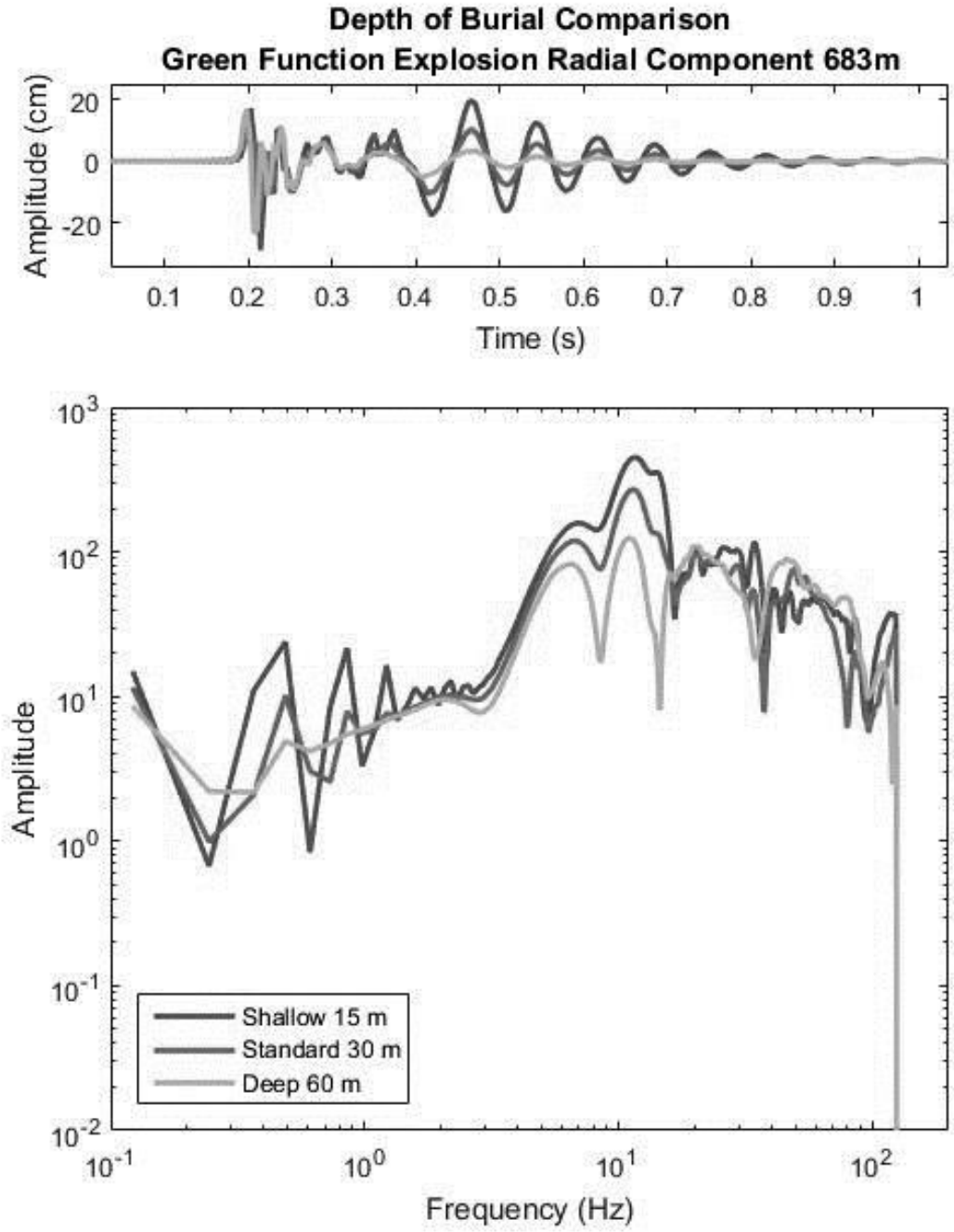

Figure 1.7 – Variable DOB CLVD radial Green's function component at 683 m distance. Dark, medium and light traces are sources at half (15 m), standard (30 m) and twice (60 m) DOB respectively.

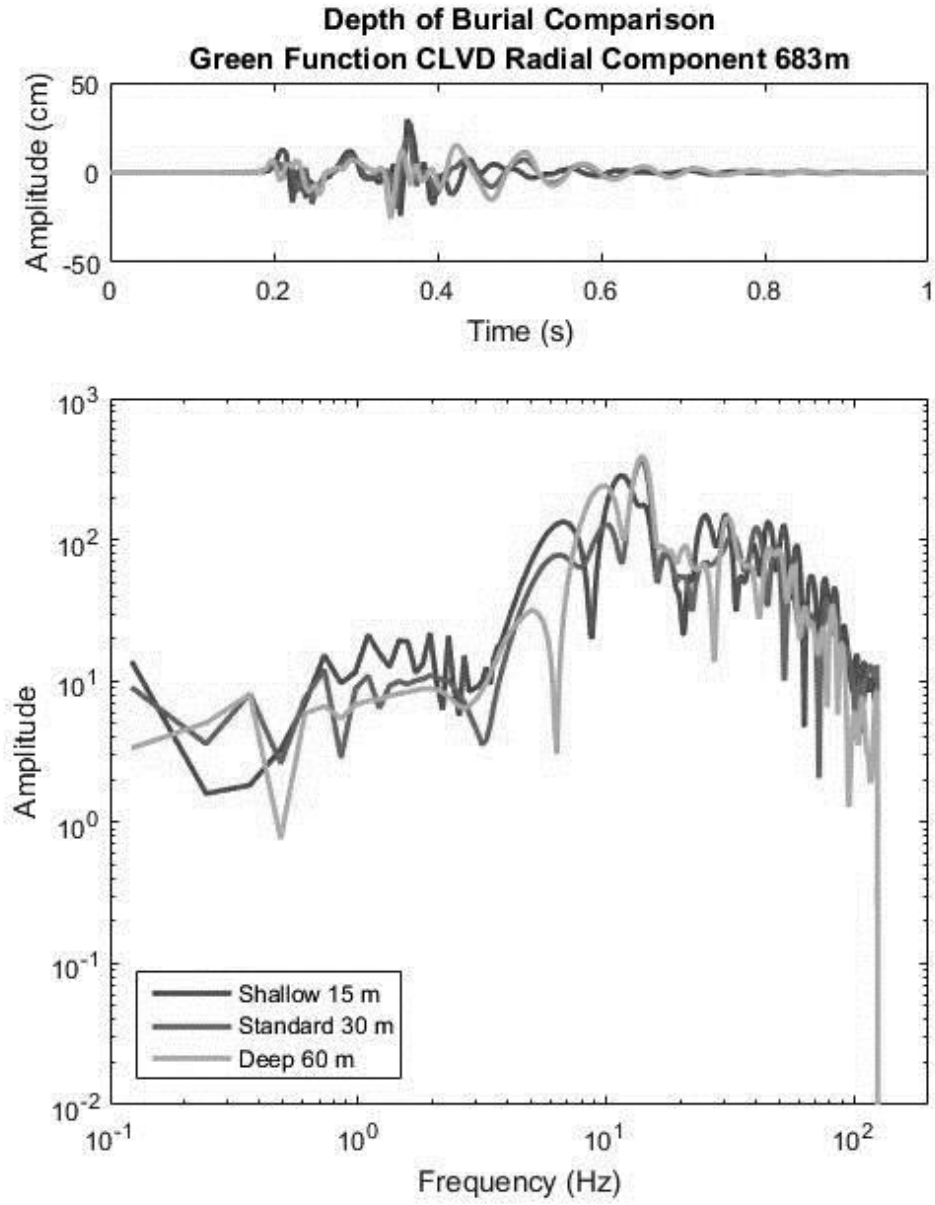

Figure 1.8 – Variable shear wave velocity explosion radial Green function component at 683 m distance. Dark, medium and light traces are fast (0.15), standard (0.25) and slow (0.40) V_S, respectively.

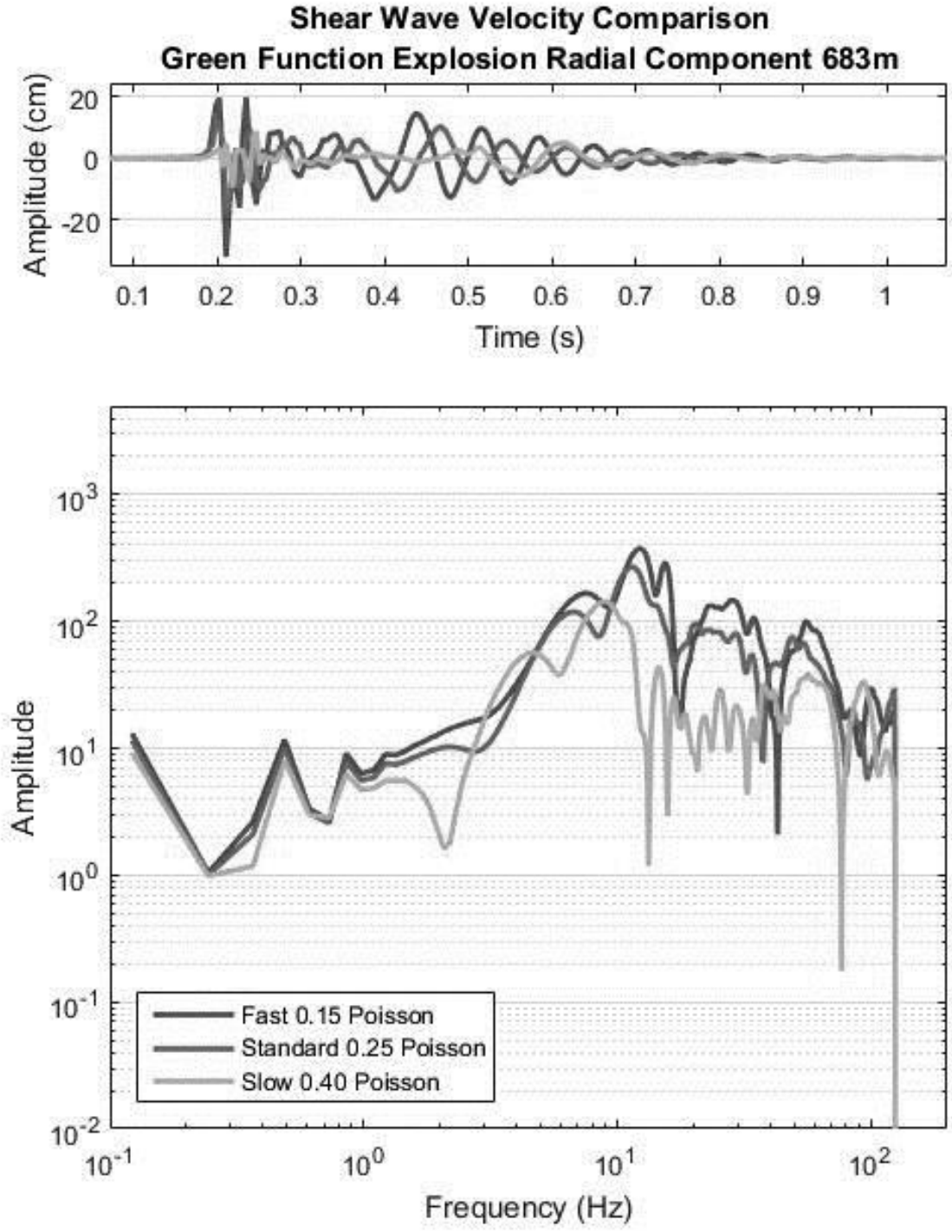

Figure 1.9 – Variable shear wave velocity CLVD vertical Green function component at 401 m distance. Dark, medium and light traces are fast (0.15), standard (0.25) and slow (0.40) Vs, respectively.

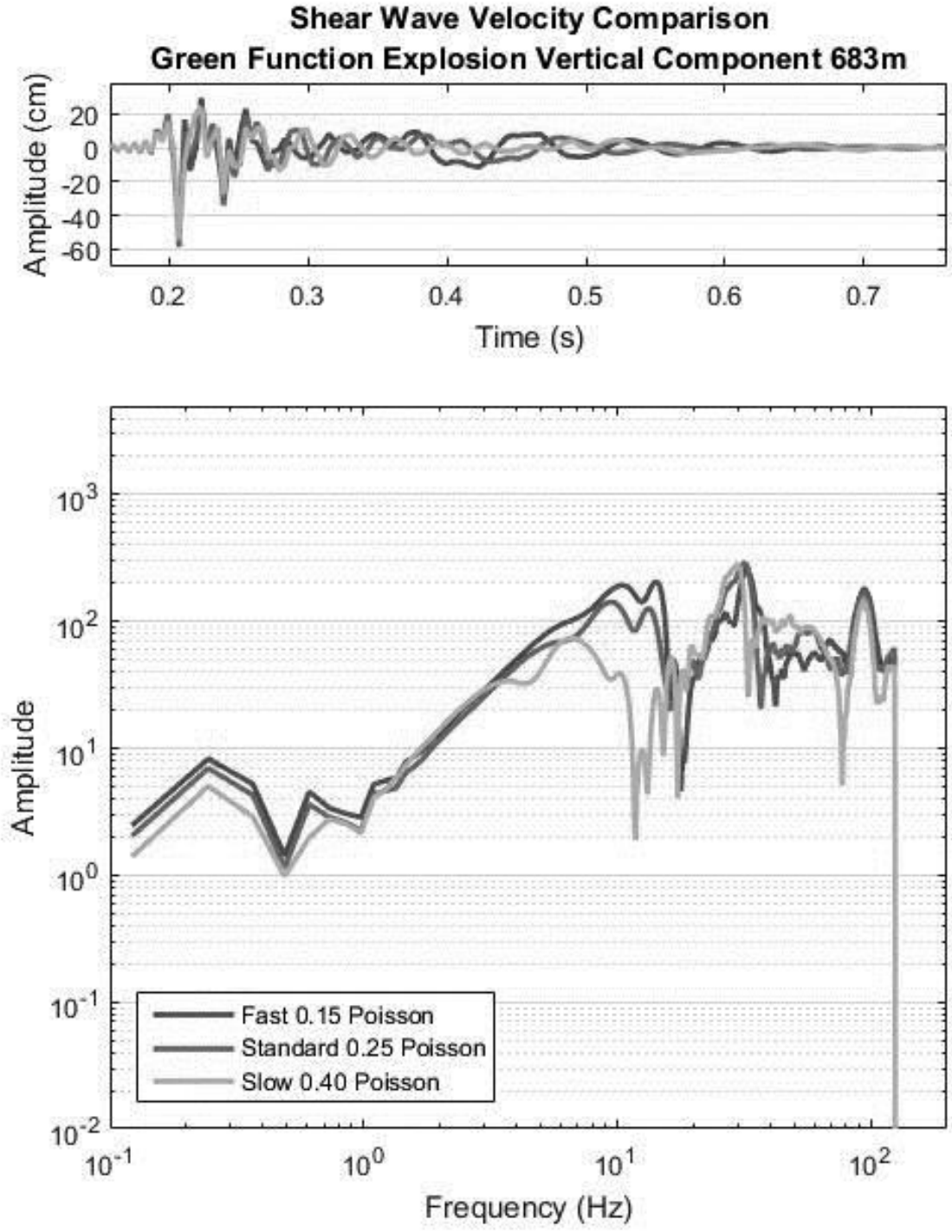

Figure 1.10 – Variable DOB explosion vertical Green function components and spectral ratios at 683 m distance. black, dark grey and light grey traces are sources at half (15 m), standard (30 m) and twice (60 m) DOB respectively. Dashed black and dashed light grey are standard/shallow (30m/15m)

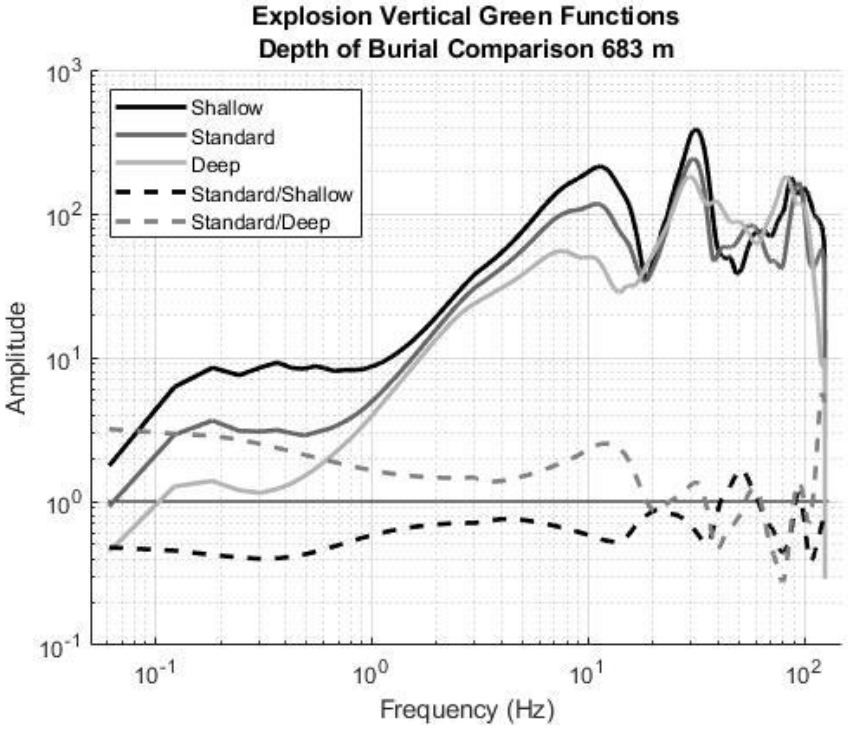

Figure 1.11 – Variable shear wave velocity explosion vertical Green function component and spectral ratios at 683 m distance. Black, dark grey and light grey traces are fast (0.15), standard (0.25) and slow (0.40) V_s respectively. Dashed black and dashed dark grey traces are standard/fast (0.25/0.15) and standard/slow (0.25/0.4) respectively.

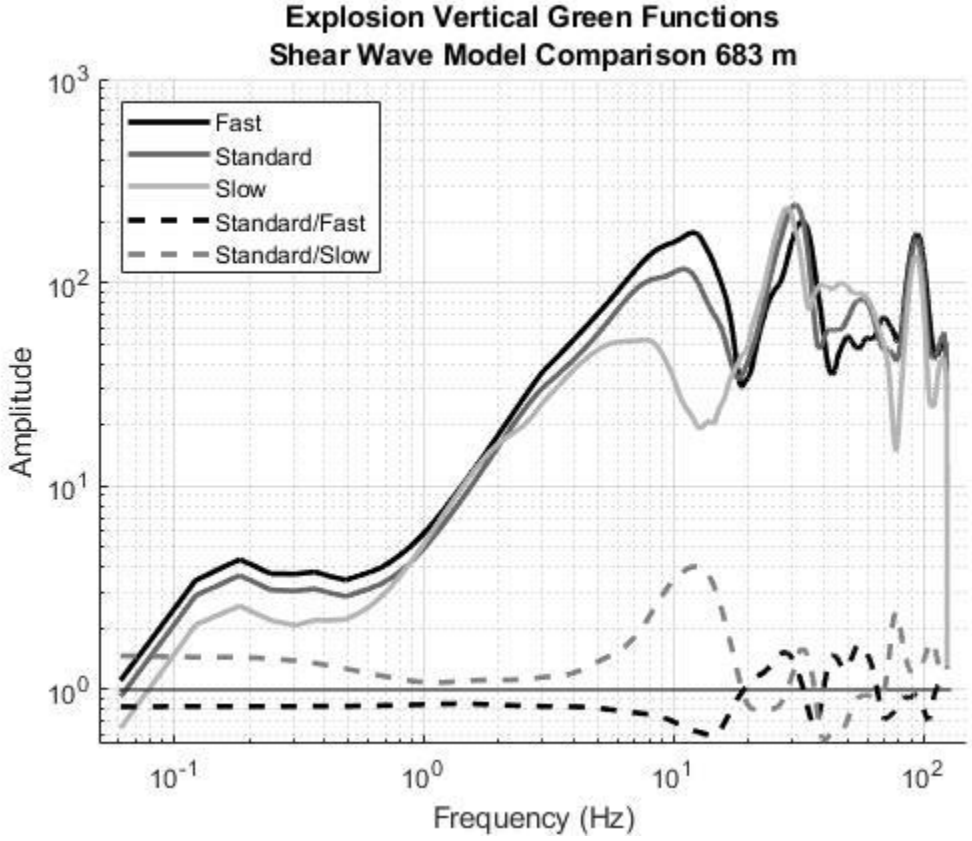

Figure 1.12 – Estimated moment tensor for shot B4 using stations in the 150-680 m range. Values are peak amplitudes.

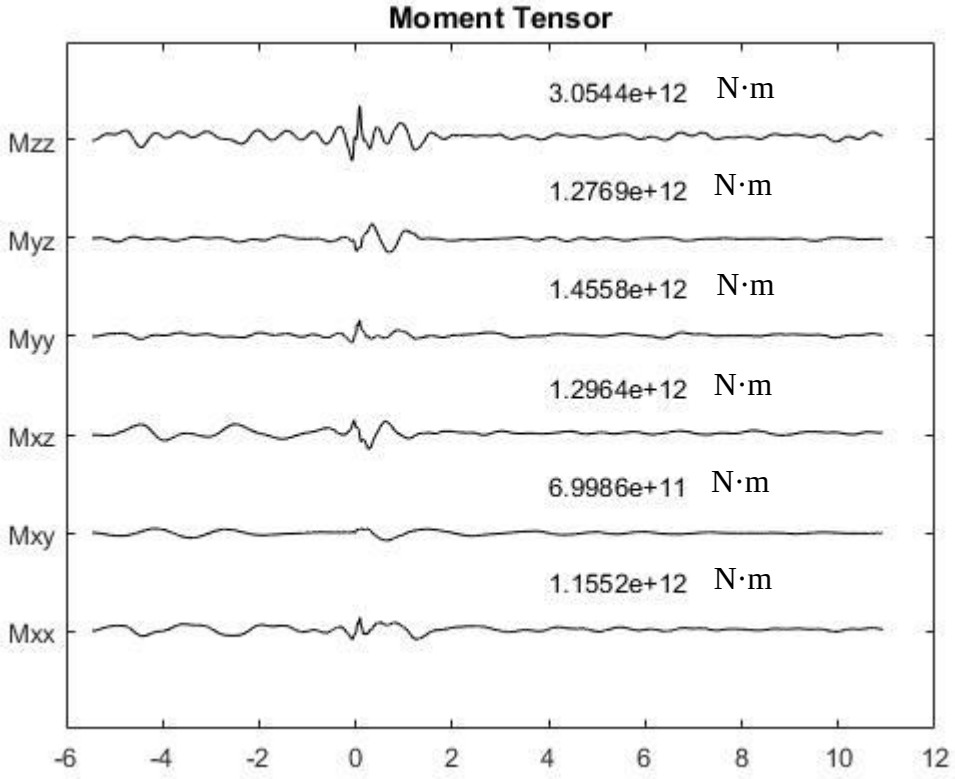

Figure 1.13 – Moment-rate tensor M_{zz} component time series and spectrum.

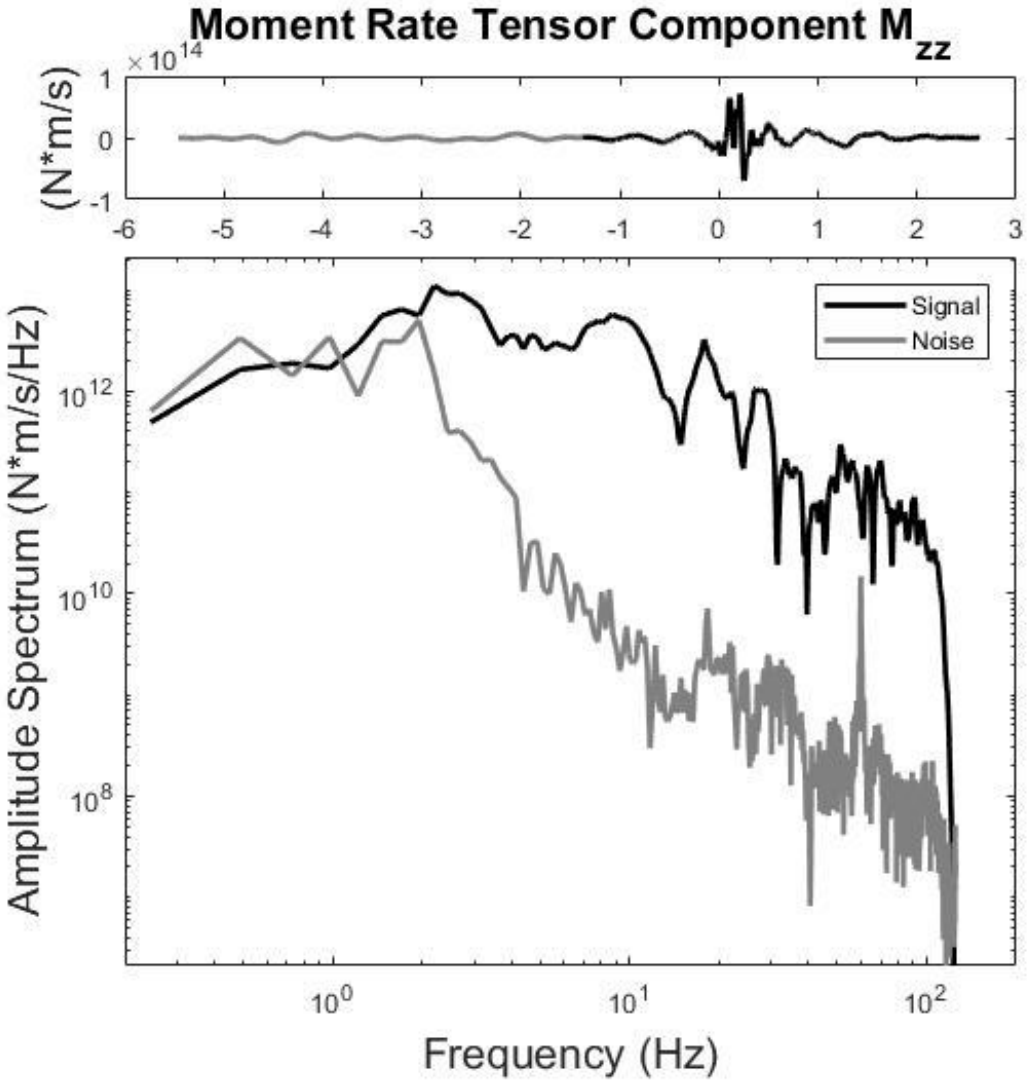

Figure 1.14 – Station 2 ground motion data time series and amplitude spectrum

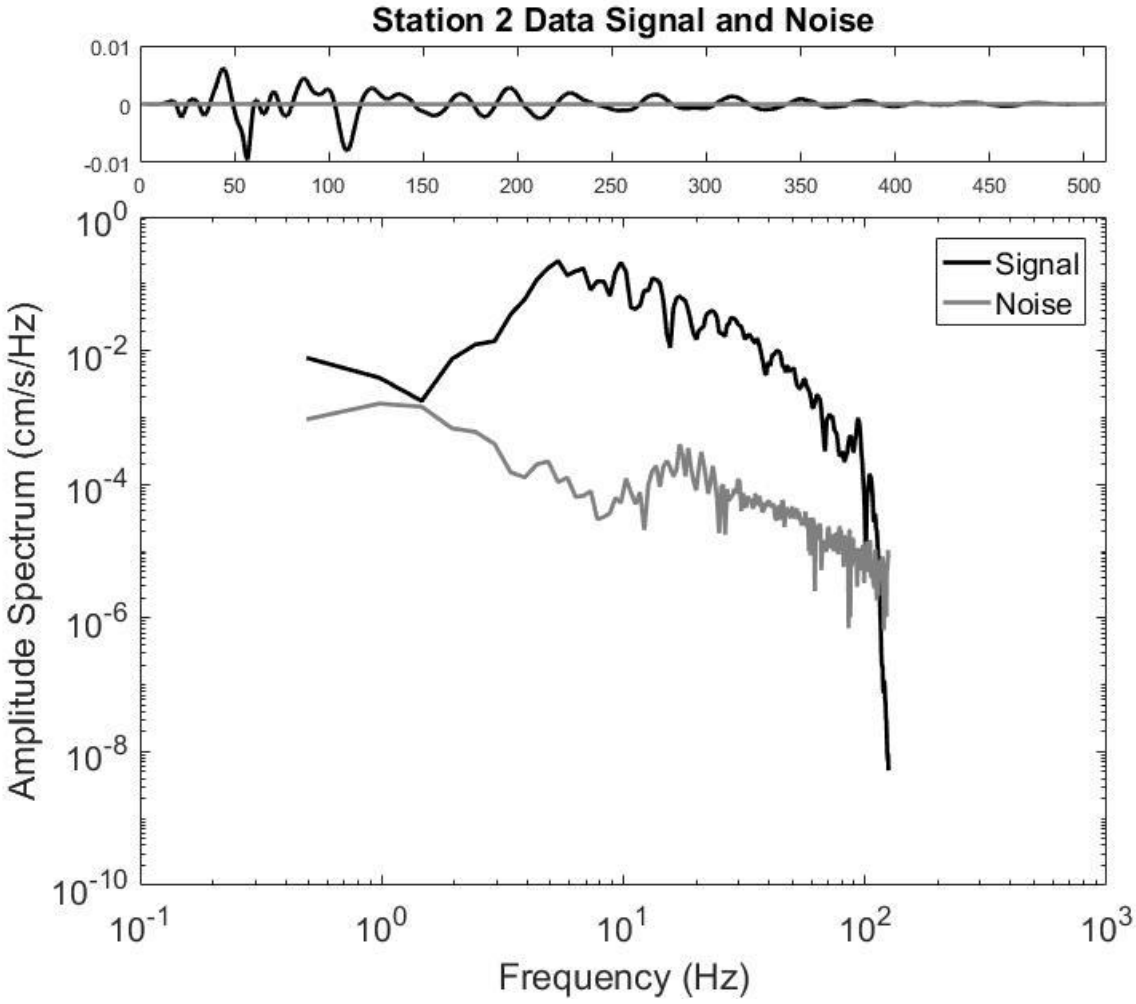

Figure 1.15 – Fitted and observed seismograms for this data set using the standard Morenci model parameters unfiltered with respective and mean cross-correlation coefficients.

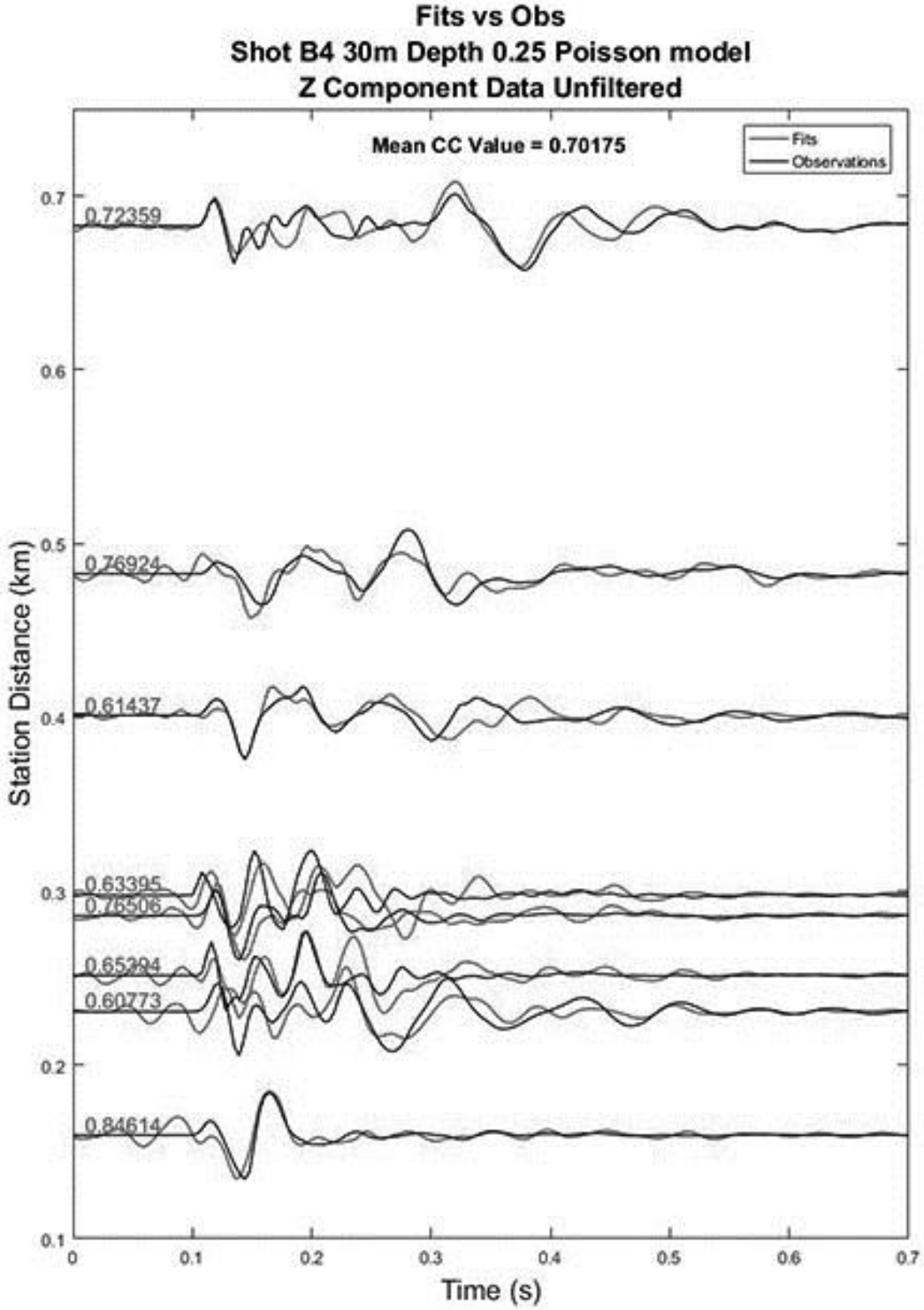

Figure 1.16 –a) Fitted and observed seismograms for this data set using the standard Morenci model parameters bandpass filtered from 2-10 Hz. **b)** Fitted and observed seismograms for this data set using the standard Morenci model parameters bandpass filtered from 2-20 Hz.

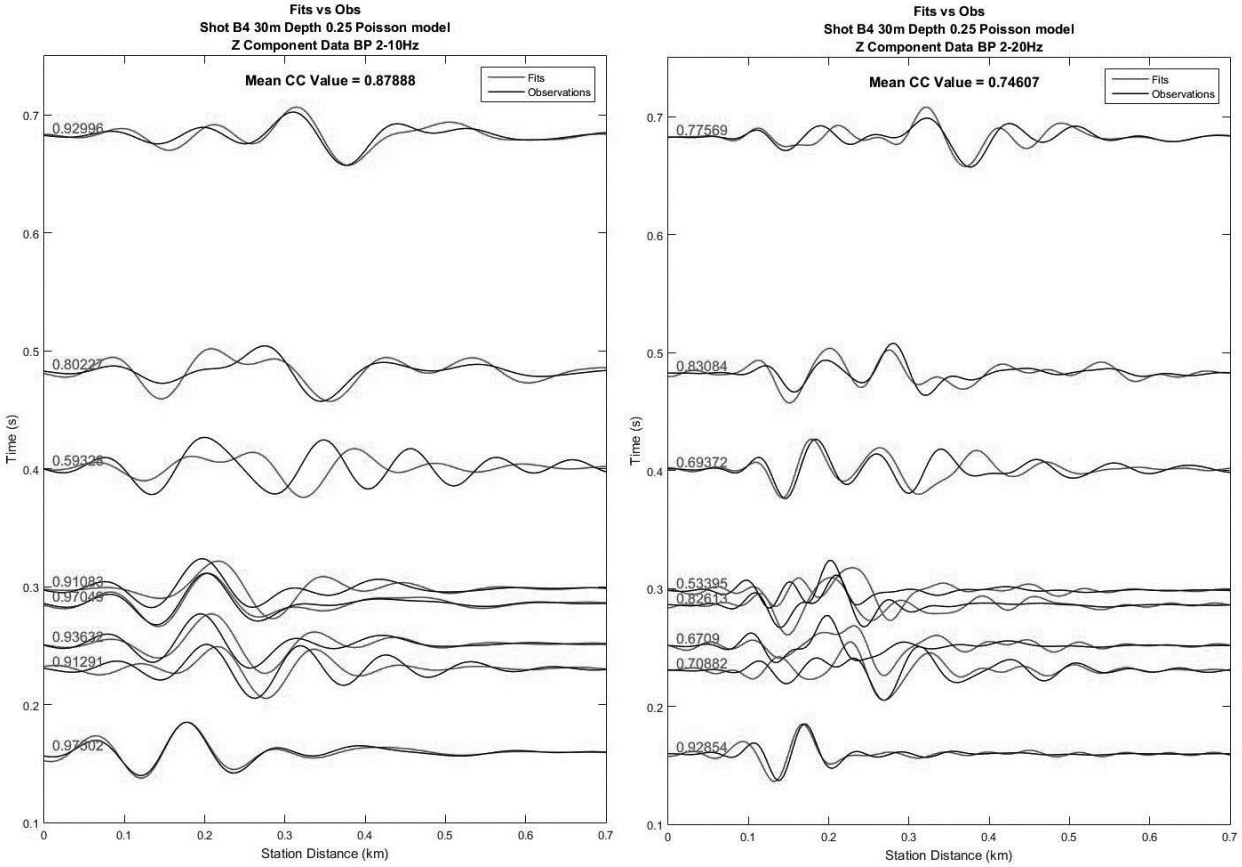

Figure 1.17 –Mean cross-correlation values of the unfiltered Z component fits and observations for all six velocity models at all three depths of burial for stations. Mean values calculated with only the eight stations within the linear zone.

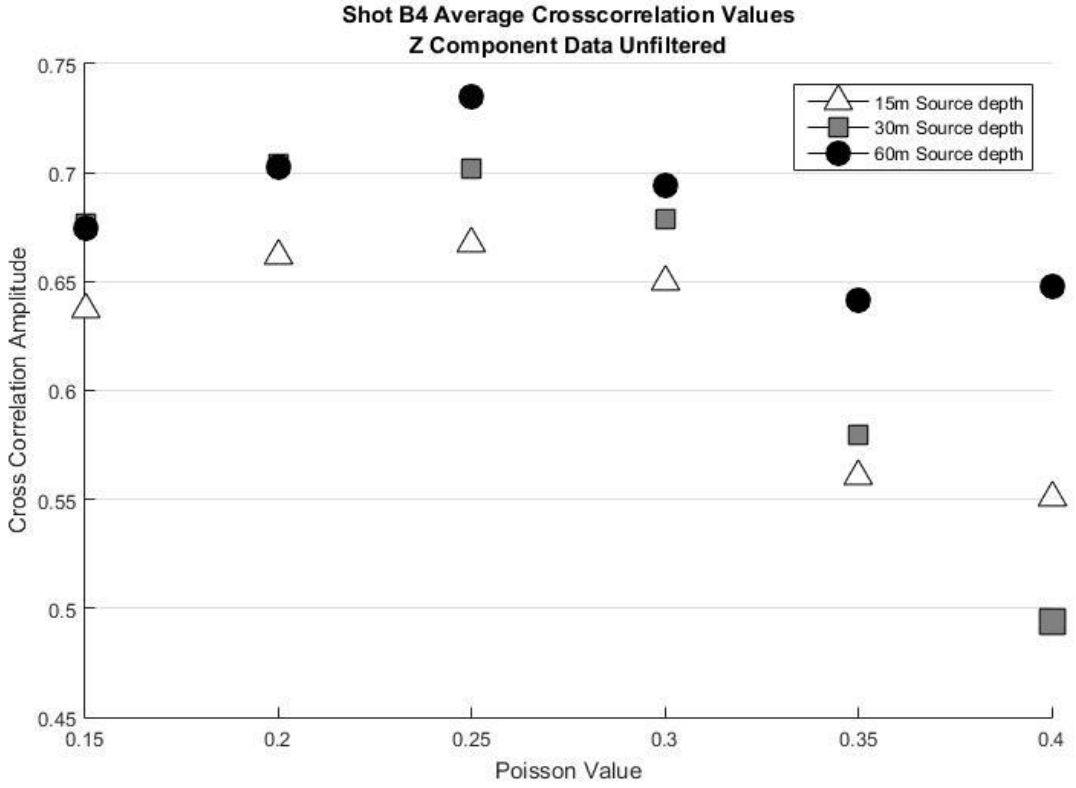

Figure 1.18 –Shot B4 Mzz and Mtr moment rate spectra plotted with the MM71, DJ91 and Revised Heard Ackerman source models in granite. The spectrums were smoothed with a 1 Hz smoothing window.

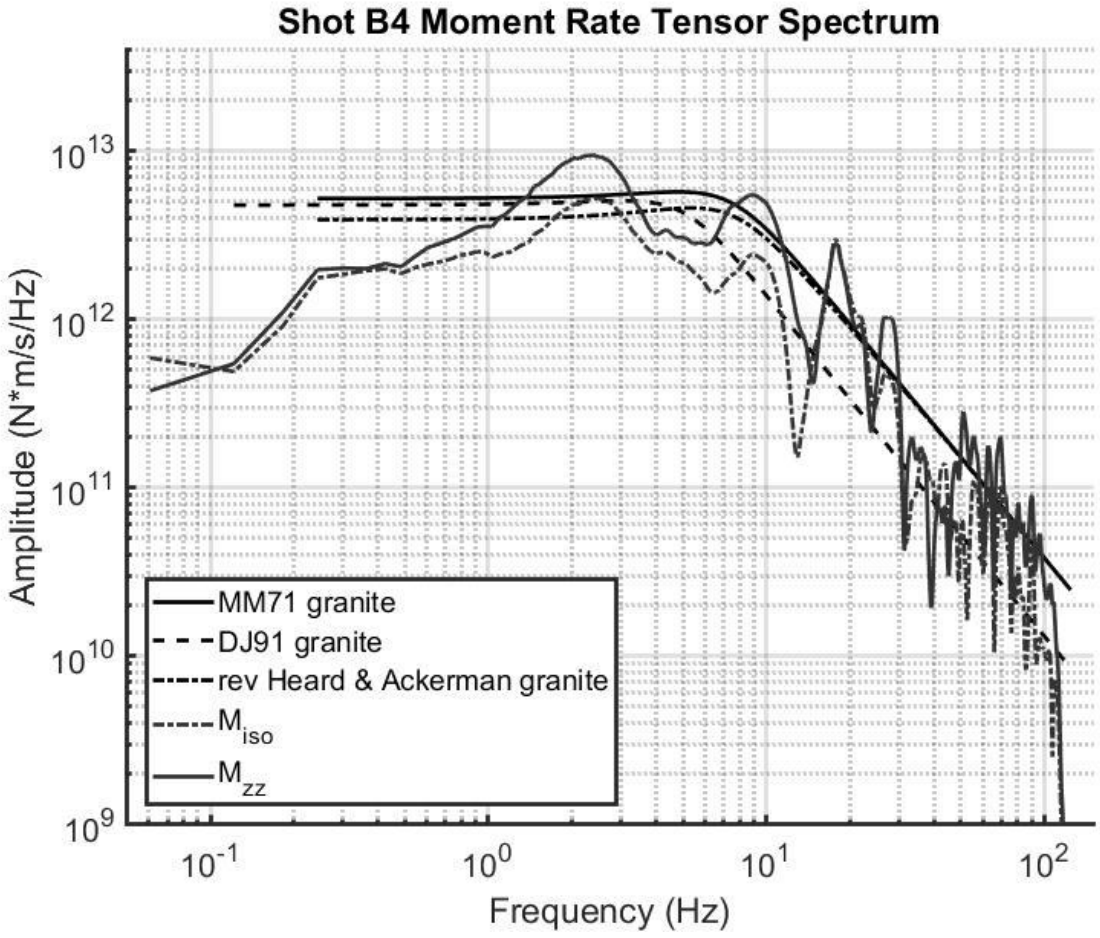

Figure 1.19 –Hudson diagram for the frequency domain moment tensor inversions plotted in source type space from 0.06-20 Hz with the red highlighted rectangle our source representation area of interest. The red rectangle will be used to highlight later figures.

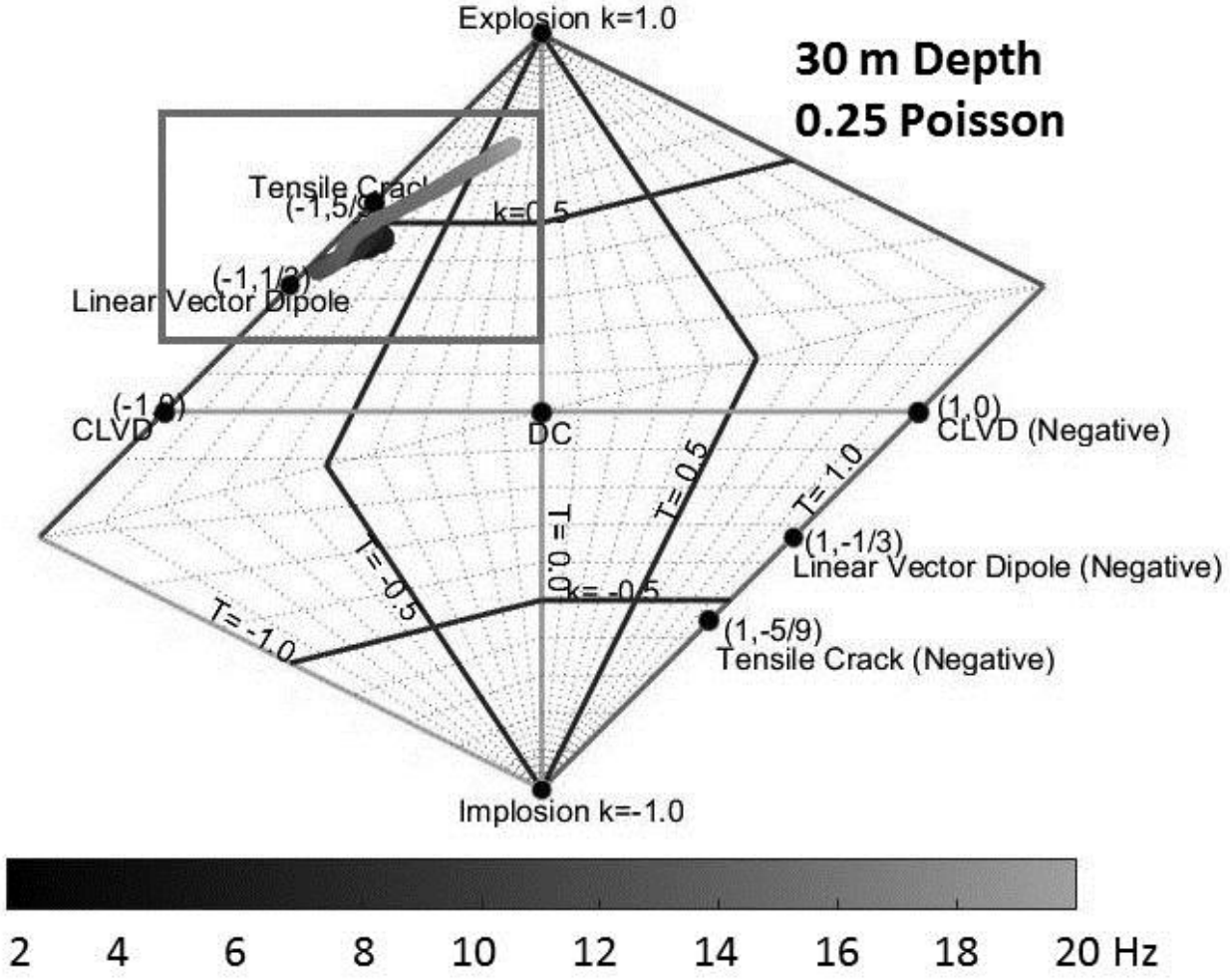

Figure 1.20 –The six moment tensor component spectra for the three depths of burial, 15 m (upper left), 30 m (upper right) and 60 m (lower right). All three depths use the standard (0.25 Poisson value) V_s model.

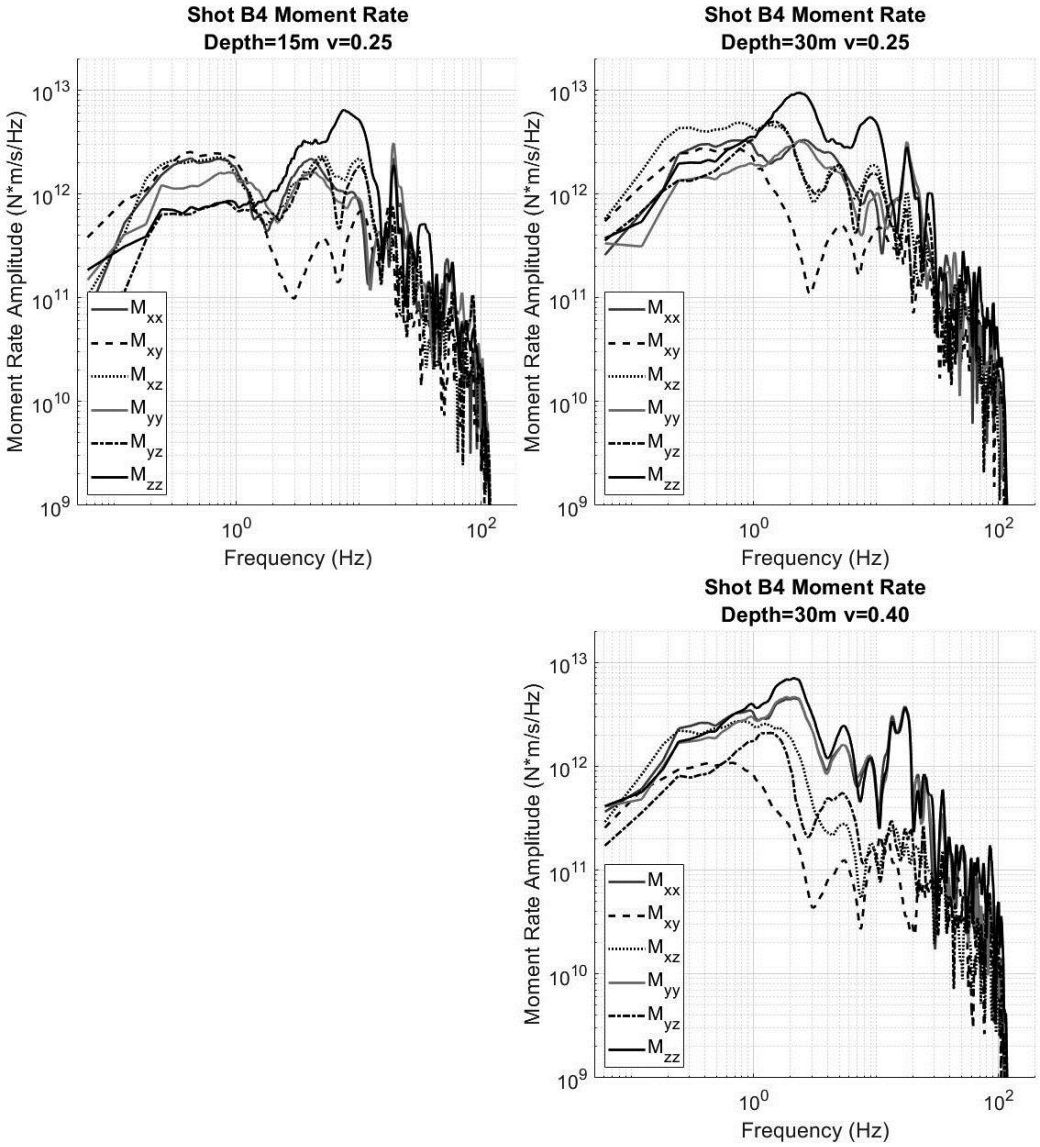

Figure 1.21 –The six moment tensor component spectra for the standard 30 m depth of burial spanning three Vs structure models. The fastest 0.15 Poisson value (left), standard 0.25 (middle) value and slowest 0.40 (right).

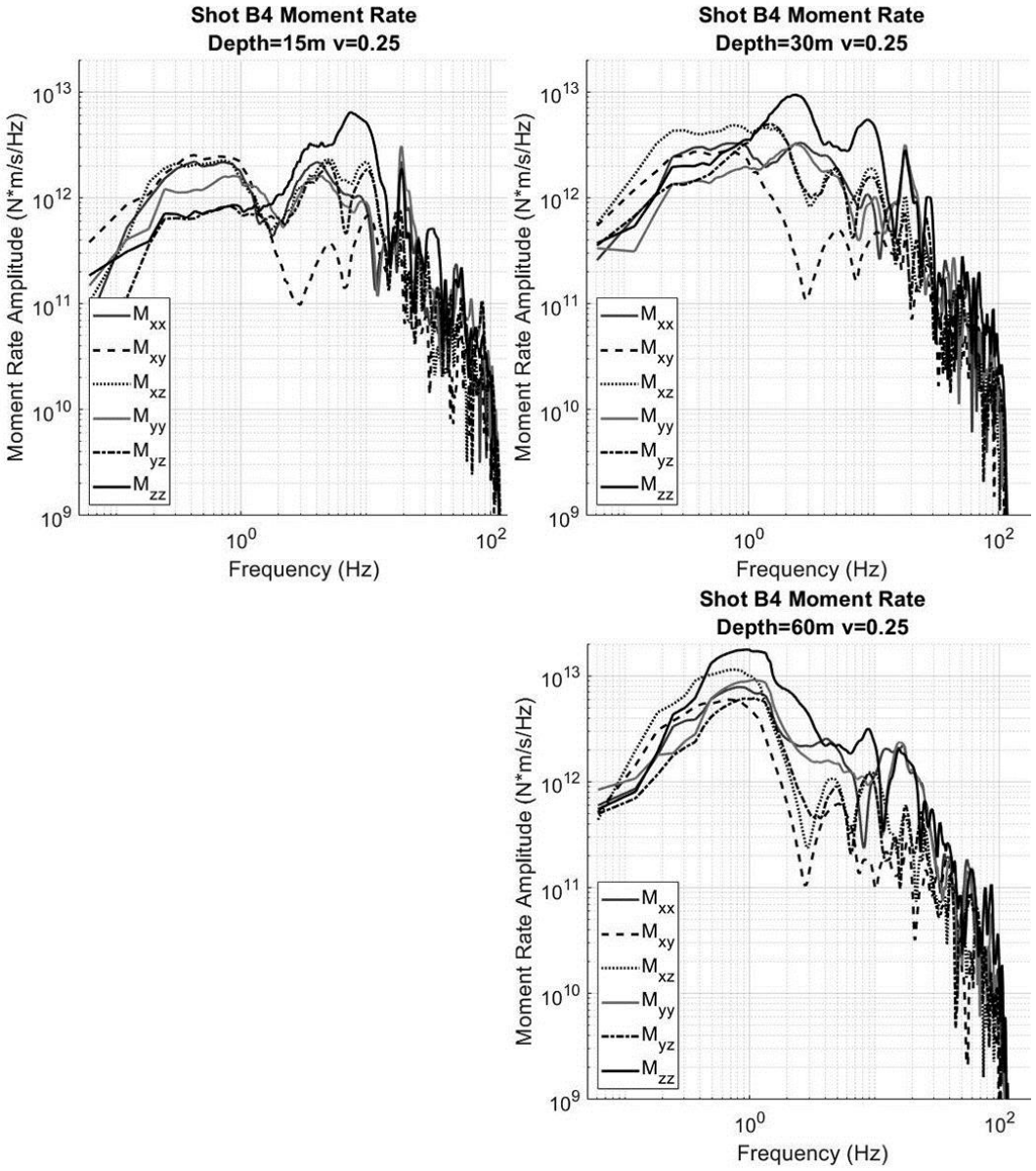

Figure 1.22 –Source type plots with 30 m source depth of burial for 0.15 (left), 0.25 (middle) and 0.40 (right) Poisson values (scale follows figure 1.20).

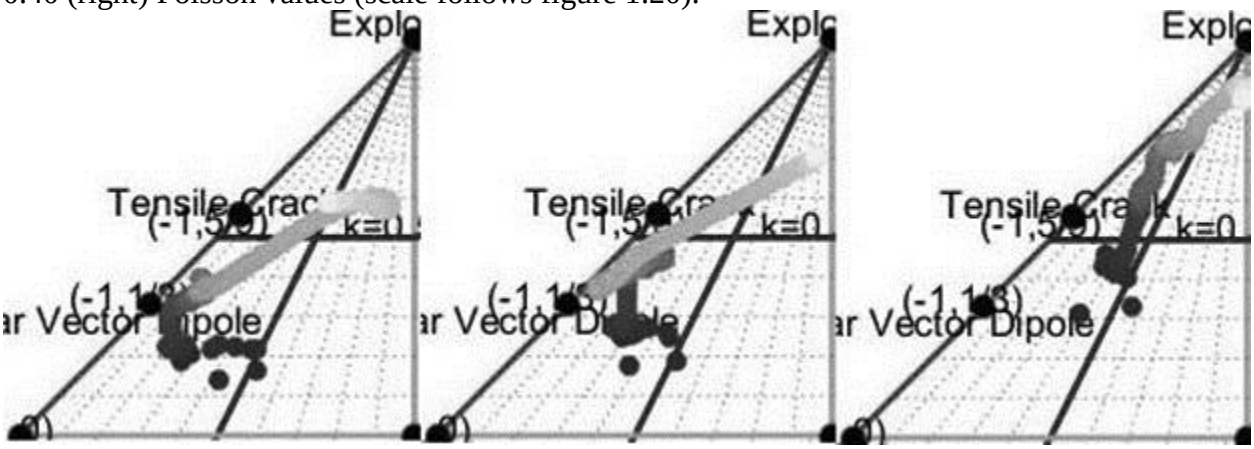

Figure 1.23 –Ratio of the vertical force dipole, M_{zz}, relative to the two horizontal dipoles, M_{xx} and M_{yy} for all the depths of burial.

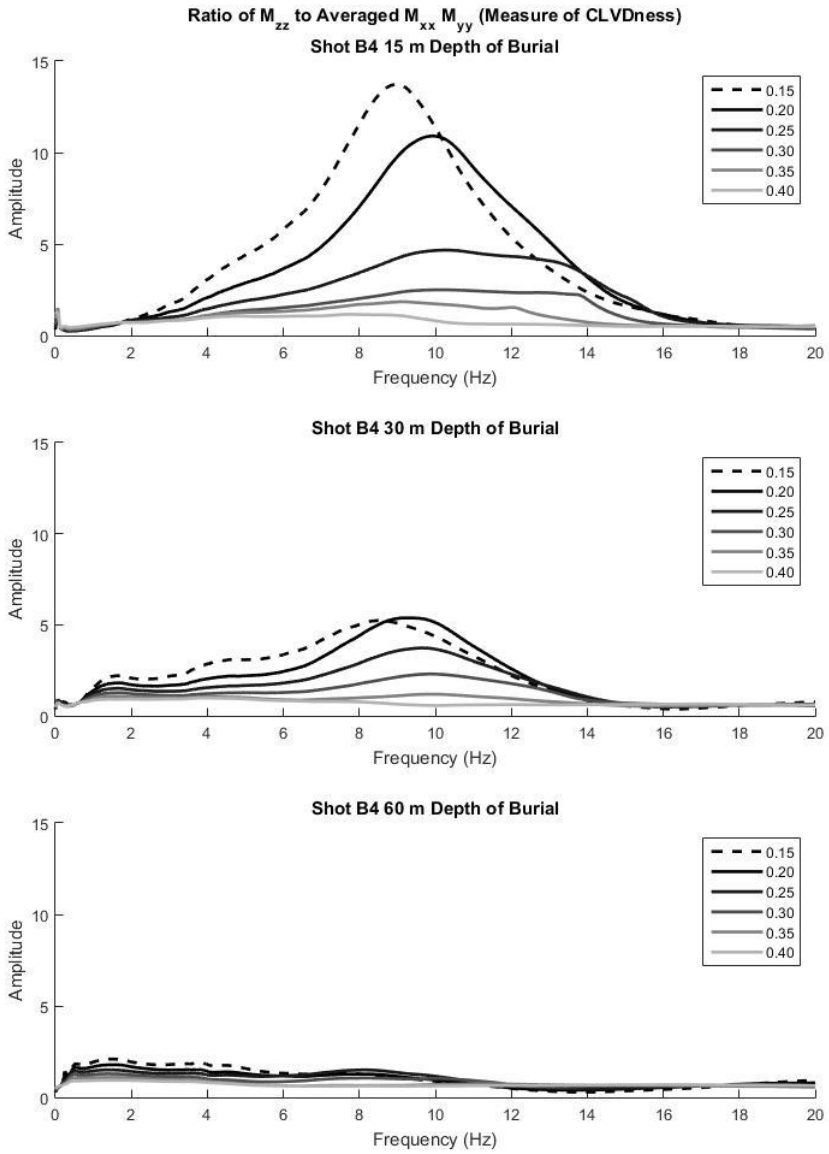

Figure **1.24 –**Yield vs isotropic moment modified from Denny and Johnson comparing chemical explosions (W < 0.001 kt) and nuclear explosions (W > 1 kt) to this study's shot B4, doubling the yield and using different source depths and shear wave velocity models. The deepest source depth, 60 m, with a range of shear wave velocities are plotted as black X's. The standard source depths, 30 m, are plotted as dark grey X's. The shallowest source depths, 15 m, are plotted as light grey X's.

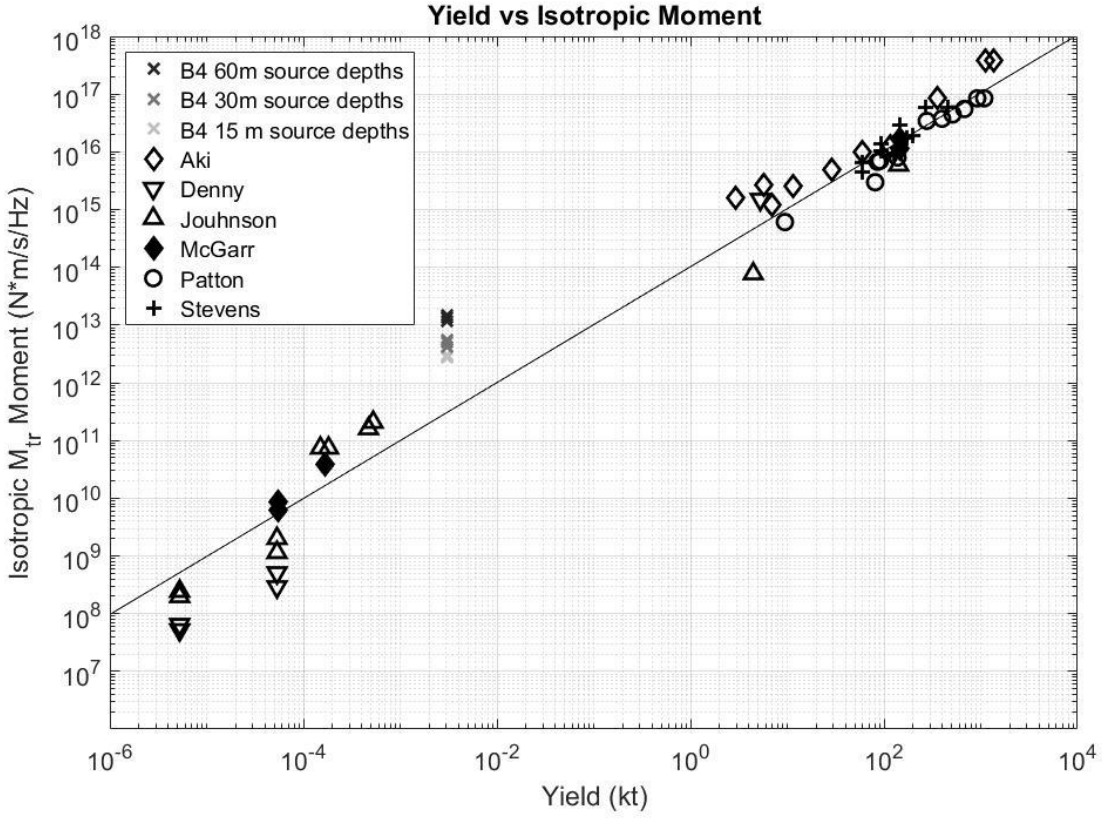

REFERENCES

Aki, Keiiti, and Paul G. Richards. *Quantitative seismology*. Vol. 1. 2002.

Antoun, T. H., Xu, H., Vorobiev, O. Y., Herbold, E. B., Glenn, L. A., & Lomov, I. N. (2011). Analysis and simulation of near-field wave motion data from the Source Physics Experiment explosions. LAWRENCE LIVERMORE NATIONAL LAB CA.

Bonner, Jessie L., et al. "Source phenomenology experiments in Arizona." *Proceedings of the 27th Seismic Research Review, Ground-based Nuclear Explosion Monitoring Technologies* (2005): 519-528.

Bonner, Jessie, et al. "The surface wave magnitude for the 9 October 2006 North Korean nuclear explosion." *Bulletin of the Seismological Society of America* 98.5 (2008): 2498-2506.

Bonner, Jessie L., Anastasia Stroujkova, and Dale Anderson. "Determination of Love-and Rayleigh-wave magnitudes for earthquakes and explosions."*Bulletin of the Seismological Society of America* 101.6 (2011): 3096-3104.

Bonner, J. L., Russell, D. R., & Reinke, R. E. (2013). Modeling surface waves from aboveground and underground explosions in alluvium and limestone. *Bulletin of the Seismological Society of America*, *103*(6), 2953-2970.

Chiang, Andrea, et al. "Source Characterization of Underground Explosions from Combined Regional Moment Tensor and First-Motion Analysis." *Bulletin of the Seismological Society of America* (2014).

Chun, K-Y., Y. Wu, and G. A. Henderson. "Magnitude estimation and source discrimination: A close look at the 2006 and 2009 North Korean underground nuclear explosions." *Bulletin of the Seismological Society of America* 101.3 (2011): 1315-1329.

Denny, Marvin, et al. "Seismic results from DOE's Non-Proliferation Experiment: A comparison of chemical and nuclear explosions." *Monitoring a Comprehensive Test Ban Treaty*. Springer Netherlands, 1996. 355-364.

Day, S. M., N. Rimer and T. Cherry, 1983. Surface waves from underground explosions with spall: Analysis of elastic and nonlinear source models, *Bull. Seism. Soc. Am.* **73**, 247-264.

Ford, Sean R., Douglas S. Dreger, and William R. Walter. "Source analysis of the Memorial Day explosion, Kimchaek, North Korea." *Geophysical Research Letters* 36.21 (2009).

Ford, Sean R., Douglas S. Dreger, and William R. Walter. "Identifying isotropic events using a regional moment tensor inversion." *Journal of Geophysical Research: Solid Earth* 114.B1 (2009).

Goldstein, P., and S. Jarpe, (1994). Comparison of chemical and nuclear explosion source spectra from close-in, local and regional seismic data, *Proceedings of the Symposium on the Non-Proliferation Experiment (NPE): Results and Implications for the Test Ban Treaties,* Rockville, Maryland, CONF 9404100, Lawrence Livermore National Laboratory, 19-21 April 1994.

Hayward, C., R.-M. Zhou and B. Stump, (2004), QuickLook Report: 2004 January Morenci Refraction Experiments and Morenci Refraction Interpretation, February 2004, Southern Methodist University.

Hudson, J. A., R. G. Pearce, and R. M. Rogers. "Source type plot for inversion of the moment tensor." *Journal of Geophysical Research: Solid Earth* 94.B1 (1989): 765-774.

Jost, ML U., and R. B. Herrmann. "A student's guide to and review of moment tensors." *Seismological Research Letters* 60.2 (1989): 37-57.

Minson, Sarah E., and Douglas S. Dreger. "Stable inversions for complete moment tensors." *Geophysical Journal International* 174.2 (2008): 585-592.

Kim, W. Y., and P. G. Richards. "North Korean Nuclear Test: Seismic Discrimination at Low Yield." *Eos* 88.14 (2007).

Koper, Keith D., Robert B. Herrmann, and Harley M. Benz. "Overview of open seismic data from the North Korean event of 9 October 2006."*Seismological Research Letters* 79.2 (2008): 178-185.

Mueller, Richard A., and John R. Murphy. "Seismic characteristics of underground nuclear detonations Part I. Seismic spectrum scaling." *Bulletin of the Seismological Society of America* 61.6 (1971): 1675-1692.

Muller, G., "The reflectivity method: a tutorial", Geophys. 58,153-174.

Murphy, John R., and Richard A. Mueller. "Seismic characteristics of underground nuclear detonations Part II. Elastic energy and magnitude determinations." *Bulletin of the Seismological Society of America* 61.6 (1971): 1693-1704.

Murphy, John R., et al. *Exploitation of the IMS and other data for a comprehensive, advanced analysis of the North Korean nuclear tests*. SCIENCE APPLICATIONS INTERNATIONAL CORP MCLEAN VA, 2010.

Murphy, John R., et al. "Supplemental analysis of the seismic characteristics of the 2006 and 2009 North Korean nuclear tests." *Proc. of the 2011 Monitoring Research Review: Ground-Based Nuclear Explosion Monitoring Technologies, Tucson, Arizona* (2011): 13-15.

Murphy, J. R., et al. "Advanced seismic analyses of the source characteristics of the 2006 and 2009 North Korean nuclear tests." *Bulletin of the Seismological Society of America* 103.3 (2013): 1640-1661.

Patton, H. j., 1990. Characterization of spall from observed strong ground motions on Pahute Mesa, *Bull. Seism. Soc. Am.* **80,** 1326-1345.

Patton, H. J. (2012b). A revised cavity radius scaling relationship for explosions detonated in a granite medium, Los Alamos National Laboratory, LA-UR-12-27099, pp. 12.

Patton, Howard J., and Steven R. Taylor. "Effects of shock-induced tensile failure on mb-Ms discrimination: Contrasts between historic nuclear explosions and the North Korean test of 9 October 2006." *Geophysical Research Letters* 35.14 (2008).

Selby, Neil D. "Relative locations of the October 2006 and May 2009 DPRK announced nuclear tests using International Monitoring System seismometer arrays." *Bulletin of the Seismological Society of America* 100.4 (2010): 1779-1784.

Stump, Brian W., D. Craig Pearson, and Robert E. Reinke. "Source comparisons between nuclear and chemical explosions detonated at Rainier Mesa, Nevada Test Site." *Bulletin of the Seismological Society of America* 89.2 (1999): 409-422.

Stump, Brian W. "Constraints on explosive sources with spall from near-source waveforms." *Bulletin of the Seismological Society of America* 75.2 (1985): 361-377.

Stroujkova, A., Leidig, M., & Bonner, J. L. (2015). Effect of the detonation velocity of explosives on seismic radiation. Bulletin of the Seismological Society of America, 105(2A), 599-611.

Tape, Walter, and Carl Tape. "A geometric setting for moment tensors."*Geophysical Journal International* 190.1 (2012): 476-498.

Tape, Walter, and Carl Tape. "A geometric comparison of source-type plots for moment tensors." *Geophysical Journal International* 190.1 (2012): 499-510.

Tape, Walter, and Carl Tape. "The classical model for moment tensors."*Geophysical Journal International* (2013): ggt302.

Titley, Spencer R., S. A. Anzalone, and Elizabeth Y. Anthony. "IGC Field Trip N38: Porphyry Copper Deposits in the American Southwest." *Porphyry Copper Deposits in the American Southwest: Tucson to Globe-Miami, Arizona July19-23, 1989*: 1-24.

Vavryčuk, Václav. "Tensile earthquakes: Theory, modeling, and inversion."*Journal of Geophysical Research: Solid Earth* 116.B12 (2011).

Vavryčuk, Václav. "Moment tensor decompositions revisited." *Journal of Seismology* 19.1 (2015): 231-252.

Wen, Lianxing, and Hui Long. "High-precision location of North Korea's 2009 nuclear test." *Seismological Research Letters* 81.1 (2010): 26-29.

Zhou, R., B. W. Stump, and X. Yang. "Moment tensor inversions of single-fired mining explosions at a copper mine in Arizona." *AGU Fall Meeting Abstracts*. Vol. 1. 2005.

Zhou, Rong-Mao, and Brian W. Stump. "Frequency-domain scaling of single-fired mining explosions with different confinements and explosive weights detonated in porphyry granite." *Bulletin of the Seismological Society of America* 97.6 (2007): 1862-1879.

Zhao, Lian-Feng, et al. "Regional seismic characteristics of the 9 October 2006 North Korean nuclear test." *Bulletin of the Seismological Society of America* 98.6 (2008): 2571-2589.

Zhao, Lian-Feng, et al. "Yield estimation of the 25 May 2009 North Korean nuclear explosion." *Bulletin of the Seismological Society of America* 102.2 (2012): 467-478.

Yang, Xiaoning and J. L. Bonner, 2009. Characteristics of Chemical Explosive Sources from Time-Dependent Moment Tensors, *Bull. Seism. Soc. Am.* **99**, 36-51, doi: 10.1785/0120080243.

Yang, X. (1998). MineSeis--A MATLAB {reg_sign} GUI program to calculate synthetic seismograms from a linear, multi-shot blast source model (No. LA-UR-98-1486). Los Alamos National Lab., NM (United States).

CHAPTER 2

YIELD SCALING OF FREQUENCY DOMAIN MOMENT TENSORS FROM CONTAINED CHEMICAL EXPLOSIONS DETONATED IN GRANITE

Abstract

The Source Phenomenology Experiment (*SPE - Arizona*) was a series of nine, contained and partially contained chemical explosions within the porphyry granite at the Morenci copper mine in Arizona. Its purpose was to detonate, record and analyze seismic waveforms from these single-fired explosions for purposes of characterizing the explosion seismic source representation as well as its absolute coupling. Ground motion data from the *SPE* is used in this study to estimate the frequency domain moment tensor source representation and then assess its ability to quantify yield scaling. Green's functions were computed for each of the explosions based on a 1D velocity model developed for the *SPE* site. The Green's functions for the 16, near-source stations span the distance range from 37 to 680 m. This study analyzes the 3 deepest, fully contained explosions in the series, all with a depth of burial of 30 m and yields of 0.77 $x10^{-3}$, 3.08 $x10^{-3}$ and 6.17 $x10^{-3}$ kt, in order to quantify yield scaling. Inversions are conducted in the frequency domain and moment tensors are decomposed into deviatoric and isotropic components to evaluate the effects of yield on the representation. Isotropic moments are compared to those for other contained explosions as reported by Denny and Johnson, 1991, (DJ91) and are in

general agreement with their scaling results, although consistently on the high side of their predictions. The explosions in this study have isotropic moments of $1.2x10^{12}$, $3.1x10^{12}$ and $6.1x10^{12}$ N*m. Isotropic and M_{zz} moment tensor spectra are compared to Mueller and Murphy, 1971 (MM71), DJ91 and revised Mueller and Murphy, 2012 (MMP12), models and suggest that the explosions fit the revised MMP12 model better but that none of the models fully parameterize the spectrum. Secondary source effects resulting from free surface interactions including the effects of spallation contribute to the resulting moment tensors which include a CLVD component. Hudson diagrams, using frequency domain moment tensor data, are computed as a tool to assess the source representation. The analysis in this study suggests that, within the band of interest (1-20 Hz), as frequency increases, the source representation becomes more explosion like, peaking at the highest frequency.

Motivation

This study explores trade-offs between source depth and yield scaling (Denny and Johnson, 1991; Mueller and Murphy, 1971; Lay et al., 1984; Stump et al., 1991; Stump et al., 1999) for chemical explosions when a source medium, in our case granite, is known. Source depth of burial and yield affect the explosion source representation in terms of absolute seismic coupling, containment and source symmetry as expressed in terms of secondary source contributions such as those that result from wavefield interactions with the free surface (Day et al., 1983; Stump, 1985; Patton, 1990) among others. Secondary source effects may additionally impact the ability to discriminate explosion and earthquake sources.

Scaling relations derived by Mueller and Murphy (1971), hereafter referred to as MM71, Denny and Johnson (1991), hereafter referred to as DJ91, and Patton's revised Heard Ackerman (2012) , hereafter referred to as MMP12, show that isotropic seismic source functions are

dependent on yield, source depth and emplacement medium for nuclear explosions. Source depth and yield are critical in the assessment of seismic interactions with the free surface and resulting secondary source contributions as well. MM71, developed a seismic spectrum scaling model and find that strict cube root scaling is inappropriate as a result of overburden pressure. Their model is based on an analytical approximation to the nuclear seismic source function. Analytical explosion models considering instantaneous rise time, finite rise times and ones lacking a steady state-value are examined by DJ91. Conducting a regression analysis, DJ91 compares the relationships of moment and corner frequency parameters to the cavity size and find that cube root scaling is appropriate after consideration of overburden stress. After discussion with Jack Murphy, Patton (2012) revises MM71's cavity scaling relationship for granitic material. Different static pressure values are predicted by the equivalent formulation of the MM71 model and Stevens and Day, 1985, prompted this change. These models will be compared to seismic moment tensors estimated using the experimental ground motion data from this set of contained chemical explosions detonated in granite.

For a contained explosion, as the upward traveling compressional wave reflects off the free surface directly above the source, the tensile downward traveling wave sends the upper geology into ballistic freefall. This momentum transfer and reflected wave complicates the source representation by generating a non-spherical secondary spallation force later in time (Day et al., 1983; Stump, 1985; Patton, 1990). This secondary source can be represented in terms of compensated linear vector dipole (CLVD) that contaminates the primarily isotropic explosion source. The CLVD source component generates enhanced S_v and surface wave energy as a result of its cylindrical symmetry. Dreger et al, 2016, estimated nuclear explosion source parameters using a regional distance seismic waveform moment tensor inversion procedure to

develop a source type discrimination capability. They found that when viewing the explosions on a Hudson (1989) diagram, the explosions separated from populations of earthquakes and cavity collapses with some CLVD contribution.

In an attempt to identify similarities and possible differences between nuclear and chemical explosions, the Department of Energy (DOE) conducted the Non-Proliferation Experiment (NPE) (Denny et al., 1996), detonating 1.29 million kilograms of ammonium nitrate fuel oil (ANFO) at Rainier Mesa. Stump et al., 1999, illustrate that, within the bandwidth of 0.36 to 100 Hz, there is no apparent spectral difference between the nuclear and single-fired chemical source. Their study used comparisons between the Hunters Trophy (HT) nuclear explosion and the NPE at near-source distances and suggests that chemical explosions can be utilized to empirically explore explosion source models that are applicable to nuclear explosions. Glen and Goldstein, 1996, assessed the sensitivity of explosion source functions to material properties by means of numerical simulations and found that the long period value of the RDP for explosions with ANFO such as that used in the NPE were larger by a factor of 1.9 relative to a nuclear explosion yield. Goldstein and Jarpe, 1994, find that the source spectrum below 1 Hz from the NPE is approximately twice as large as those of nearby nuclear explosions. Patton, 2015, in contrast, suggests that a doubling of yield is inappropriate and that the chemical explosion yield is identical to that of a nuclear explosion with no difference in long-period spectral levels for the two.

Seismic discrimination of underground nuclear explosions from other types of seismic sources motivates a physical understanding of the similarities and differences of seismic source functions. The Democratic People's Republic of Korea (DPRK), North Korea (NK), have detonated a total of six underground nuclear explosions (UNE) (2006, 2009, 2013 and 2016-2,

and 2017) at the Punggye test site around Mount Manthap in northeastern NK. Many of these UNE, particularly that of 2006, had low magnitudes, resulting in the need to assess possible trade-offs between the depth estimate and yield (Murphy et al., 2010, 2011; Selby, 2010; Wen and Long, 2010). In addition, the relative excitation of body and surface waves may affect the robustness of the M_s vs m_b discriminant (Kim and Richards, 2007; Bonner et al., 2008, 2011; Koper et al., 2008; Patton and Taylor, 2008; Zhao et al., 2008, 2012; Chun et al., 2011). Anomalously high surface waves skewed the M_s vs m_b discriminant for the NK explosions with the 2006 event in the earthquake population and the 2009 event directly on the discrimination line (Murphy et al., 2013). Estimation of yield as well as the physical interpretation of seismic observations used for discrimination may also be affected by source depth, emplacement material and propagation path. The CLVD, isotropic and other deviatoric components of the moment tensor representation may have implications for yield scaling, explosion source models and discrimination. Using intermediate period (10-50 sec) complete waveform modeling, Ford, Dreger and Walter, 2009, perform a series of source inversions for the May 2009 North Korean nuclear explosion. They find that pure explosions scalar seismic moments fit the data approximately as well as the full moment tensor solution. As noted earlier, they also use Hudson, 1989, diagrams to compare earthquakes and source estimates for nuclear explosions at the Nevada Test Site using the resulting moment tensors. The North Korean nuclear explosion separates from the earthquakes and plots within the same region as other nuclear explosions.

Our goal is to quantify the effects and possible tradeoffs between yield, depth and geology. DJ91, MM71 and MMP12 source models will be compared to our source spectra in an attempt to better understand how they relate to the three explosions with different yields but identical depths. The source representation may be complicated by secondary sources due to the

free surface and a second goal is to quantify how these effects impact the isotropic explosion source representation. We also want to investigate possible insights into the chemical and nuclear explosion source equivalence by comparing the new source estimates to existing scaling relations since this equivalence remains an open question.

Experiment Site

The data for this study comes from the Source Phenomenology Experiment (SPE) in Arizona. The goals of the experiment included the characterization of contained, single-fired chemical explosion seismic source representations in both a hard and soft rock environment (Bonner at al., 2005). Additionally, the experiments were designed to quantify differences between delay-fired mining explosions and contained single-fired chemical explosions (a proxy for nuclear explosions). Details of the experiment are outlined in Bonner at al., 2005 and MacPhail et al., 2018a. This paper focusses on the characterization of the explosions conducted at the Morenci Mine where the explosions were detonated in porphyry granite.

The SPE consists of nine shots with varying yields and containments. This paper analyzes three of the nine shots (B4, B6 and B10) in order to focus on the effects of yield on the source scaling relations. Shots B4, B6 and B10 were detonated with a measured centroid depth of 30 m. The boreholes were 31 cm in diameter, 10 m apart and drilled to approximately 36 m total depth. After loading the bottom of the hole with 12 m of explosive, 773 kg, the holes were backfilled to the surface. Simultaneously detonating one, four, and eight boreholes provided nominal explosive weights of 773, 3091, and 6182 kg, for B6, B4 and B10, respectively (Stump and Zhou, 2007). **Figure 2.2** is an overhead view of the test bench and shot positions, demonstrating borehole geometry. Ground motion instrumentation deployed across the test bench is documented in **Figure 2.3** and spans from very close (35 m) to the detonations, which capture

non-linear processes such as near-surface spallation, to more distant stations (< 700 m) that document linear-elastic wave propagation.

The source centroids for all three explosions are 30 m, with varying scaled depths as a result of yield differences produced with multiple, closely spaced boreholes. The yields of B6, B4 and B10 are $0.77x10^{-3}$, $3.08x10^{-3}$ and $6.17x10^{-3}$ kt producing scaled depths of burial of 260, 164 and 130 $kt/m^{0.33}$, respectively, based on the 122 kt/m^3 criteria.

Instrumentation and Data

Instrumentation was deployed (**Figure 2.3**) from 35 – 680 m in order to capture the full wavefield from within the region of tensile failure out to linear elastic propagation. Details of the instrumentation are described in Bonner at al., 2005 and MacPhail et al., 2018a. Data were sampled at 250 samples per second. Acceleration data was converted to velocity by simple integration including a correction for a static offset producing a consistent set of velocity data for subsequent analysis.

Good signal to noise ratios were critical to the experiment with pre-shot predictions from Bonner et al. (2005), providing the opportunity to optimize it as well as the bandwidth of the data, which is displayed in **Figure 2.4**. This shows a SNR of over three orders of magnitude at the maximum. This example is similar to the signal to noise at all stations. The resulting bandwidth of interest driven by the maximum signal to noise band as well as the fidelity of Green's functions discussed subsequently is estimated as 1 – 20 Hz (MacPhail et al., 2018 a).

Data were used to quantify the zone of linear elasticity, in particular the region separating free surface spallation from the region without the effect. Acceleration waveforms were evaluated for spall signatures, two peaks in the time series separated by a -1 g dwell, exemplifying the tensile failure of the near surface geology and subsequent ballistic freefall

followed by re-impact. Stations at distances less than 150 m showed these characteristics and were thus excluded from the linear elastic source inversions.

Theory

An explosion detonated in an arbitrary, elastic, homogenous medium can be represented by a purely isotropic source. Sharpe, 1942, developed the solution for such a source in terms of Lame parameters and rigidity. MM71, DJ91 and others use this isotropic representation to develop seismic source models based on observational data and modified to include the effects of yield, depth of burial and emplacement medium to define seismic spectrum scaling appropriate for underground nuclear explosions. These representations do not always take into account the effects of local geological layering as well as complex free surface effects that may contribute to non-isotropic source contributions.

Containment depends on the depth of the explosion relative to its yield and emplacement material with full containment representing an explosion that is fully coupled to the solid earth with no direct release of explosive energy into the atmosphere. Containment is often represented by the source's scaled depth of burial, the ratio of its depth to yield to the 1/3 power, assume cube root scaling. Explosions with scaled depth of burials greater than 122 $m/kt^{0.33}$ are defined by Los Alamos National Labs as fully contained as a result of experimental practice accompanying the testing of nuclear explosions (Olsen, C. W, 1993). The scaled depths of burial for the three SPE explosions analyzed in this paper are compared in **Figure 2.5**. The three explosions, B6, B4 and B10, have scaled depths of burials of 260, 164 and 130 $m/kt^{0.33}$, respectively, all greater than the nominal value of 122 $m/kt^{0.33}$.

Fully contained explosions can generate spallation of near-surface layers (Viecelli, 1973; Stump, 1985). Failure, due to high stress loading, causing tensile failure of geologic layering

above the explosion results in a secondary cylindrical source delayed in time relative to the isotropic explosion. The upward going compressive wave from the isotropic source reflects off the free surface, generating tensile stresses as the wave propagates away from the surface, and if large enough in amplitude, can cause falure of near-surface layers, resulting in ballistic freefall for an finite time and thus creating secondary source that is cylindrical in symmetry as a result of the free surface above the explosion (Rinehart, 1959; Chilton, et al., 1966; Eisler et al., 1966; Day et al., 1983; Stump, 1985; Patton, 1990)).

Many nuclear explosions excite Love waves, producing radially asymmetric non-isotropic radiation (Aki et al., 1969; Toksöz et al., 1971; Aki and Tsai, 1972; Wallace et al., 1983, 1985). This is seen in explosions detonated in North Korea as well (Ford et al., 2009; Murphy et al., 2013; Barth, 2014). Love waves should not be generated by a radially symmetric source (Massé, 1981). Love wave and SH excitation have been attributed to tectonic stress released by both a triggered tectonic earthquake on a fault in close proximity (Archambeau, 1972) and by stress relaxation in a highly fractured area close to the detonation location (Archambeau, 1972; Harkrider, 1977; Minster and Suteau, 1977).

Murphy et. al., 2013, analyzed source characteristics of the 2006 and 2009 North Korean nuclear tests and found anomalously high M_s/m_b ratios. They discussed the triggered release of preexisting tectonic strain energy by the explosion that has been shown to bias M_s estimates from explosions at other test sites. Seismic characteristics of explosions detonated at the Semipalatinsk nuclear test site show very strong thrust-type tectonic release that significantly decreased M_s values (Helle and Rygg, 1984; Ekstrom and Richards, 1994) and thus improved discrimination from earthquakes as a result of decreased M_s/m_b ratios. Thus, a complete physical understanding of the explosion source is needed to interpret such observations.

In order to assess the range of yields, containments and source representations, a general second order moment tensor representation is employed in this study, thus capturing all the possible source components under the assumption of a point source relative the wavelengths of the seismic data analyzed. The details of the applied source inversion procedure are documented in MacPhail and Stump., 2018a. The representation used in this study is similar to other near-source seismic studies, in that the inversions are completed in the frequency domain in order to provide a complete representation of the source, with the six unique time functions of the symmetric moment tensor (Yang et al., 2018; Yang and Bonner, 2009; Stump and Johnson, 1984; Stump, 1985). The moment tensors estimated can be used to predict waveforms and in turn compared to the observations as a measure of the adequacy of the representation.

For the general seismic point source (Jost and Herrmann, 1989), the generalized moment tensor can be decomposed into isotropic (iso) and deviatoric(dev) components. This process is explained and applied in MacPhail and Stump., 2018a in order further explorer the source representation.

In addition to the isotropic contribution the diagonal elements of the deviatoric component can include a CLVD component, a combination of two double couples or three orthogonal force dipoles, where the force dipoles in one direction have a unit strength twice that of the dipoles in the other two orthogonal directions. In the case of interactions with the free surface, the largest dipole would be oriented in the vertical direction with the other two constrained to the horizontal plane.

In order to improve the interpretation of the general moment tensor source that includes isotropic, deviatoric, and CLVD contributions, Hudson (1989) suggested the use of a set of diagrams. He proposed the use of a two-dimensional graphical display to convey the relative

sizes of the three principle moments and associated probability densities from a given set of data. Dreger et al (2014) use contours of fit (variance reduction) to regional data for a uniform distribution of sources on source-type plots. In Hudson's representation, the parameter *T* characterizes the constant volume (shear) source component and *k* characterizes the proportion of volume change. In order to account for the source orientation uniquely, the relative sizes of the three principal moments from the eigen decomposition of the moment tensor are arranged as

$$M_X > M_Z > M_y$$

In terms of Hudson, 1989, isotropic component is defined as

$$3M = M_X + M_y + M_Z$$

Where M is the dilational component of the moment tensor and the three constant volume components are

$$M_x' = M_x - M$$

$$M_y' = M_y - M$$

$$M_z' = M_z - M$$

Three cases exist ($M_z' > 0$, $M_z' = 0$ and $M_z' < 0$) and must be considered to avoid division by zero. For each of the three cases, all moments are scaled with *k* and *T* defined in terms of the ordered principal moments, M_X, M_y and M_Z

$$k = \frac{M}{|M| - M_y'} \qquad M_z' \geq 0 \qquad -1 \leq k \leq 1$$

$$k = \frac{M}{|M| - M_x'} \qquad M_z' \leq 0 \qquad -1 \leq k \leq 1$$

and

$$T = \frac{2M_z'}{M_y'} \qquad M_z' \geq 0 \qquad 0 < T \leq 1$$

$$T = 0 \qquad M_z' = 0$$

$$T = \frac{2M_z'}{M_x'} \qquad M_z' < 0 \qquad -1 \leq T < 0$$

The combined scaling factors for every case are

$$\frac{2k}{M} = \frac{2}{|M| - M_y'} \qquad M_z' \geq 0$$

$$\frac{2k}{M} = \frac{2}{|M| - M_x'} \qquad M_z' \leq 0$$

The scaled moments become

$$\bar{\bar{M}}_x = 2k + (2 - T)(1 - |k|) \qquad T \geq 0$$

$$\bar{\bar{M}}_y = 2k - 2(1 - |k|) \qquad T \geq 0$$

$$\bar{\bar{M}}_x = 2k + 2(1 - |k|) \qquad T \leq 0$$

$$\bar{\bar{M}}_y = 2k + (2 + T)(1 - |k|) \qquad T \leq 0$$

$$\bar{\bar{M}}_z = 2k + T(1 - |k|)$$

$$\bar{\bar{M}} = \frac{\bar{\bar{M}}_x + \bar{\bar{M}}_y + \bar{\bar{M}}_z}{3} = 2k$$

T and *k* span from -1 to 1 and the dilatational component, $\bar{M} = 2k$, spans from -2 to 2. The non-isotropic constant volume component is given by the deviatoric moments

$$\bar{\bar{M}}_x' = (1 - |k|)(2 - T) \qquad T \geq 0$$

$$\bar{\bar{M}}_y' = (1 - |k|)(-2) \qquad T \geq 0$$

$$\bar{\bar{M}}_x' = (1 - |k|)(2) \qquad T \leq 0$$

$$\bar{\bar{M}}_y' = (1 - |k|)(-2 - T) \qquad T \leq 0$$

$$\bar{\bar{M}}_z' = (1 - |k|)(T) \qquad -1 \leq T \leq 1$$

This representation is used in the interpretation of the moment tensors from the explosive sources in this study.

Velocity Model

A detailed velocity model is required for the estimation of the moment tensor. The less accurate the Green's functions, the less well constrained the source model is, since it is based on a linear model. MacPhail et al., 2018a investigate the sensitivity of moment tensor estimates to changes in the V_s model and the assumed source depth when the compressional wave velocity is well constrained, which is characteristic of this dataset. Multiple P-wave refraction surveys were completed at the Morenci Mine in order to constrain the source emplacement and geologic propagation path. **Figure 2.6** summarizes the refraction study and results therein with the compiled model for V_p, V_s, ρ (density), attenuation Q_α and Q_β.

The shear wave attenuation model, described in Bonner et al., 2005, examined surface waves recorded by a Texan deployment and the refraction study. Rayleigh wave particle velocity (u) for one station can be described by the amplitude recorded at another station by the equation:

$$u_2 = u_1 \sqrt{\frac{R_1}{R_2}} e^{-\alpha(R_1 - R_2)}$$

Where R_1 and R_2 are epicentral station distances and α is the attenuation coefficient. Attenuation coefficients were then converted to Q in different frequency bands. Using P-wave first arrivals, V_p structure was estimated. The structure model was compiled at its deepest to model the crustal structure for regional waveforms but for this experiment the upper most 7 layers (1 km) are the most important.

To further constrain V_S, R_g dispersion curves were estimated from data recorded on the N-S broadband station profile (Hayward et al., 2004). The empirical dispersion curves vary systematically with distance, implying that a lateral variation in the velocity structure across the mine exists (Bonner et al, 2005). Inversion of the ground roll dispersion curves for the test bed constrained the shear wave velocity structure in the mine, as described in MacPhail et al., 2018a.

Green's functions are computed using the reflectivity method (Müller, 1985) for different source depths and velocity models. In MacPhail et al., 2018 a, explosion and CLVD components of the Green's functions are analyzed in terms of their sensitivity to assumed source depth and a range of shear wave models. For an assumed V_p, Poisson's values ranging between 0.15 and 0.4 were investigated, increasing and decreasing, respectively from the empirical shear wave velocity of the layered model. These V_s values were used to build a shear wave velocity model for each of the respective Poisson values. Green's functions based on the varying velocity structures were calculated and predicted phases analyzed.

For the Green's function explosion components, there is a strong depth dependence for frequencies above 10 Hz. All phases have lower amplitudes using the slower shear wave velocity structures. Surface waves are delayed as expected with the slower V_s but compressional waves are relatively unaffected, consistent with holding the P-wave model fixed. For the CLVD components, surface waves exhibit a much more pronounced effect on Poison's ratio, with as much as 7 times higher amplitudes for the slowest V_s model below 20 Hz, thus the assumed Poisson's ratio can affect the final source representation.

The single model used in this study is best constrained by the site investigation discussed earlier but inversion results could still be subject to the assumed source depth (MacPhail et al., 2018a). **Table 2.1** displays the uppermost parameterized layers. All shots for this study (B6, B4

and B10) are located in the third layer, and as such, are the source parameters for the study. Preliminary to the actual inversions, forward models were calculated to better understand the expected phases. **Figure 2.7** displays the vertical component synthetic record section for shot B4 with a Poisson ratio of 0.25 and source depth at 30 m. These forward synthetics are based on a Mueller-Murphy source model using shot parameters relevant to the geology at the Morenci copper mine. Three source models of different yields were calculated, emulating B6, B4 and B10 explosions and their emplacement. Parameters for these model are reproduced in **Table 2**. These source models were convolved with the Green's functions calculated for the mine, yielding synthetic observations. Synthetics are dominated by body waves and Rayleigh waves, evident by their retrograde elliptical particle motion.

Inversions

Source inversions focus on shots B6, B4 and B10 as these are the three twice depth (30m) shots from the SPE and provide the opportunity to assess yield and coupling for the three contained explosions of different yield. Inversions were performed using ground motion data from receivers within the linear zone of elasticity. The inversions used data from the eight stations covering ranges from 150 - 700 m with partial azimuthal coverage and each station providing three-component. These data sets provided for source solutions that were over determined. The full moment tensor is denoted as a capital M_{mn}, where m and n are the x, y or z components. The decomposed isotropic Mtr is also denoted with a capital M, where m and n are the x, y or z components. The deviatoric, non-volumetric components are denoted as m_{mn}, where m and n are the x, y or z components.

The original ground motion data were windowed with the same absolute time for each shot at all stations. Stations 2 failed to record data for shot B4. The data were then integrated to

velocity. The three-component data were rotated into radial, transverse and vertical components based on source and station locations. Shots B6 and B10 had no data for stations 2 and 10. The data were then windowed beginning 500 data points before the first P-wave. The Green's functions data were windowed in a similar manner so that the first onset of the observations at all distances were 0.1 seconds behind the first onset of the Green's functions. This alignment is aids in the ability to assess the causality of the resulting moment tensor in the time domain.

Following the windowing and alignment of the observations and Green's functions, a complex, frequency domain linear inversion was completed. The Green's functions and observations are each 4096 data points long. Subsets of data were selected to test inversion sensitivity to parameters like azimuthal coverage and station distance as well as limiting R, T and Z components. Following the linear zone studies, only stations at distances beyond 150 m were used. Data and Green's functions were tapered, demeaned and weighted by 1/r before transforming into the frequency domain where the inversion is conducted frequency by frequency. The distance weighting is designed to take into account geometrical spreading so that the more distant observations have nearly the same weight as the closer stations in the inversion.

Using singular value decomposition, an inversion at each frequency sample from the zero frequency to the Nyquist (125 Hz) was performed. These inversions provide a complex moment rate at 2048 frequency points. The resulting moment tensors were inverse Fourier transformed into the time domain in order to assess the resulting time functions. The source model, determined from the inversions, is convolved with the Green's functions and compared to the original observational data with cross-correlation values estimated to quantify how well the data fit the predictions.

Figure 2.8 displays a record section of the velocity data, in black, overlaid on the fitted observations in grey, both unfiltered. The synthetics well-matched the data at all stations and distances for all shots. As expected, lower frequencies are better fit better than the higher frequencies. Correlation values for unfiltered data were around 0.7 while band pass filtering 10-20Hz provided the best cross-correlation values of 0.9. Radial and transverse data (unfiltered) had cross-correlation values of 0.72 and 0.65. The signal to noise ratio is extremely high for the data from 150 – 680 m used in the inversions. P-wave and surface wave arrival times in the synthetics match the velocity data. The high correlation values between the observational data and the predicted observations paired with low noise further supports the appropriateness of the Green's functions and subsequent source interpretation.

The isotropic, deviatoric, M_{zz} and relative amplitudes of M_{xx} and M_{yy} with respect to M_{zz} are compared to explore the source representation strength relative to the explosion yield. **Table 2.3** (full moment tensor) and **Table 2.4** (decomposed moment tensor) document the maximum time series amplitudes for all three shots.

The M_{zz} components, for all three shots, have the greatest amplitudes. M_{zz} maximum amplitudes scale linearly with yield. B10 (eight boreholes) is roughly eight times larger than B6 (1 borehole) and B10 is twice as large at B4 (4 boreholes), with amplitudes of 1.9×10^{13}, 7.15×10^{13} and 1.51×10^{14}.

The maximum M_{zz} amplitude for shot B4 (7.15×10^{13} N*m/s) is roughly twice that of the M_{xx} (4.26×10^{13} N*m/s) and M_{yy} (4.09×10^{13} N*m/s) with the same polarity, demonstrating a linear vector dipole (LVD). This is true for B6 and B10 as well. **Figure 2.9** compares these trace components while also displaying the off-diagonal components for B4.

The full moment tensor, in the time domain, is decomposed into isotropic and deviatoric components for all three explosions. The M_{zz} deviatoric component maximum amplitude, for all three explosions, is roughly twice that of the M_{xx} and M_{yy} with opposite polarities, demonstrating a prominent CLVD component. **Figure 2.10** displays the isotropic and deviatoric components showing the isotropic component is roughly 15% greater in amplitude than that of the deviatoric M_{zz} component for B4. Maximum amplitudes for B4's deviatoric components M_{xz} ($3.28x10^{13}$), M_{yz} ($3.15x10^{13}$) and M_{zz} ($4.15x10^{13}$) are larger than the M_{xx} ($1.31x10^{13}$), M_{xy} ($1.02x10^{13}$) and M_{yy} ($1.88x10^{13}$).

Isotropic and M_{zz} moment rate spectrums long period levels (LPL) and corner frequencies are compared. **Table 2.3** describes these from shots B6, B4 and B10. The isotropic moments are later used for comparison to other well studied explosions.

The M_{tr} and M_{zz} component moment rate spectrum, from shots B6 ($W=0.77x10^{-3}$ kt), B4 ($W=3.08x10^{-3}$ kt) and B10 ($W=6.17x10^{-3}$ kt) from D.C. to 125 Hz are compared to better understand the scaling relations between the explosions. **Figure 2.11** displays the M_{zz} and M_{tr} spectrum of shot B6, B4 and B10 superimposed. They have isotropic moments of 1.2, 3.1 and $6.1x10^{12}$ N*m, respectively. The M_{zz} LPL in each of the three explosions is approximately 1.7 times larger than the M_{tr} LPL but mimics the shape in our band of interest. From 1 – 10 Hz, the amplitude spectrums scale roughly equally in log space for both. From 10 – 20 Hz, the two largest explosions (B4 and B10), have roughly the same M_{tr} component and M_{zz} amplitude. B6 is almost an order of magnitude less in this band. Below 1 Hz and above 20 Hz, there is no clear trend. Peak spectral amplitude levels are at 2 Hz. m_{tr} long period levels are roughly half that of

the M_{zz} component but produce similar trends with yield. Other than a doubling of spectral amplitude, the M_{zz} and M_{tr} are similar in shape and trend.

Table 2.3 summarizes the corner frequencies for the isotropic moment rate spectra. B6, B4 and B10 have respective corner frequencies of 10.6, 10.1 and 8.5 Hz. As expected, with increasing yield and moment, the corner frequencies decrease.

Moment, Yield Scaling and Source Models

Most explosion models are isotropic so the full moment tensor is decomposed into its isotropic and deviatoric components and displayed with the full moment tensor. The M_{zz} component of the full moment tensor gives insight into the importance of free surface interactions in the complete representation. The isotropic component gives is compared to the isotropic explosion models.

The three models compared to the source estimates are MM71, DJ91 and MMP12. These three models are used to assess and contrast to the moment tensor spectra for granite. A factor of two in yield is not used for comparison purposes.

When analyzing source spectra, Denny and Johnson (1991) explored corner frequency, roll-off, overshoot and long period level to define models to fit moment tensor spectra. The DJ91 model uses cavity elastic radius scaling. It is assumed that the pressure function is a step function with peak shock pressure equaling the steady state pressure.

The MM71 model also uses cavity radius scaling but differs in that it is based on an initial peak shock pressure that decays at some rate defined by an empirical factor alpha and then settles to a steady state pressure in contrast to the step pressure time function assumed in DJ91. As noted earlier, MM71 includes a specific depth of burial effect. Patton, in correspondence

with Murphy, revised the MM71 scaling model for granite. The cavity scaling relationship predicted a different static pressure value from equivalent formulations of MM71 and Stevens and Day, 1985. The leading coefficient was reduced 9.2% from 16.3 to 14.8, effecting the long period level. For our parameters, the short period amplitude and corner frequencies are the same for both the MMP12 and MM71, only decreasing the long period level for the MMP12 model illustrating the effect of revising the static pressure in the model.

Yang, 2016, analyzed moment tensor spectra from four explosions from the source physics experiment in the Nevada National Experiment Site (NNES), particularly the corner frequencies and long period levels. Yang found that the moment tensors could not be fit by traditional source models so they were fit with a model derived from the regression of observed values against source depth and yield and resulted in its own cavity pressure estimate, independent of the other models.

The LPL and corner frequencies from the empirical isotropic component moment rate spectra in this study were calculated and compared to existing models (MM71, DJ91, and the MMP12 model for granite) discussed above. **Figure 2.12** compares these models with the moment tensor spectra. **Table 2.3** displays the corner frequencies (f_c) and LPLs of our spectra and the models. The corner frequencies were estimated from the spectra after the long period level and slope of the high frequency decays were calculated. The f_c was determined as the intersection of that slope and 3dB lower than the long period level. The long period levels were determined by a log space distribution of points then averaged from 1 – 10 Hz.

All three explosion's corner frequencies are higher than the DJ91 model. B6, B4 and B10, respectively, have corner frequencies of approximately 10.6, 10.1 and 8.5 Hz. The f_c is most accurately fit by the MMP12 with values of 14.4, 9.9 and 8.3 Hz, respectively. High

frequency decay slopes fall off as approximately f^{-2} for each of the explosions consistent with the model.

The LPL from shot B6 ($1.2x10^{12}$ N*m/s), fits the DJ91 long period amplitude level ($1.18x10^{12}$ N*m/s) better, having an amplitude closer to that of the model. One can see, from **Table 2.3**, that when considering all three shots and their scaling, the MMP12 model's amplitude values are closer to that of our data's spectrum. B10's high frequency decay trend fits more accurately than do B4 and B6.

Over all, the MMP12 model's LPL, high frequency decay slope and amplitude are closer to the values of our data. As with Yang (2016) and Rougier and Patton (2015), the models do not completely fit the LPL and corner frequency. Future work could include parameterizing the data and creating a model based up them as was the case with Yang (2016).

Denny and Johnson, 1991, examined many explosions, both chemical and nuclear, from several authors in order to develop a consistent set of scaling relations. **Figure 2.13** displays an augmented plot from Denny and Johnson, 1991, comparing shots B6, B4 and B10's moments to other chemical and nuclear explosions. The moments are adjusted using equation 43 from Denny and Johnson (1991). The explosions from this study fill a data gap between the smaller chemical explosion and larger nuclear explosions. The three explosions span an order of magnitude, in yield space, between the smaller, chemical, explosions and the larger, nuclear, explosions and are consistent with other explosions along the trend line, although consistently higher than their scaling relation, without doubling the chemical explosion yield.

Source Interpretation

Hudson (1989) diagrams are used to increase the physical interpretation of the empirical moment tensor determined in this study. After the moments are scaled, seismic sources populate different areas of the graph, depending on the relative moments.

Typically, Hudson diagrams are applied to time series but for our study, frequency domain moment tensor components are used for the Hudson plots. Because we use frequency domain inversions, it was convenient to look at how the source representation changes as a function of frequency. A 6 Hz smoothing window was used based on the bandwidth time product (Harris, 1991). This mitigates differences in phase between moment tensor components while minimizing scatter.

Hudson diagrams are calculated in the frequency band of interest for all three explosions. Figure 14 displays shot B4, which is characteristic of all three shots. The general shape as a function of frequency is similar for each of the explosions, independent of yield. Lower frequencies have a larger CLVD component and as frequency increases the source becomes more explosion like. This frequency dependence has implications for source identification using different wave phases and suggests that the importance of the free surface interaction is frequency dependent. Thus, different phases, dependent upon frequency content, might reflect a different aspect of the source representation. Body waves with higher frequency content might be more explosion like while surface waves with their lower frequency content produce a more CLVD like source representation.

Conclusions

Moment tensor inversions were conducted using data from three small contained explosions with varying yields detonated in granite at a copper mine in Arizona. The resulting

source representations are analyzed in order to better understand how the explosions compare to existing source models in granite for both yield and depth scaling as well as source representation. The effects of scaled depth of burial and free surface interactions on the source representations are also assessed. These results give insight into the importance of secondary sources that contribute to the explosion source representation. M_{zz} and M_{tr} moment tensor components are compared because of their different contributions to the source representation. These component's spectra have similar shapes but the M_{zz} component is larger by a factor of 2 in amplitude.

Full moment tensors from these explosions show a strong LVD component, where, for all three explosions, all trace component's first motions are positive and M_{zz} is approximately twice the size of the M_{xx} and M_{yy}. After decomposing the moment tensor, deviatoric moment tensor components are consistent with a CLVD source, where, for each of the explosions, M_{xx} and M_{yy} have an opposite polarity and roughly half the amplitude of the deviatoric M_{zz}. These variations in moment tensor component ratios give evidence of secondary sources not inherent in a pure explosion and possibly due to free surface interactions. These explosions are considered fully contained using standard guidelines from NTS explosions but still show evidence of a strong free surface interaction.

MM71, DJ91 and the revised MMP12 source models were used to model our explosions. The source parameters for our explosions and geology were input and compared to the actual source spectra. All high frequency decay slopes are matched by the model's with a decay of f^{-2}. The long-period level of B6's spectra matches that of the MMP12 model's long period but has a

higher corner frequency. The larger B4 and B10 shot's spectral long period levels were also best fit better by the MMP12 model but are slightly less than MMP12 predicts. Their corner frequencies are very similar with a 0.2 Hz difference. The MMP12, overall, fits the data the best, having closer moments, corner frequencies and high frequency decay slopes. The revision in cavity radius scaling lowers the model's long period level amplitude closer to our explosions moment but a further revision might be needed to bring the level down to match the spectra. The leading coefficient used in MMP12 model is 14.8. Modifications to values of ~13.7 and ~14.0, respectively, lower the models to align with the spectra from shots B4 and B10, suggesting the possibility that this leading term may be slightly smaller than the current model.

The three explosions are compared to other explosions, both nuclear and chemical using results from Denny and Johnson 1991. Our explosion yields fill a gap in yield of over three orders of magnitude in the original data that was used to develop the model. Our explosions have larger yields than the plotted chemical explosions but smaller than the nuclear explosions. When plotting yield vs isotropic moment, the SPE explosions plot above the DJ91 trend line but along a consistent trend with other explosions.

Modified Hudson diagrams for the moment tensors provides a frequency dependent interpretation of the source. Our moment tensor at higher frequencies, within the 1 – 20 Hz band, show an increasing larger explosion component as frequency increases. Lower frequencies have an enhanced CLVD component. In the frequency domain, the larger the explosion, the higher the maximum explosion component, peaking in the 15-20 Hz range. This result suggests that when evaluating the Rayleigh wave frequency bands, the source can look more CLVD like and when looking at higher body wave frequencies, the source could be more isotropic.

Our study does not use a factor of two increase in yield for chemical explosions when making a comparison to nuclear explosions in our baseline comparisons. **Figure 2.15** compares shot B6's isotropic component spectrum to the MMP12. The moment rate spectrum long period level was calculated from 1-10 Hz and displayed in the figure as a thin black line. With a factor of 2 increase in yield, the MMP12 model predict a higher long period level and fits our data less well than the same model without a factor of 2 increase in yield.

TABLES

Table 2.1 – The Morenci test site material property model used in the moment tensor inversions

Layer top (km)	V_p (km/s)	V_s (km/s)	Poisson values	$\boldsymbol{\rho}$ (g/cm^3)	$\boldsymbol{Q_\alpha}$	Q$\boldsymbol{\beta}$
0.0000	0.61	0.35	0.25	2.0	12.0	5.0
0.0005	3.05	1.76	0.25	2.1	20.0	10.0
0.0023	3.72	2.15	0.25	2.2	50.0	25.0
0.1500	4.49	2.59	0.25	2.3	80.0	40.0
0.5500	4.92	2.84	0.25	2.4	100.0	50.0
0.9500	4.97	2.87	0.25	2.6	200.0	100.0

Table 2.2 – Source model parameters for shots B6, B4 and B10. Where V_p is P-wave velocity, V_S is S-wave velocity, ρ is density, A is the source medium dependent constant and k is the proportionality factor.

Shot	**V_p (m/s)**	**V_s (m/s)**	**ρ (g/cc)**	**Source Depth (m)**	**Yield (kt)**	**A**	**k**
B6	**3.72**	**2.15**	**2.2**	**30**	**.00077**	**1**	**2**
B4	**3.72**	**2.15**	**2.2**	**30**	**.0031**	**1**	**2**
B10	**3.72**	**2.15**	**2.2**	**30**	**.0062**	**1**	**2**

Table 2.3 – Isotropic long period levels (LPL) and corner frequencies from B6, B4 and B4 and their respective models (MM71, DJ91, MMP12)

	Isotropic LPL (N*m)	**MM71 LPL (N*m)**	**DJ91 LPL (N*m)**	**MMP12 LPL (N*m)**
B6	$1.2x10^{12}$	$1.57x10^{12}$	$1.18x10^{12}$	$1.16x10^{12}$
B4	$3.1x10^{12}$	$4.73x10^{12}$	$4.72x10^{12}$	$3.87x10^{12}$
B10	$6.1x10^{12}$	$9.45x10^{12}$	$9.48x10^{12}$	$7.08x10^{12}$
	Isotropic f_c (Hz)	**MM71 f_c (Hz)**	**DJ91 f_c (Hz)**	**MMP12 f_c (Hz)**
B6	10.6 Hz	12.5	8.4	14.4
B4	10.1 Hz	8.6	5.3	9.9
B10	8.5 Hz	7.1	4.2	8.3

Table 2.4 – Full moment tensor maximum time series amplitudes (all $x10^{13}$)

Shot	**# of boreholes**	**M_{xx}**	**M_{xy}**	**M_{xz}**	**M_{yy}**	**M_{yz}**	**M_{zz}**
B6	1	1.09	0.298	0.823	1.27	0.862	1.90
B4	4	4.26	1.02	3.28	4.09	3.15	7.15
B10	8	6.02	1.81	5.61	7.65	5.96	15.1

Table 2.5 – Decomposed moment tensor maximum time series amplitudes (all x1013)

Shot	**# of boreholes**	**M_{tr}**	**m_{xx}**	**m_{xy}**	**m_{xz}**	**m_{yy}**	**m_{yz}**	**m_{zz}**
B6	1	1.39	0.752	0.298	0.823	0.571	0.862	1.04
B4	4	4.69	1.31	1.02	3.28	1.88	3.15	4.15
B10	8	9.19	4.89	1.81	5.61	4.05	5.96	8.94

FIGURES

Figure 2.1 – Morenci Copper mine is located in southeastern Arizona along the New Mexico border, shown as the large red star.

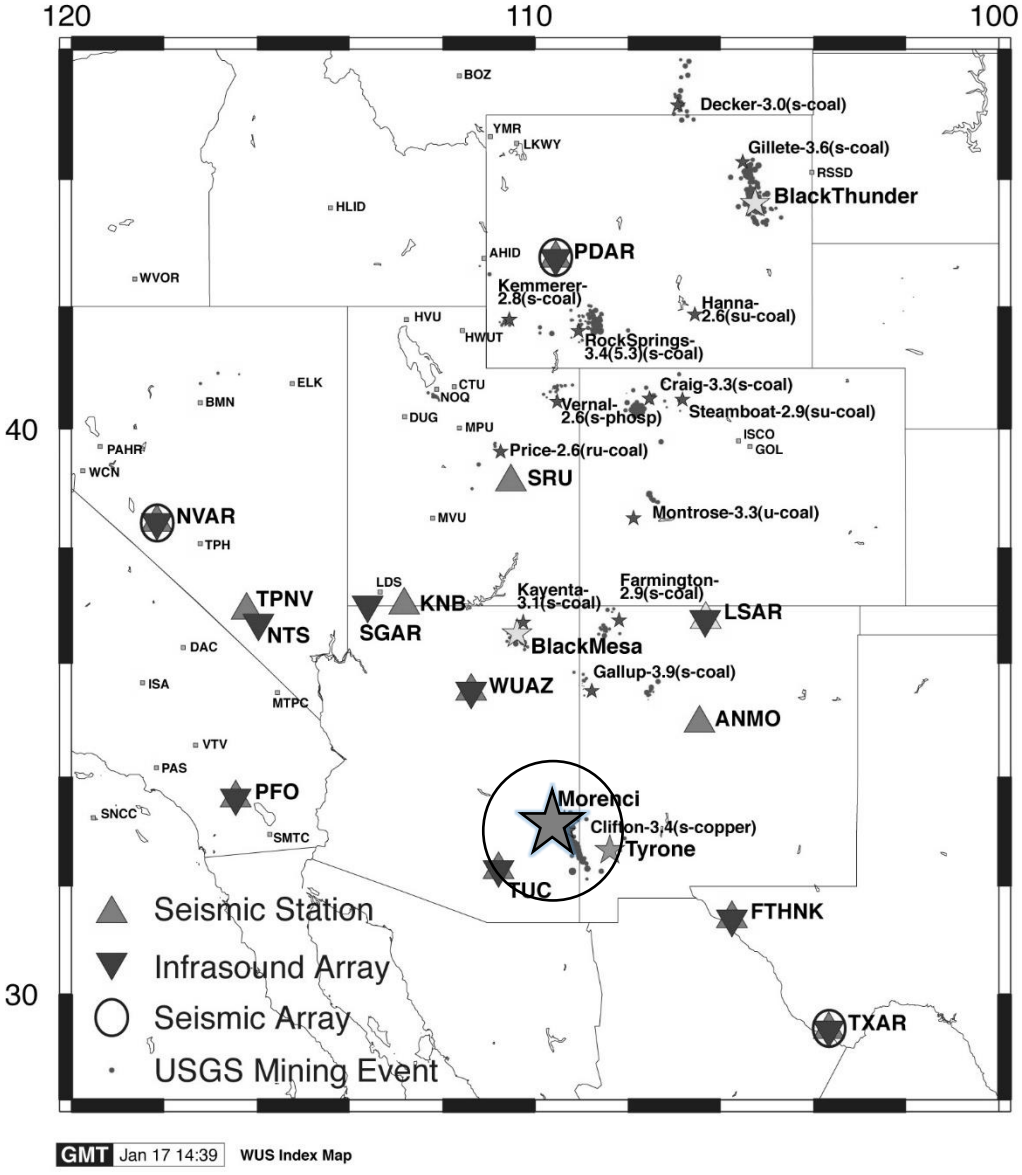

Figure 2.2 – Plan view of the test bench with explosion borehole positions, not completely to scale, demonstrating borehole geometry

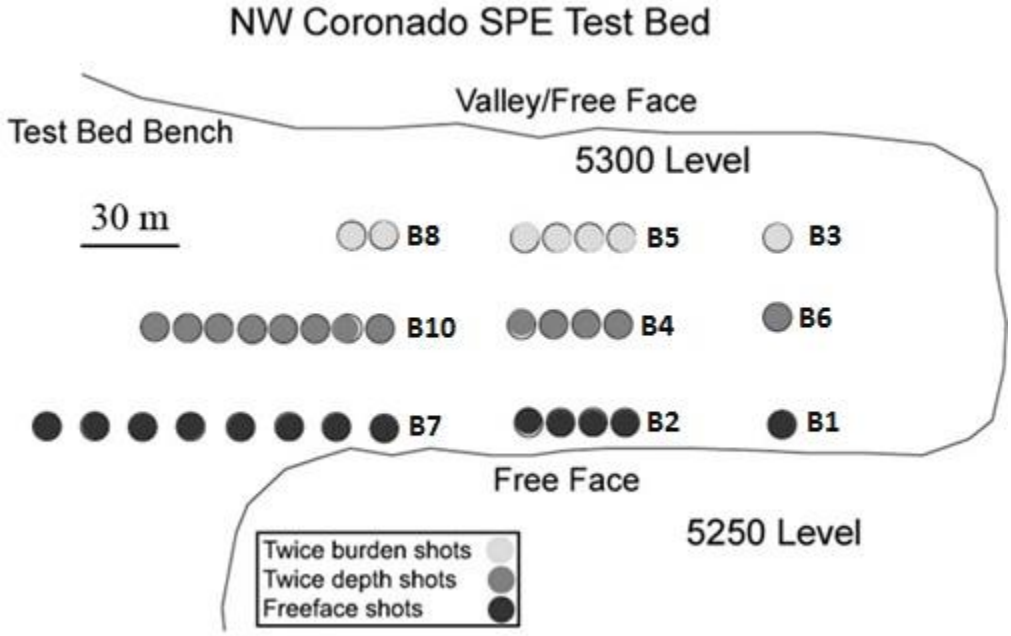

Figure 2.3 – Map of near-field instrumentation from 35 m to ~700 m. Dark stars are hi-g accelerometers, light stars are low-g accelerometers and stars with black dots are velocity transducers.

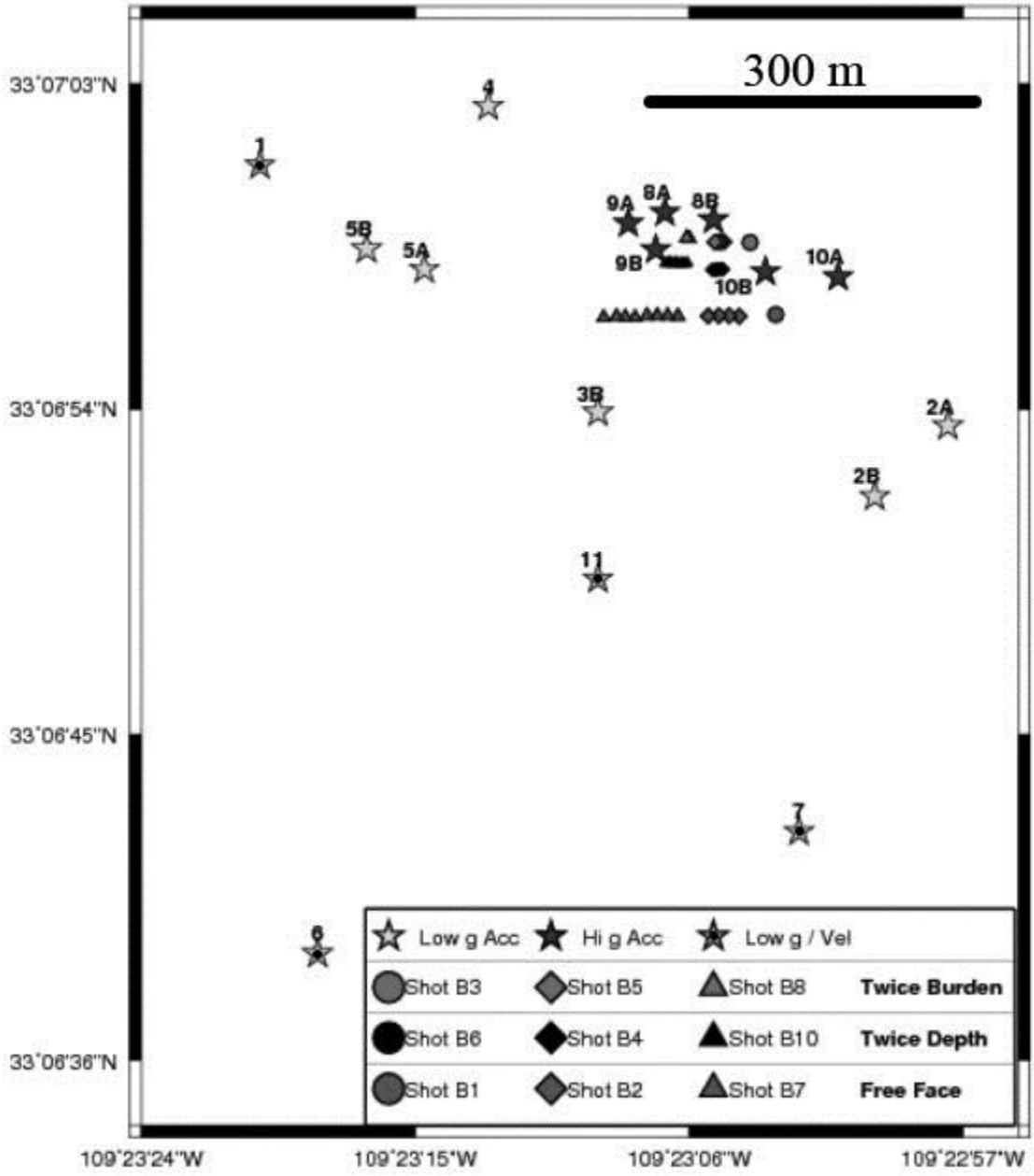

Figure 2.4 – Signal vs Noise for station 6B vertical velocity from shot B4 observed at 680 m.

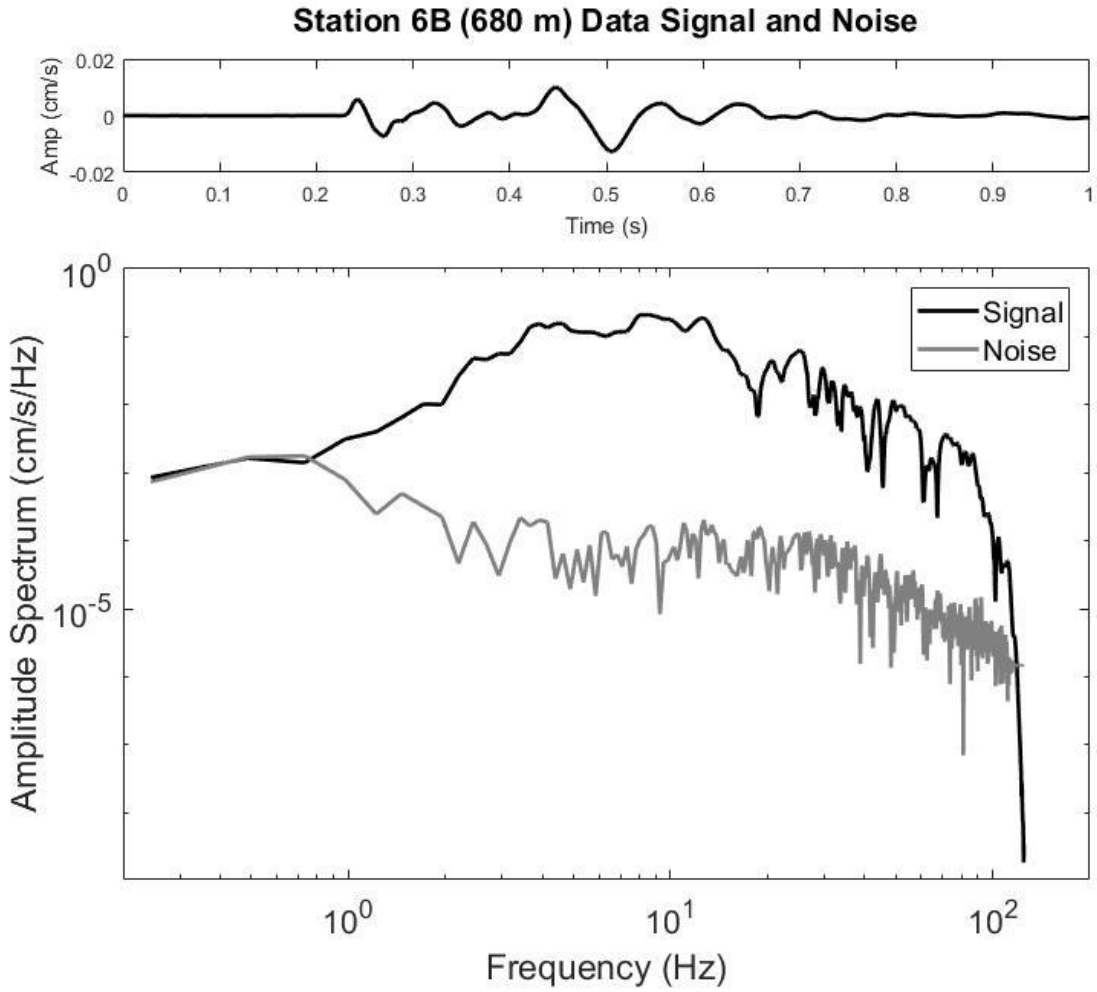

Figure 2.5 – Scaled Depth of Burials for shots B6, B4 and B10.

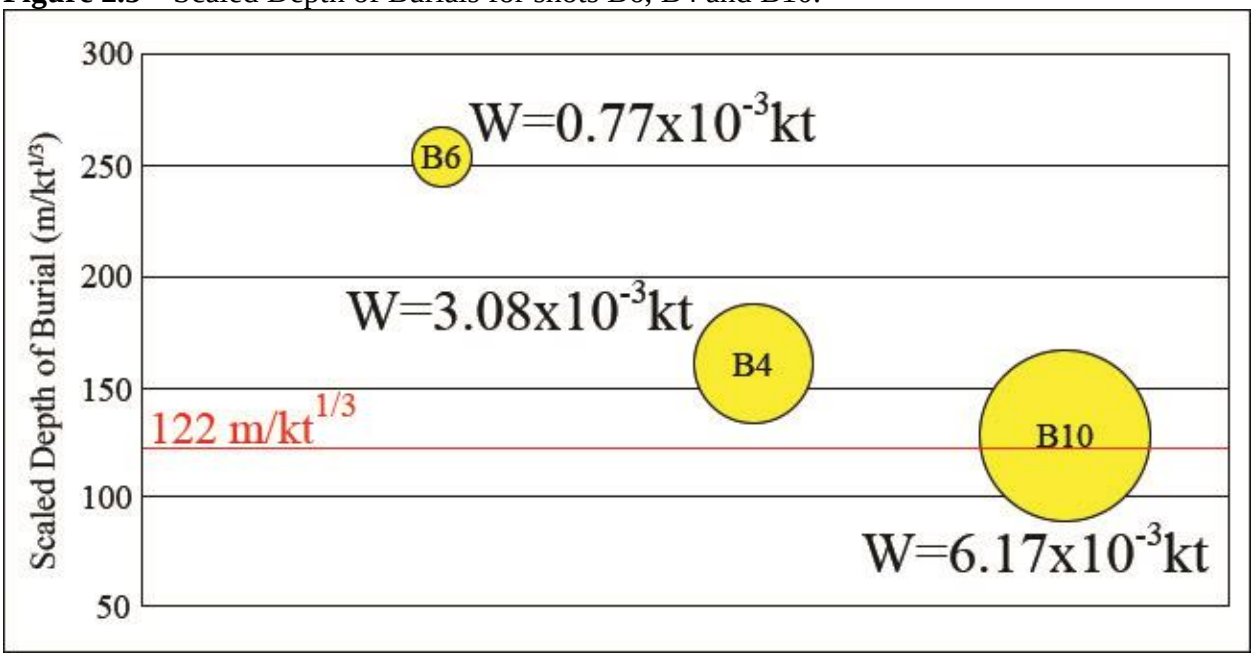

Figure 2.6 – One dimensional test site model for Morenci.

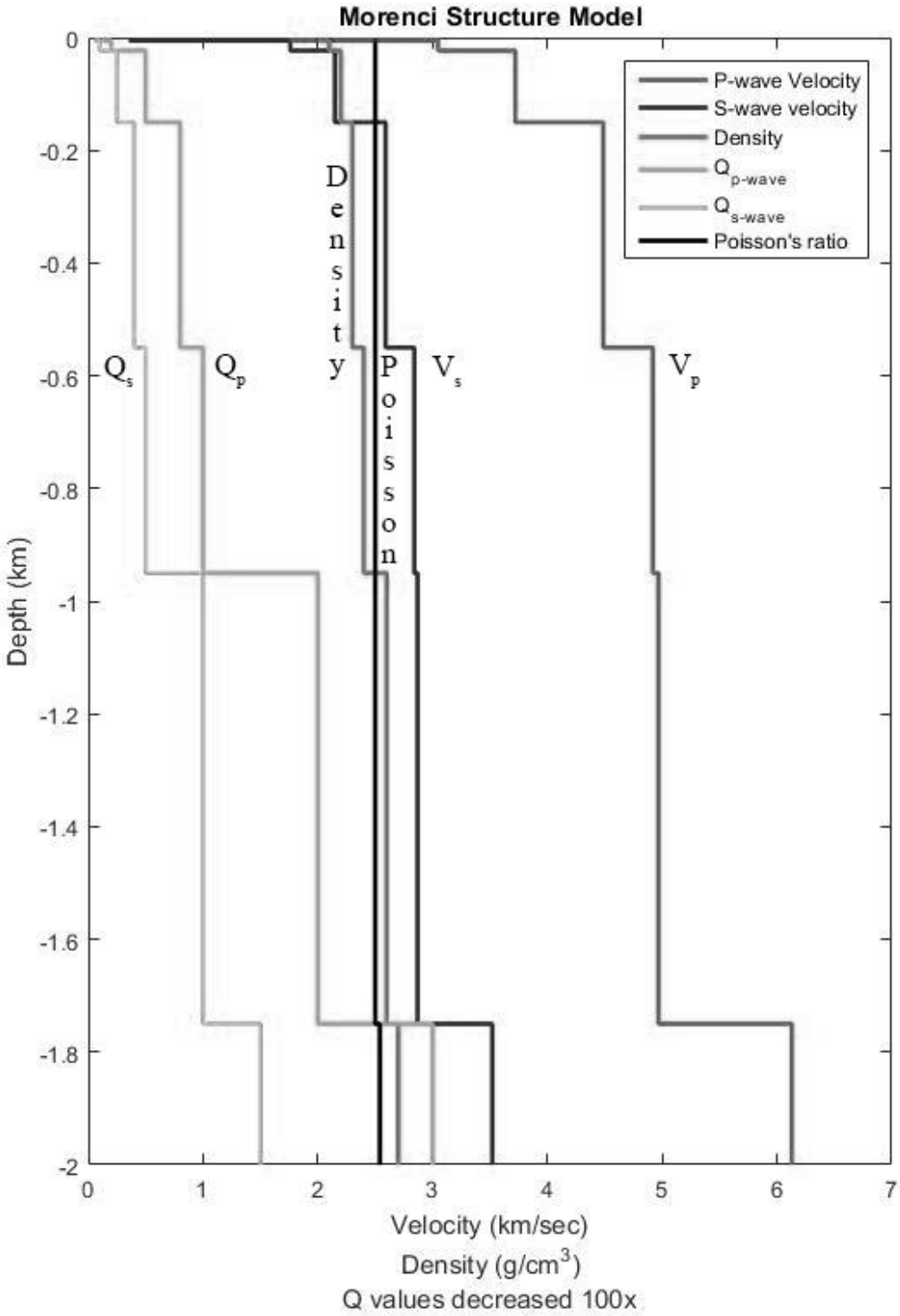

Figure 2.7 – Synthetic record section for shot B4 based on the Morenci model and a MM71 isotropic source model.

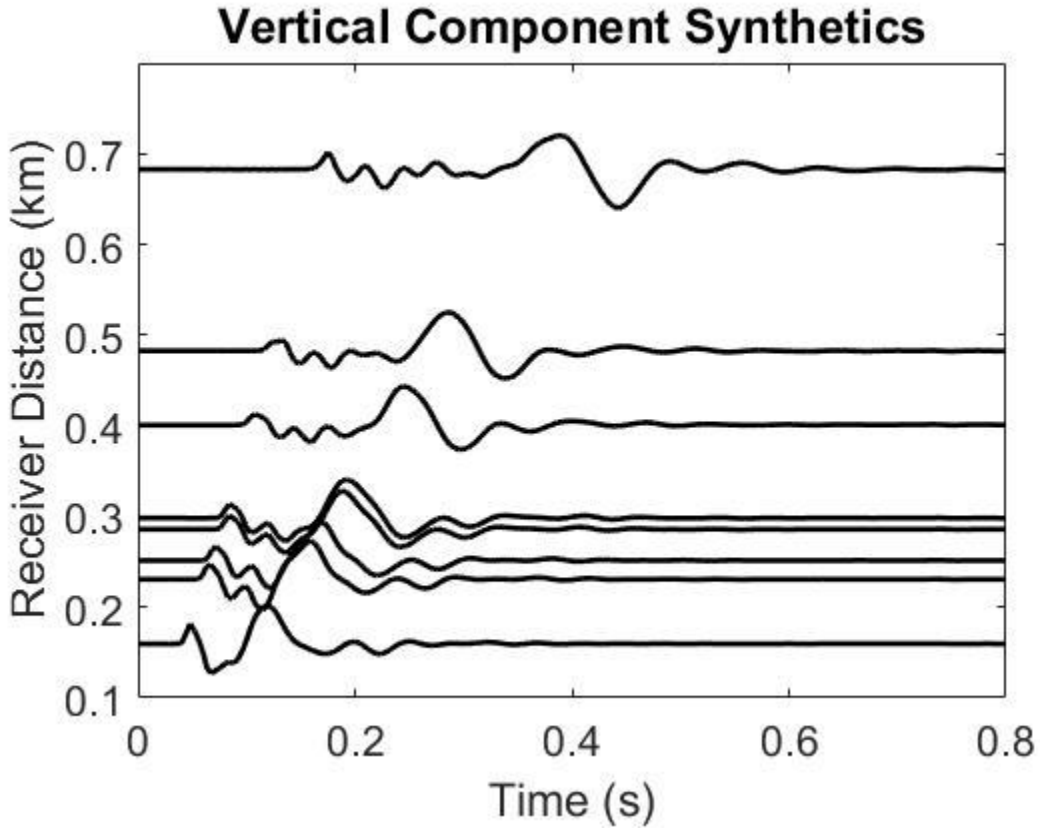

Figure 2.8 – Predicted (fitted) observations and actual data for unfiltered Z component with mean cross correlation for all stations within the linear elastic zone for shot B4.

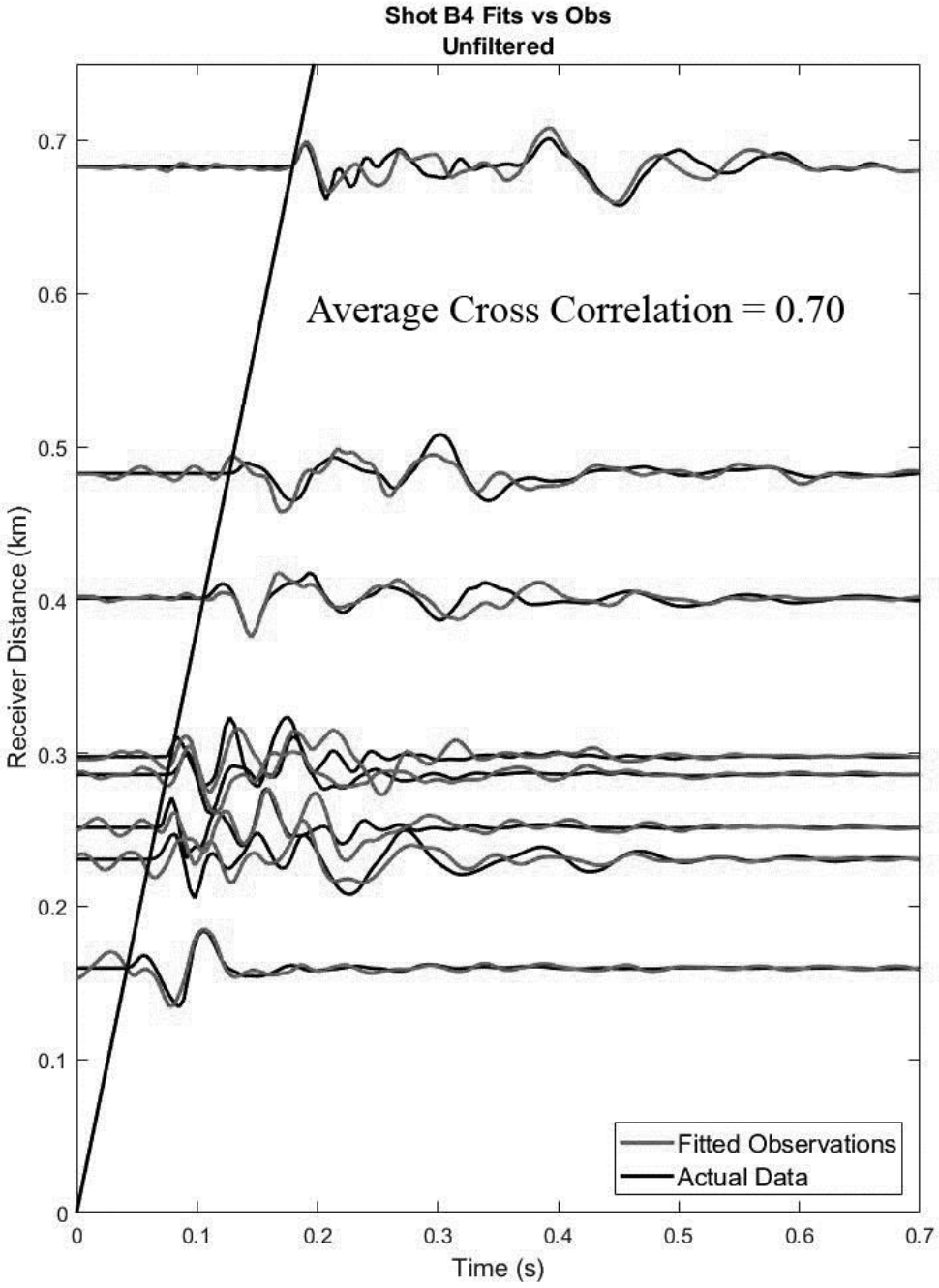

Figure 2.9 – Full moment rate tensor time series for shot B4. Maximum values displayed on figures in N*m/s.

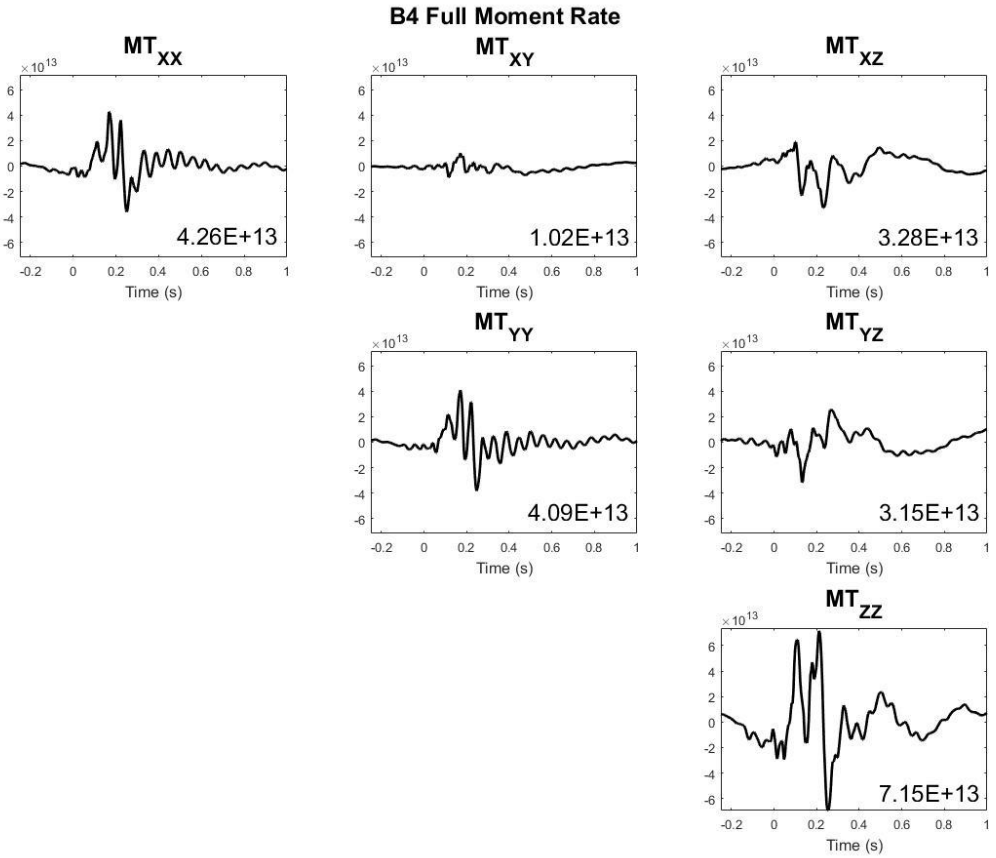

Figure 2.10 – Decomposed moment rate tensor component time series for shot B4. Maximum values displayed on figures in N*m/s.

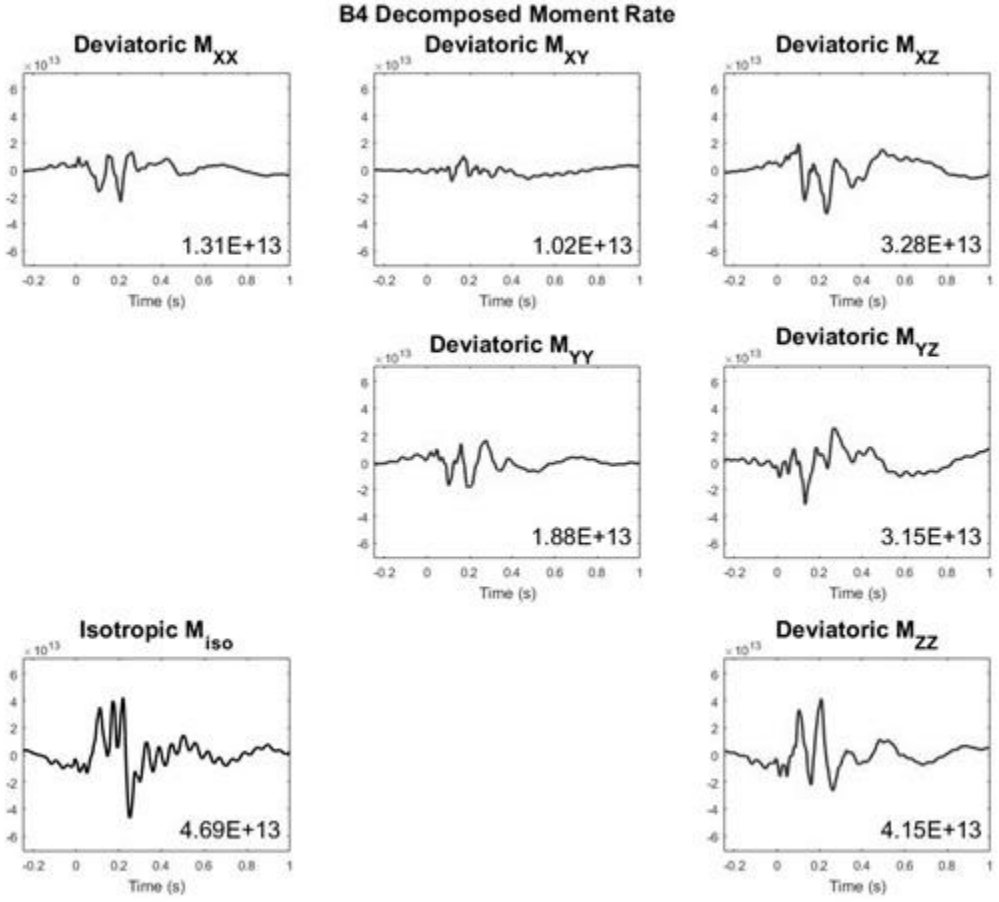

Figure 2.11 – Mzz component moment rate spectrum from shots B6 (W=0.77x10-3 kt), B4 (W=3.08x10-3 kt) and B10 (W=6.17x10-3 kt) from D.C. - 125 Hz

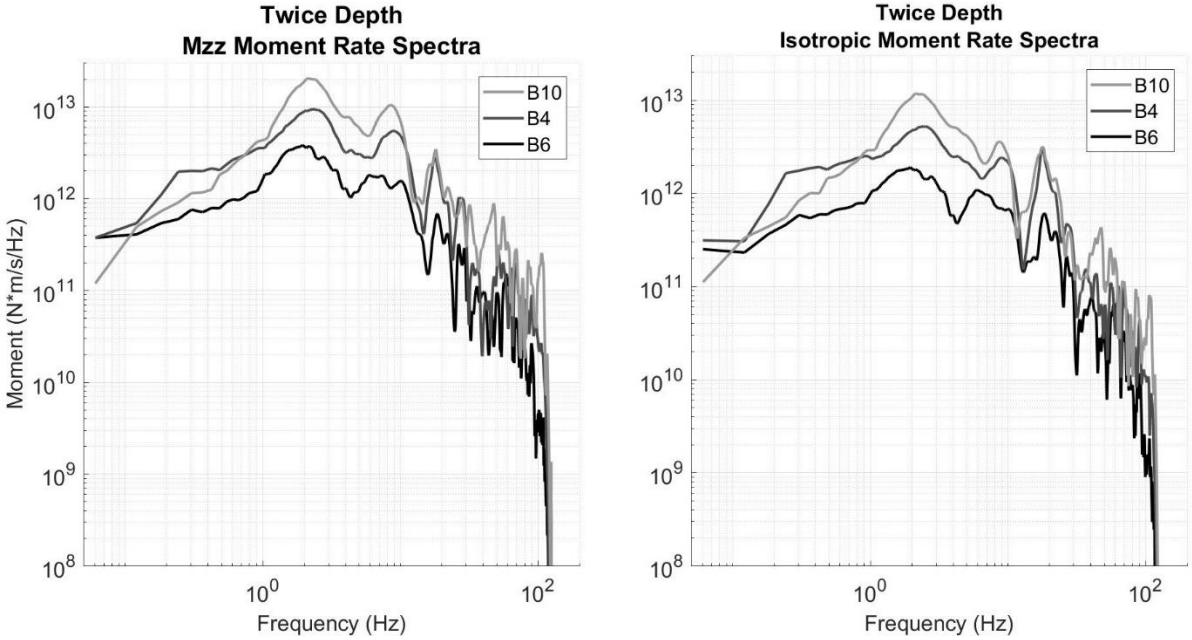

Figure 2.12 – Mzz and Mtr moment rate spectrums for shots B6, B4 and B10 with Mueller Murphy, 1971, Denny and Johnson, 1991, and revised Heard and Ackerman source models for Granite overlaid.

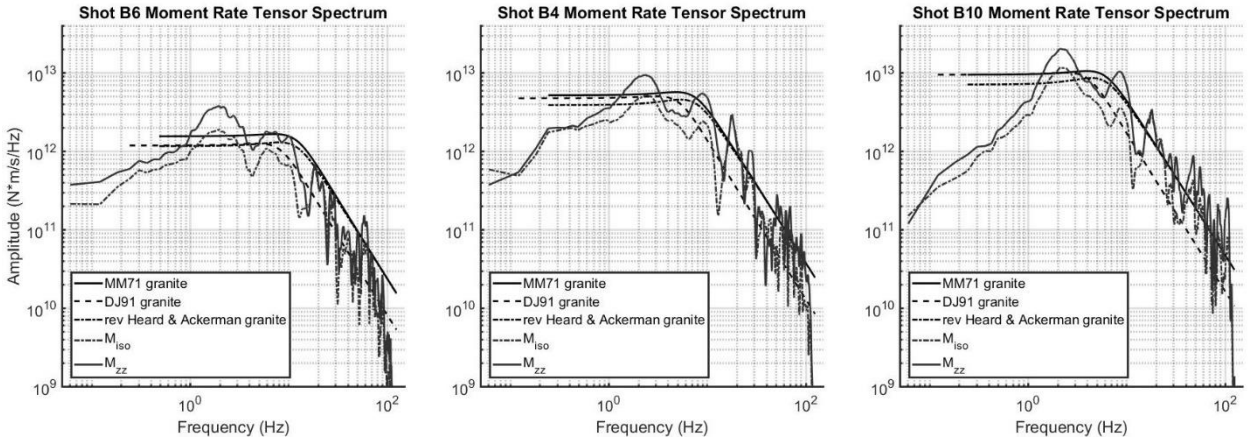

Figure 2.13 – Displays an augmented plot from Denny and Johnson, 1991, comparing shots B6, B4 and B10's moments to other chemical and nuclear explosions. Moments are adjusted using equation 43 from Denny and Johnson (1991).

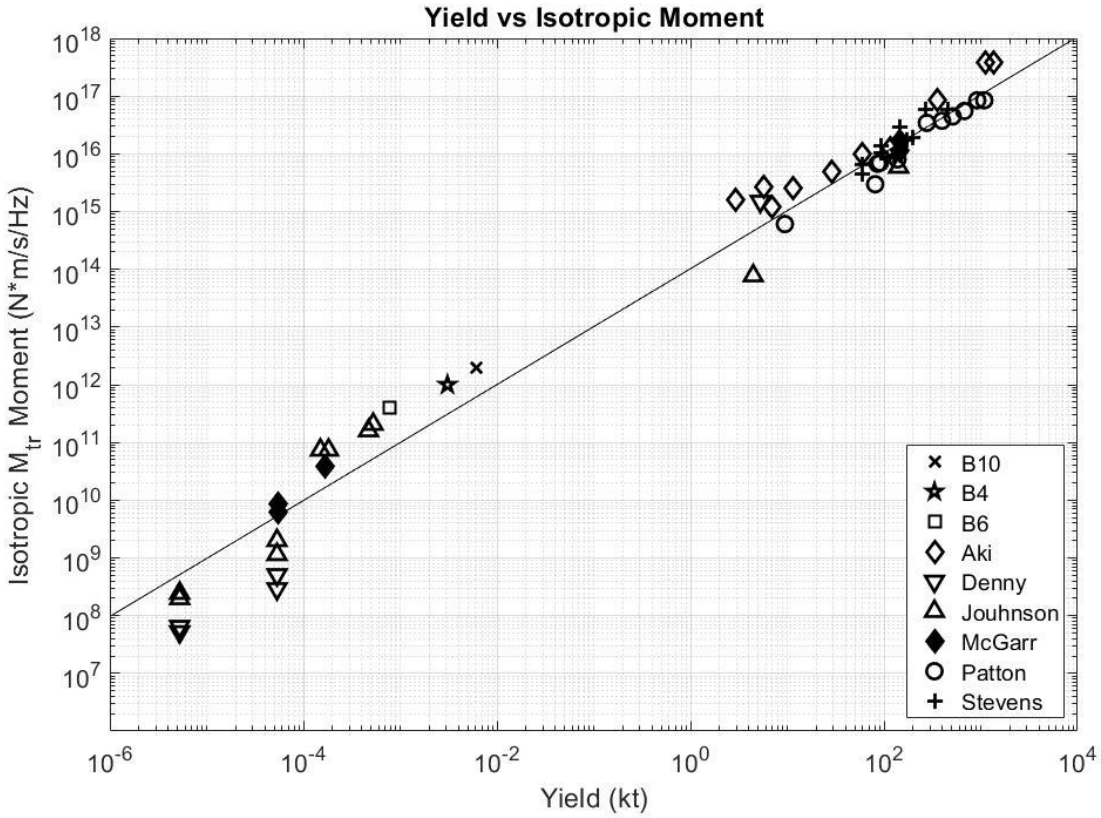

Figure 2.14 – Empirical moment tensor source representation displayed on a Hudson (1989) plot as a function of frequency from DC to 20 Hz for shot B4.

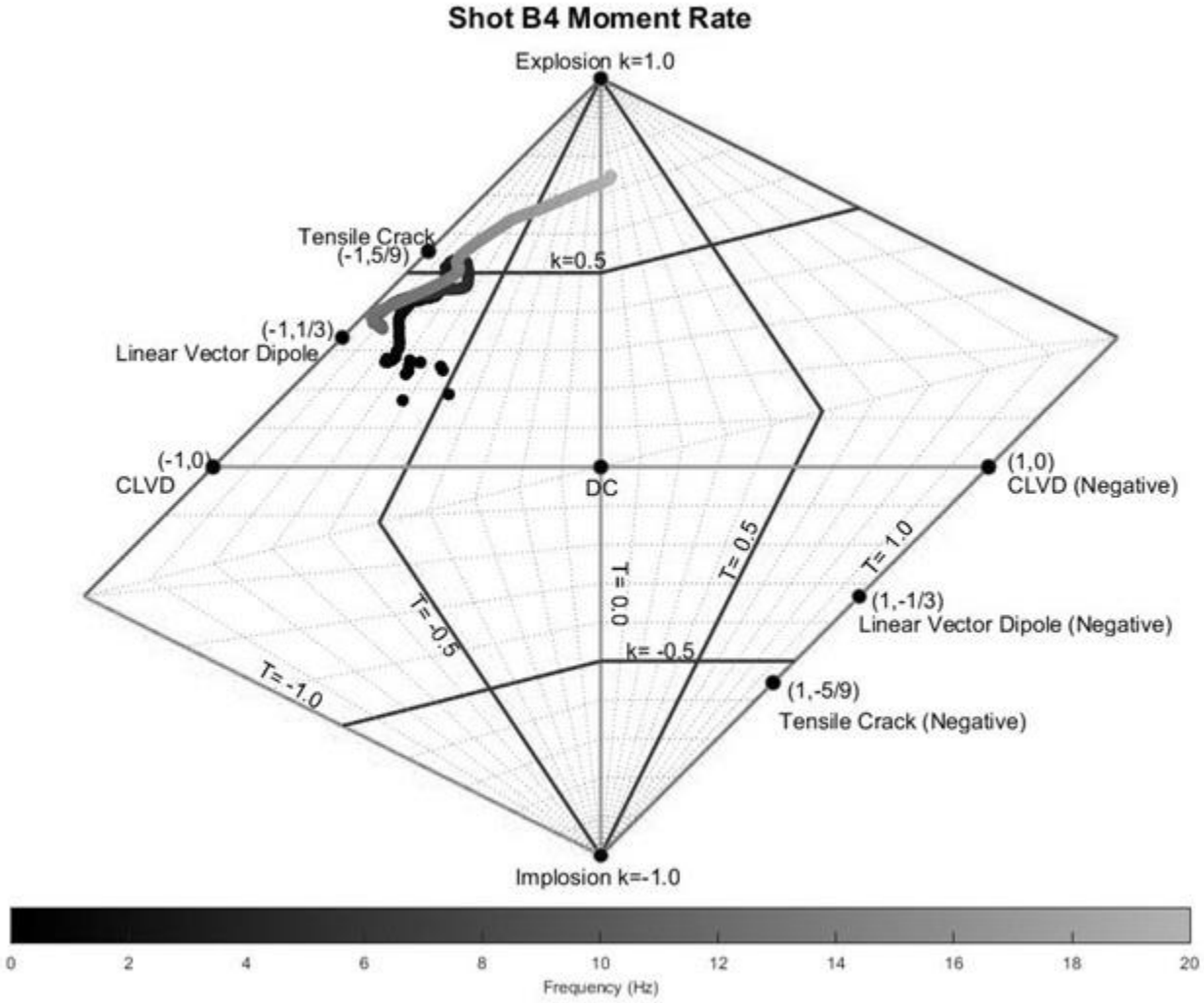

Figure 2.15 – Shot B6 spectrum compared to MMP12 models using yields with a factor of 1 and 2. M_{iso} spectral level shown as a thin line from 1-10 Hz, where the long period level was calculated.

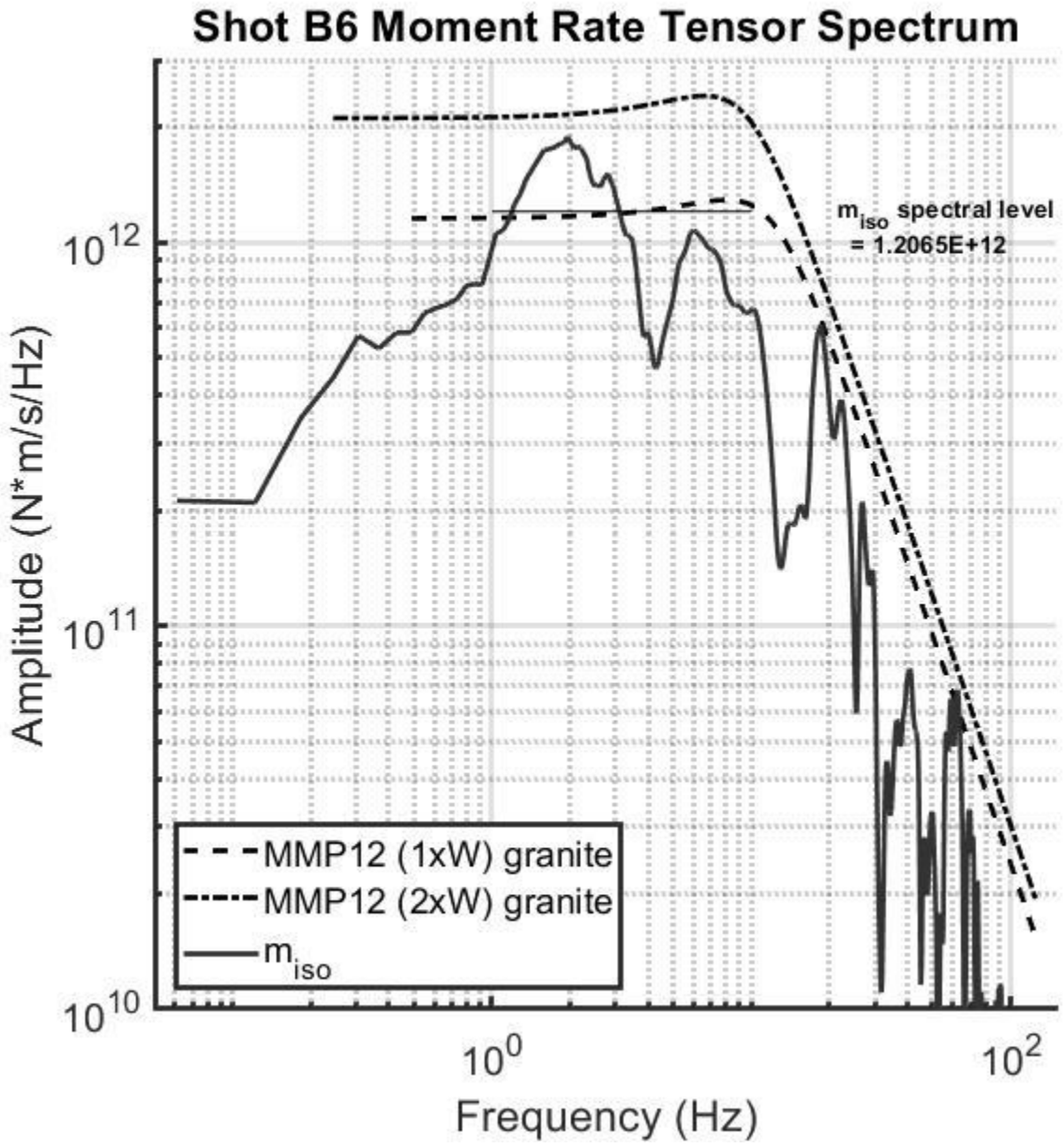

REFERENCES

Aki, K., P. Reasenberg, T. DeFazio, and Y.-B. Tsai (1969), Near-field and far-field seismic evidences for triggering of an earthquake by the BENHAM explosion, Bull. Seismol. Soc. Am., 59, 2197–2207.

Aki, K., and Y. Tsai (1972), The mechanism of Love wave excitation by explosive sources, J. Geophys. Res., 77, 1452–1475, doi:10.1029/JB077i008p01452.

Archambeau, C. B. (1972), The theory of stress wave radiation from explosions in prestressed media, Geophys. J., 29, 329–366.

Barth, A. (2014), Significant release of shear energy of the North Korean nuclear test on February 12, 2013, J. Seismol., 18, 605–615.

Day, Steven M., Norton Rimer, and J. Theodore Cherry. "Surface waves from underground explosions with spall: Analysis of elastic and nonlinear source models." Bulletin of the Seismological Society of America 73.1 (1983): 247-264.

Denny, Marvin D., and Lane R. Johnson. "The explosion seismic source function: Models and scaling laws reviewed." Explosion Source Phenomenology (1991): 1-24.

Donald B. Larson, Lawrence Livermore National Laboratory, Proceedings of the Department of Energy Sponsored Cavity Decoupling Workshop, Pajaro Dunes, California, July 29-31, 1985.

Dreger, Douglas, et al. Refinement of regional distance seismic moment tensor and uncertainty analysis for source-type identification. CALIFORNIA UNIV BERKELEY, 2014.

Dreger, Douglas S., Sean R. Ford, and William R. Walter. Identifying Isotropic Events using an Improved Regional Moment Tensor Inversion Technique. No. LLNL-TR-713716. Lawrence Livermore National Laboratory (LLNL), Livermore, CA, 2016.

Ford, S. R., D. S. Dreger, and W. R. Walter (2009), Source analysis of the Memorial Day explosion, Kimchaek, North Korea, Geophys. Res. Lett., 36, L21304, doi:10.1029/2009GL040003.

Glenn, L. A., & Goldstein, P. (1994). The influence of material models on chemical or nuclear-explosion source functions (No. UCRL-JC-116428; CONF-9404100-8). Lawrence Livermore National Lab., CA (United States).

Goldstein, P., and S. Jarpe. "Comparison of chemical and nuclear explosion source spectra from close-in, local and regional seismic data." Proc. of the Symposium on the Non-Proliferation Experiment (NPE): Results and Implications for the Test Ban Treaties. 1994.

Harkrider, D. G. (1977), Elastic relaxation coefficients for a spherical cavity m a prestressed medium of arbitrary orientation, Geophys. J., 50, 487–491.

Harris, D. B. (1991). A waveform correlation method for identifying quarry explosions, Bull. Seism. Soc. Am. 81, 2395-2418.

Heard, H. C., and F. J. Ackerman (1967). Prediction of cavity radius from underground nuclear explosions, Rep. UCRL-50324, Lawrence Radiation Laboratory, Livermore, CA.

Latter, A. L., et al. "A method of concealing underground nuclear explosions." Journal of Geophysical Research 66.3 (1961): 943-946.

Lay, Thorne, Don V. Helmberger, and David G. Harkrider. "Source models and yield-scaling relations for underground nuclear explosions at Amchitka Island." Bulletin of the Seismological Society of America 74.3 (1984): 843-862.

M. Nafi Toksöz, Harold H. Kehrer; Tectonic Strain Release by Underground Nuclear Explosions and its Effect on Seismic Discrimination, Geophysical Journal International, Volume 31, Issue 1-3, 1 December 1972, Pages 141–161

Massé, R. P. (1981), Review of seismic source models for underground nuclear explosions, Bull. Seismol. Soc. Am., 71, 1249–1268.

Minster, J. B., and A. M. Suteau (1977), Far-field waveforms from an arbitrarily expanding, transparent spherical cavity in a prestressed medium, Geophys. J., 50, 215–233.

Mueller, Richard A., and John R. Murphy. "Seismic characteristics of underground nuclear detonations Part I. Seismic spectrum scaling." Bulletin of the Seismological Society of America 61.6 (1971): 1675-1692.

Murphy, J. R., J. L. Stevens, B. C. Kohl, and T. J. Bennett (2013), Advanced seismic analyses of the source characteristics of the 2006 and 2009 North Korean nuclear tests, Bull. Seismol. Soc. Am., 103(3), 1640–1661.

Murphy, J., and B. Barker (1995). A Comparative Analysis of the Seismic Characteristics of Cavity Decoupled Nuclearand Chemical Explosions, Pl-TR-95-2117, Phillips Laboratory, 96 pp

Murphy, J. R., et al. "Seismic characteristics of cavity decoupled explosions in limestone: An analysis of Soviet high explosive test data." Journal of Geophysical Research: Solid Earth 102.B12 (1997): 27393-27405.

Olsen, C. W. Site selection and containment evaluation for LLNL nuclear events. No. UCRL-JC--113334; CONF-9309103--1. Lawrence Livermore National Lab., CA (United States), 1993.

Patton, Howard J. "Characterization of spall from observed strong ground motions on Pahute Mesa." Bulletin of the Seismological Society of America 80.5 (1990): 1326-1345.

Patton, Howard J. "Seismic moment estimation and the scaling of the long-period explosion source spectrum." Explosion Source Phenomenology (1991): 171-183.

Patton, Howard J., and Steven R. Taylor. "The apparent explosion moment: Inferences of volumetric moment due to source medium damage by underground nuclear explosions." Journal of Geophysical Research: Solid Earth 116.B3 (2011).

RODGERS, A.J. and WALTER, W.R. (2002) Seismic discrimination of the May 11, 1998 Indian nuclear test with short-period regional data from Station NIL (Nilore, Pakistan), Pure Appld. Geophys., v.159, pp.679-700, doi:10.1007/s00024- 002-8654-6.

Rougier, Esteban, and Howard J. Patton. "Seismic source functions from free-field ground motions recorded on SPE: Implications for source models of small, shallow explosions." *Journal of Geophysical Research: Solid Earth* 120.5 (2015): 3459-3478.

Stevens, Jeffry L., and Steven M. Day. "The physical basis of mb: Ms and variable frequency magnitude methods for earthquake/explosion discrimination." Journal of Geophysical Research: Solid Earth 90.B4 (1985): 3009-3020.

Stump, Brian W., D. Craig Pearson, and Robert E. Reinke. "Source comparisons between nuclear and chemical explosions detonated at Rainier Mesa, Nevada Test Site." Bulletin of the Seismological Society of America 89.2 (1999): 409-422.

Brian W. Stump, Lane R. Johnson; Near-field source characterization of contained nuclear explosions in tuff. Bulletin of the Seismological Society of America ; 74 (1): 1–26. doi:

Brian W. Stump; Constraints on explosive sources with spall from near-source waveforms. Bulletin of the Seismological Society of America ; 75 (2): 361–377. doi:

Viecelli, James A. "Spallation and the generation of surface waves by an underground explosion." Journal of Geophysical Research78.14 (1973): 2475-2487.

Toksöz, M. N., K. C. Thomson, and T. J. Ahrens (1971), Generation of seismic waves in prestressed media, Bull. Seismol. Soc. Am., 61(6), 1589–1623.

Wallace, T. C., D. V. Helmberger, and G. R. Engen (1983), Evidence of tectonic release from underground nuclear explosions in long-period P waves, Bull. Seismol. Soc. Am., 73(2), 593–613.

Wallace, T. C., D. V. Helmberger, and G. R. Engen (1985), Evidence of tectonic release from underground nuclear explosions in long-period S waves, Bull. Seismol. Soc. Am., 75(1), 157–174.

Ekstrom G. Richards P. (1994). Empirical measurements of tectonic moment release in nuclear explosions from teleseismic surface waves and body waves, Geophys. J. Int. 117, 120–140.

Helle H. B. Rygg E. (1984). Determination of tectonic release from surface waves generated by nuclear explosions in eastern Kazakhstan, Bull. Seismol. Soc. Am. 74, 1883–1898.

Xiaoning Yang, Jessie L. Bonner; Characteristics of Chemical Explosive Sources from Time-Dependent Moment Tensors. Bulletin of the Seismological Society of America ; 99 (1): 36–51. doi: https://doi.org/10.1785/0120080243

CHAPTER 3

EFFECTS OF CONTAINMENT AND YIELD ON SOURCE REPRESENTATIONS FOR SMALL DECOUPLED CHEMICAL EXPLOSIONS DETONATED IN GRANITE

Abstract

The Source Phenomenology Experiment (*SPE - Arizona*) was a series of nine, contained and partially contained chemical explosions within the porphyry granite at the Morenci Copper mine in Arizona. Its purpose was to detonate, record and analyze seismic waveforms from these single-fired explosions for purposes of characterizing the explosion seismic source representation as well as its absolute coupling. Ground motion data from the *SPE* is used in this study to estimate the frequency domain moment tensor source representation and then assess its ability to quantify yield scaling and coupling. Green's functions were computed for each of the explosions based on a 1D velocity model developed for the *SPE* site. The Green's functions for the sixteen, near-source stations span the distance range from 37-680 m. This chapter explores yield but focuses more on containment effects as the sources analyzed are detonated closer to a free face or free surface. This study uses the full suite of nine explosions from the SPE. Three detonations at the free face, three detonations twice that distance from the free face (twice burden) but at the same source depth and three detonations twice the depth of the previous six explosions. These sets of explosions each have varying yields as well. This investigation probes how the source

representation is affected by containment as well as yield and bridges to typical source configurations characteristic of mining explosions.

Motivation

This study focuses on containment effects and yield scaling from small chemical explosions when a source medium, in our case porphyritic Granite, is known. Scaled depth of burial, distance from a free surface, yield and emplacement medium affect the explosion source representation, both by decoupling or a later secondary source, possibly spall, at a free surface. MacPhail et al. (2018a) focuses on the trade-offs between source representation and model assumptions such as source depth and propagation models, for explosions that are assumed to be fully contained. MacPhail et al. (2018b) then assesses yield scaling effects for a set of contained explosions spanning three different yields with the same source depth. This study specifically addresses changes in coupling as the centroid of the explosion approaches the free surface in some tests and a vertical free face for others. This third study provides not only a characterization of energy loss to the free surface interaction but also possible changes to the moment tensor representation. Of particular importance is the change in source representation for explosions close to the vertical free face, typical of mining explosions, and thus may impact the separation of mining explosions from contained explosions based on seismic observations. This source comparison also provides a basis for assessing the use of mining explosions as surrogates for seismic discrimination studies.

Scaling of explosions, both chemical and nuclear, is an important facet of using chemical explosions as proxies for their nuclear counterparts due to the generally smaller yields of chemical explosions (MacPhail, 2018 b). With the exception of nuclear explosions coupling less

energy into the surrounding earth, chemical explosions can be used to study nuclear explosions due to the fact that the same physics is involved (MacPhail, 2018 b).

Free surface interactions of seismic energy play a key role in near-source explosion phenomenology. Spall of near surface material is a well-documented component of contained underground nuclear explosions (Eisler et al (1964); Chilton et al. (1966); Viecelli (1973); Springer, (1974)). For a contained explosion, after detonation, a compressive wave travels upward toward the free surface and as this pressure wave reflects, it transitions to a tensile wave failing the near-surface geologic layers and sending them into ballistic freefall as a result of the imparted momentum. The source representation is complicated by this momentum transfer from the purely spherical wavefield into the cylindrical secondary spallation force occurring later in time (Day et al. (1983), Stump (1985), Patton (1990)).

When detonating explosions near a vertical free face, free surface failure from the reflection casts material laterally and downward, often used in mining scenarios. These failure processes remove energy from the source, both the nonlinear failure as well as the degradation of the overall solid earth coupling. Bonner et al (2005) detonated a series of explosions at a copper mine in Arizona with varying lateral distances from a free surface. Spectral ratios of twice depth to free face data are relatively flat at all frequencies but indicate a reduction of coupling with a factor of roughly 2-4 for the free face shots. Zhou and Stump (2007) document seismic coupling differences from these single-fired explosions with different yields and confinements. They found little difference in spectra levels for the contained and uncontained shots at frequencies above 3 Hz, suggesting differences in mechanisms for high frequency and long period energy. Hooper et al (2006) took this same data set and showed important differences between R_g amplitudes of confined and unconfined explosions in an attempt to better discriminate mining

events. They find that unconfined shots have R_g decoupling factors ranging from 0.5 to 8.2 between 0.5 and 11 Hz with largest decoupling in the 1 to 3 Hz Rg band. They also show an azimuthal dependence of coupling with a spectral increase of a factor of 1.5 behind the bench.

Yang et al. (1999) characterized eight, single-hole shots typical of mining blasts with charge sizes ranging from 59 to 296 kg detonated 6 m from a vertical free face. The shots have a large isotropic component (~80%) but show a significantly large degree of asymmetry along the diagonal components inconsistent with what is expected from the cylindrical source geometry at a vertical free face. Bonner et al. (2003) modeled cast blasts at a free face and theoretical radiation patterns showing amplitudes perpendicular to the free face as much as 2.5 times greater than those parallel to the face. McLaughlin et al. (2004) modeled observed short-period Love and Rayleigh waves from a quarry in Texas and found that the free face collapse of material is the dominant mechanism leading to the asymmetries.

Anandakrishnan et al., 1997, based on a set of experiments at a coal mine in Wyoming developed a linear elastic model to simulate regional-distance seismograms from mining cast blasts in an attempt to separate the effects due to the explosion as well as the horizontal and vertical movement of mass from the free face in order to get a better physical understanding of the resulting waveforms. One observational result was the excitation of 8-12 s surface waves from the cast blasts. Another result was the insensitivity of peak amplitude to total explosive size for normal blasting practices, which used delay-fired explosions. The horizontal force component from the mass of rock impacting the pit creates an azimuthally dependent enhancement of Rayleigh waves. The vertical force component is roughly equal to the explosion contribution at pit depths of 10 m, but dominate for pit depths greater than 20 m. Hedlin et al., 2002, conducted two experiments with recorded data from kiloton class, delay-fired cast blasts

and instantaneous calibration shots from within a coal mine in Wyoming. The data shows significant spectral modulation below 10 Hz and low frequency modulations below 5 Hz. Their modeling failed to reproduce the modulation in detail but does show a spectral roughness in part from long inter-row delays and source finiteness. Their analysis yields enhanced, azimuthally dependent 2-10 s surface waves due mostly to extended source duration and to a lesser extent the re-impactment of spalled material. Stump et al., 2002, focus on seismic wave characteristics from mining explosions for purposes of event identification. They review and discuss a collection of tools and techniques used for identifying mining explosions, such as, P/L_g at low and high frequencies, surface wave to body wave amplitudes, time-varying spectral estimates, low frequency modulations and correlation analysis.

Decoupling is the reduction of seismic wave amplitudes relative to a fully contained explosion and is described in terms of the decoupling factor (DF). The DF is theoretically and experimentally found to be frequency dependent and greater for lower frequencies (Larson, 1985; Murphy and Barker, 1995). First proposed by Latter et al (1961), energy decoupling by means of a cavity can be used as an evasion scenario for nuclear explosion monitoring. To date, three sets of nuclear explosion experiments have been conducted in salt (GNOME, SALMON and STERLING) and one set of chemical explosions in salt (COWBOY), Herbst et al (1961). From the Sterling experiment, Springer and Denny (1968) conclude that a nuclear explosion can be decoupled by a factor of 70±20. Denny and Goodman, 1990, reevaluated the STERLING and SALMON experiment and found refined decoupling estimate of 72.

Stroujkova et al (2014) detonated two explosions (each 111 kg of ANFO) at the same shot point in limestone, the second shot being detonated within the cavity and damaged zone of the first shot, on a pedestal of sand, thus being decoupled from the surrounding geology. They

calculated a decoupling factor based on work by Atchison et al (1964) for limestone of 3.6 with the average for limestones being 3.41. Stroujkova et al (2016) found that chemical and nuclear explosions in granite obey the cube root scaling law. They also found that scaled cavity radii are mostly independent of the source depth and determined by the source rock properties, including strength and elastic moduli. Stroujkova et al (2013) investigated seismic radiation from explosion in low coupling media. Explosions were detonated within and outside of fractured zones. They found a frequency dependent reduction in P-wave amplitudes within the fractured zones of a factor of 2-3. The overshoot parameter in the explosion source model was higher for the explosions within the previously undetonated media and that corner frequency correlated more closely with this overshoot parameter, rather than the yield. Stroujkova (2015) examined the effect of total gaseous by-products from small chemical explosions on seismic source signatures. Explosions were detonated using various types of explosives with different burn rates, densities and energy contents per unit mass. These explosives produce different amounts of gaseous by-products that Stroujkova (2015) found may explain better seismic coupling and higher amplitudes at larger distances.

In a comprehensive manner a complete assessment of decoupling might best include a complete suite of depth of burst and height of burst explosions with explosions detonated below the free surface being the best coupled and those detonated above the free surface producing significantly decreased seismic coupling. At the free surface, an explosion is uncontained. Koper et al (2002) evaluate truck bombs by analyzing local seismic and acoustic data to estimate the yield of uncontained events. Ford et al (2014) examine height-of-burst/depth-of-burst (HOB/DOB) with the aim of developing quantitative energy partitioning models and a methodology to estimate yield and HOB/DOB. Pasyanos and Ford (2015) use their previous

amplitude envelope method and expand it to consider explosions at the air-Earth interface to examine source characteristics of near surface explosions. Bonner at al., (2005) detonated a series of nine explosions with different depths and confinements to better understand how distance from the free surface affects the source representation. Surface explosions studies examining coupling between acoustic overpressure and Rayleigh wave propagation have been presented by several authors (Murphy, 1981; Murphy and Shah, 1988)

Explosions and impacts at or close to the free surface not only experience reduced coupling but energy is imparted into the cratering process (Nordyke, 1961). Perhaps the most studied field is that of surface cratering from meteors and meteorites (Shoemaker, 1959; Holsapple and Housen, 2013; Holsapple and Housen, 2017). An uncontained explosion creates craters at the surface a subject that has been explored by many authors (Orphal, 1977, 1979; Short, 1965; Brode, 1968; Holsapple and Schmidt, 1980).

Seismic discrimination of underground nuclear explosions based on ground motion data from local to teleseismic distances motivates a physical understanding of the similarity and differences of seismic source functions from explosions detonated under a broad range of physical conditions including explosions that are decoupled. Some larger mining explosions can be large enough to have magnitudes within the range of small nuclear explosions and for this reason discrimination techniques are needed to separate the two different explosion detonation characteristics.

Both the estimation of total explosion yield as well as the physical interpretation of seismic observations used for discrimination is important from a monitoring perspective and is related to the yield of the explosion, source distance from the free surface, possibly the vertical bench in a mining environment as well as the emplacement material. Mueller and Murphy (1971)

and Denny and Johnson (1991) developed seismic spectrum scaling models based on nuclear and a combination of nuclear and chemical explosions, respectively where only a free surface is exists. Chapter 1, investigated the uniqueness of the seismic source representation by quantifying the effects and possible trade-offs between yield, depth and geology in a granitic environment for a fully contained explosion. The wave propagation model was computed with a range of depths and shear wave velocities in order to quantify the effects of these parameters. Green's functions were calculated, based on these variables and subsequently analyzed. It was found that, for the 2 to 20 Hz band, the explosion Green's function had greater amplitudes for the shallowest source with the same moment. This propagation path effect then decreases the estimate of moment tensor amplitude because of the inverse proportionality between propagation path and source effects. The geologic models with slower shear wave velocities yielded lower amplitudes for all explosion radial component wave phases.

MacPhail et al. (2018 b) used the results of MacPhail et al., (2018 a) to extend the analysis from the one shot to a suite of three yields in order to assess existing scaling models. The three contained explosions with the same source depth but with different yields constrains scaling relations in granite. The source representations were plotted as a function of frequency on Hudson (1989) diagrams. As yield increases, it was found the source representation shifts to a greater explosion component and less CLVD component, peaking at 20 Hz.

When two explosions are detonated sufficiently close to one another with respect to the wave lengths of interest, the ratio between the observations can be estimated and as a result of the convolutional model, the propagation path effects cancel out. Spectral ratios can be used to constrain explosive yield, emplacement material and depth of burial (Murphy, 1996). Stump et al. (1999) studied a series of nuclear and chemical explosions detonated closely together at

Rainer Mesa and used spectral ratios to illustrate that there are no apparent spectral difference between nuclear and chemical explosions of similar yields. Stump et al. (2003) investigate source scaling relations using spectral ratios of observational data from multiple chemical explosions detonated within a mine in northeast Wyoming. Zhou and Stump (2007) evaluated spectral ratios of ground motion data from small chemical explosion detonations with varying containments and yields within a copper mine in Arizona. Individual ratios of regional wave phase displacement amplitude spectra for the nearly collocated first two DPRK UNEs were used for source studies due to common path effect elimination (Kim et al., 2009).

The experiments that generated the data used in this analysis were designed to explore containment on total signal strength as well as the resulting moment tensor representation. Explosions with different yields and different distances from the free surface and free face, as in the case of a mining scenario, change different moment tensor components in the frequency and time domain. We are motivated to better understand how these changes affect the source representation. For purposes of both yield determination and discrimination single-fired, small chemical mining explosions are used as surrogates to nuclear explosions but in reality they have different detonation mediums, geometries and locations which also need quantification. Our goal is to better understand the phenomenology of these small scale single-fired chemical explosions with varying yields and containments in an attempt to understand their applicability to nuclear explosion analysis.

Experiment Site

Data for this study was recorded during the Source Phenomenology Experiment (*SPE – Arizona*, Bonner *et al.*, 2005). The SPE was designed to empirically constrain the seismic source representation of explosions detonated in hard and soft rock, with granites the hard rock

environment as described by Bonner et al. (2005). A series of nine, single and simultaneously fired, small contained chemical explosions were detonated. The explosions consist of closely spaced linear patterns of simultaneously detonated boreholes

The hard rock component of the SPE consisted of nine shots with varying yields and containments. This analysis utilizes all nine shots with three containment scenarios detailed in **Table 3.1**. The free face scenario, shots B1, B2 and B7, are detonated 9 m from the test bench's vertical face (normal mine burden for fracturing the rock) and have a centroid depth of 12.2 m. The twice burden scenario, shots B3, B5 and B8, are detonated at the same centroid depth (12.2 m) but are twice the distance from the vertical face (18 m). Shots B4, B6 and B10 were detonated at roughly twice standard source depth with a centroid depth of 30.5 m as well as well removed from the free face. **Figure 3.2** shows a plan view diagram of the test bench.

Typical drilling practices at the mine produced 31 cm borehole diameters with depths of 18.3 m. All boreholes for this study are filled with 12.2 m (773 kg) of explosive and stemmed to the surface for containment. Simultaneously detonating one, four, and eight boreholes provided nominal explosive masses of 773, 3091, and 6182 kg (Stump and Zhou, 2007). These drilling practices were implemented for the free face (B1, B2 and B7) and twice burden shots (B3, B8 and B5). The difference between the two scenarios is distance from the free face (burden). Shots B6, B4 and B10, are drilled twice the centroid depth as the six other shots. **Figure 3.3** shows a side view diagram of these three containment scenarios.

Ground motion instrumentation deployed across the test bench is summarized in **Figure 3.4** and spans distances to the explosions from very proximal (35 m) to the detonations, that capture non-linear processes such as near surface spallation, to more distant stations (< 700 m) that document linear-elastic wave propagation. Spallation signatures were investigated using the

acceleration data to assess both the zone of spallation and thus the extent of nonlinear behavior. The signature time series double peaks separated by a -1 g dwell, showing the geology failing and subsequently being cast into ballistic freefall, was noted at each station. Where the signature occurred, a perimeter was set where data for the linear inversions was not used. This boundary was empirically found to be between 100 and 150 m from the borehole at the surface.

Scaled depth of burials and nominal yields are summarized in **Table 3.1**, providing an assessment of coupling relative to both the free surface and the free face in the mine. All twice depth shots are fully contained based on the 122 $kt/m^{1/3}$ criteria but only explosions with the smallest yields from the twice burden and free face are contained with respect to the free surface. The twice burden shots were originally planned to have 1, 4 and 8 boreholes, as with the twice depth and free face, but 6 of the eight boreholes from B8 collapsed. This resulted in twice burden shots (B3, B5 and B8) with respective yields of $0.77x10^3$, $1.54x10^3$ and $3.08x10^3$ kt. Twice depth (B6, B4 and B10) and free face (B1, B2 and B7) have respective yields of $0.77x10^3$, $3.08x10^3$ and $6.13x10^3$ kt.

Fracturing and cratering occurred above all twice burden and free face shots with the twice burden shots providing no relief along the free face. There was no surface fracturing or cratering from any of the twice depth shots. Significant cratering occurred and material was cast into the pit below from all three of the free face shots. Fracture size from B1 and B2 was relatively uniform, with individual rocks as large as 0.25 m visible at the surface. Shot B3 consisted of a linear configuration of 4 boreholes but created a cylindrically symmetrical rubble zone as a surface expression, roughly 20 m in diameter. This event produced a slightly larger rubble size with fragments roughly 1 m in diameter. Shot 7 which consisted of 8 boreholes in a

linear configuration, but due to its shallower depth and increased total length due to the number of boreholes, created a linear surface rubble zone bulking to as high as 2 m above the bench with some rock fragments as large at 1 m.

Instrumentation and Data

In order to capture the full wavefield from within the region of tensile failure out to linear elastic propagation, a variety of instrumentation was deployed (**Figure 3.4**) at the test site from 35 – 680 m, detailed in MacPhail et al (2018 a,b).

Theory

An explosion detonated in a homogenous medium, can be represented by a purely isotropic source. Sharpe, 1942, developed this solution in terms of rigidity and Lamé parameters. Mueller and Murphy (1971), here forward referred to as MM71, Denny and Johnson (1991), here forward referred to as DJ91 as well as others use this isotropic representation to develop refined seismic source models to include effects of source depth, yield, source medium and containment to define seismic spectrum scaling appropriate for underground chemical and nuclear explosions. These source representations do not take into account geologic layering or complex free surface effects that could add complexity to the source representation, possibly non-isotropic.

Explosion coupling to seismic waves in these models is dependent on the distance from any arbitrary boundary, in our case a free surface or free face, relative to the explosion's yield and emplacement material. A fully contained explosion is represented as fully coupled to the sold earth with no direct loss of energy to the atmosphere.

Containment is often defined by the source's scaled depth of burial, yield divided by depth to the 1/3 power. Scaled depths greater than 122 m/kt$^{1/3}$, as defined by LANL for NTS

nuclear explosions, are deemed fully contained as a result of experimental practice accompanying the testing of nuclear explosions (Olsen, C. W, 1993). This study uses the same containment definition for comparison purposes. Containments for all nine shots in this study are detailed in **Table 1** including scaled depth and minimum scaled distance to either the free surface or the free face.

Fully contained explosions can generate spall within surficial layers (Viecelli, 1973; Stump, 1985). Tensile failure due to high stress loading causing tensile failure of geologic layering above an explosion can result in a secondary cylindrical source delayed in time relative to the isotropic explosion. The upward traveling pressure wave, generated by the isotropic source, reflects off the free surface creating tensile stresses as the wave propagates down away from the surface. If large enough in amplitude, the tensile stresses can fail near-surface layers resulting in ballistic freefall for a finite time and thus creating a secondary source that is cylindrical in symmetry as a result of the free surface above the explosion (Rinehart, 1959; Chilton, et al., 1966; Eisler et al., 1966; Day et al., 1983; Stump, 1985; Patton, 1990).

Detonations at a vertical free face removes energy from the source in the direction of the free face as a result of tensile failure along this interface and will alter the moment tensor representation reducing amplitudes. Cast blasting is a mining process using this to its advantage, failing materials behind the interface, imparting both vertical and horizontal momentum to these materials allowing miners to gathering rubble created adjacent and below the bench of the explosion. Cast blasting uses a linear series of delayed detonation, casting rock horizontally into the pit below.

In order to assess containments under a range of yields and source emplacement geometries, a general second order moment tensor representation is used in this study.

Quantification of this representation based on the observational data will allow us to capture all the possible source components under the assumption of a point source relative to the longer wavelengths of the seismic data analyzed. The details of the frequency domain moment tensor inversion process are documented in MacPhail et al., 2018a. The approach used in this study is similar to other near-source seismic studies. The inversions are completed in the frequency domain and provide a complete representation of the source with six unique time functions for the second rank symmetric moment tensor (Yang et al., 2018; Yang and Bonner, 2009; Stump and Johnson, 1984; Stump, 1985).

The moment tensor can be decomposed into an isotropic and CLVD component, a combination of two double couples, where the direction of one force couple has a unit strength twice that of the other two orthogonal directions in addition to other deviatoric source components. To visualize moment tensor source estimates and aid in the interpretation of the explosion source functions, Hudson (1989) suggested the use of a set of diagrams. He proposed the use of two-dimensional graphical displays to quantify the relative amplitudes of the three principle moments. This approach provides a method of representing the probability density of the relative sizes from a given set of data. In this representation the parameter *T* characterizes the constant volume (shear) source component and *k* characterizes the proportion of volume change.

A comparative tool designed to assess source representation differences between can include spectral ratios of seismic moment tensors. Spectral ratios of the observational data yields a single source frequency difference.

$$\frac{U_{ki1}(f)}{U_{ki2}(f)} = \frac{S_1(f)\cdot G_{ki1}(f)\cdot W_i(f)\cdot R_{ki}(f)}{S_2(f)\cdot G_{ki2}(f)\cdot W_i(f)\cdot R_{ki}(f)} = \frac{S_1(f)}{S_2(f)} \qquad (1)$$

where $U_{kij}(f)$ is the data spectrum of the *k*th component (1, vertical; 2, radial; 3, transverse) at the *i*th receiver from the *j*th source, $G_{kij}(f)$ is the propagation path effect, W_i (f) is the local site effect at the receiver, $R_{ki}(f)$ is the instrument function for the *k*th component and *i*th receiver and M_{ij} is the six component moment tensor. For our moment rate tensors

$$\frac{U_{ki1}(f)\cdot G_{ki1}^{-1}(f)}{U_{ki2}(f)\cdot G_{ki2}^{-1}(f)} = \frac{M_{ij1}(f)}{M_{ij2}(f)} \qquad (2)$$

where the variables are the same as above with the exception of $G_{ki1}^{-1}(f)$, the inverted Green's functions.

Spectral ratios from the actual data as documented in Stump, 2007, will be compared to spectral ratios of the Moment Rate Isotropic and Mzz components. Spectral ratios remove the propagation path effects and gives us a better look at the source. We look at frequency dependent amplitudes to better understand how the moment rate components differ from the actual data in an attempt to assess coupling and differences in subsequent radiated energy. These differences can contribute to explosion discrimination.

Velocity Model

A precise velocity model is essential to the accurate estimation of the moment tensor. The less accurate the Green's functions, the greater the trade-off with the estimated moment tensor, impacting its uniqueness as a source representation. MacPhail et al., 2018a investigated the sensitivity of moment tensor estimates at this site to changes in the assumed source depth and shear wave model when the P-wave velocity is well constrained. These constraints are characteristic of this dataset. A comprehensive P-wave refraction study was conducted within the mine to constrain the source emplacement parameters and geologic propagation path. **Figure 3.5** summarizes the refraction study and results therein with the compiled model for V_p, V_s, ρ

(density), and attenuation coefficients (Q_α and Q_β). The shear wave attenuation model procedure, described in Bonner et al., 2005, evaluates surface waves recorded by the refraction study and a regional Texan deployment. P-wave and S-wave constraints to the velocity model are discussed in MacPhail et al 2018 b.

The reflectivity approach (G. Müller, 1985) is used to calculate Green's functions for different source depths and velocity models in order to capture effects of all spherical waves including body and surface waves which are characteristic of these shallow sources. In MacPhail et al., 2018 a, CLVD and explosion components of the Green's functions are analyzed in terms of their sensitivity to a range of assumed source depths shear wave models. Poisson's ratios ranging between 0.15 and 0.4, for an assumed V_p, were investigated, increasing and decreasing, respectively, from the empirical shear wave velocity of the layered model. Shear wave velocity models for the range of ν values were used to calculate a range of Green's functions and the various phases from each of the calculated models were analyzed. As a result of this analysis, MacPhail et al., 2018 b, used the actual source depths of the deepest three shots with the velocity model for ν=0.25. In this study, data from the nine shots encompass two depths resulting in two different models, both with the same velocities (ν=0.25) and layering. The model is the one best constrained by the site investigation from MacPhail et al., 2018 a, but could be subject to the assumed source depth variability associated with secondary sources. **Table 3.2** describes the uppermost parameterized layers. Shots for this study are located in the second and third layer.

Forward models, preliminary to the actual inversions, were calculated to better understand the expected phases. **Figure 3.6** displays the vertical component synthetic record section for shot B4. These synthetics use a Mueller-Murphy isotropic source model with parameters relevant to the emplacement medium within the mine at the detonation point. Nine

source models were calculated, emulating all nine explosions and their emplacements parameters and depths. These nine source models were convolved with the Green's functions calculated for the mine, yielding synthetic observations. As with previous studies (MacPhail et al, 2018 a, b), these synthetics are dominated by body waves and Rayleigh waves, the latter evident by their retrograde elliptical particle motion.

Inversions

As noted in the introduction, source inversions are completed for all shots from the SPE and provide a unique opportunity to assess the three different yield and containment scenarios. The frequency domain inversion procedure is the same as that used in MacPhail et al. (2018 a,b). As with these previous two studies, predicted seismograms using the Green's functions and the estimated moment tensors were compared to the actual data and their similarities quantified. These comparisons are good and similar to those of the other studies.

Due to the multitude of shots, confinements and yields, a naming convention is introduced for clarification in the subsequent discussion. The free face shots, B1, B2 and B7, with respective yields of $0.77x10^{-3}$ kt, $3.08x10^{-3}$ kt and $6.16x10^{-3}$ kt, will hence fourth be referred to as B1FF077, B2FF308 and B7FF616. The twice burden shots, B3, B5 and B8, with respective yields of $0.77x10^{-3}$ kt, $3.08x10^{-3}$ kt and $1.54x10^{-3}$ kt, will hence fourth be referred to as B3TB077, B5TB308 and B8TB154. The twice depth shots, B6, B4 and B10, with respective yields of $0.77x10^{-3}$ kt, $3.08x10^{-3}$ kt and $6.16x10^{-3}$ kt, will hence fourth be referred to as B6TD077, B4TD308 and B10TD616. With the collapse of B8TB154 and an anomalously high moment of shot B2FF308 the only constant yield scenario that spans three shots is that of the smallest shot group, with B1FF077, B3TB077 and B6TD077. For this reason the analysis is described first for the previously mentioned three, then move to B2FF077, B5TB077 and

B4TD077 and then move up in yield to the explosions with the largest yields (B7FF616 and B10TD616).

Cross-correlations between the fitted and observed seismograms were calculated to determine how well the estimated moment tensors replicated the data. **Figure 3.7** displays unfiltered record sections of the fits (grey) and actual data (black) for shots B1FF077 and B3TB077. These shots are the smallest of the free face and twice burden shots and due to their lower containment, might have a lower cross-correlation values as a result of nonlinear interactions with the free surfaces compared to the well confined twice depth explosions. With limited containment, energy escape at the free face is expected to impact the estimated moment tensors, and in doing so, alter the fits due to possibly unmodeled secondary source effects. The unfiltered fits do replicate the observations, with a crosscorrelation value of 0.58 for B1FF077and 0.64 for B3TB077. At low frequency, where the surface waves dominate, the fits improve. From MacPhail, 2018 b, shot B6TD077, with the same yield as B1FF077 and B3TB077, had calculated cross-correlation value of 0.7. In this analysis the fits to the data degrade above 20 Hz. This mis-fit was one of the motivations for identifying the bandwidth of interest. This bandwidth was also used in MacPhail (2018 a, b). The lower end of the bandwidth of interest ~2 Hz is where the signal spectrum diverged from the noise spectrum.

The full moment tensor (denoted as M_{mn} , where m and n are any x, y or z components) time series as well as the decomposed isotropic (denoted as M_{tr}) and deviatoric (denoted as m_{mn}, where m and n is any x, y or z component) component, after subtracting the isotropic moment tensor from the three diagonal elements of the full moment tensor, are analyzed. Isotropic, deviatoric, M_{zz} and relative amplitudes of M_{xx} and M_{yy} with respect to M_{zz} are compared to

explore the source representation strength relative to explosion yield and containment (**Table 3.3** and **Table 3.4)**.

Moment tensor time series from shots with different confinements but with the same yields are first compared. The smallest shots will be compared with each other, followed by the medium shots and finally the largest shots. B1FF077 is detonated 9 m from a vertical face (burden). B3TB077, with the same depth and yield, is detonated at 18 m of burden, opposite the bench. **Figure 3.8 a** and **3.8 b** display the six components of B1FF077 and B3TB077full moment tensor time series,respectively. The relative difference identified between B1FF077 and B3TB077 are reproduced for B1FF077and B6TD077, as well. Evaluating the time series for all six components of the moment tensors for each explosion, the maximum amplitude ratios of M_{zz}/M_{xx} and M_{zz}/M_{yy} for B1FF077, B3TB077and B6TD077are 1.8, 1.8 and 1.6 respectively, demonstrating the importance of the Linear Vector Dipole (LVD) component of the estimated source despite the differences in confinement. B2FF308, B4TD308 and B5TB308 have different containments, all with respect to the free surface and a free face. They have the same yield and are the medium sized shots in the experiment. All three shots show an LVD component with the M_{zz} being, respectively, 2.3, 1.7 and 3.1 times the maximum amplitude as the M_{xx} and M_{yy}. B10TD616 and B7FF616 have different containments, both with respect to the free surface and a free face. They have the same yield and are the largest shots in the experiment. Both shots show an LVD component with the M_{zz} being 2.2 and 2.0 times the maximum amplitude as the M_{xx} and M_{yy}. The isotropic components for all shots are less than their respective M_{zz} components, with M_{tr}/M_{zz} ratios ranging from 0.5-0.75. These comparisons suggest that the dominant effect of the LVD source from all the experiments is consistent across yields and containment. Since

the free face events are typical of mining explosions these results are consistent with the utilization of mining explosions as surrogates for some aspects of seismic radiation from contained explosions. Moment tensor time series maximum amplitudes illustrate that for a given yield, higher containment produces higher maximum amplitudes. All shots produce significant LVD, with the ratios of maximum M_{zz} to averaged maximum M_{xx} and M_{yy} ranging from 1.7 to 3.1 (**Table 3.3**).

Comparing the shots with the same confinements but with different yields, as yield increases so does the M_{zz} to M_{xx} and M_{yy} ratio. The one exception is for shot B2FF308, having a larger ratio than B7FF616. The trend does follow with the larger the peak amplitudes the higher the ratio of M_{zz} to M_{xx} and M_{yy}. For a given confinement, the higher the peak amplitudes, the higher the ratio of M_{zz} to its respective $M_{xx \text{ and }} M_{yy}$. Twice burden, free face then twice depth have respectively decreasing M_{zz} ratios, so it cannot be said that decreasing containment show decreasing M_{zz} ratios.

The full moment tensor in the frequency domain is used to estimate moment, corner frequency and high frequency decay. **Table 3.5** contains the long-period level and corner frequencies for all nine shots. The spectrums, from 1-10 Hz, were windowed and resampled evenly in the log domain to calculate the long period levels (LPL). The corner frequencies were estimated from the spectra after the LPL and slope of the high frequency decays were calculated, taking the value 3 dB below the LPL along the high frequency decay line as the corner frequency. Shots with the same yield but different containments are compared in the frequency domain.

Shot B1FF077 and B3TB077 have the same yield, but B3TB077 has a factor of two increase in M_{zz} isotropic amplitude. B6TD077 M_{zz} has a long period level three times that of B3TB077, within our bandwidth of interest, and almost six time that of B1FF077 quantifying the increase in coupling from the free face to the twice depth of burial. B2FF308 and B4TD308 have similar M_{zz} and isotropic long period levels and spectral shapes but B5 has half the long period levels. B10TD618 has 3.8 times a higher moment than B7FF616. B7FF616 is deficient fivefold in frequencies in the 1-3 Hz band where B10 doubles in that band. Thus, except for B2, the effect of coupling and proximity to a vertical or horizontal free face significantly effect absolute moment.

Shots with the same confinements but different yields are explored to better understand yield scaling under varying confinement. Shots B6TD077 B4TD308 and B10TD616 have respectively increasing yields, with B4/B6, B10/B4, and B10/B6 having ratios of, respectively, 2.6, 2.0 and 5.1. All three shots have fivefold increase in the 1-5 Hz band as compared to the 5-10 Hz band. B6, B4 and B10 have corner frequencies that scale with yield and moment, having frequencies of 10.6, 10.1 and 8.5. Twice burden shots B3TB077, B8TB154 and B5TB308 are all deficient in the 1-5 Hz band by an order of magnitude compared with the 5-10 Hz band. The long period levels do not scale with yield, having values of 4.2, 3.5 and 11.5×10^{11}, respectively. The corner frequencies to not scale with yield either. Free face shots B1FF077, B2FF308 and B7FF616 have spectral shapes similar to that of the twice burden shots, with the order of magnitude decrease in the 1-5 Hz band, with the exception of B2FF308. B2 has a moment and spectral shape closely resembling the fully contained twice depth shots with a moment double that of the larger B7FF616.

In summary, the moment rate M_{zz} and isotropic spectra have similar shapes but the M_{zz} long period level ranges from 1.5 to 2 times that of its isotropic counterpart for all confinement scenarios. In the frequency domain, the more fully contained shots have greater moments, on average a 50% increase from free face to twice burden and another 50% increase from twice burden to twice depth, with the exception of the anomalously high B2FF308 with respect to its containment free face counterparts. Corner frequencies are much less affected.

Moment and Yield Scaling

Explosions are theoretically isotropic. Because of this, we decompose the full moment tensor into its isotropic and deviatoric components as well as look at the full moment tensor. The M_{zz} component is evaluated to help understand secondary sources that develop from interactions with the free surface. We use the isotropic component to compare to explosion models from other authors as a comparison.

To better understand containment effects and scaling relations, the M_{tr} and M_{zz} component moment rate spectrum for all shots, from D.C. to the Nyquist (125 Hz) are compared. **Table 3.5** describes the moments (LPL) for all nine shots. Comparisons between yields and between containment scenarios are explored to better understand how containment and yield manifests itself in the frequency domain. **Figure 3.9** displays spectra from B1, B3 and B6. These are the shots with the smallest yields ($0.77x10^{-3}$ kt) detonated in the three different containment scenarios. **Figure 3.10** and **Figure 3.11** display the same containment, free face and twice burden, respectively, but with differing yields.

For the multiple containment scenarios spectra (**Figure 3.9**), as expected, the twice depth shot (B6) has the highest amplitudes for our band of interest (1-20 Hz). Roughly an order of

magnitude from 1–3 Hz, approximately equal from 3-8 Hz and 10-20% higher from 8-20 Hz. The twice burden and free face shots have a similar spectral shape but B3 is roughly 10-20% greater in amplitude from 1-10 Hz and similar from 10-20 Hz. Higher frequencies, above our bandwidth of interest, show no clear trends.

For the free face shots with varying yields (**Figure 10**), B1 and B7 have a similar spectral shape with just a static offset of a factor of 10 greater for B7. The yield difference for these two shots is a factor of 8. B2 despite have a yield factor of 14.9 relative to B1 has an anomalously high spectral level below 8 Hz, even greater than B7.

Twice burden spectra (**Figure 3.11**) scale with yield from 8-15 Hz. Below 8 Hz and above 15 Hz, there is no scaling trend. All three spectra have the same general shape with the characteristic 4–20 Hz lobe.

All nine shots, regardless of yield or containment scenario, display a hump, or lobe, from roughly 4 – 17 Hz, depending upon the shot. Amplitudes within this band are quite consistent and smoothly varying. Amplitudes below this frequency band are more scattered and less well behaved. Many of the spectra also demonstrate a dip in amplitude below this lobe at low frequency. These results are consistent with some aspects of spall models where conservation of momentum results in a peaked spectrum in the band consistent with spall duration and then decreasing at long periods as a result of conservation of momentum (Stump, 1985). A complex source model that includes both spallation as represented by a LVD and an explosion that is purely isotropic will then be dominated by the isotropic component at the longest periods. The increasingly peaked nature of the source spectra with diminished confinement also suggests the isotropic part of the source may be more strongly impacted by confinement. In summary, as containment increases the source strength increases and similarly as yield increases the moment

increases with the nature of the spectra becoming increasingly peaked as confinement is decreased.

Source Interpretation - Isotropic Explosion Source Model Comparisons

The moment tensor representation is an energy radiation description. The use of physical source models that match our empirical results provide the ability to validate these models, thus, empirically assessing the ability of these models to extrapolate to other geological and yield environments. We compare four models in this study, Mueller and Murphy, 1971 (MM71), Denny and Johnson, 1991 (DJ91) and Patton's revised Mueller, Murphy, 2012 (MMP12) and Walter and Ford, 2018 (WF18). We use these four models to assess and contrast our moment tensor spectra for granite in order to highlight the effects of containment in contrast to yield effects. For comparison purposes, a factor of two difference in yield from chemical to nuclear explosions is not used in this study as discussed in MacPhail et al. (2018 a and b).

MM71 developed spectral models for various emplacement mediums for sources at different depths and source yields for nuclear explosions. Building on Sharpe's, 1942, analytical elastic response, a new pressure function applied after the elastic radius was developed. This representation was both constrained by and found consistent with seismic free-field data from many nuclear explosions. The MM71 model uses cavity radius scaling but differs in that the initial peak shock pressure decays at fixed rate defined by alpha until it reaches a steady state pressure. The DJ91 model analyzes nuclear and chemical explosions and uses cavity elastic radius scaling. DJ91 assumes the pressure function is a step function with peak shock pressure equaling the steady state pressure. As noted earlier, a specific depth of burial effect is included. When analyzing source spectra, Denny and Johnson (1991) explored corner frequency, roll-off, overshoot and long period level to define models to fit moment tensor spectra. Patton, in

correspondence with Murphy, revised the MM71 scaling model for granite. Equivalent formulations of MM71 and Stevens and Day, 1985, for cavity scaling relationships, predicted different static pressure values. A leading coefficient reduction of 9.2%, from 16.3 to 14.8, effected the long period level.

Yang, 2016, analyzed moment tensor spectra from four chemical explosions conducted at the Nevada National Experiment Site (NNES). The corner frequencies and long period levels were of particular interest. He found that they could not be fit by current source models so the explosions were fit with a parameterized model by regressing observed values against source depth and yield. The values were calculated from corner frequencies and measured source moments. Rougier and Patton (2015) explore free field data from the NTS.

Walter and Ford (2018), here forward referred to as WF18, recently created a new P-wave explosion spectral model and started by following Sharpe (1942) formulation of defining an elastic radius and pressure function acting at that radius to create the far-field P-wave explosion seismic spectrum. They defined the corner frequency in terms of V_p over the elastic radius in contrast to DJ91 who use V_s instead. This shifts the corner frequency to a higher value. WF18 use half the elastic radius as that of DJ91's source radius. WF18 determine the long period explosion moment using DJ91's moment regression formula.

The moment rate spectra from the M_{zz} and the isotropic component were calculated and compared to existing models (MM71, DJ91, MMP12 and the WF18) for granite. Spectra from all nine shot are not displayed. For display purposes, **Figure 3.12** includes shots B1, B3 and B6 with the models overlain with the spectra. This provides a comparison between a free face shot (B1), a twice burden shot (B3) and a fully contained twice depth shot (B6) all at the same yield.

The fully contained shots (B6, B4 and B10) are best fit by the four source models analyzed in this study. Our empirical isotropic spectra's corner frequencies lie within the models ranges and ratios of empirical moments to model estimates are 0.87, 0.80 and 1.03, respectively (**Table 3.5**). As containment decreases the fits of the models to moments and corner frequencies degrade illustrating the coupling differences as a function of frequency for these models relative to the models. Averages of moment to model ratios for the twice depth, twice burden and free face are 0.88, 0.30 and 0.23, respectively quantifying the strong effect of coupling that is not included in the models. This comparison neglects shot B2's anomalously high moment. With the exception of B2, all corner frequencies, from the free face and twice burden, are higher than model predictions (**Table 3.5**), while the moments are as much as a factor of 20 lower. This comparison is strongly impacted by the decrease in moment amplitude in the 1 to 4 Hz band. B2 does not have this characteristic decrease and appears as an anomaly with respect to the other explosions, possibly related to either the explosive loads to the boreholes or the manner in which the explosives were detonated. Unfortunately, these experiments made no direct borehole measurements of explosive performance, which would have provided additional information to address shot B2 anomalies.

As with Yang (2016) and Rougier and Patton (2015), for the shots with reduced containment, the models do not fit the data well. Future work could include parameterizing the data and creating a model based up them as was the case with Yang (2016).

Denny and Johnson, 1991, examined many chemical and nuclear explosions from a variety of sources. Our explosions sit in a data gap between the smaller chemical explosion and larger nuclear explosions. **Figure 3.13** is an augmented plot from Denny and Johnson, 1991, comparing moments from all of our explosions including the three different containment

scenarios. Our explosions span an order of magnitude, in yield space, between the smaller, chemical, explosions and the larger, nuclear explosions. The fully contained shots (B6, B4 and B10) are underestimated by the trend line but follow the line consistent with other explosions. All other shots plot near the trend line.

Source Interpretation – Hudson Diagrams

Hudson (1989) diagrams are used to help visualize the data in a more intuitive manner quantifying how the complete moment tensor representation changes as a function of frequency, yield and containment. Depending upon the relative ratios of the individual moment tensor components, points plot in different areas of the diagram manifesting themselves as different source types. We use a frequency domain inversion and so the source representation is plotted as a function of frequency in order to identify any frequency dependent changes in representation. For our study, the band of interest is from 1-20 Hz. Based upon the bandwidth time product (Harris, 1991), a 6 Hz smoothing window is used that mitigates differences in phase between moment tensor components, minimizing scatter.

Figure 14 displays free face shot B7 from D.C. to 20 Hz. The Hudson diagram for B7 is in general agreement with the diagrams for all nine shots in that the source representation becomes more explosion like as frequency increases. At long period levels, the points approach the CLVD part of the diagram. Above 10 Hz, the source representation begins to move closer to the explosion part of the figure. As a result of this general trend, we compare the location of the 20 Hz point on the Hudson diagram for all shots with the *K* value which measures the degree of isotropic component of the source. *K* values are subsequently compared among all nine explosions as a function of yield and containment. **Figure 3.15** displays all nine shots from left to right with increasing yield and containment. *K* value increases as containment and yield

increase. Shot B5 is anomalously low, possibly due to damage in the source region. **Figure 3.16** plots *K* versus yield again illustrating that *K* increases with yield, neglecting B5.

This frequency dependent source representations impact source identification using different seismic phases. Body waves have a higher frequency content where our empirical source representations produce a larger isotropic component. Surface waves, in contrast, have longer periods where our empirical source representations are more CLVD like. As yield and containment increase so does the explosion component of the source representation in most cases. Again this suggests that using mining explosions as surrogates for contained, single-fired explosions may be dependent upon frequency content and wave type.

Spectral Ratios

Spectral ratios of the moment rate tensor spectra are compared to the spectral ratios of the observations calculated by Zhou and Stump (2007). Typical empirical spectral ratios remove propagation effects when the sources are sufficiently close. Zhou and Stump, 2007, compute the spectral ratios of ground motion data acquired from the SPE to investigate empirical scaling relations for different explosions with different confinements and this data is compared to spectral ratios of our moment rate spectra. An alternate approach to relative source comparisons is to directly estimate the spectral ratios of the estimated moment tensors. This alternate relative measure offers the opportunity to assess how the source representations changes as a function of frequency when comparing sources of different yield or confinement, information that is lost in the more common spectral ratio approach. The common spectral ratio approach offers a statistical advantage as multiple spectral ratios can be smoothed or averaged in addition to frequency domain smoothing. In this new approach only spectral smoothing can be applied, which intrinsically leads to higher variances.

Figure 3.17 displays the M_{zz} and M_{tr} moment rate spectral ratios for the free face shots with the R, T and Z component ground motion spectral ratios from Zhou and Stump (2007). Zhou and Stump (2007) used 6 Hz smoothing window, giving a BT product of >100 as suggested in Harris (1991). For comparison purposes, this same window was used for this figure. Other smoothing windows were explored, ranging from 0.5 – 6 Hz but 6 Hz was used to match that of the observations. Our bandwidth of interest is from 2-20 Hz. The general shape is preserved for the moment rate spectral ratios, matching that of the data, but with greater negative and positive swings. A peak at 10 Hz and 20 Hz is evident in both the observational and moment rate spectral ratios. The anomalously high moment of B2, greater than that of B7, causes a deviation in the spectral ratios, mostly in the 2-4 Hz band. The greater moment for B2 relative to B7 could be due to source material destruction affecting B7's long period level. The M_{zz}/M_{iso} scales the same as the $M_{zz}/Avg(m_{xx},m_{yy})$

Conclusions

Moment tensor inversions were completed using explosion data from the SPE experiment within a copper mine in Arizona with the goal of assessing how containment, yield and the free surface affect the resulting source representation in granite at near source ranges. The full and decomposed moment tensor components in time and frequency are compared in order to assess different physical contributions to the source representation. Our explosion data is compared to prevailing models as well as other explosions as documented by Denny and Johnson, 1991. The frequency domain moment rate tensors are used to create Hudson diagrams to further analyze how the source representation changes as a function of frequency and possibly impacts explosion discrimination based on different seismic phases.

Cross-correlation of fitted seismograms to the actual data documents the ability of the inversion to reproduce the observations and resolve the moment tensor using an accurate geological model with the data. Typical condition numbers in the inversions are about 50, adequate for resolving the six moment tensor components, as seen from analysis in MacPhail (2018 a). The synthetics based on the empirical moment tensors match the data well at all stations and distances for all shots. As expected, higher frequency waveforms fit less well than the lower frequency waveforms. Correlation values for unfiltered data ranged from 0.58 to 0.73 while band pass filtering 10-20Hz provided the best cross correlation values of around 0.9.

Maximum amplitudes from moment rate time series are compared to explore the source representation strength relative to explosion yield and containment. The isotropic components for all shots are less than their respective M_{zz} components, with M_{zz}/M_{tr} ratios ranging from 1.3-2. When looking at the ratios of M_{zz}/M_{tr} and comparing them to Mzz/avg(M_{xx}, M_{yy}), they show the same trends, indicating that that the isotropic and M_{zz} are effectively equally. As with the full moment tensor components, all deviatoric time series show components of LVD with M_{zz} /[avg(M_{xx} and M_{yy})] ratios ranging from 1.6 to 2.6. Our analysis shows that for a given yield, higher containments generally have higher maximum amplitudes. Similarly, all explosions irrespective of containment have a large LVD component.

In the frequency domain, the full moment tensor spectra have similar shapes except at long periods, where decreasing confinement results in decreasing long period levels and more peaked spectra at intermediate frequencies. The more fully contained shots as a result have greater moments at long period. On average there is a 50% increase in the twice burden shot

long period moment compared to that of the similar yield free face explosion. There is another approximate 50% increase in long period moment for the twice depth shots of the same yield.

All nine shots, regardless of yield or containment scenario, display a peaked source spectrum from roughly 4 – 17 Hz, with the degree of the peak relative to the long periods increasing with decreasing containment. Amplitudes within this band are smoother than those above and below the band. Because of the differences from 1-20 Hz, this band was broken down into three parts (1-3 Hz, 3-8 Hz and 8-20 Hz) and quantified. In general, for all the areas of the 1-20 Hz band, as containment increases, amplitude increases and, as expected, as yield increases, moment increases.

The moment rate spectra from the M_{zz} and the isotropic component were calculated and compared to existing source models (MM71, DJ91, MMP12 and the WF18 model for granite). The source parameters for the site geology and our explosions were input and compared to the actual source spectra. The high frequency decay, corner frequency and long period levels were examined and compared to the models. The fully contained shots (B6, B4 and B10) are best fit by the models. Our spectra's corner frequencies lie within these model bounds. Shot B6, B4 and B10 have moments 0.81, 1.04 and 0.86 that of their respective MMP12 models within the 1-10 Hz band. As containment decreases, model fits to moment and corner frequency degrade partially due to the increased peaking in the mid frequency band. With the exception of B2, all corner frequencies, from the free face and twice burden, are higher than the models predict and the moments are much lower, as much as a factor of 20. This comes about from a decrease in moment amplitude in the 1-4 Hz frequency band. B2 does not have this characteristic decrease in amplitude. Generally, the shots with decreased containment are not well fit by the models.

Denny and Johnson, 1991, examined many chemical and nuclear explosions from several authors and the isotropic moments and yields of our explosions are compared to them. Our explosions are, although consistently higher than their scaling relation, consistent with other explosions along the yield trend line. The model predictions discussed above from MM71, DJ91 MMP12 and WF18 plot above ours along the trend line.

Hudson (1989) diagrams were used to help visualize the source representation on these diagrams as a function of frequency from D.C. to 20 Hz. At long period levels, the points plot near a CLVD source. After about 10 Hz, the source representation moves towards the pure explosion source becoming most explosion like near 20 Hz. We quantify the 20 Hz mark for all shots and plot the K value that quantifies the explosion vs yield and containment. The K value increases with containment and yield. All nine shots have an increase in the CLVD component below 10 Hz and move toward higher K values as frequency increases to 20 Hz. This characteristic has implications for using quarry blasts for discrimination as it suggests that the overall source representation isn't strongly affected by containment, except for the decrease in long period spectral level.

Spectral ratios were calculated from moment rate spectra and compared to spectral ratios of the observations, yielding similar spectral trends. A peak at 10 Hz and 20 Hz is evident in both the observational and moment rate spectral ratios. The anomalously high moment from B2 causes a deviation in the spectral ratios, mostly in the 2-4 Hz band.

TABLES

Table 3.1 – Depth, containment and yield for nine explosions in this study.

Shots	**Yield (kt)**	**Centroid depth (m)**	**Scaled distance from closest free face ($m/kt^{1/3}$)**	**Scaled depth ($m/kt^{1/3}$)**	**Containment**
B1	$0.77x10^{-3}$	12.2	98	133	Free face
B2	$3.08x10^{-3}$	12.2	61	84	Free face
B7	$6.17x10^{-3}$	12.2	49	67	Free face
B6	$0.77x10^{-3}$	30.5	436	333	Twice Depth
B4	$3.08x10^{-3}$	30.5	274	210	Twice Depth
B10	$6.17x10^{-3}$	30.5	218	166	Twice Depth
B3	$0.77x10^{-3}$	12.2	196	133	Twice Burden
B5	$3.08x10^{-3}$	12.2	124	84	Twice Burden
B8	$1.54x10^{-3}$	12.2	156	106	Twice Burden

Table 3.2 – Uppermost layers of the velocity model used for Green's functions in the inversions.

Layer top (km)	**V_p (km/s)**	**V_s (km/s)**	**Poisson values**	**ρ (g/cm^3)**	Q_α	Q_β
0.0000	0.61	0.35	0.25	2.0	12.0	5.0
0.0005	3.05	1.76	0.25	2.1	20.0	10.0
0.0023	3.72	2.15	0.25	2.2	50.0	25.0
0.1500	4.49	2.59	0.25	2.3	80.0	40.0
0.5500	4.92	2.84	0.25	2.4	100.0	50.0
0.9500	4.97	2.87	0.25	2.6	200.0	100.0

Table 3.3 – Full moment rate maximum time series amplitudes (all x10^{13} N*m/s)

Shot	**# of boreholes**	**M_{xx}**	**M_{xy}**	**M_{xz}**	**M_{yy}**	**M_{yz}**	**M_{zz}**	**Mzz/ avg(M_{xx}, M_{yy})**
B1	1	0.680	0.142	0.454	0.645	0.165	1.19	1.80
B2*	4	5.27	1.24	6.71	2.96	3.66	9.61	2.34
B7	8	5.66	1.25	2.28	4.79	3.73	1.04	1.99
B3	1	1.11	0.233	0.547	0.968	0.396	1.87	1.80
B8	2	1.03	0.398	0.790	0.926	0.634	2.55	2.61
B5	4	1.97	0.827	1.91	2.05	1.65	6.29	3.13
B6	1	1.09	0.298	0.823	1.27	0.862	1.90	1.61
B4	4	4.26	1.02	3.28	4.09	3.15	7.15	1.71
B10	8	6.02	1.81	5.61	7.65	5.96	15.1	2.21

Table 3.4 – Decomposed moment rate maximum time series amplitudes (all x1013 N*m/s)

Shot	**# of boreholes**	M_{tr}	$\mathbf{m_{xx}}$	$\mathbf{m_{xy}}$	$\mathbf{m_{xz}}$	$\mathbf{m_{yy}}$	$\mathbf{m_{yz}}$	$\mathbf{m_{zz}}$
B1	1	0.73	0.34	0.14	0.45	0.30	0.17	0.56
B2	4	4.55	2.50	1.24	6.71	2.46	3.66	5.17
B7	8	5.99	2.98	1.25	2.28	3.14	3.73	5.45
B3	1	1.17	0.46	0.23	0.55	0.57	0.40	1.02
B8	2	1.32	0.64	0.40	0.79	0.68	0.63	1.41
B5	4	3.19	1.08	0.83	1.91	2.20	1.65	3.96
B6	1	1.39	0.75	0.30	0.82	0.57	0.86	1.04
B4	4	4.69	1.31	1.02	3.28	1.88	3.15	4.15
B10	8	9.19	4.89	1.81	5.61	4.05	5.96	8.94

Table 3.5 – Isotropic component long period level and corner frequencies for all shots in this experiment.

Shot	**Isotropic LPL (N*m)**	**MM71 LPL (N*m)**	**DJ91 LPL (N*m)**	**MMP12 LPL (N*m)**
B1	0.21 $x10^{12}$	1.34 $x10^{12}$	1.67 $x10^{12}$	1.00 $x10^{12}$
B2	3.18 $x10^{12}$	4.46 $x10^{12}$	6.66 $x10^{12}$	3.34 $x10^{12}$
B3	0.43 $x10^{12}$	1.34 $x10^{12}$	1.67 $x10^{12}$	1.00 $x10^{12}$
B4	3.10 $x10^{12}$	5.17 $x10^{12}$	4.72 $x10^{12}$	3.87 $x10^{12}$
B5	1.17 $x10^{12}$	4.46 $x10^{12}$	6.66 $x10^{12}$	3.34 $x10^{12}$
B6	1.20 $x10^{12}$	1.55 $x10^{12}$	1.18 $x10^{12}$	1.16 $x10^{12}$
B7	1.58 $x10^{12}$	8.16 $x10^{12}$	13.32 $x10^{12}$	6.11 $x10^{12}$
B8	0.36 $x10^{12}$	3.55 $x10^{12}$	4.08 $x10^{12}$	2.66 $x10^{12}$
B10	6.12 $x10^{12}$	9.44 $x10^{12}$	9.45 $x10^{12}$	7.07 $x10^{12}$
	Isotropic f_c (Hz)	**MM71 f_c (Hz)**	**DJ91 f_c (Hz)**	**MMP12 f_c (Hz)**
B1	14.8	8.9	5.8	10.2
B2	4.5	6.1	3.7	7.1
B3	10.4	8.9	5.8	10.2
B4	10.1	8.6	5.3	9.9
B5	9.9	6.1	3.7	7.1
B6	10.6	12.5	8.3	14.4
B7	13.8	5.1	2.9	5.9
B8	17.1	7.5	4.5	8.7
B10	8.5	7.1	4.2	8.2

FIGURES

Figure 3.1 – Morenci Copper mine is located in southeastern Arizona along the New Mexico border, shown as the large star.

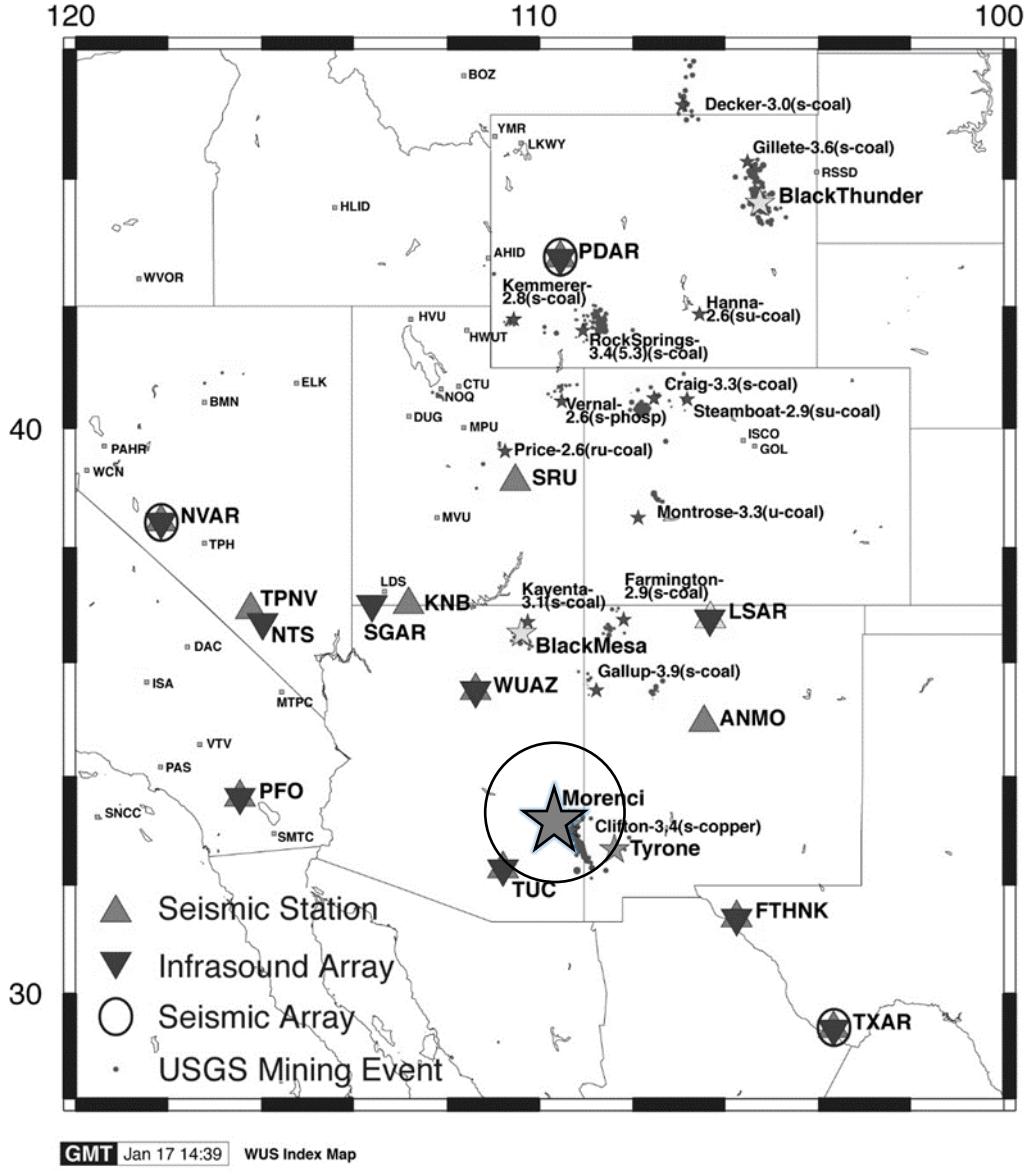

Figure 3.2 – Plan view of the test bench with explosion borehole positions, demonstrating borehole geometry

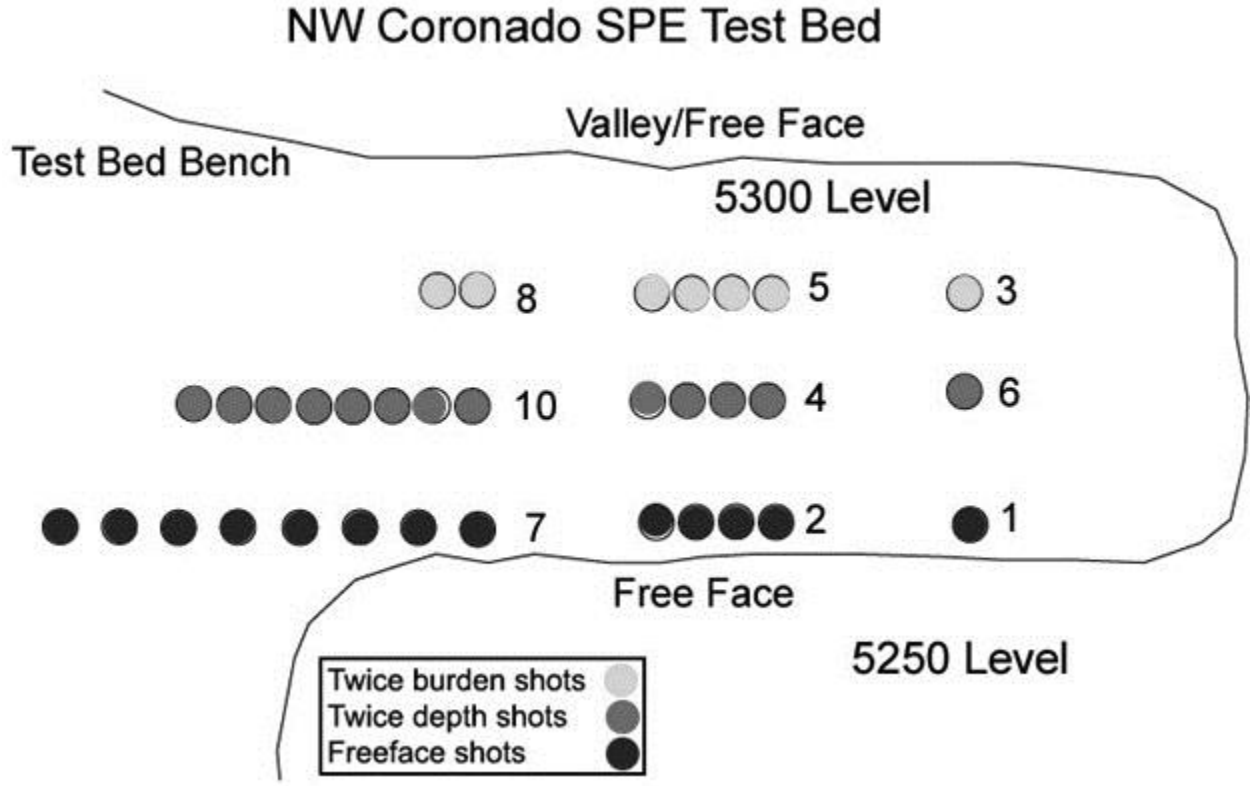

Figure 3.3 – Side view diagram of test bench geometry. Three containment scenarios exist: (1) twice depth; (2) twice burden; and (3) free face (normal burden).

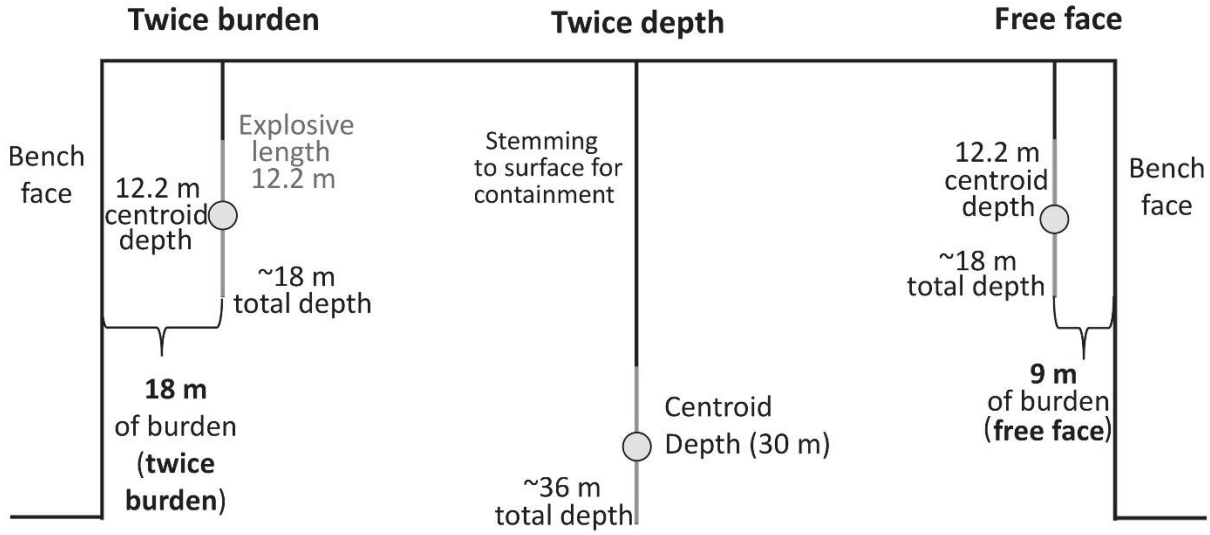

Figure 3.4 – Map of near-field instrumentation from 35 m to ~700 m. Dark grey stars are hi-g accelerometers, light grey stars are low- g accelerometers and stars with dots in their centers are velocity transducers.

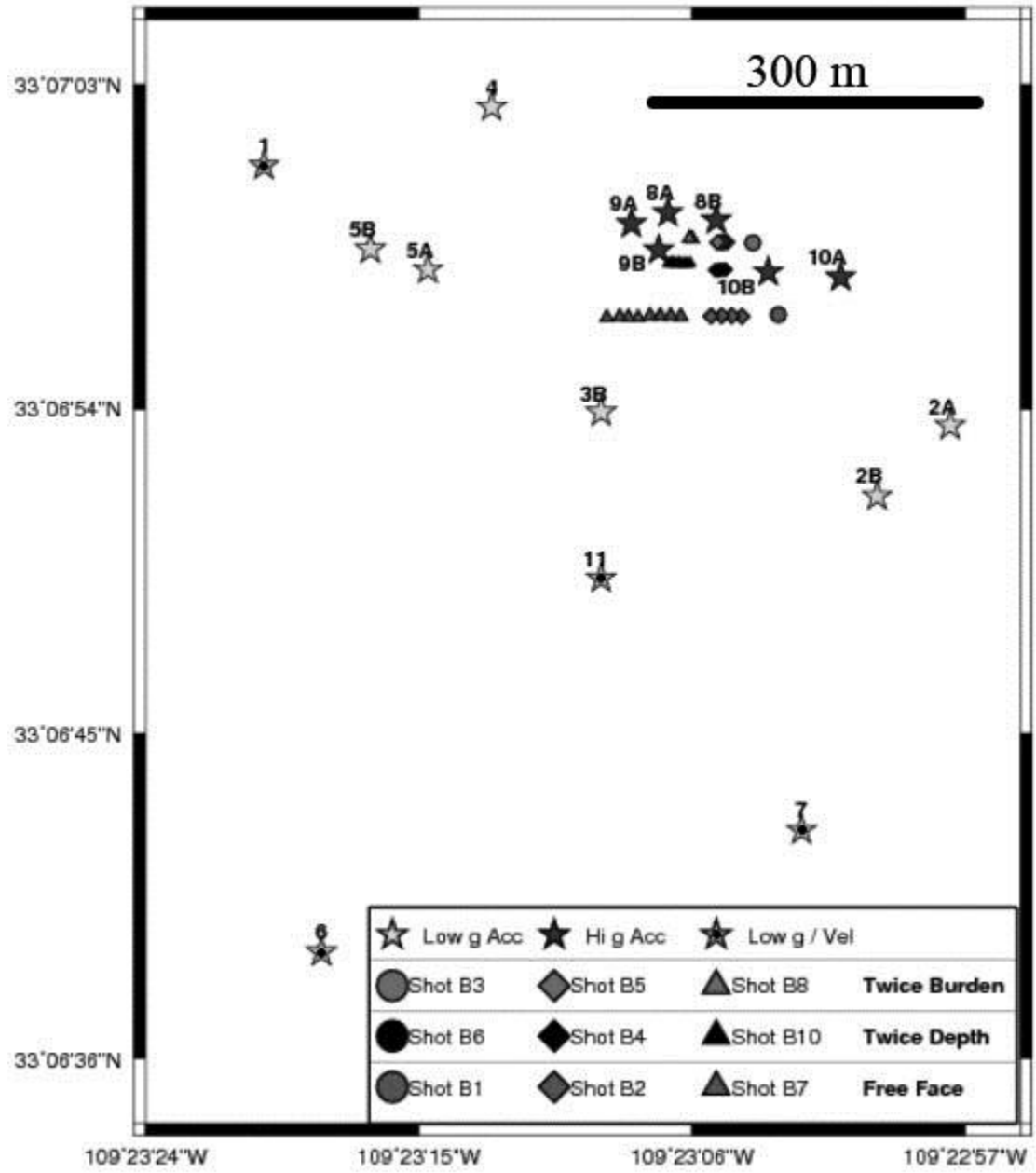

Figure **3.5** – Refraction study results with the compiled model for Vp, Vs, ρ (density), and attenuation (Qα and Qβ)

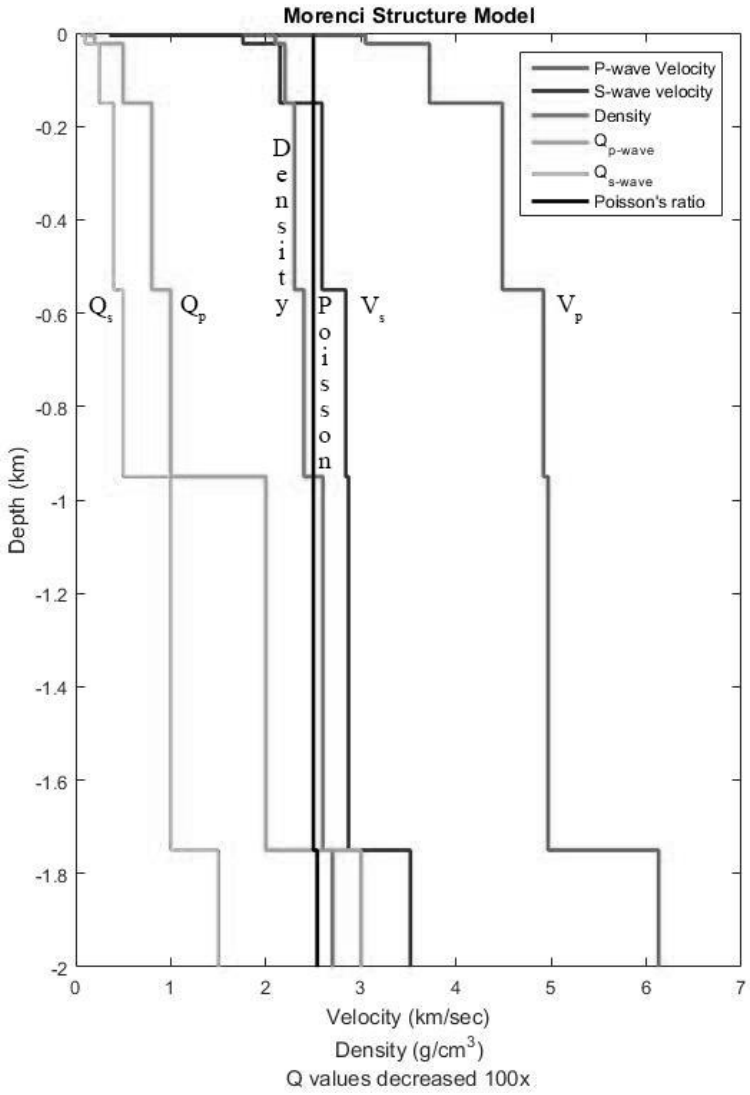

Figure 3.6 – Forward synthetic record section, scaled to largest amplitude, using convolution of Mueller-Murphy source function (calculated with source parameters from shot B4) with Green's functions computed from velocity model for Morenci copper mine (Figure 5).

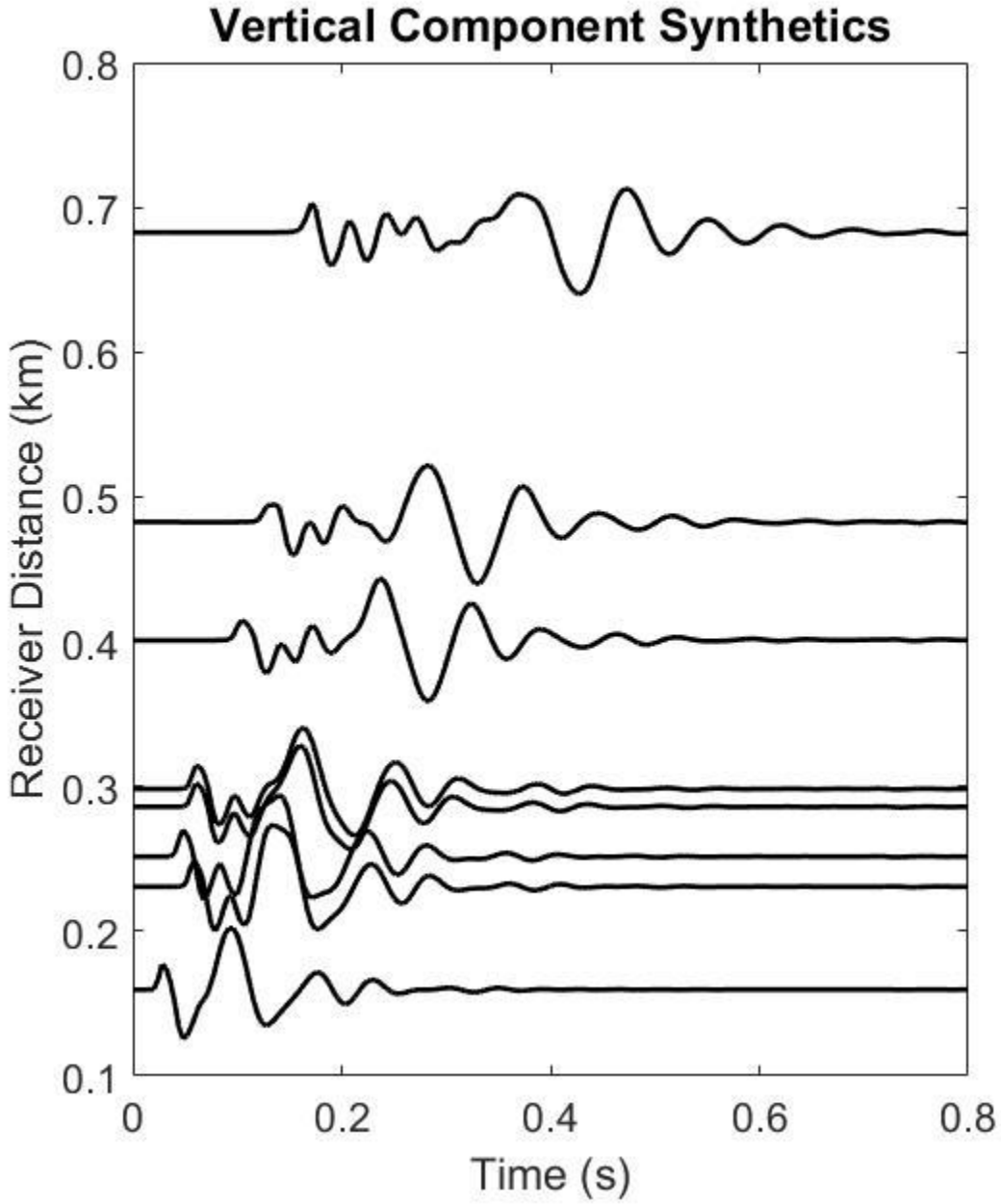

Figure 3.7 – Unfiltered record sections of the fits (grey) and actual data (black) for shots B1 and B3.

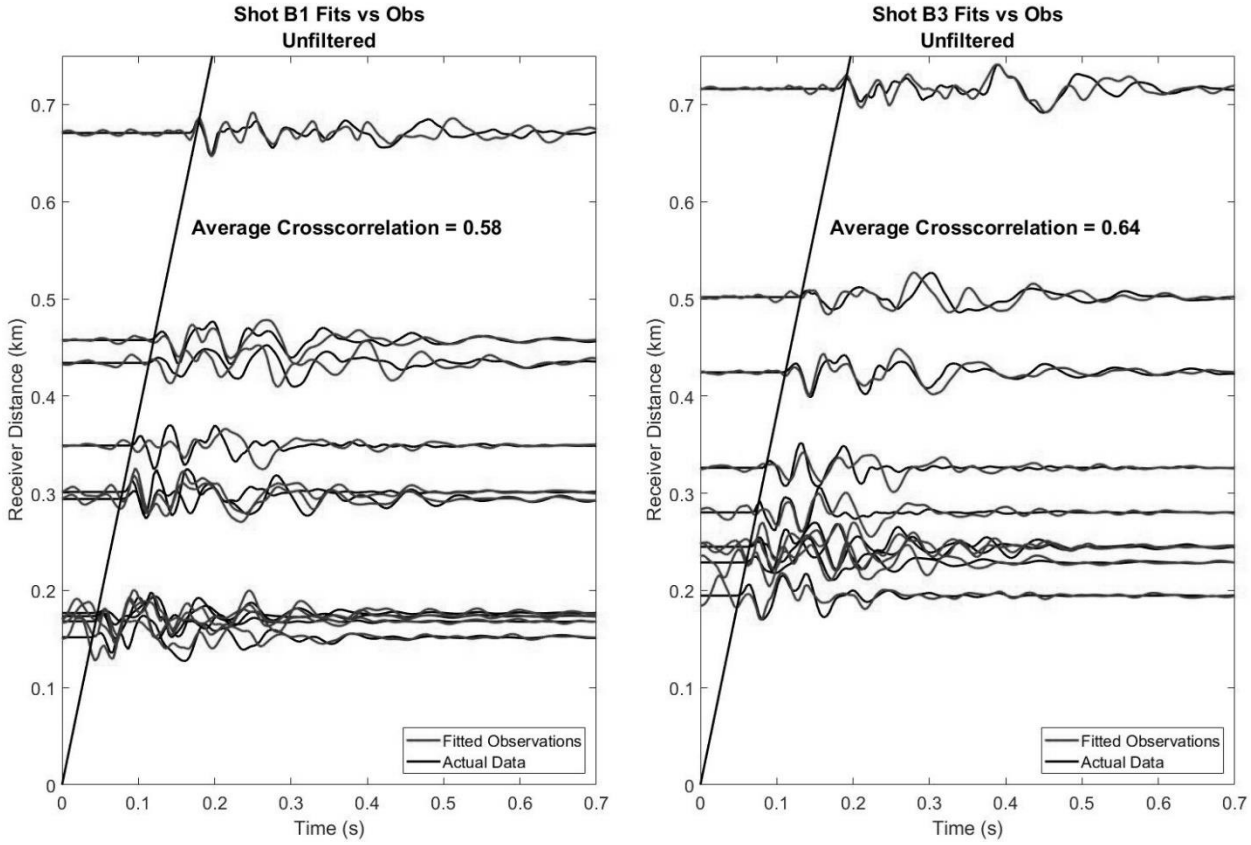

Figure 3.8 – Full moment rate time series for a) shot B1 and b) shot B3.

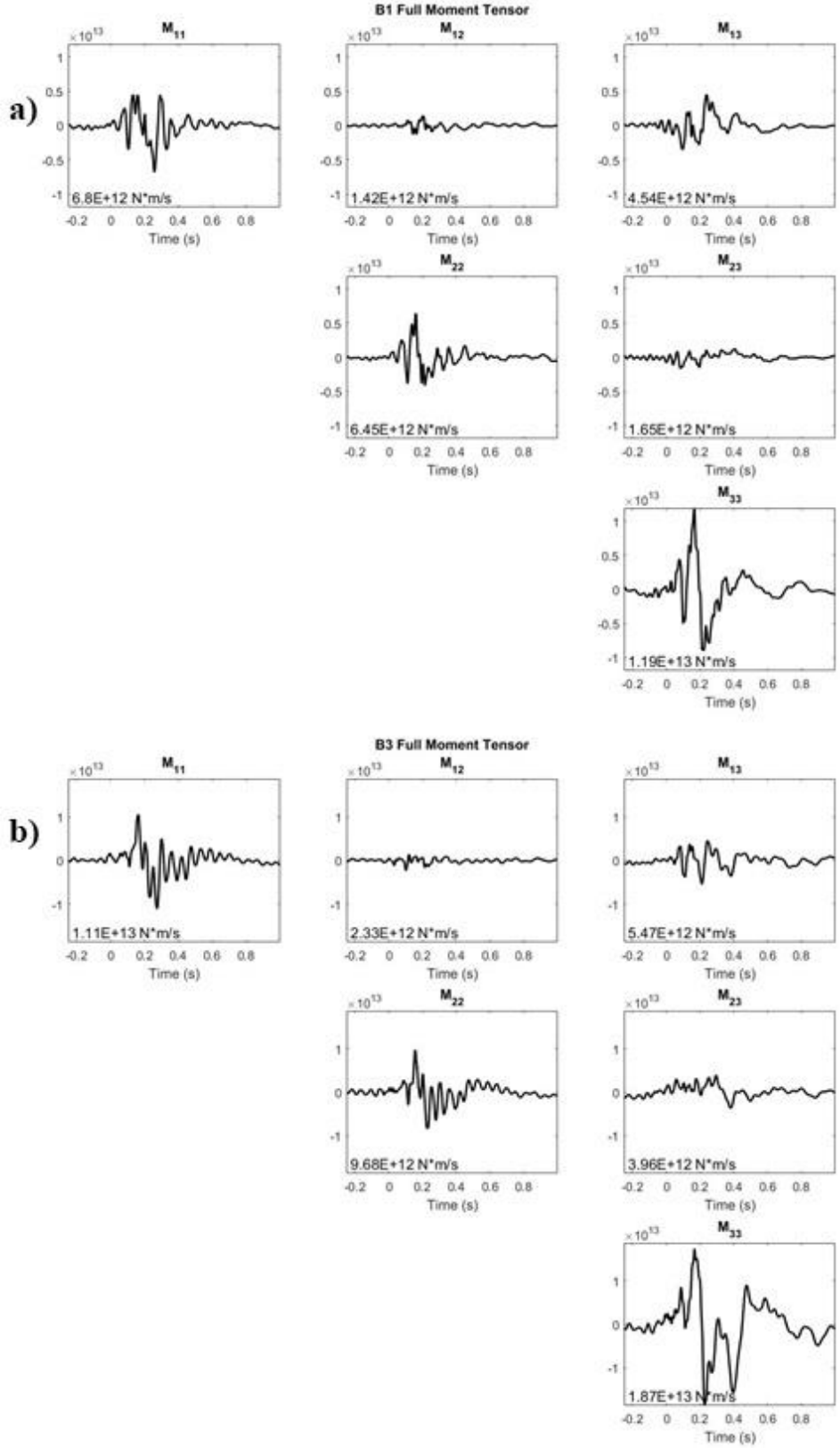

Figure 3.9 – Isotropic moment rate spectra for B1FF077, B3FF077 and B6FF077, representing three different containments with the same yield.

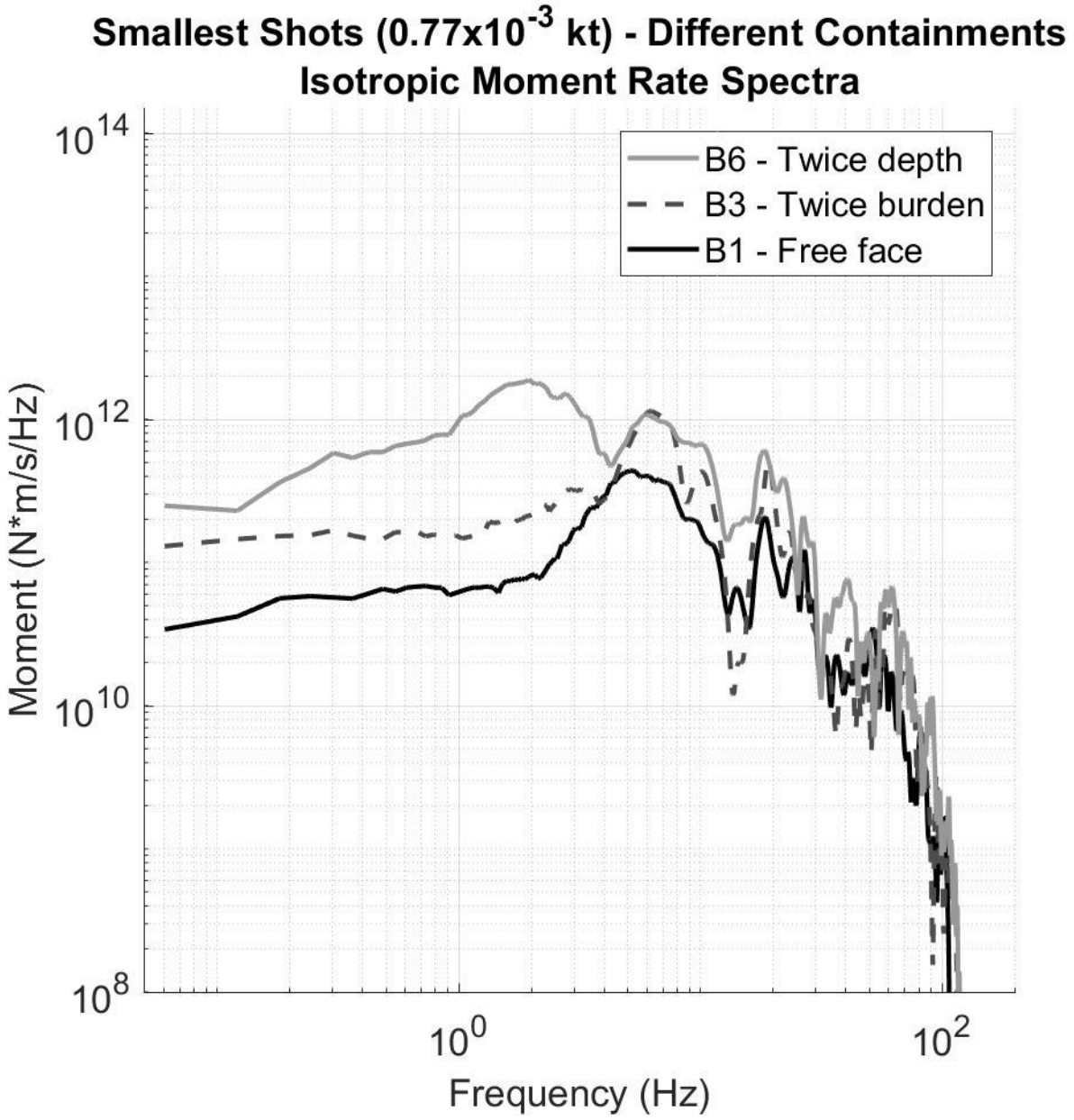

Figure 3.10 – Isotropic moment rate spectra for B1, B2 and B7, representing three different yields with the same containment (free face).

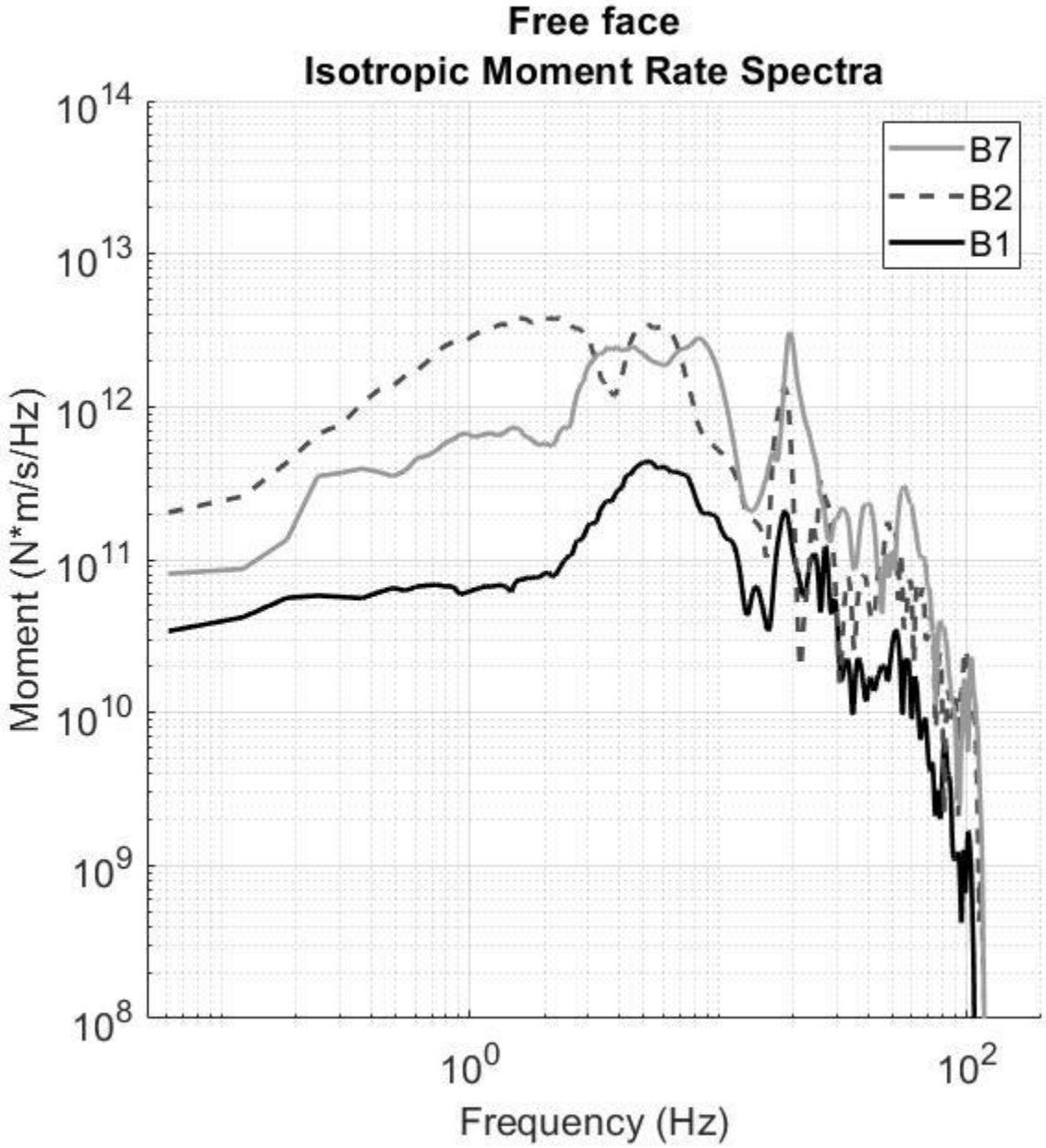

Figure 3.11 – Isotropic moment rate spectra for B3, B5 and B8, representing three different yields with the same containment (twice burden).

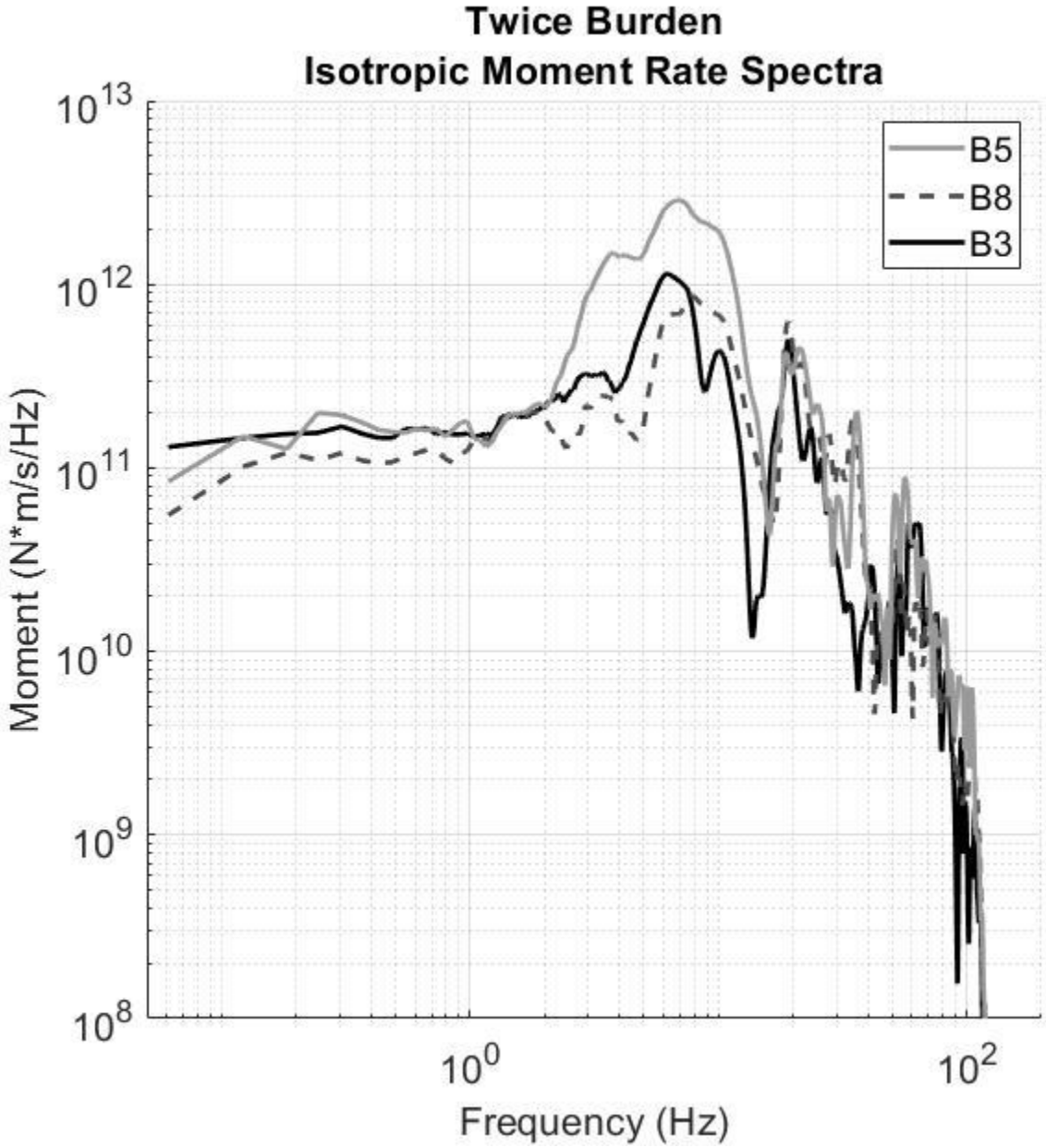

Figure 3.12 – Shots B1FF077, B3FF077 and B6FF077 M_{zz} and M_{tr} component moment rate spectra with MM71, DJ91, MMP12 and WF18 models overlain.

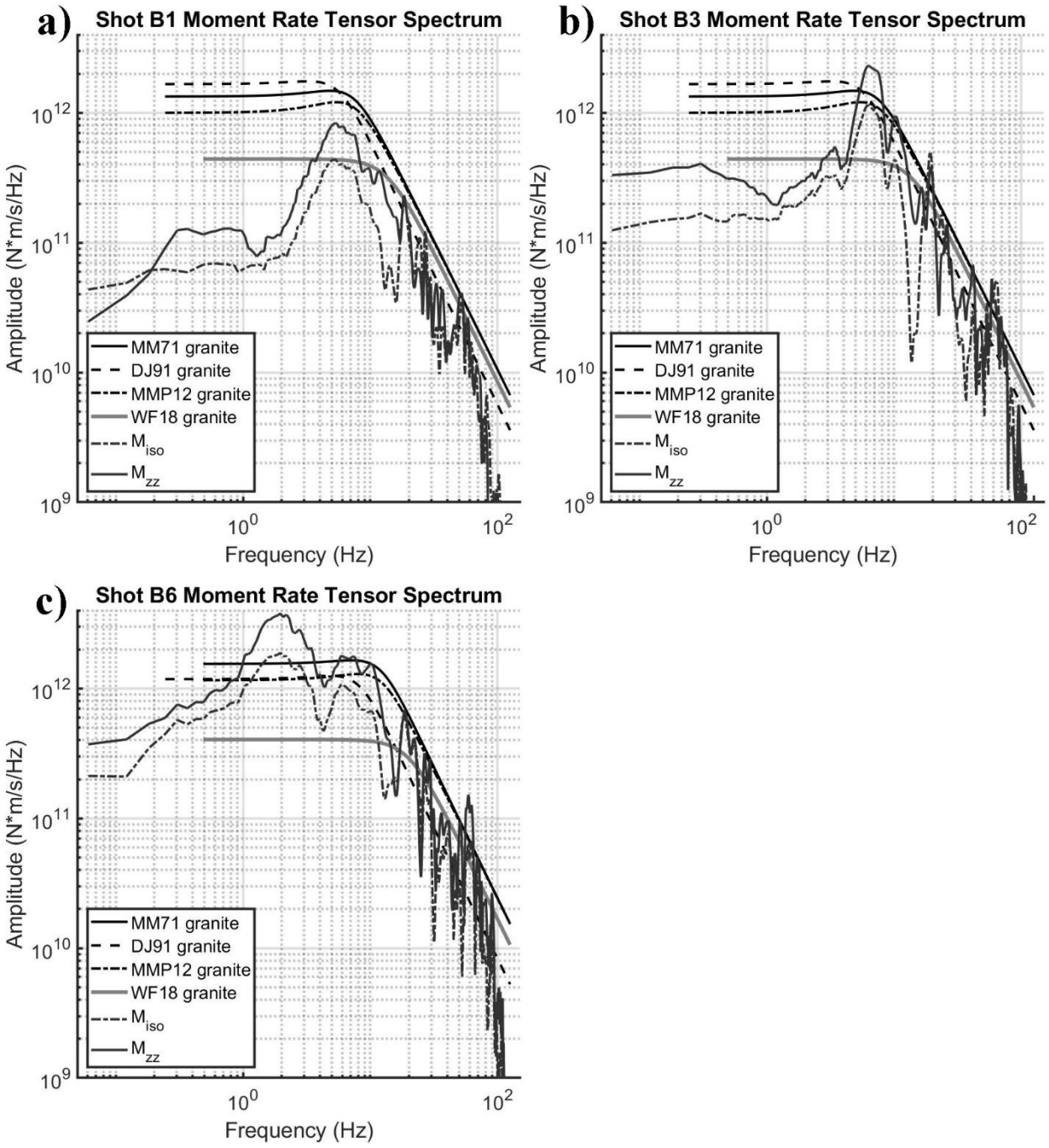

Figure 3.13 – Modified plot from Denny and Johnson, 1991, with all nine shots overlain. Moments are corrected using equation (41) in Denny and Johnson (1991).

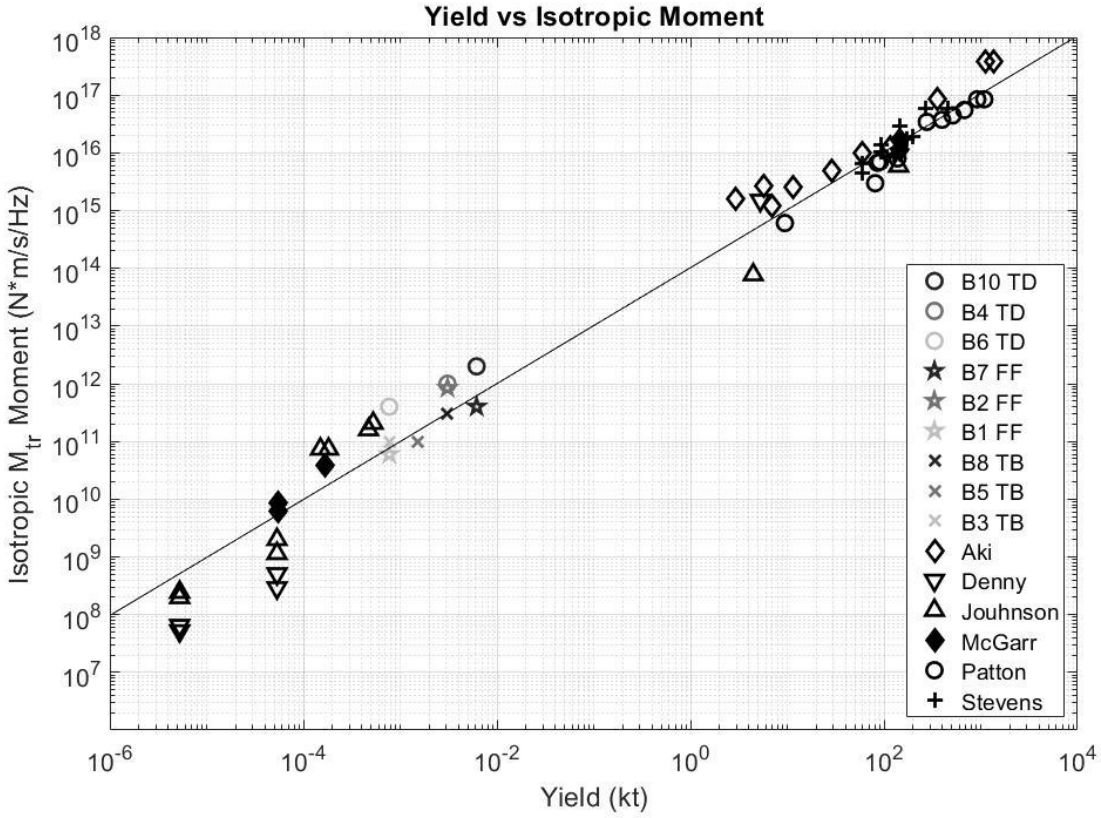

Figure 3.14 – Source type plot for shot B7 as a function of frequency from D.C. to 20 Hz.

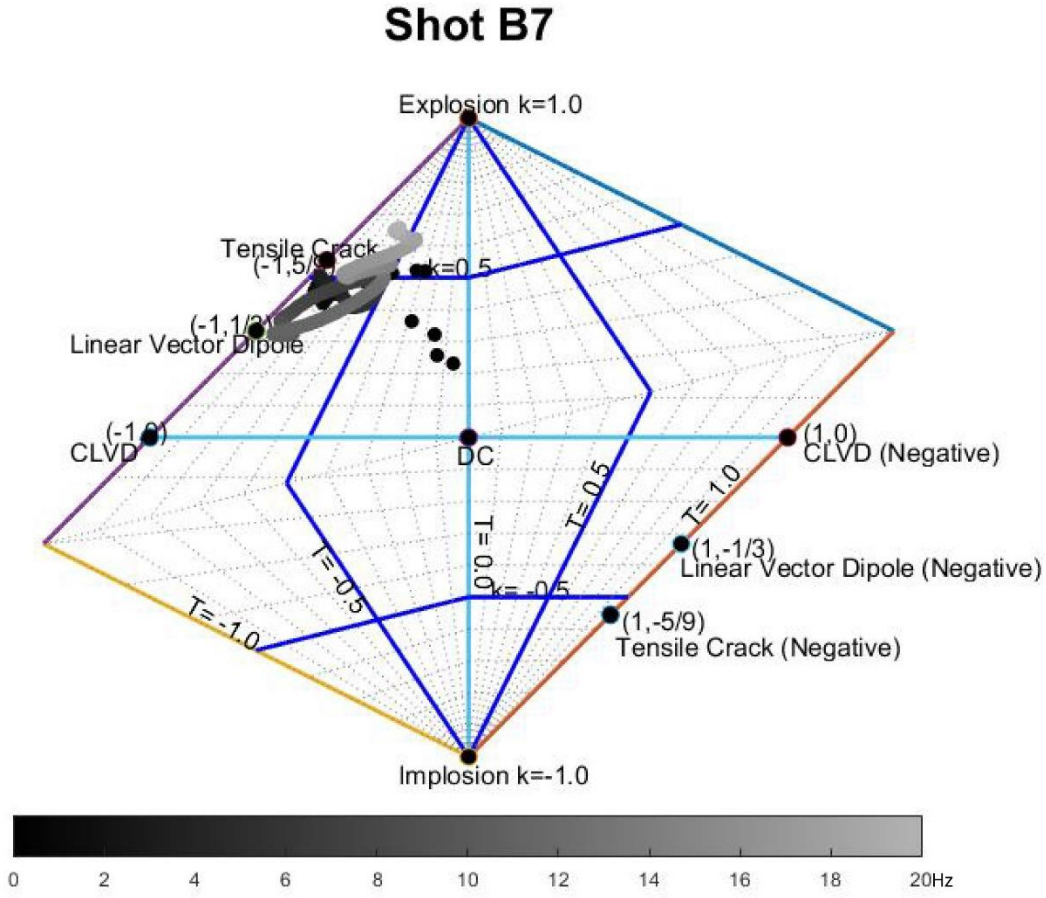

Figure 3.15 – K value for all nine shots at 20 Hz

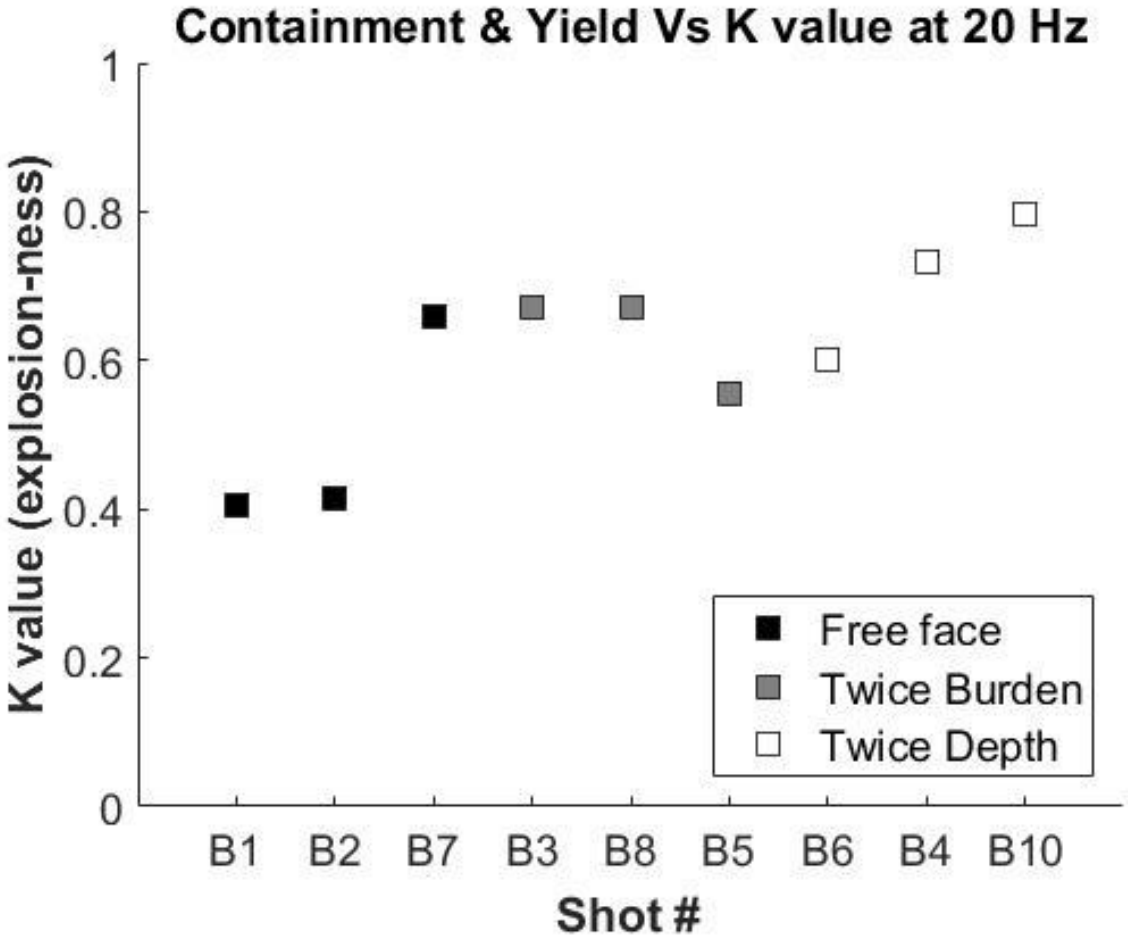

Figure 3.16 – Yield vs K value for all nine shots.

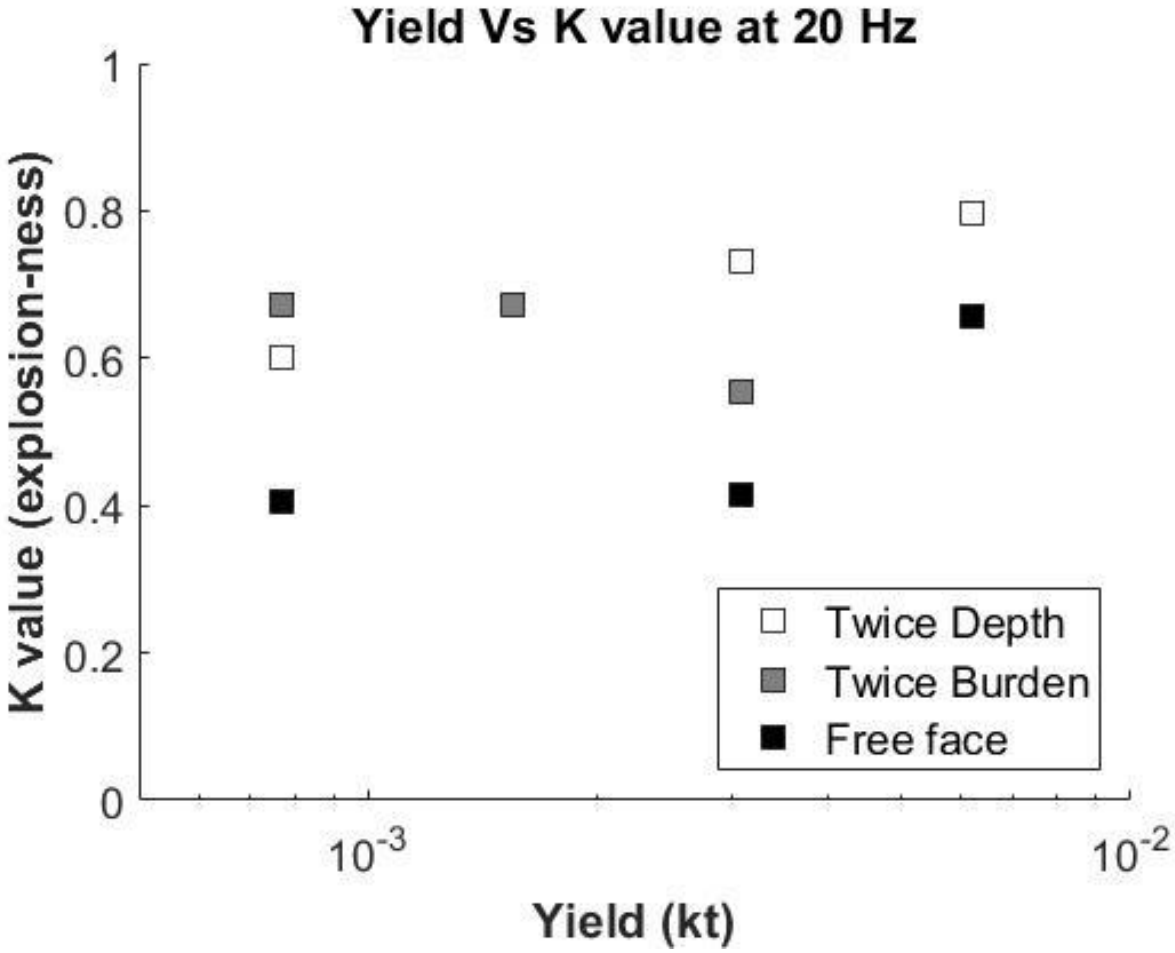

Figure 3.17 – Spectral ratios of ground motion data with Mzz and Mtr moment rate from free face shots.

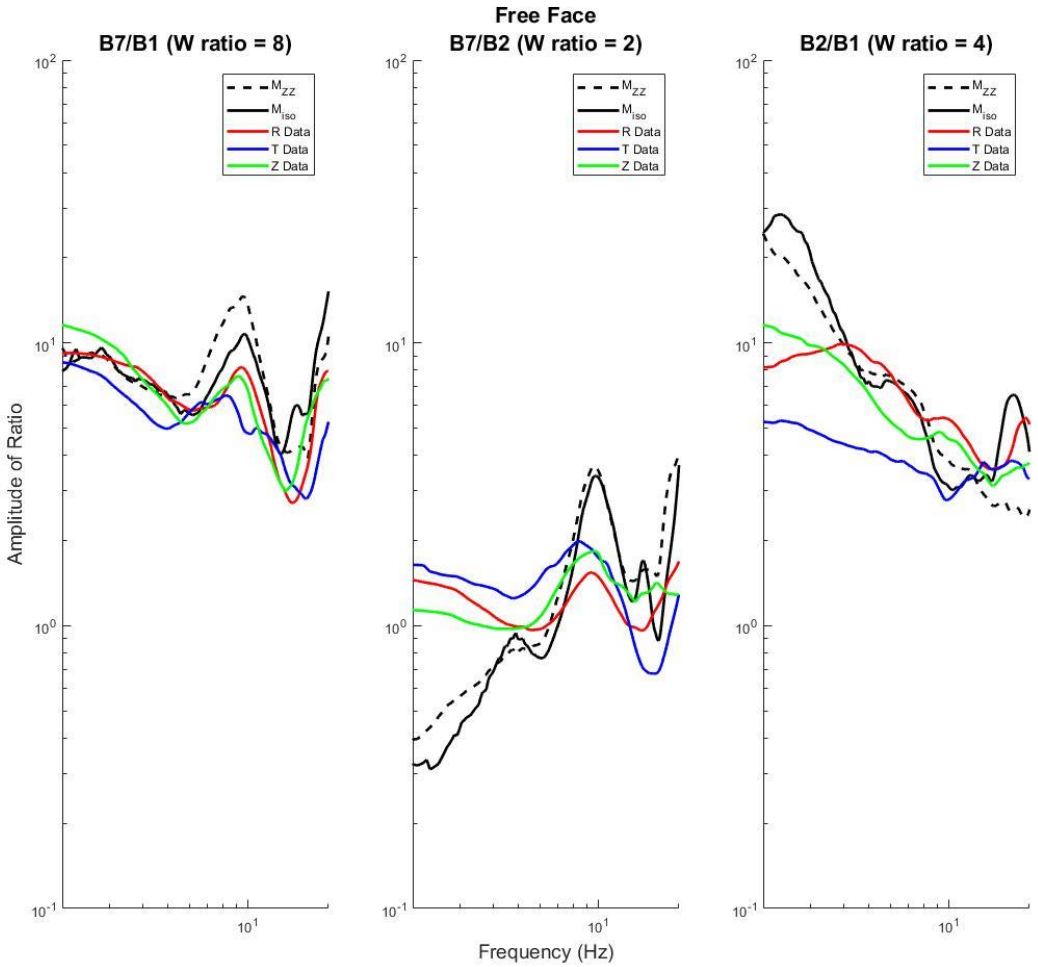

REFERENCES

Anandakrishnan, S., Taylor, S. R., & Stump, B. W. (1997). Quantification and characterization of regional seismic signals from cast blasting in mines: a linear elastic model. *Geophysical Journal International*, *131*(1), 45-60.

Atchison, T. C., & Pugliese, J. M. (1964). *Comparative studies of explosives in limestone* (Vol. 6395). US Dept. of the Interior, Bureau of Mines.

Barker, T. G., K. L. McLaughlin, and J. L. Stevens. Numerical simulation of quarry blast sources. No. SSS-TR-93-13859. S-CUBED LA JOLLA CA, 1993.

Bonner, Jessie L., et al. Source phenomenology experiments in Arizona. No. WG-2005-02. Weston Geophysical, 2005.

Bonner, Jessie, et al. "The surface wave magnitude for the 9 October 2006 North Korean nuclear explosion." Bulletin of the Seismological Society of America 98.5 (2008): 2498-2506.

Bonner, Jessie L., Anastasia Stroujkova, and Dale Anderson. "Determination of Love-and Rayleigh-wave magnitudes for earthquakes and explosions." Bulletin of the Seismological Society of America 101.6 (2011): 3096-3104.

Bowers, David, and John A. Hudson. "Defining the scalar moment of a seismic source with a general moment tensor." Bulletin of the Seismological Society of America 89.5 (1999): 1390-1394.

Brode, Harold L. "Review of nuclear weapons effects." Annual review of nuclear science 18.1 (1968): 153-202.

Chiang, Andrea, and Douglas S. Dreger. "27 Moment Tensor Analysis of Shallow Sources." (2013).

Chilton, F., J. Eisler, and H. Henback (1966). Dynamics of spalling of the earth's surface caused by underground explosions, J. Geophys. Res. 71, 5911.

Chun, K-Y., Y. Wu, and G. A. Henderson. "Magnitude estimation and source discrimination: A close look at the 2006 and 2009 North Korean underground nuclear explosions." Bulletin of the Seismological Society of America 101.3 (2011): 1315-1329.

Day, S. D., M. Rimer, and J. T. Cherry (1983). Surface waves from underground explosions with spall: analysis of elastic and nonlinear source models, Bull. Seism. Soc. Am. 73,247-264.

Denny, Marvin, et al. "Seismic results from DOE's Non-Proliferation Experiment: A comparison of chemical and nuclear explosions." Monitoring a Comprehensive Test Ban Treaty. Springer, Dordrecht, 1996. 355-364.

Denny, Marvin D., and Lane R. Johnson. "The explosion seismic source function: Models and scaling laws reviewed." Explosion Source Phenomenology (1991): 1-24.

Denny, Marvin D., and Dennis M. Goodman. "A case study of the seismic source function: Salmon and Sterling reevaluated." Journal of Geophysical Research: Solid Earth 95.B12 (1990): 19705-19723.

Dickinson and W. D. Payne, Arizona Geological Society Digest Volume XIV, 1981, Tucson, Arizona.

Eisler, J., F. Chilton, and F. Sauer (1966). Multiple subsurface spalling by underground nuclear explosions, J. Geophys. Res. 71, 3923.

Ford, Sean R., Douglas S. Dreger, and William R. Walter. "Source analysis of the memorial day explosion, Kimchaek, North Korea." Geophysical Research Letters 36.21 (2009).

Ford, Sean R., Douglas S. Dreger, and William R. Walter. "Identifying isotropic events using a regional moment tensor inversion." Journal of Geophysical Research: Solid Earth 114.B1 (2009).

Ford, Sean R., et al. "Partitioning of seismoacoustic energy and estimation of yield and height-of-burst/depth-of-burial for near-surface explosions." Bulletin of the Seismological Society of America 104.2 (2014): 608-623.

Glenn, L. A., and P. Goldstein. The influence of material models on chemical or nuclear-explosion source functions. No. UCRL-JC--116428; CONF-9404100--8. Lawrence Livermore National Lab., CA (United States), 1994.

Goldstein, P., and S. Jarpe. "Comparison of chemical and nuclear explosion source spectra from close-in, local and regional seismic data." Proc. of the Symposium on the Non-Proliferation Experiment (NPE): Results and Implications for the Test Ban Treaties. 1994.

Hayward, C., R.-M. Zhou and B. Stump, (2004), QuickLook Report: 2004 January Morenci Refraction Experiments and Morenci Refraction Interpretation, February 2004, Southern Methodist University.

Herbst, Roland F., Glenn C. Werth, and Donald L. Springer. "Use of large cavities to reduce seismic waves from underground explosions." Journal of Geophysical Research 66.3 (1961): 959-978.

Holsapple, K. A., and R. M. Schmidt. "On the scaling of crater dimensions: 1. Explosive processes." Journal of Geophysical Research: Solid Earth 85.B12 (1980): 7247-7256.

Holsapple, K. A., and K. R. Housen. "The third regime of cratering: spall craters." Lunar and Planetary Science Conference. Vol. 44. 2013.

Holsapple, Keith A., and Kevin R. Housen. "Craters from Impacts and Explosions." (2017).

Hudson J.A. Pearce R.G. Rogers R.M. , 1989. Source time plot for inversion of the moment tensor, J. geophys. Res. , 94(B1), 765774.

Hooper, Heather, Jessie Bonner, and Mark Leidig. "Effects of confinement on short-period surface waves: observations from a new dataset." Bulletin of the Seismological Society of America 96.2 (2006): 697-712.

Julian, Bruce R., and Gillian R. Foulger. "Microearthquake Focal Mechanisms." GRC Bulletin (2004): 166-171.

Koper, Keith D., et al. "Empirical scaling laws for truck bomb explosions based on seismic and acoustic data." Bulletin of the Seismological Society of America 92.2 (2002): 527-542.

Koper, Keith D., Robert B. Herrmann, and Harley M. Benz. "Overview of open seismic data from the North Korean event of 9 October 2006." Seismological Research Letters 79.2 (2008): 178-185.

Larson, Donald. Lawrence Livermore National Laboratory, Proceedings of the Department of Energy Sponsored Cavity Decoupling Workshop, Pajaro Dunes, California, July 29-31, 1985

Latter, A. L., et al. "A method of concealing underground nuclear explosions." Journal of Geophysical Research 66.3 (1961): 943-946.

Lay, Thorne, Don V. Helmberger, and David G. Harkrider. "Source models and yield-scaling relations for underground nuclear explosions at Amchitka Island." Bulletin of the Seismological Society of America 74.3 (1984): 843-862.

MacPhail et al., “Quantification of the Effects of Assumed Source Depth and Shear Wave Structure on Resulting Moment Tensors from a Small, Contained Chemical Explosion in Granite“, (2018 a)

MacPhail et al.,” Effects of Source Emplacement and Yield on Source Representations for Small Chemical Explosions in Granite”, (2018 b)

MineSeis--A MATLAB GUI program to calculate synthetic seismograms from a linear, multi-shot blast source model, X Yang, Los Alamos National Lab., NM (United States)

Mueller, Richard A., and John R. Murphy. "Seismic characteristics of underground nuclear detonations Part I. Seismic spectrum scaling." Bulletin of the Seismological Society of America 61.6 (1971): 1675-1692.

Müller, G. (1985). The reflectivity method: a tutorial, J. Geophys. 58, 153-174

Murphy, J., and B. Barker (1995). A Comparative Analysis of the Seismic Characteristics of Cavity Decoupled Nuclear and Chemical Explosions, Pl-TR-95-2117, Phillips Laboratory, 96 pp

Murphy, John R., et al. Exploitation of the IMS and other data for a comprehensive advanced analysis of the North Korean nuclear tests. No. SAIC-10/2201. SCIENCE APPLICATIONS INC MCLEAN VA, 2010.

Murphy, John R., et al. "Supplemental analysis of the seismic characteristics of the 2006 and 2009 North Korean nuclear tests." Proc. of the 2011 Monitoring Research Review: Ground-Based Nuclear Explosion Monitoring Technologies, LA-UR-11 4823 (2011): 513-523.

Murphy, John R. "P wave coupling of underground explosions in various geologic media." Identification of Seismic Sources—Earthquake or Underground Explosion. Springer, Dordrecht, 1981. 201-205.

Murphy, J. R., and H. K. Shah. "An analysis of the effects of site geology on the characteristics of near-field Rayleigh waves." Bulletin of the Seismological Society of America 78.1 (1988): 64-82.

Murphy, J. R., et al. "Advanced seismic analyses of the source characteristics of the 2006 and 2009 North Korean nuclear tests." Bulletin of the Seismological Society of America 103.3 (2013): 1640-1661.

Nordyke, Milo D. On cratering: a brief history, analysis, and theory of cratering. No. UCRL-6578. California. Univ., Livermore. Lawrence Radiation Lab., 1961.

Olsen, C. W. Site selection and containment evaluation for LLNL nuclear events. No. UCRL-JC--113334; CONF-9309103--1. Lawrence Livermore National Lab., CA (United States), 1993.

Orphal, D. L. "Calculations of explosion cratering. II-Cratering mechanics and phenomenology." Impact and Explosion Cratering: Planetary and Terrestrial Implications. 1977.

Orphal, D. L. "Depth, thickness and volume of the breccia lens for simple explosion and impact craters." Lunar and Planetary Science Conference. Vol. 10. 1979.

Patton, Howard J. "Characterization of spall from observed strong ground motions on Pahute Mesa." Bulletin of the Seismological Society of America 80.5 (1990): 1326-1345.

Patton, H. J. (2012b). A revised cavity radius scaling relationship for explosions detonated in a granite medium, Los Alamos National Laboratory, LA-UR-12-27099, pp. 12.

Patton, Howard J., and Steven R. Taylor. "Effects of shock-induced tensile failure on mb-Ms discrimination: Contrasts between historic nuclear explosions and the North Korean test of 9 October 2006." Geophysical Research Letters 35.14 (2008).

Pasyanos, Michael E., and Sean R. Ford. "Determining the source characteristics of explosions near the Earth's surface." Geophysical Research Letters 42.10 (2015): 3786-3792.

Pearce, R. G., and R. M. Rogers. "Determination of earthquake moment tensors from teleseismic relative amplitude observations." Journal of Geophysical Research: Solid Earth 94.B1 (1989): 775-786.

Rinehart, J. S. {1959). Spalling and Large Blasts, Proceedings of the 2nd Plow Share Symposium, San Francisco, May 13-15, 1959, Part I, 135-155, UCRL-5675.

Rougier, Esteban, and Howard J. Patton. "Seismic source functions from free-field ground motions recorded on SPE: Implications for source models of small, shallow explosions." Journal of Geophysical Research: Solid Earth 120.5 (2015): 3459-3478.

Selby, Neil D. "Relative locations of the October 2006 and May 2009 DPRK announced nuclear tests using international monitoring system seismometer arrays." Bulletin of the Seismological Society of America 100.4 (2010): 1779-1784.

Sharpe, Joseph A. "The production of elastic waves by explosion pressures. I. Theory and empirical field observations." Geophysics 7.2 (1942): 144-154.

Shoemaker, Eugene Merle. Impact mechanics at Meteor crater, Arizona. No. 59-108. US Geological Survey], 1959.

Short, Nicholas M. "A comparison of features characteristic of nuclear explosion craters and astroblemes." Annals of the New York Academy of Sciences 123.1 (1965): 573-616.

Springer, D. (1974). Secondary sources of seismic waves from underground nuclear explosions, Bull. Seism. Soc. Am. 64, 581-594

Springer, D., et al. "The Sterling Experiment: Decoupling of seismic waves by a shot-generated cavity." Journal of Geophysical Research 73.18 (1968): 5995-6011.

Stroujkova, Anastasia, et al. "Cavity Decoupling of Small Explosions in Limestone." Bulletin of the Seismological Society of America 104.3 (2014): 1205-1211.

Stroujkova, Anastasia, Mario Carnevale, and Oleg Vorobiev. "Cavity Radius Scaling for Underground Explosions in Hard Rock." Bulletin of the Seismological Society of America 106.6 (2016): 2500-2510.

Stroujkova, Anastasia, and Igor Morozov. "Seismic source studies for chemical explosions in granite." Bulletin of the Seismological Society of America 104.1 (2013): 174-183.

Stroujkova, Anastasia. "Effect of gaseous products of underground chemical explosions on seismic coupling." Bulletin of the Seismological Society of America 105.5 (2015): 2367-2378.

Stump, Brian W., and Lane R. Johnson. "Near-field source characterization of contained nuclear explosions in tuff." Bulletin of the Seismological Society of America 74.1 (1984): 1-26.

Stump, Brian W., D. Craig Pearson, and Robert E. Reinke. "Source comparisons between nuclear and chemical explosions detonated at Rainier Mesa, Nevada Test Site." Bulletin of the Seismological Society of America 89.2 (1999): 409-422.

Stump, Brian W. "Constraints on explosive sources with spall from near-source waveforms." Bulletin of the Seismological Society of America 75.2 (1985): 361-377.

Tape, Walter, and Carl Tape. "The classical model for moment tensors." Geophysical Journal International 195.3 (2013): 1701-1720.

Titley, S. R., 1981, Geologic and Geotectonic Setting of Porphyry Copper Deposits in the Southern Cordillera, in Relations of Tectonics to Ore Deposits in the Southern Cordillera, edited by W. R.

Viecelli, J. A. (1973). Spallation and the generation of surface waves by an underground explosion, J. Geophys. Res. 78, 2475-2487.

Walter, W. R., & Ford, S. R. (2018). *A Preliminary Explosion Seismic Spectral Model for Saturated/Hard Rock* (No. LLNL-TR-754292). Lawrence Livermore National Lab.(LLNL), Livermore, CA (United States).

Walter, William R., Kevin M. Mayeda, and Howard J. Patton. "Phase and spectral ratio discrimination between NTS earthquakes and explosions. Part I: Empirical observations." Bulletin of the Seismological Society of America 85.4 (1995): 1050-1067.

Wen, Lianxing, and Hui Long. "High-precision location of North Korea's 2009 nuclear test." Seismological Research Letters 81.1 (2010): 26-29.Kim and Richards, 2007

Xiaoning Yang; Source Spectra of the First Four Source Physics Experiments (SPE) Explosions from the Frequency-Domain Moment Tensor Inversion. Bulletin of the Seismological Society of America ; 106 (4): 1637–1651. doi: https://doi.org/10.1785/0120150263

Yang et al., “Moment Tensor Solutions - A Useful Tool for Seismotectonics”, in press

Yang, Xiaoning, and Jessie L. Bonner. "Characteristics of chemical explosive sources from time-dependent moment tensors." Bulletin of the Seismological Society of America 99.1 (2009): 36-51.

Zhou, Rong-Mao, and Brian W. Stump. "Frequency-domain scaling of single-fired mining explosions with different confinements and explosive weights detonated in porphyry granite." Bulletin of the Seismological Society of America 97.6 (2007): 1862-1879.

Zhao, Lian-Feng, et al. "Regional seismic characteristics of the 9 October 2006 North Korean nuclear test." Bulletin of the Seismological Society of America 98.6 (2008): 2571-2589.

Zhao, Lian-Feng, et al. "Yield estimation of the 25 May 2009 North Korean nuclear explosion." Bulletin of the Seismological Society of America 102.2 (2012): 467-478.

CONCLUSIONS

Trade-offs between the source representation, source depth, and S-wave velocity need further quantification in explosion source studies. Slower V_S models increase Green's function amplitudes in a similar fashion to a shallower source.

Cross-correlations between the velocity data and predicted observations were conducted and the mean of all values for each inversion calculated to determine how well the estimated moment tensors replicated the actual data for each of the given assumed depth and V_S models. An alternative method is the calculation of the sum of the squares of the residuals between the observations and the predictions. This measure will be calculated and assessed relative to the cross-correlation analysis.

Secondary source components in empirical moment tensor calculations are not replicated by isotropic source models. The CLVD component may need to be incorporated into the source models if we are to have an accurate explosion representation.

A factor of two chemical to nuclear yield equivalence may not be supported by the data in this experiment and is dependent upon the interpretation of the CLVD component. The spectral peaks, hypothesized to be from the CLVD component, extend upward to the factor of two long period level. The isotropic source models, from this study, do not accurately represent all of the source spectra. A better understanding of the spall contribution to the source is needed.

In the future, spall models will be calculated and added to the isotropic source function to better represent the explosion source with secondary source contamination.

The source representation changes as a function of frequency. The representation for these small chemical explosions have a higher CLVD component at lower frequencies and begin to have a higher explosion component as it increases in frequency, peaking around 20 Hz.

Free face explosions, typical of mining explosions, suggest factor of 5 decoupling, relative to fully contained shots. The unaffected source representations show that even the more decoupled explosions can provide surrogates for seismic discrimination.

APPENDIX

A 1 – Shot B1 full moment rate tensor time series, bandpass filtered from 2-20 Hz.

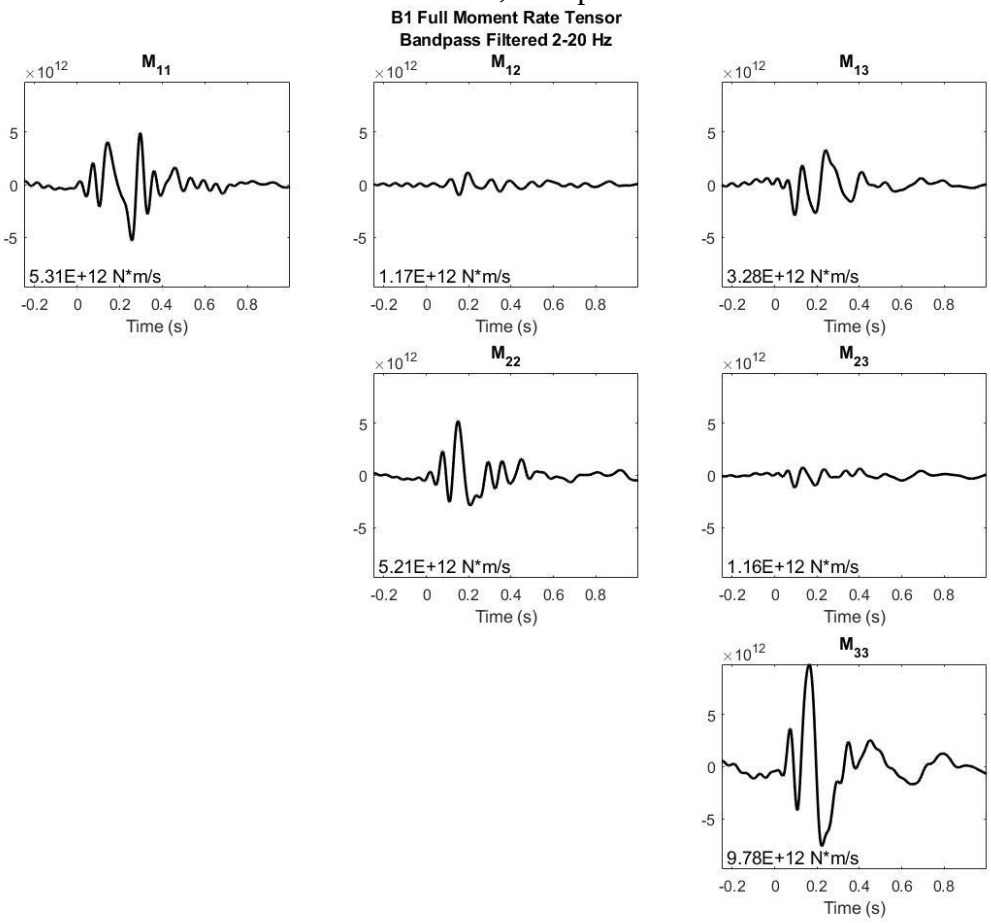

A 2 – Shot B2 full moment rate tensor time series, bandpass filtered from 2-20 Hz.

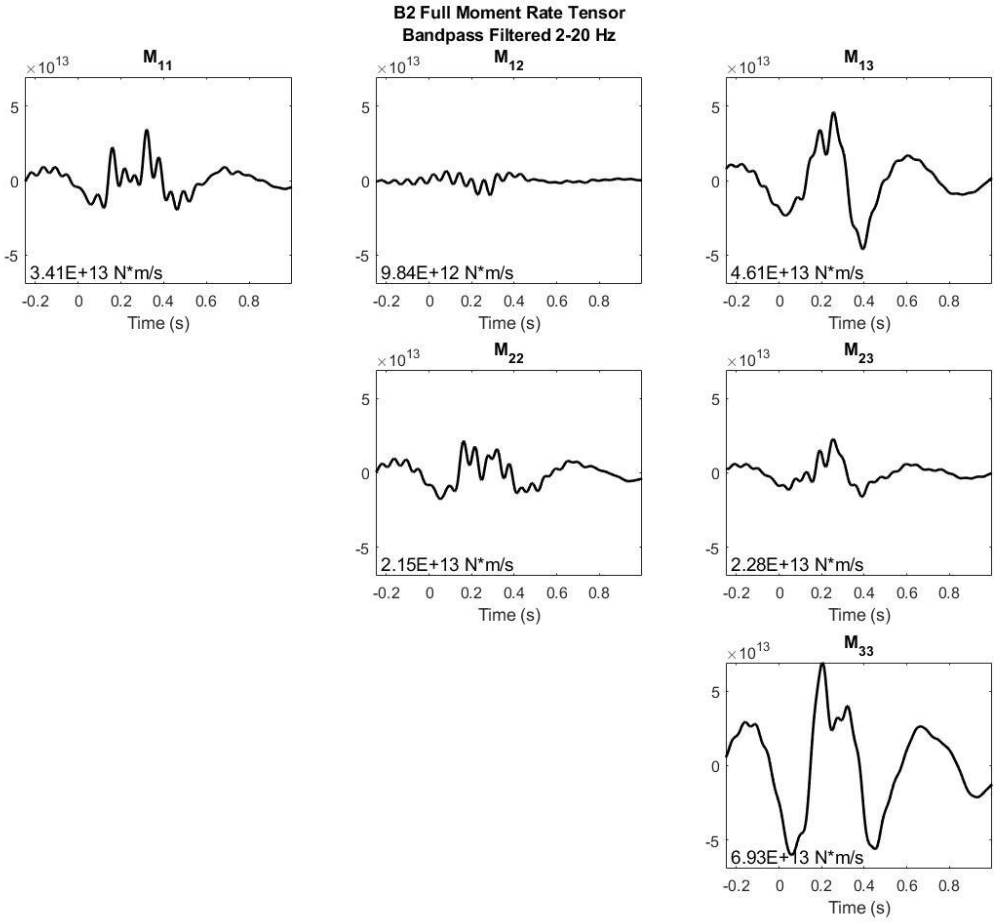

A 3 – Shot B3 full moment rate tensor time series, bandpass filtered from 2-20 Hz.

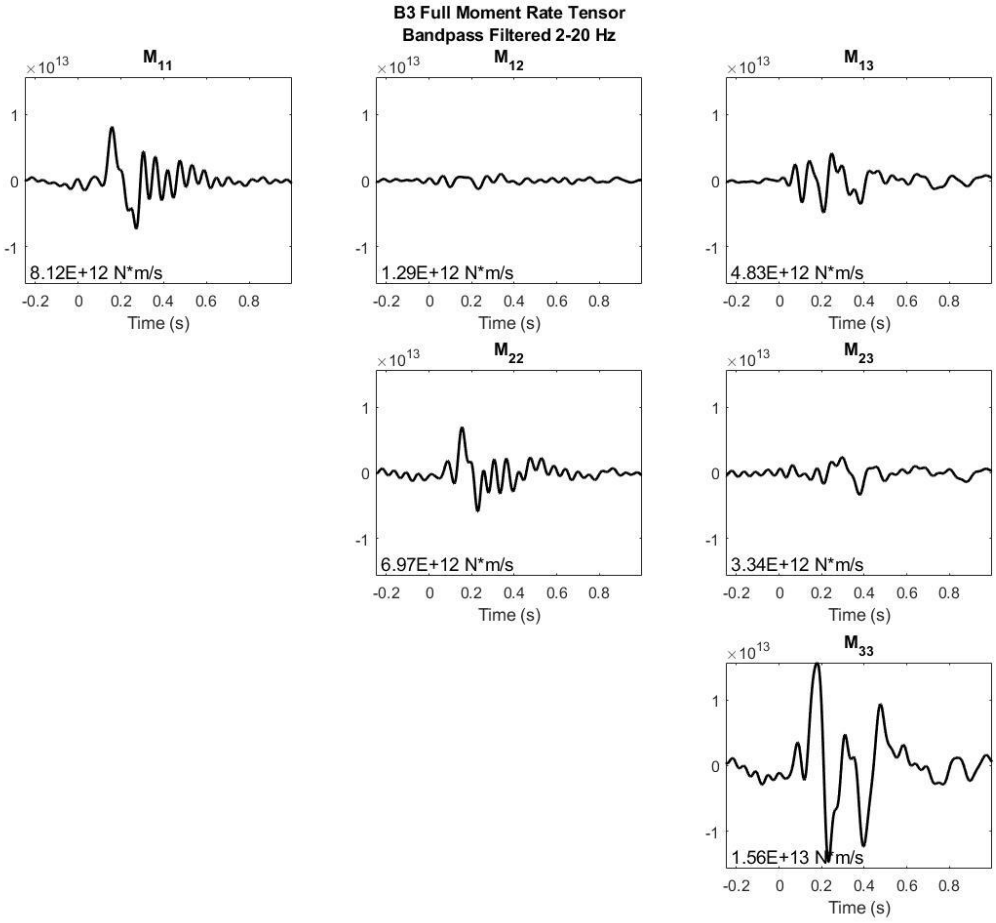

A 4 – Shot B4 full moment rate tensor time series, bandpass filtered from 2-20 Hz.

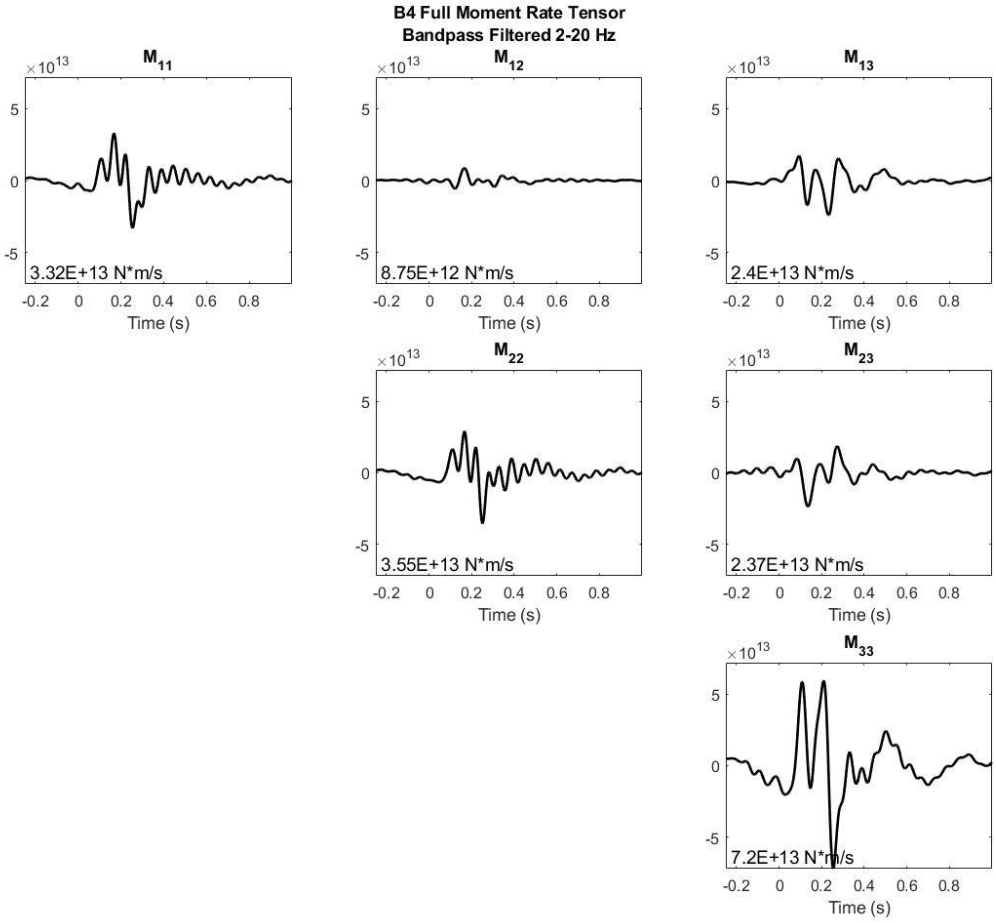

A 5 – Shot B5 full moment rate tensor time series, bandpass filtered from 2-20 Hz.

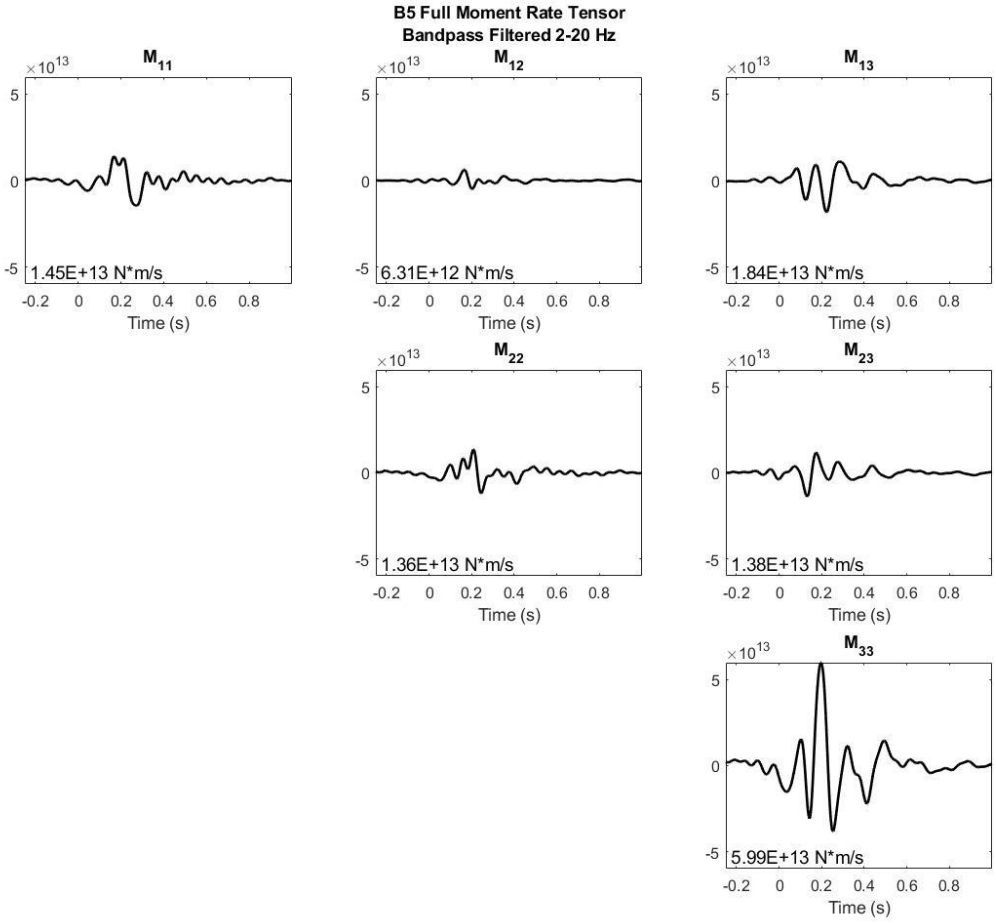

A 6 – Shot B6 full moment rate tensor time series, bandpass filtered from 2-20 Hz.

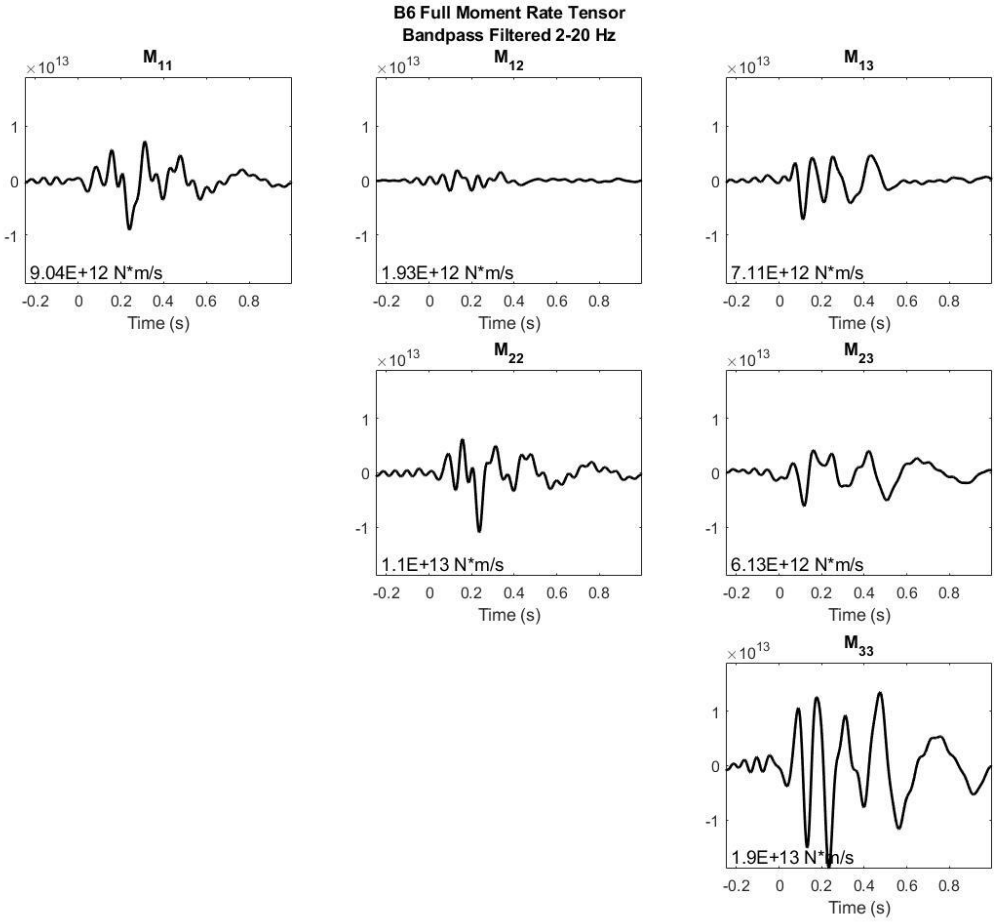

A 7 – Shot B7 full moment rate tensor time series, bandpass filtered from 2-20 Hz.

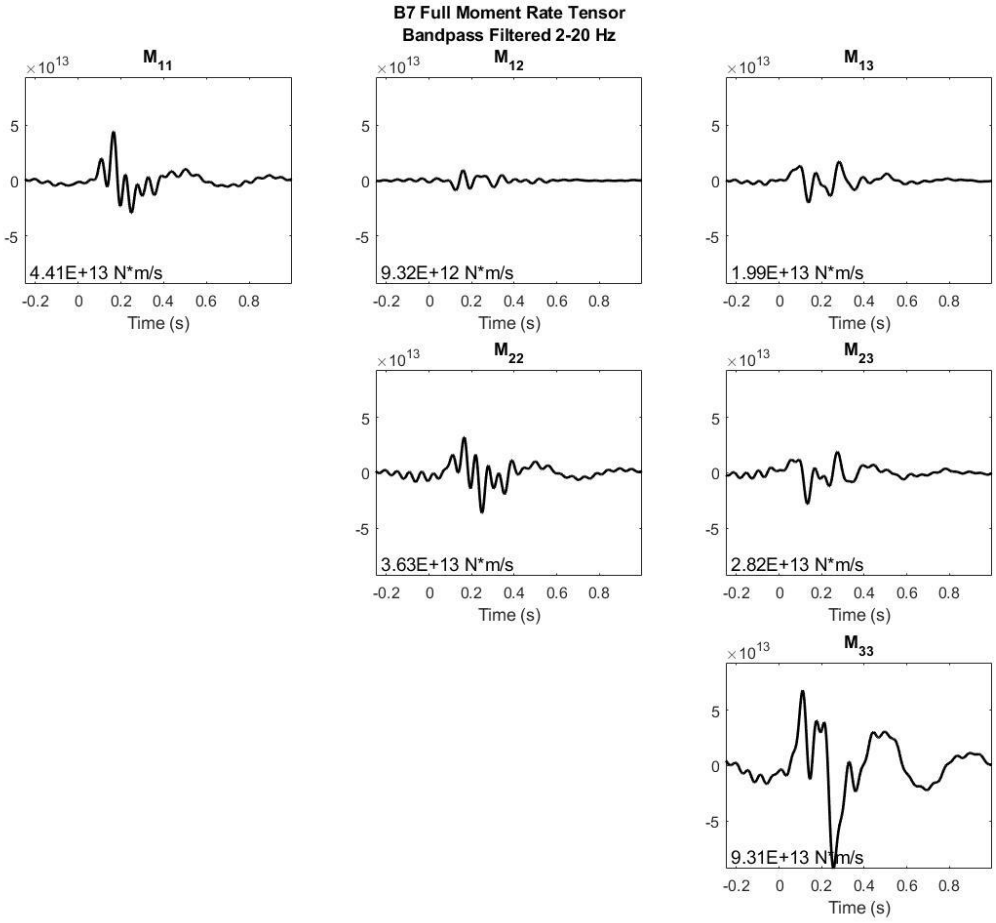

A 8 – Shot B8 full moment rate tensor time series, bandpass filtered from 2-20 Hz.

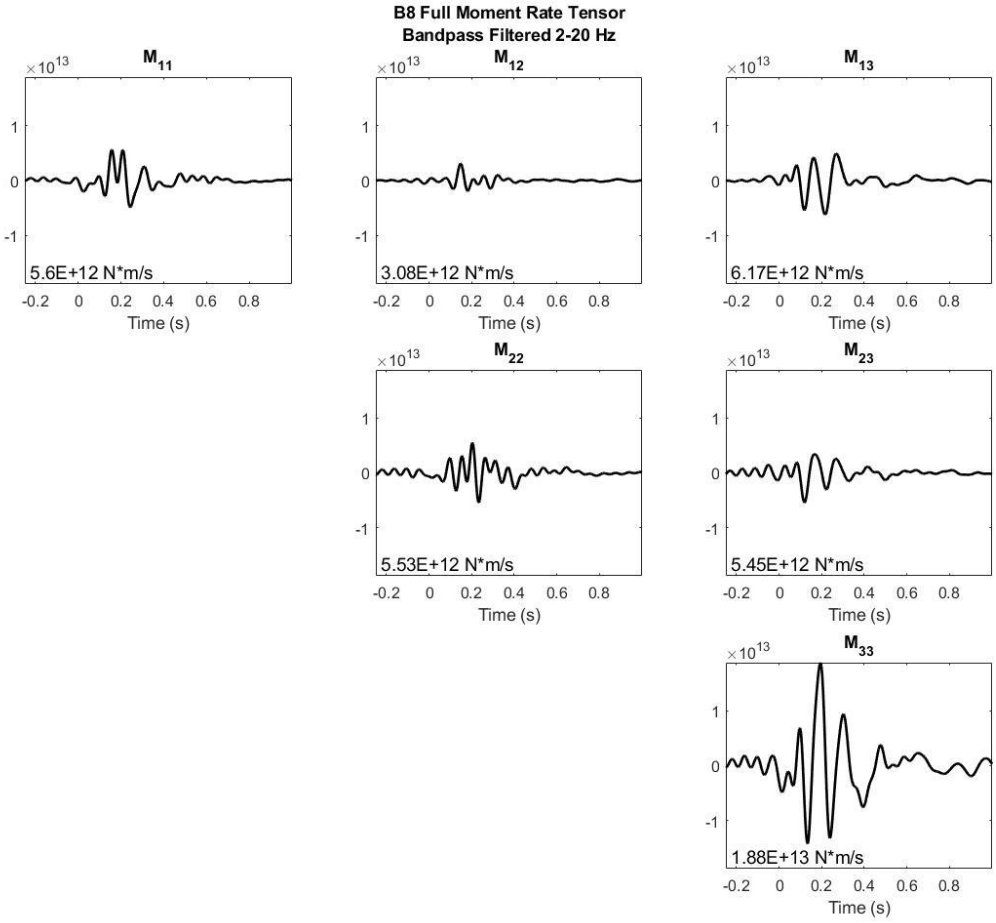

A 9 – Shot B10 full moment rate tensor time series, bandpass filtered from 2-20 Hz.

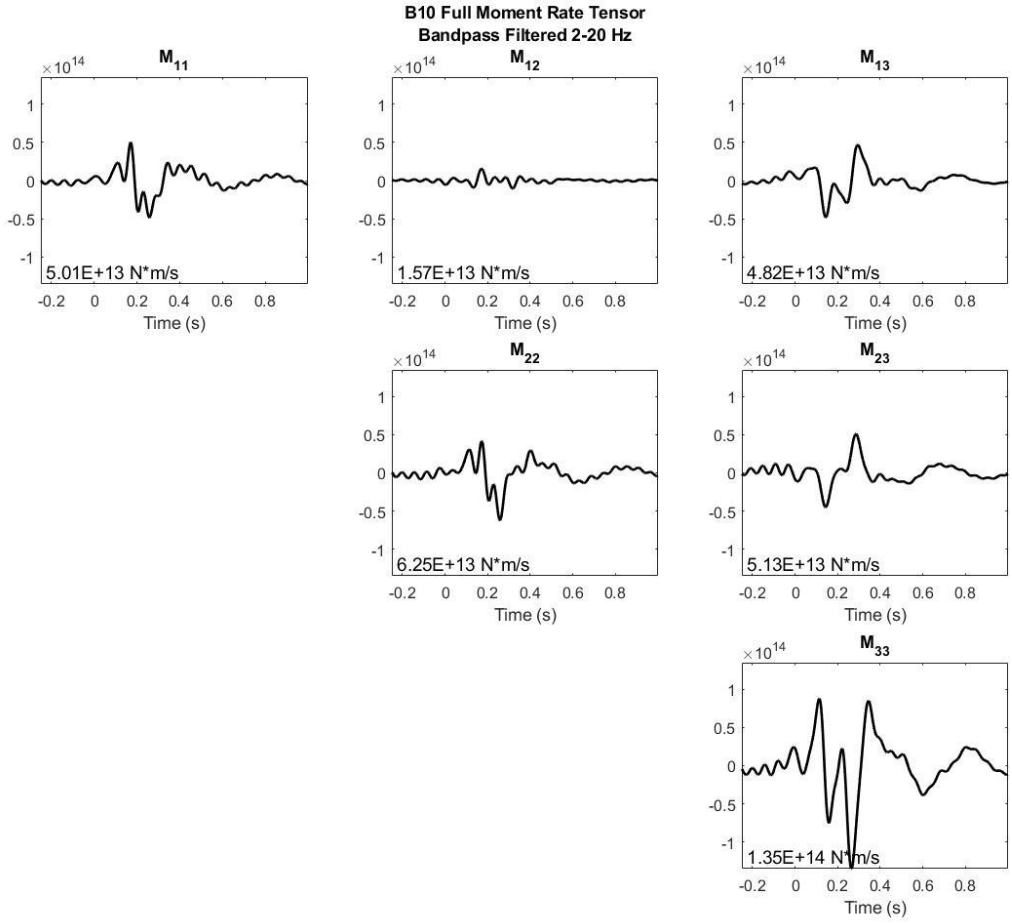

A 10 – Shot B1 M_{tr} and M_{zz} moment rate tensor time series with current prevailing isotropic source models. Isotropic component long period level marker bar and isotropic spectra corner frequency star also shown.

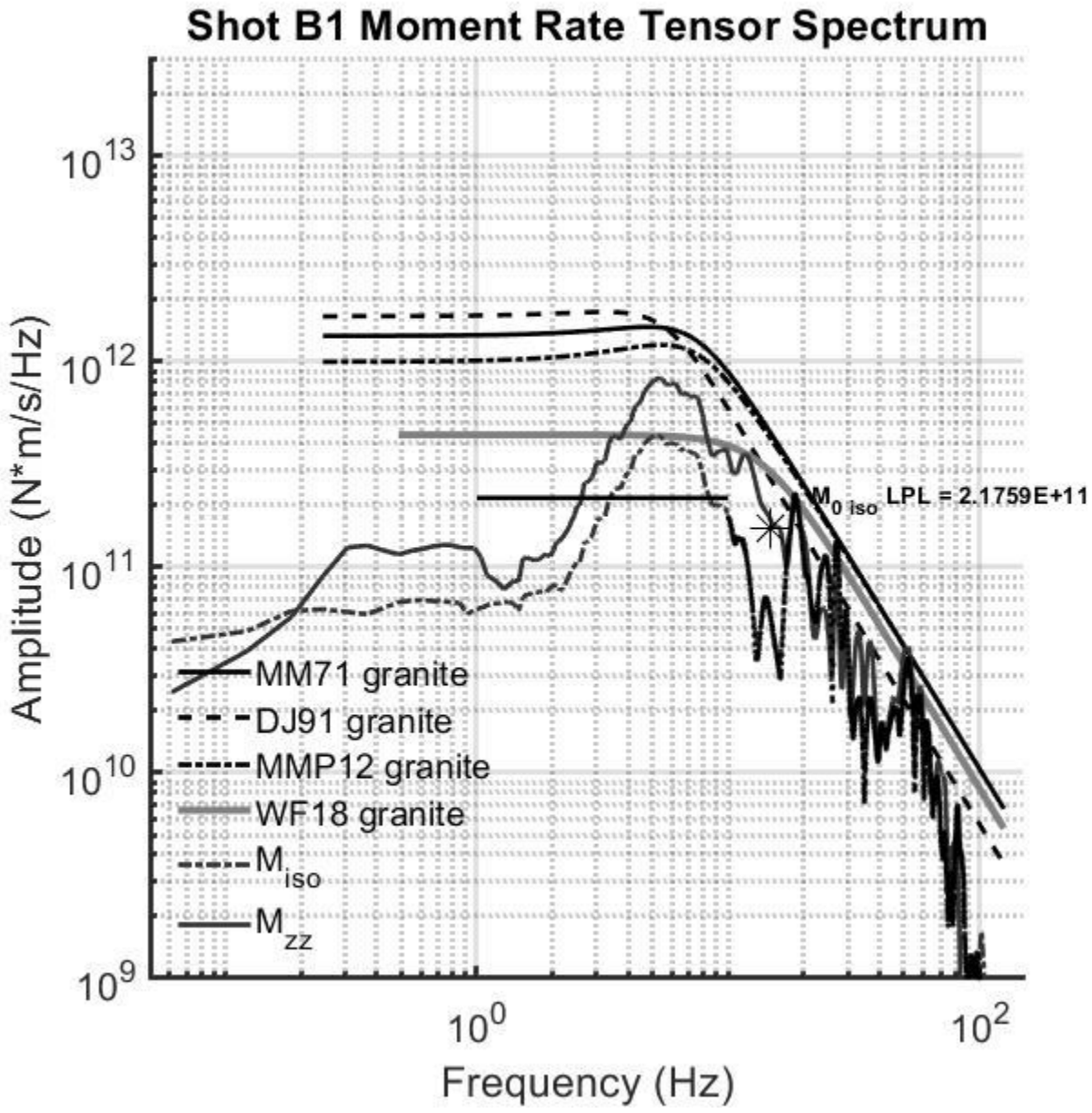

A 11 – Shot B2 M_{tr} and M_{zz} moment rate tensor time series with current prevailing isotropic source models. Isotropic component long period level marker bar and isotropic spectra corner frequency star also shown.

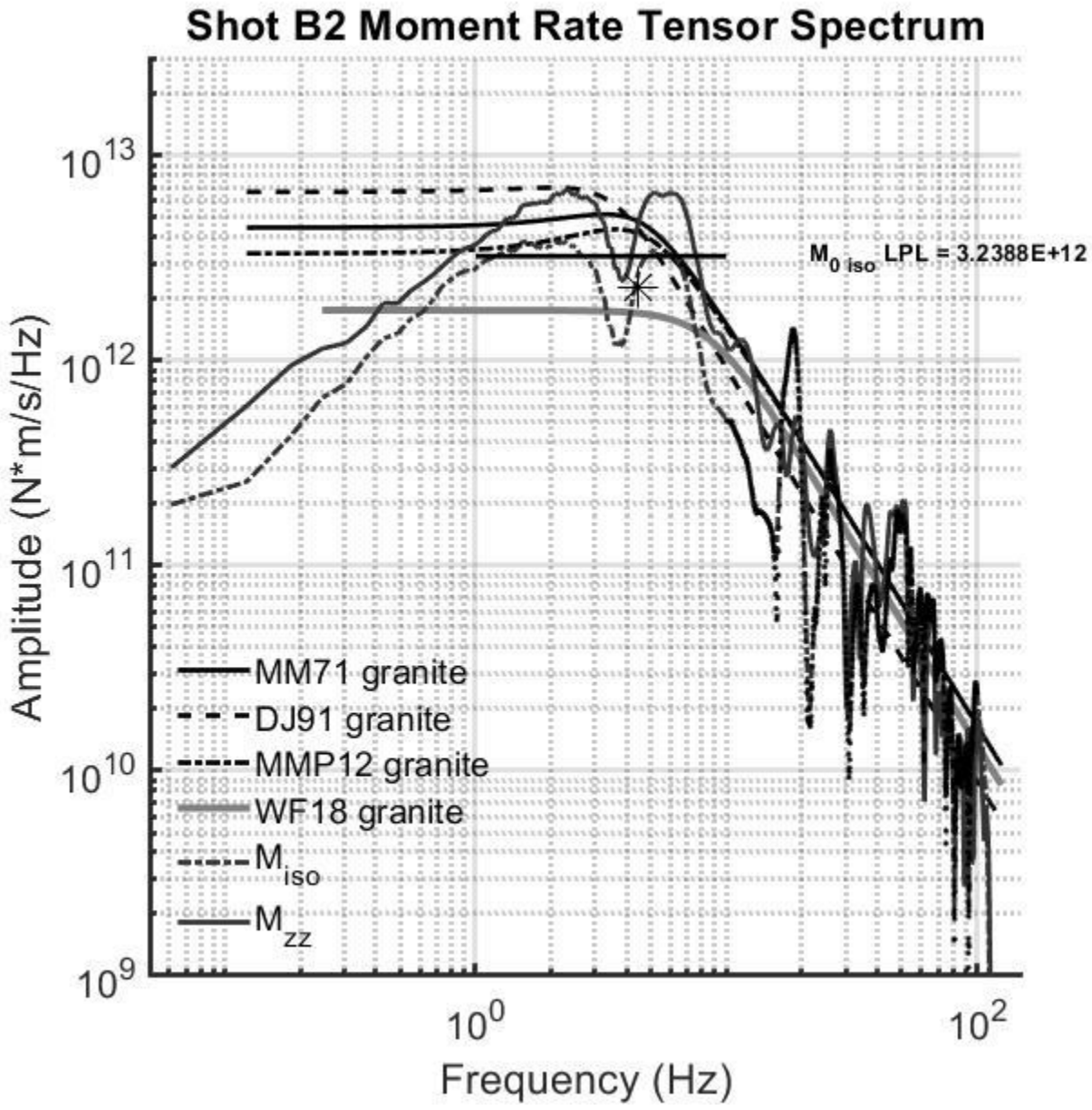

A 12 – Shot B3 M_{tr} and M_{zz} moment rate tensor time series with current prevailing isotropic source models. Isotropic component long period level marker bar and isotropic spectra corner frequency star also shown.

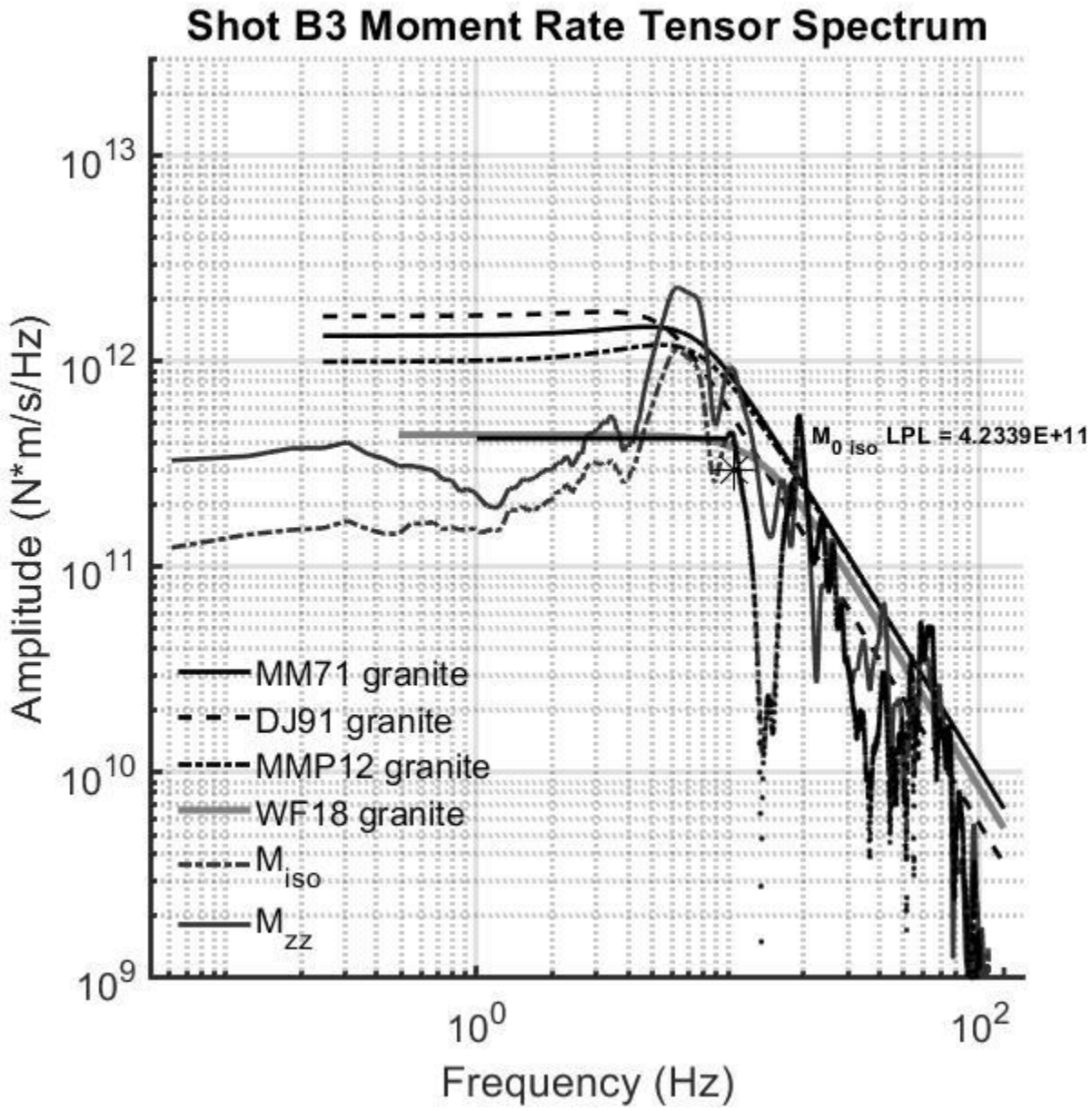

A 13 – Shot B4 M_{tr} and M_{zz} moment rate tensor time series with current prevailing isotropic source models. Isotropic component long period level marker bar and isotropic spectra corner frequency star also shown.

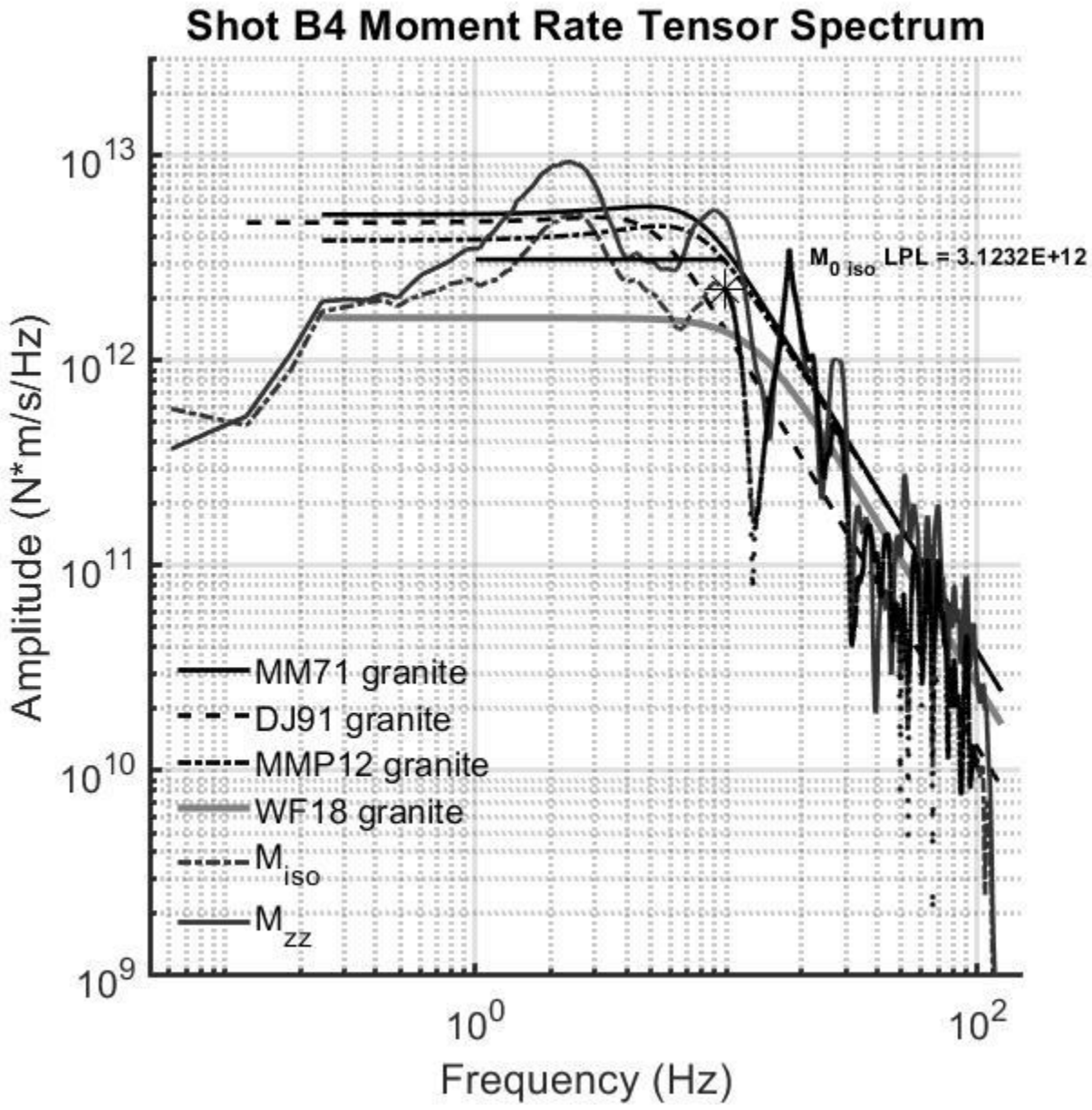

A 14 – Shot B5 M_{tr} and M_{zz} moment rate tensor time series with current prevailing isotropic source models. Isotropic component long period level marker bar and isotropic spectra corner frequency star also shown.

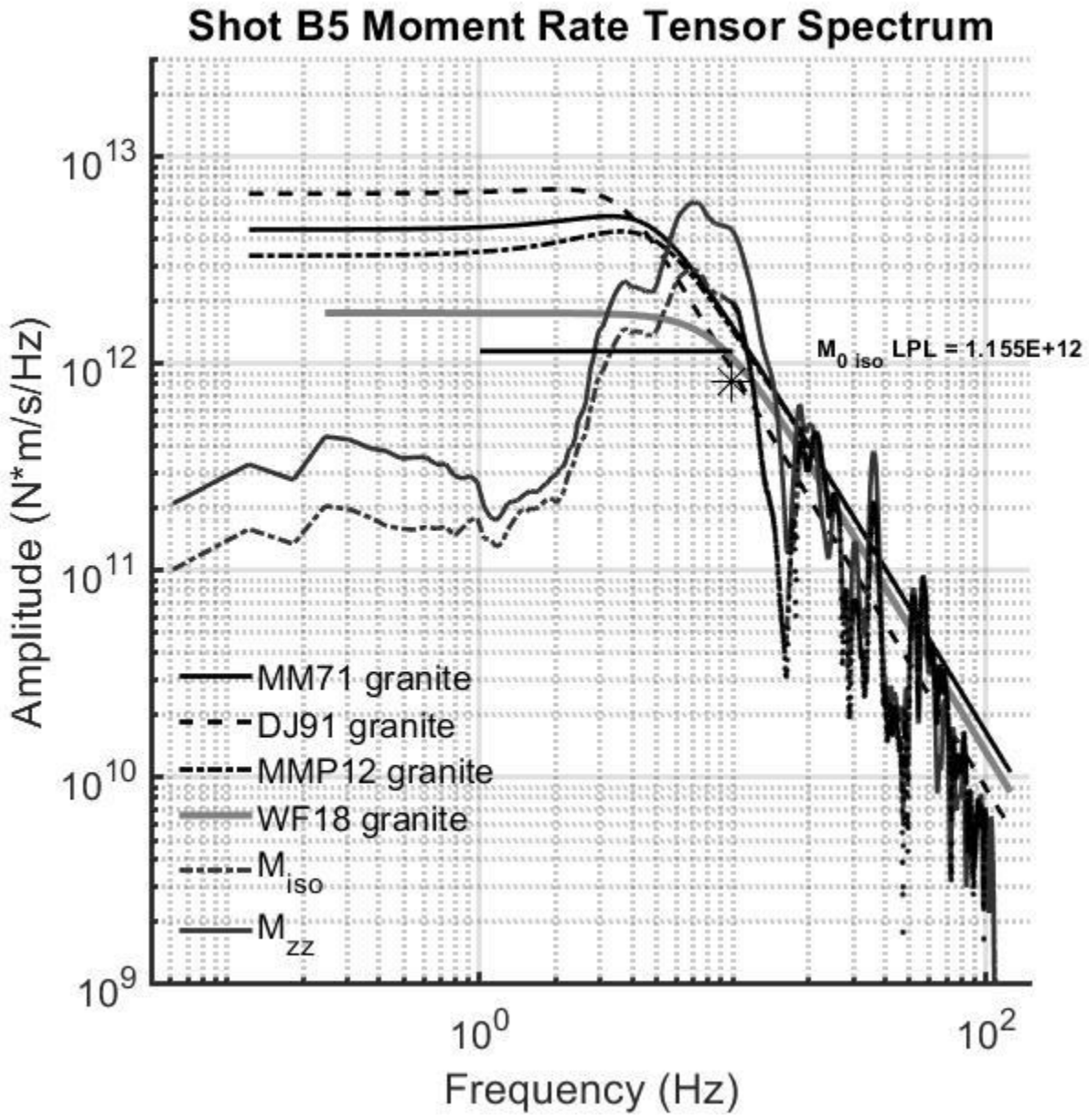

A 15 – Shot B6 M_{tr} and M_{zz} moment rate tensor time series with current prevailing isotropic source models. Isotropic component long period level marker bar and isotropic spectra corner frequency star also shown.

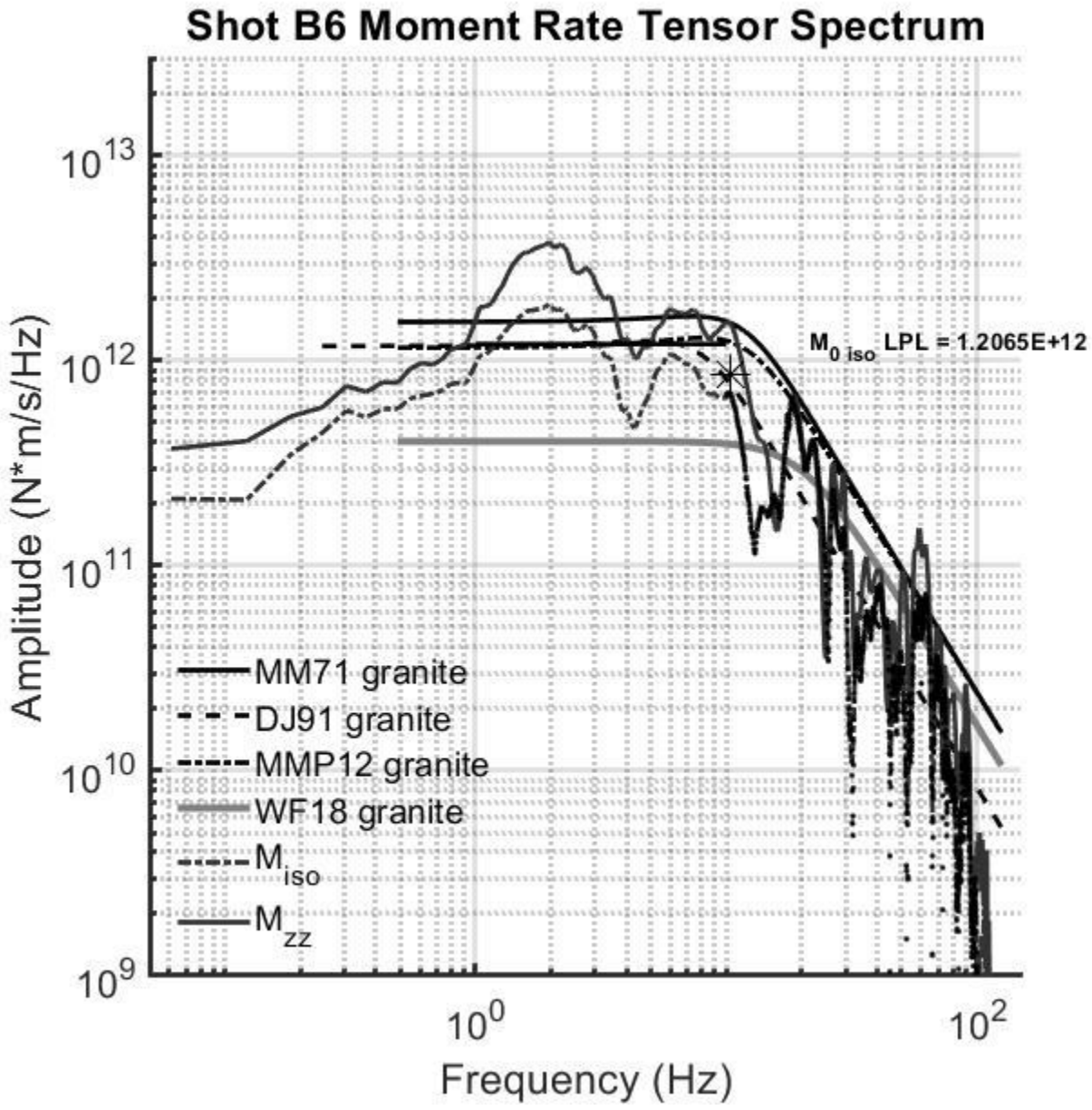

A 16 – Shot B7 M_{tr} and M_{zz} moment rate tensor time series with current prevailing isotropic source models. Isotropic component long period level marker bar and isotropic spectra corner frequency star also shown.

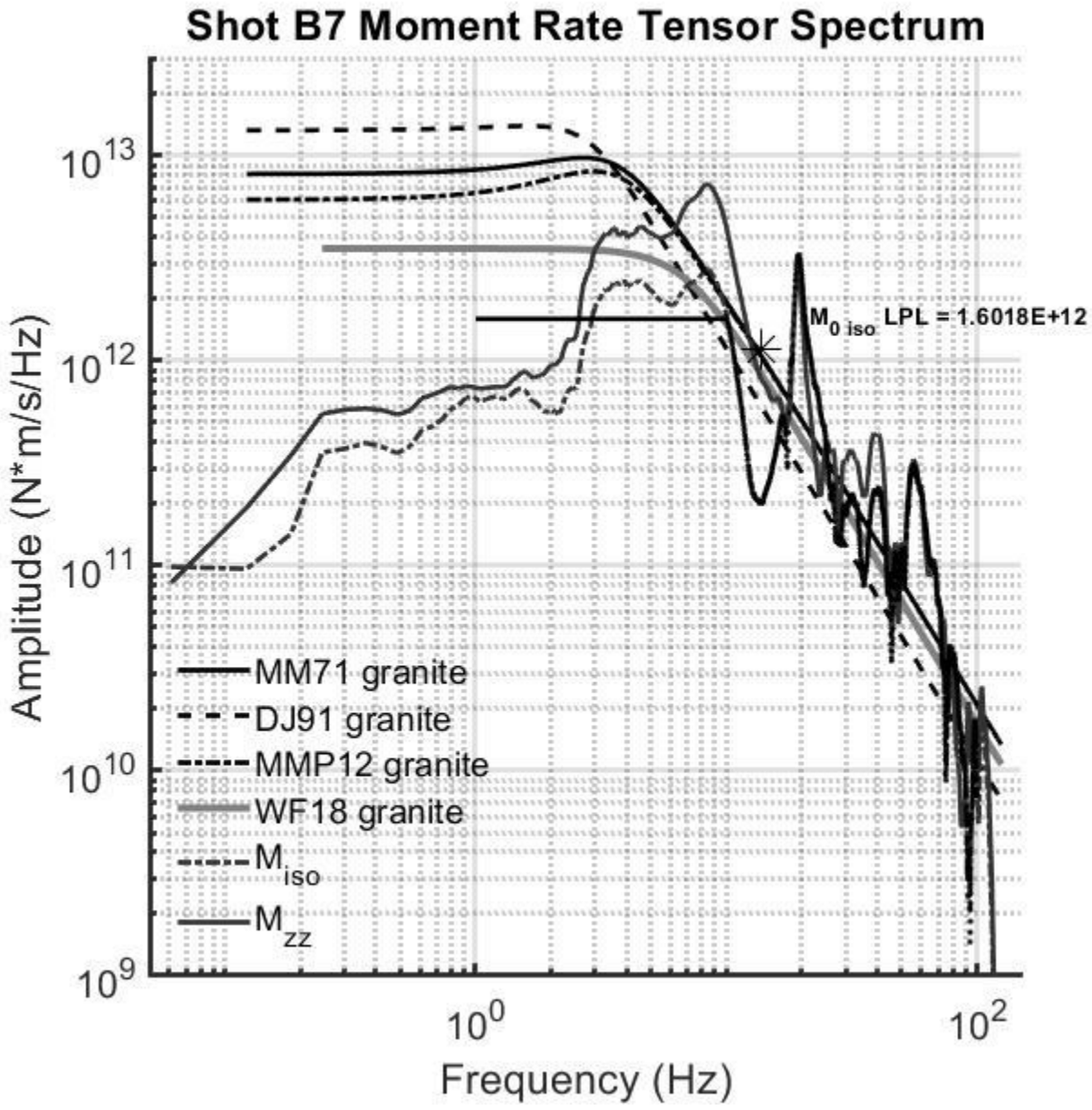

A 17 – Shot B8 M_{tr} and M_{zz} moment rate tensor time series with current prevailing isotropic source models. Isotropic component long period level marker bar and isotropic spectra corner frequency star also shown.

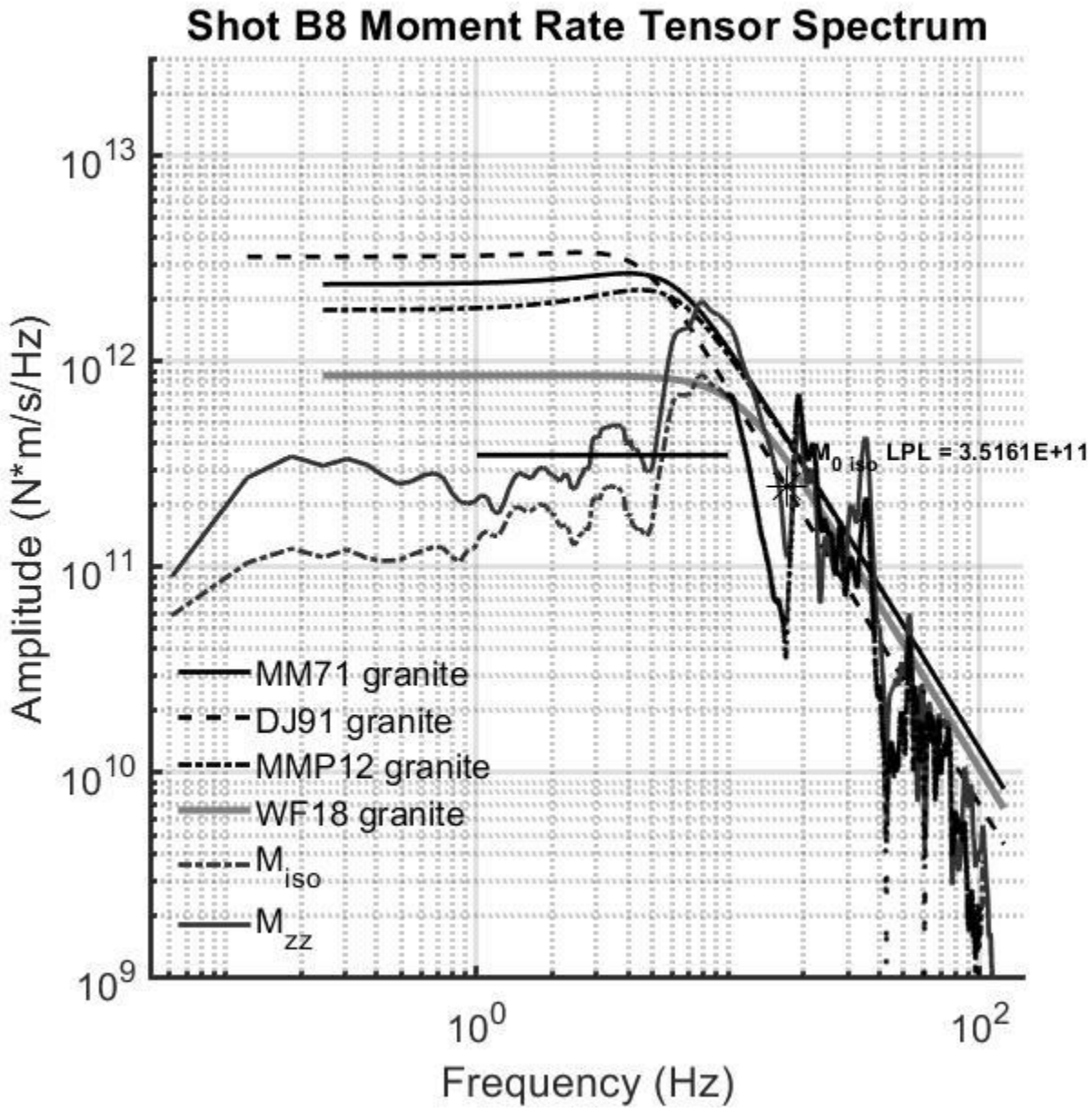

A 18 – Shot B10 M_{tr} and M_{zz} moment rate tensor time series with current prevailing isotropic source models. Isotropic component long period level marker bar and isotropic spectra corner frequency star also shown.

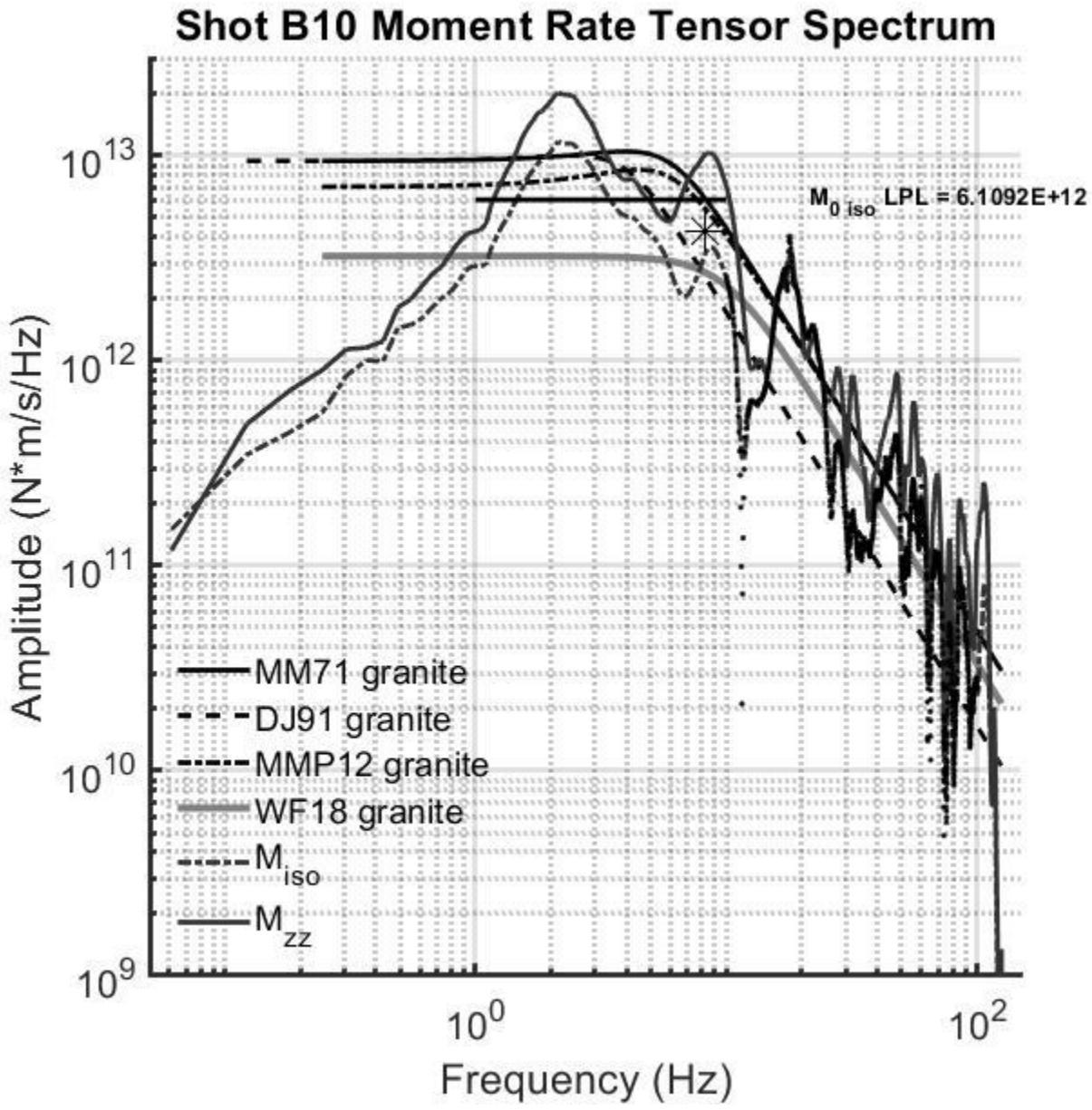

A 19 – Shot B1 Hudson diagram shown for all inversions from D.C. to 20 Hz.

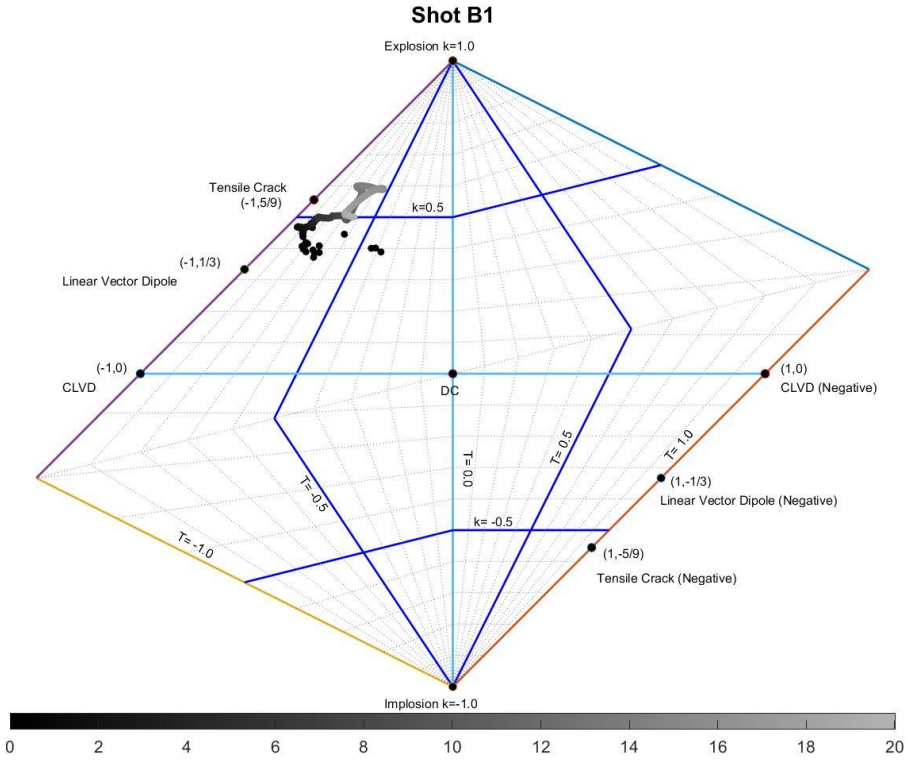

A 20 – Shot B2 Hudson diagram shown for all inversions from D.C. to 20 Hz.

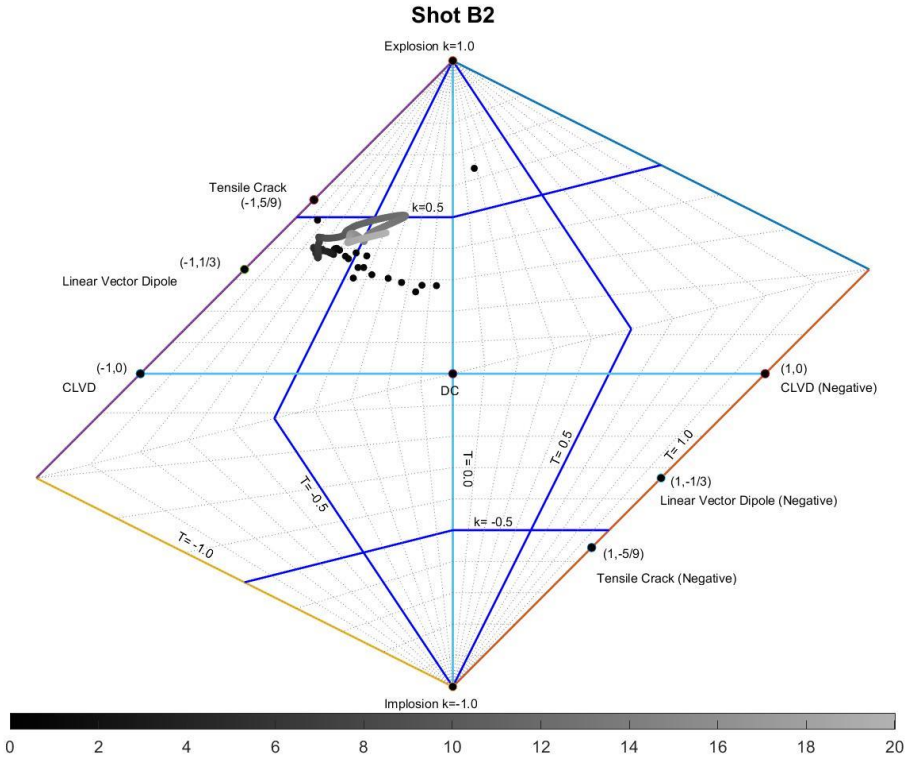

A 21 – Shot B3 Hudson diagram shown for all inversions from D.C. to 20 Hz.

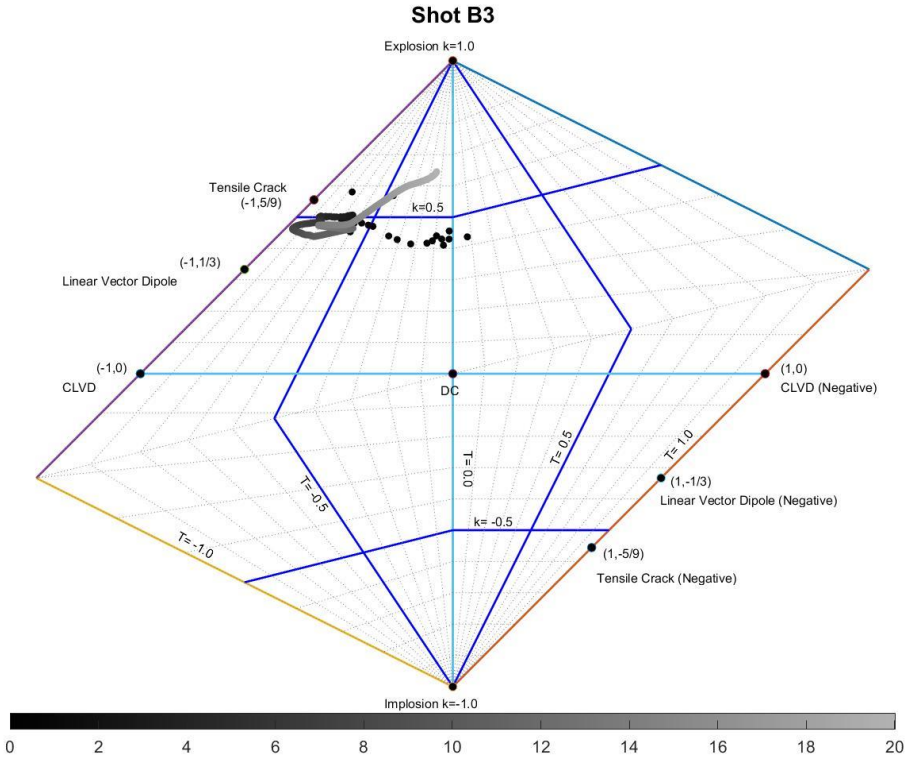

A 22 – Shot B4 Hudson diagram shown for all inversions from D.C. to 20 Hz.

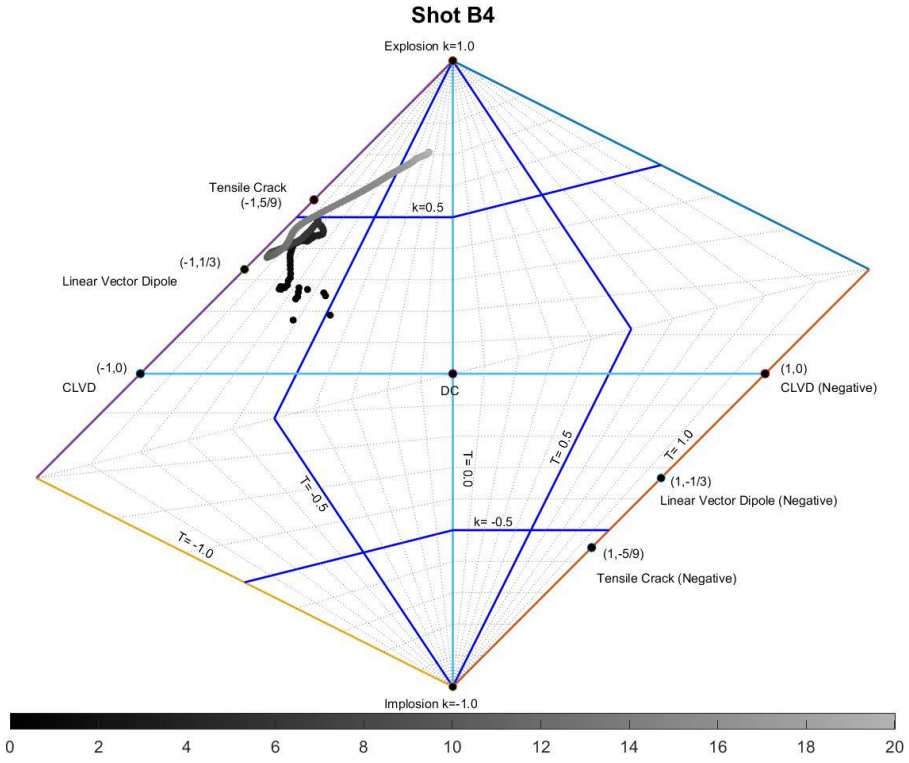

A 23 – Shot B5 Hudson diagram shown for all inversions from D.C. to 20 Hz.

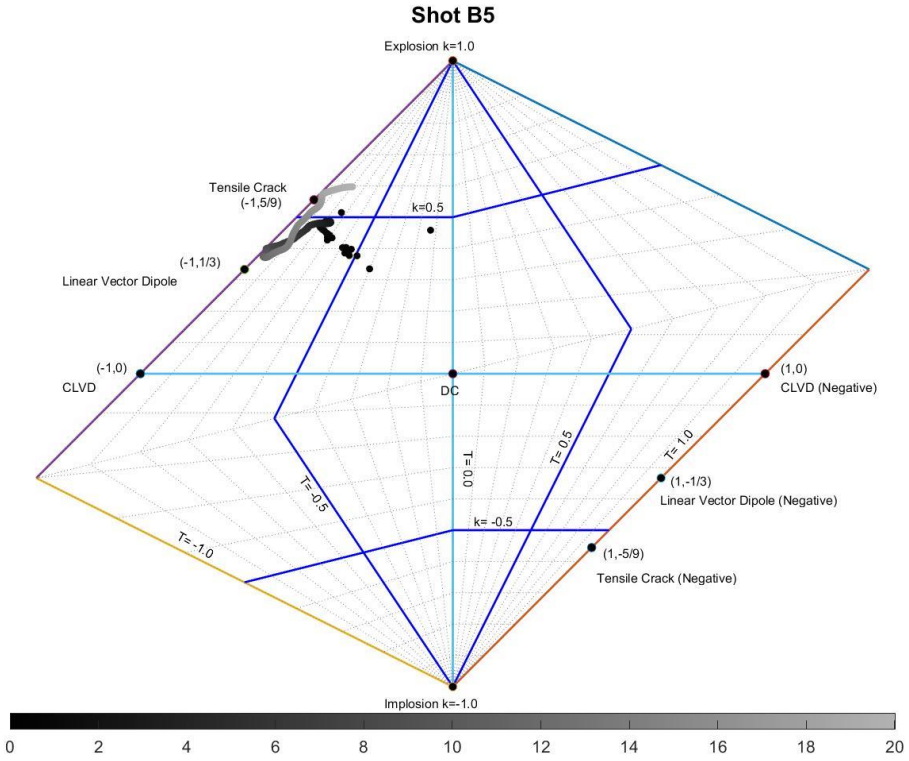

A 24 – Shot B6 Hudson diagram shown for all inversions from D.C. to 20 Hz.

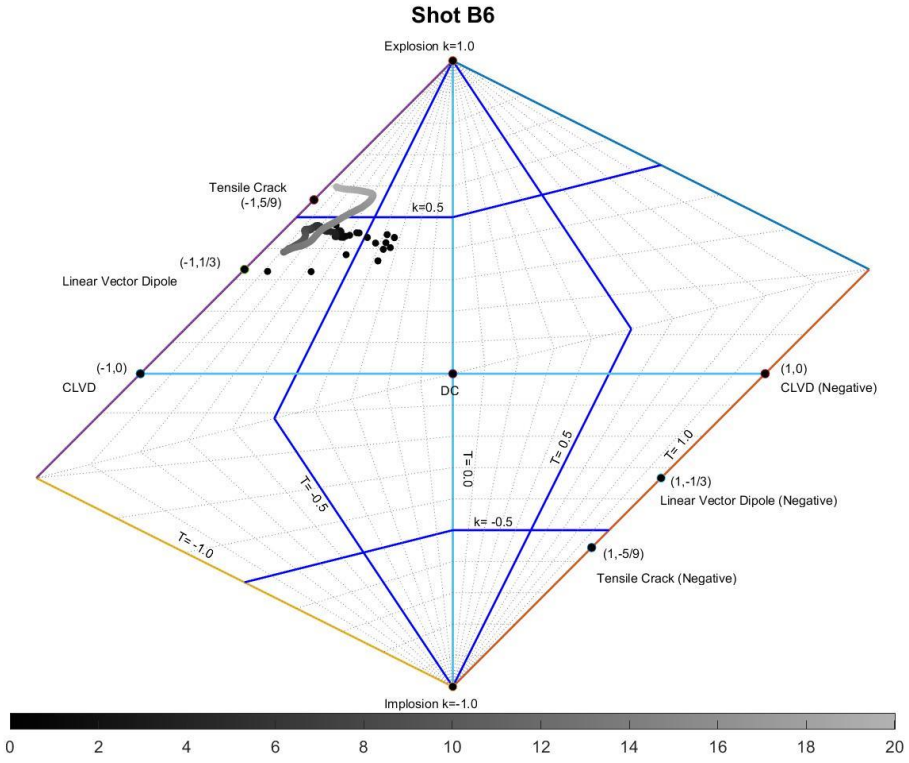

A 25 – Shot B7 Hudson diagram shown for all inversions from D.C. to 20 Hz.

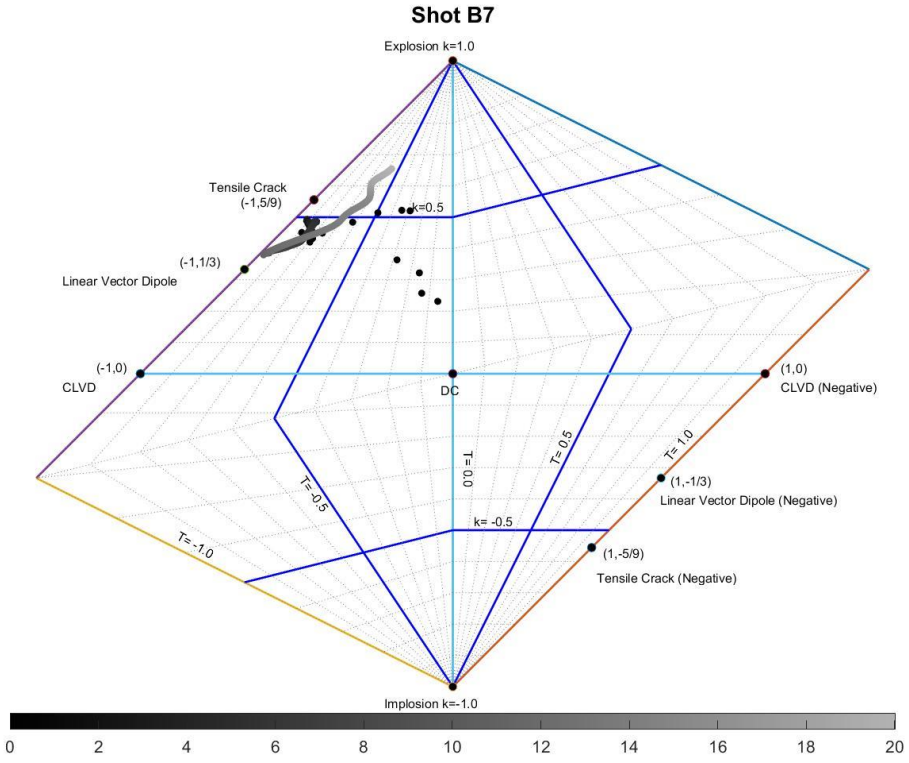

A 26 – Shot B8 Hudson diagram shown for all inversions from D.C. to 20 Hz.

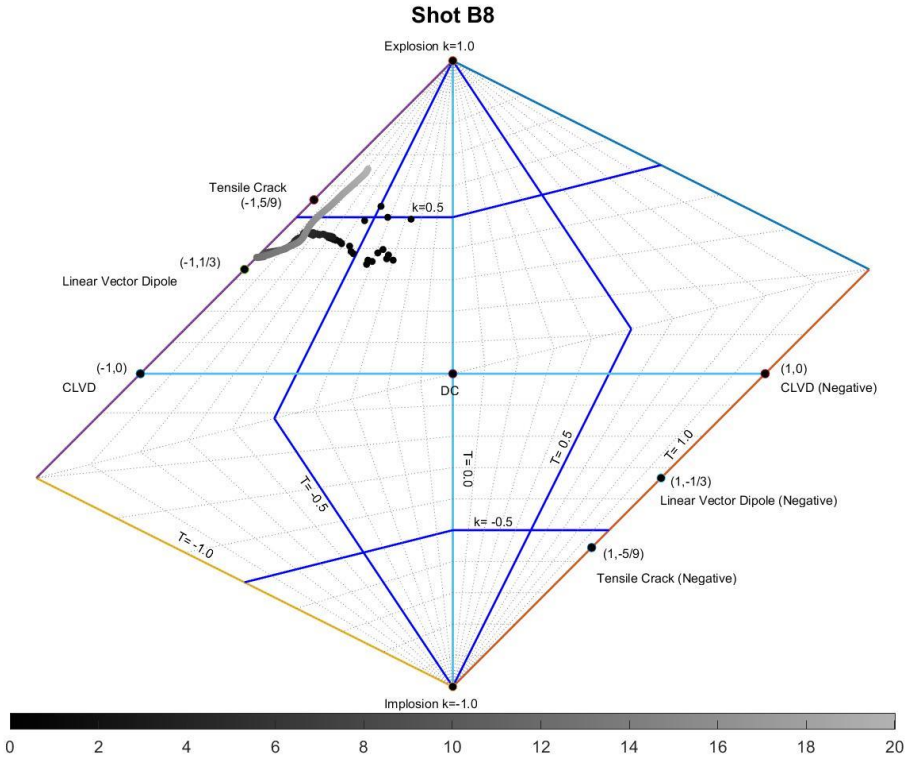

A 27 – Shot B10 Hudson diagram shown for all inversions from D.C. to 20 Hz.